INAUGURAL-DISSERTATION

ZUR

ERLANGUNG DER DOKTORWÜRDE

DER

NATURWISSENSCHAFTLICH-MATHEMATISCHEN

GESAMTFAKULTÄT

DER

RUPRECHT-KARLS-UNIVERSITÄT

HEIDELBERG

VORGELEGT VON

DIPLOM-GEOLOGIN KATHERINA FIEGE

AUS: ROSTOCK

TAG DER MÜNDLICHEN PRÜFUNG: 19.06.2013

THEMA

Compositional Analysis of Interstellar Dust as seen by the Cassini Cosmic Dust Analyzer

Gutachter:
Prof. Dr. Mario Trieloff
PD Dr.-Ing. Ralf Srama

Abstract:

The main goal of this thesis is to evaluate constraints on the composition of interstellar dust (ISD) grain candidates, obtained via impact ionization time-of-flight-mass spectrometry with the Cosmic Dust Analyzer (CDA) onboard the Cassini spacecraft at Saturn. For this work, spectra of 13 extremely rare ISD candidates were extracted from the vast Cassini CDA data set, based on the evaluation of their dynamical and compositional properties, namely mass, speed and trajectory. The candidates show a siliceous composition.
Space-based mass spectrometers need terrestrial calibration. Therefore, we accelerated a specifically manufactured orthopyroxene dust analogue from a natural rock onto the laboratory unit of the CDA, and onto the Large Area Mass Analyzer (LAMA). The dust analogue material underwent extensive geochemical analysis with scanning electron microscope (SEM) and electron microprobe analyses (EMPA) beforehand. In the course of this study we learned that the orthopyroxene separate used as dust analogue material contains five additional minor mineral species. Using classical four-isotope geochemical plots, data show clustering at orthopyroxene composition and asymmetric directional scatter towards the minor mineral endmembers. While a significant part of the stochastic scatter can well be due to experimental artifacts, the results imply that different compositions can be distinguished. It remained unclear why many particles - though being very small in the sub-micron range - seem to occur as mixtures.
Mass spectra both from CDA and LAMA, can be divided into different types according to the dominating mass line within the spectra, which are in agreement with the results from the chemical analysis performed on the LAMA spectra. Further, the types of both CDA and LAMA spectra are comparable, since they show similar features.
The calibration of LAMA spectra with orthopyroxene composition determined by EMPA allowed evaluation of sensitivity coefficients, and hence, to compare the chemical signatures of the in-situ spectra of the ISD candidates with typical compositions of terrestrial silicate minerals, and cosmochemically relevant reservoirs, e.g. primitive chondritic compositions resembling unaltered solar, volatile depleted or differentiated material, which experienced Fe-loss or gain due to core formation processes. A suite of Mg-Ca-rich ISD candidates tends to primitive, only slightly volatile depleted and undifferentiated matter, while a suite of Fe rich particles is similar to reduced metal or more oxidised Fe-rich silicate material.

Zusammenfassung:

Das Hauptziel dieser Arbeit ist, die Zusammensetzung der interstellaren Staubkandidaten (ISD) zu bestimmen, von welchen Flugzeit-Massenspektren vorliegen, die über Einschlagsionisation vom Cosmic Dust Analyzer (CDA) an Bord der Cassini Sonde am Saturn gewonnen wurden. Für diese Arbeit wurden 13, für interstellaren Staub typische Spektren, aus dem Cassini-CDA Datensatz extrahiert, basierend auf der Untersuchung ihrer dynamischen und kompositionellen Eigenschaften, nämlich Masse, Geschwindigkeit und Richtung. Die Spektren zeigen Partikel mit silikatischer Zusammensetzung.
Weltraum-basierende Massenspektrometer müssen im Labor kalibriert werden. Hierfür

wurde aus natürlichem Gestein speziell angefertigter Orthopyroxen-Staub auf das Labormodell des CDA und auf den Large Area Mass-Analyzer (LAMA) beschleunigt. Die Staubanaloge wurden vorher intensiv mittels Rasterelektronenmikroskop (SEM) und Elektronenmikrosonde (EMPA) analysiert. Im Laufe der Untersuchungen wurde festgestellt, dass das Orthopyroxenseparat aus fünf weiteren Mineralen besteht. In klassischen geochemischen 4-Isotopendiagrammen reflektieren die meisten Daten Orthopyroxenzusammensetzung, eine Minderheit der Daten zeigt asymmetrische Streuung in Richtung der Zusammensetzung der übrigen Mineralphasen. Während die stochastische Streuung auf experimentelle Artefakte zurückgeführt werden kann, legen die Resultate nahe, dass verschiedene Zusammensetzungen identifiziert werden können. Es blieb allerdings unklar, warum viele Partikel - mit sehr kleinen Größen im Submikrometerbereich - als Mischung verschiedener Minerale aufzutreten scheinen.
Massenspektren sowohl von CDA als auch LAMA können in verschiedene Typen unterteilt werden, ausgehend von der das Spektrum dominierenden Massenlinie. Dieses deckt sich mit den Ergebnissen der chemischen Analyse der LAMA-Spektren. Weiterhin sind die verschiedenen Typen in CDA und LAMA-Spektren miteinander vergleichbar.
Die Kalibration der LAMA Spektren mit Orthopyroxenzusammensetzung (bestimmt durch EMPA) erlaubte die Evaluierung von Sensitivitäts-Koeffizienten und somit den Vergleich der chemischen Signatur der ISD Kandidaten mit typischen terrestrischen Silikatmineralen, und kosmochemisch relevanten Reservoiren, wie z.B. primitiven Chondriten mit fast unveränderter solarer Zusammensetzung, extraterrestrischem Material verarmt an volatilen Elementen oder differenziertes Material, das Fe-Anreicherung oder Verarmung aufgrund von Kernbildungsprozessen erfuhr.
Eine Population von Mg- und Ca-reichen ISD Kandidaten tendiert zu primitiver, nur leicht an volatilen Elementen verarmter und undifferenzierter Materie, während eine Population Fe-reicher Partikel eher reduziertem Metall oder oxidierten Fe-reichen Silikaten ähnelt.

Dedicated to my family

Contents

List of Figures

List of Tables

1 Introduction

"E quindi usciemmo a riveder le stelle"
(Then we stepped out and saw the stars)
La comedia divina
Inferno XXXIV, 139

1.1 Cosmic dust in the Universe

The occurrence of dust in the Universe has been subject to scientific discussions for centuries. Giovanni Domenico Cassini was the first to scientifically investigate the zodiacal light in 1683 [Grün et al., 2001] and hence, interplanetary dust, after Joshua Childrey identified the zodiacal shine as a phenomenon caused by scattered sunlight from dust grains in 1661. It then was firstly explained by Nicolas Fatio de Duillier in 1684.

Figure 1.1: A 360 degree panorama of the Southern sky. Well visible is the Milky Way, with partly obscuring dark dust clouds, and the zodiacal light illuminated by a rising moon (ESO)

Another phenomenon was the occurrence of general cosmic light extinction, which has already long been recognized by astronomers. A first suggestion pointing into the direction of introducing some kind of matter between the stars, arose during the attempt to answer the question of the dark night sky, which could never be dark, if an infinite Universe would be uniformly filled with stars (Olbers' paradox). Thus, Loys de Cheséaux (1744), and later Olbers (1823), suggested an ether or similar. As well, dark holes in the sky, or starvoids, have been recognized and discussed during that time. W. Herschel described this phenomenon in his report " On the Construction of the heavens" in 1785, where he claimed that " such openings in the heavens" were due to the formation of star cluster, which leaves unoccupied areas behind. We know today that such "dark markings" (after E.E.Barnard), e.g. visible when observing the Milky Way, are simply due to dust clouds that obscure the starfields. Herschels opinion domineered this particular topic until the end of the 19th century, when celestial photography was applied and the concept of nebulous obscuring

matter in the universe gained more and more attention (e.g., Dorschner [2010] and references therein).

Finally, around 1930 with the works of Schalén and Trümpler, the interaction of small grains with starlight was the most plausible explanation for general interstellar exstinction for the weakening and reddening of starlight. And hence, interstellar dust research became a new branch of astrophysics.

1.1.1 The origin of dust in the interstellar medium

Figure 1.2: Examples of dusty regions in space: The Rosette nebula (left), the Sombrero galaxy (middle) and the star forming region N90 (right) (Hubble/ESA)

It is important to characterize and understand the nature of cosmic dust in the Universe, since it plays a highly important role in many chemical and physical aspects of galactic evolution. Until recently, we could only rely on remote observations when studying interstellar dust. Hence, observations were made based on the interaction of interstellar dust with electromagnetic radiation [Draine, 2011]:

- Exstinction of starlight by absorbtion and scattering
- Polarization of starlight
- Scattered light in reflection nebulae
- Thermal emission from dust
- Scattered haloes around x-ray point sources
- Microwave emission from dust
- Luminescence of dust grains

Other information about interstellar dust comes from non-electromagnetic sources:

- Presolar grains, which have been preserved in meteorites
- Depletion of refractory elements from the interstellar gas

- Abundance of H_2 in the ISM, due to possible catalysis on dust grains

About 1% in the interstellar medium (ISM) is dust. This interstellar dust is the result of a constant cycle of birth, death and rebirth of stars since the early days of galaxy formation. Stars, or stellar systems, evolve from a mixture of gas and dust in the local concentrations of the ISM, the molecular clouds - the coolest and densest structures within the ISM. After a lifetime of burning their nuclear fuels, stars die. In the case of low- and intermediate - mass stars, death is accompanied by massive mass loss due to stellar winds with stellar explosion, which leaves a white dwarf as a remnant. Massive stars experience a collapse of their core region to a neutron star, which ejects most of their mass instantly in a supernova event. Thus, about 50% to 90% of a stars' initial mass is returned into the ISM and now serves as raw material for the next generation of stars to be formed [Gail, 2010].

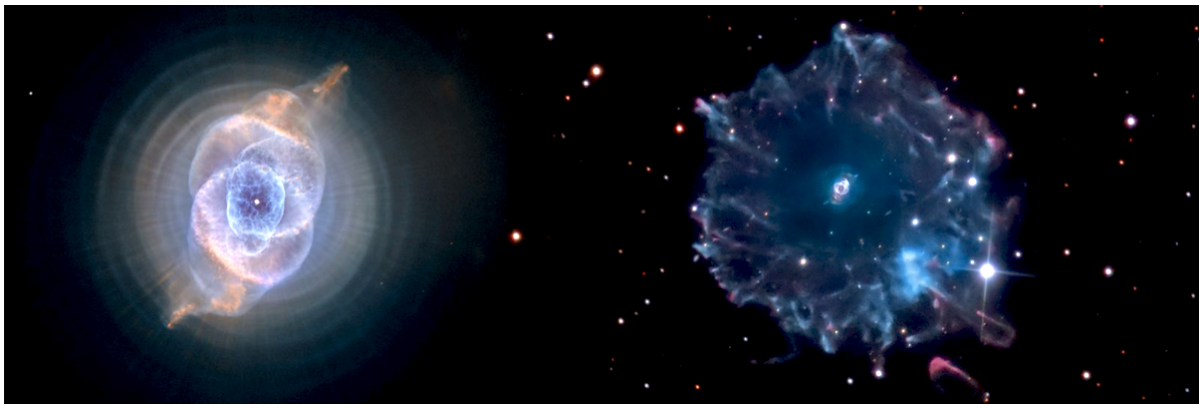

Figure 1.3: The Cat's Eye nebula in a close-up (left) and the faint gaseous halo surrounding it (right), up to three light years across (Hubble/ESA

In these cycles, the baryonic matter of a galaxy is constantly recycled between stars and the ISM, with only a fairly small fraction of new material infall, which seems to stem from intergalactic space [Gail and Hoppe, 2010]. The ISM is very homogenous in composition, since turbulent flows mix the returned matter with the ISM on rather short time scales, and thus, there is no substantial variation in composition visible, only a slow increase of heavy element content in successive stellar generations.

1.1.2 Elemental abundances and the composition of dust in the ISM

The primordial composition of the baryonic matter in the early Universe was fairly simple: H, He and minor Li. Heavier elements, from carbon to the actinides, are the result of nucleosynthetic processes in stars. Burning processes in massive stars produce elements up to iron, even heavier elements need neutron-capture processes (either r-process elements or s-process elements). The return of these elements into the ISM during the cycle of matter results in an increase of the metallicity of the ISM over time. C, O, Si, Mg, Fe, S, Al, Ca, Na, and Ni are the most interesting abundant refractory elements, since they form the dusty material. O, C, Fe, and Ni account for 80% of the mass fraction of all elements heavier than He. Si, Mg, N and S contribute 16%, and the remaining 4% are contributed by all other elements heavier than He.

In most of the lifetime of a star, its photospheric element abundances reflect the standard cosmic element abundances of the ISM at the time and the location during its formation in the molecular cloud, with only few exceptions. The latter is the case, when a star evolves off the main sequence to highly advanced stages, which results in a considerable different composition of the formed dust. Stars produce mainly silicate or carbon dust. AGB stars with spectral type M and Red Supergiants (RSG) produce silicate dust, whereas AGB stars with spectral type C, Wolf-Rayet stars, novae and supernovae produce mainly carbon dust [Gail and Hoppe, 2010]. Oxygen-rich dust particles, e.g. silicates, most likely form at an early stage on the AGB. Here, the C/O is < 1 in the stellar wind, whereas if C/O > 1, carbonaceous dust forms, at later stages on the AGB (for detailed information see e.g., Draine [2011]; Tielens [2005]; Gail [2010]; Gail and Hoppe [2010]).

A number of different dust grain compositions have been identified within the ISM via infrared spectroscopy of the vibrational resonances of the solids. Observed were graphite, amorphous carbon and hydrogenated amorphous carbon (HAC's), poly aromatic hydrocarbons (PAH's), nano-diamonds and carbides, ices, stardust, oxides, silicon and silicates. Important for this work are the silicates and thus only those will be further described here. A more detailed description about dust components in the ISM can be found in Tielens [2005] and Molster et al. [2010]. However, most species within the dust show only one significant feature, whereas amorphous and crystalline silicates show more than one distinct band, as well as $\mathrm{MgAl_2O_4}$, FeS and nanodiamonds.

Amorphous silicates in the ISM

Amorphous silicates are the most abundant grain species in interstellar space. Their IR spectra show broad bands at 9.7 μm, which is due to the Si-O stretch resonance, and at 18 μm, due to the Si-O-Si bending mode in the $\mathrm{SiO_4}$ tetrahedron [Henning, 2010] . Experimental studies with analogue material have shown that such resonances only show a minor dependence on composition [Dorschner and Henning, 1995], thus it is very difficult to derive constraints on the Mg/Fe-ratio and, more over, additional incorporation of Ca and Al, either as cations within the lattices or as grains within the Si-matrix (dirty silicates). However, as Jones and Merrill [1976] have pointed out, amorphous silicates should have a substantial opacity in the near-IR, due to additional iron, based on temperature analysis of dust condensation in the outflows of late-type stars. More recent studies, using optical constants from well characterized material for fitting the spectra of amorphous silicates (e.g., [Dorschner and Henning, 1995]; [Kemper et al., 2002]; [Demyk et al., 1999] and [Demyk et al., 2001]) , show that amorphous silicates around young stars seem to be rather similar to a pyroxene-like composition, whereas amorphous silicates around evolved cool giants are better represented by a stoichiometry similar to olivine, if some source of opacity, i.e. additional iron grains are considered. Possibly the best analogues for amorphous silicates within the ISM and around young stars seem to be glasses with embedded metals and sulfides (GEMS). These have been found in interplanetary dust particles (IDP's) and their properties show quite some similarities [Bradley et al., 1999].

The composition of interstellar silicates observed in the direction of the galactic center shows that the silicates are Mg-rich and Fe-poor, with $Mg/(Fe+Mg) \approx 0.9$, which is consistent with the amorphous silicates in GEMS [Min et al., 2007]. Interstellar silicates being

Mg-rich and Fe-poor has also been derived from X-ray absorption and scattering analysis [Costantini et al., 2005]. But up to now, distinct evidence is still missing, since the ranges in the $(Mg+Si)/Si$ in silicates at the galactic center and of the GEMS differ within wider ranges [Min et al., 2007].

Crystalline silicates in the ISM

Crystalline silicates have been actually only known to occur on Earth, in comets within our Solar System (Hanner et al. [1994]; Hanner [1996]) , in IDP's (Mackinnon and Rietmeijer [1987]; Bradley et al. [1992]) and in dusk disks around T-Tauri stars [Cohen and Witteborn, 1985] and β-Pictoris [Knacke et al., 1993]. After launching Infrared Space Observatory (ISO), which offers extended wavelengths of up to 200 μm on spectrographs onboard [Henning, 2010], scientists were finally able to study the composition of cold dust. Up to now, no convincing evidence has been found for the presence of crystalline silicates within the ISM, other than around young stars, and in the outflows of O-rich evolved stars (Sloan et al. [2008]; Waters et al. [1996]), as well as around stars that actually show a C-rich composition, with the latter probably resulting from previous heavy mass loss episodes.

Crystalline silicates show sharp features that allow accurate identification, especially in the 10 μm complex region. Most abundant seem to be forsterite (Mg_2SiO_4) and enstatite ($MgSiO_3$). Even the abundance of clino- and orthoenstatite can be investigated, by finding clear differences at wavelengths beyond 40 μm. The abundance of clino- and orthoenstatite is relatively equal around most stars. Only around stars with very high mass loss rates, orthoenstatite might be more abundant [F. J. Molster et al., 2002]. Moreover, even evidence of Ca-pyroxene, namely diopside, has been found, though it is hard to identify Ca-pyroxenes unambiguously based on only short wavelength range [Koike et al., 2000]. Thus, the identification of diopside can only be done clearly in very cool dust environments (T< 100 K) and hence, only around OH/IR stars and planetary nebulae. Crystalline silicates appear to be very Mg-rich and Fe-poor as well. This is evidenced by the 69 μm feature, indicating a high Mg/Fe-ratio in olivines in the outflows of evolved stars, and with the 40.5 μm feature in pyroxenes, as well in the dusty winds of evolved stars. However, it is not easy to determine the exact composition of these crystalline silicates around young stars by using the 69 μm feature, simply due to the lack of data. Further, results may be biased by low abundances of crystalline silicates, by high temperatures of the grains or by additional iron within the silicate matrix. All these occurrences can lead to a weakened 69 μm feature (Koike et al. [1993]; Jäger et al. [1998]).

The abundance of crystalline silicates in different environments can be estimated by using radiative transfer calculations [F. J. Molster et al., 2002]. Hence, the following conclusions can be made :

- The abundance of crystalline silicates in the winds of evolved stars is ∼10% or less
- Enstatite is roughly three times more abundant in stellar outflows than forsterite
- There seems to be no crystalline silicates around low mass loss stars (which might be a temperature effect)

- The abundance of crystalline silicates around peculiar objects can be very high, i.e. up to 75% of the grain population

All in all, even though no clear evidence has been given so far for crystalline silicates within the ISM, the upper limit of their abundance has been set to $\approx$ 2.2% (of the estimated 1% dusty matter within the ISM, that is) [Kemper et al., 2005].

1.1.3 The origin of interplanetary dust

Since this thesis has its focus on interstellar dust, this section will only give a brief overview with respect to interplanetary dust sources and dust formation mechanisms within interplanetary space. For detailed reviews see e.g., Grün et al. [2001] and Berg et al. [1975].

Interplanetary dust originates within our solar system and stems from a variety of sources, showing a diverse range of composition and dynamical properties. One can see interplanetary dust in form of the zodiacal light, which is a result of scattering sunlight off interplanetary dust particles orbiting the sun, even without any optical substitution. Interplanetary dust is a part of a complex cloud of dust and debris spreading out a few solar radii through the Kuiper Belt and farther. Sources of interplanetary dust are Comets, asteroids, atmosphereless planetary satellites, Edgeworth-Kuiper-Belt objects, Jovian and Saturnian systems and, within Earth's closer perimeter, mankind itself. Dust from comets, ejected via outgassing, shows silicates, carbonaceous matter (CHON-particles), sulphides and oxides, further metals and carbonates (Sekanina [2001]; Flynn et al. [2006]; Flynn [2008]). Cometary dust has been investigated via remote sensing techniques [Lisse et al., 2007], in situ measurements (Kissel [1986]; Kissel et al. [2004]; Dikov et al. [1989]) and returned samples.

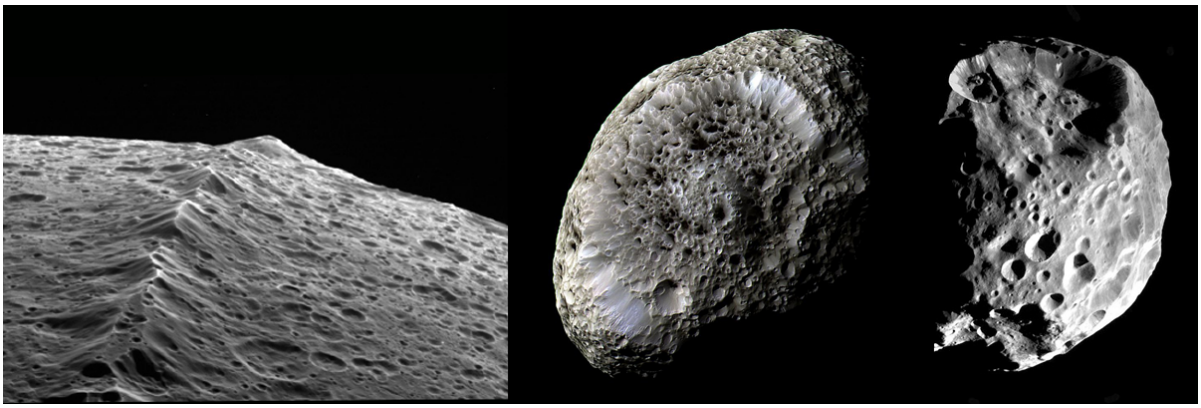

Figure 1.4: Examples of heavily cratered surfaces of satellites in the Saturnian system: the surface of Iapetus with its equatorial ridge (left), the moon Hyperion (middle), with its intriguing surface appearance and Phoebe (right), showing enormous craters (NASA/JPL)

Dust from asteroids is produced during collision events or from impact ejecta, with a composition that should resemble the composition of the surface of the body or its bulk composition, considering catastrophic events. Similar applies to atmosphereless satellites (Fig. 1.4), planets and Edgeworth-Kuiper-Belt objects. They as well experience a multitude of collisions with larger bodies and micrometeoroids, and some show further outgassing or

cryovolcanism (e.g., Enceladus, Fig. 1.5). Asteroids show mainly silicates, lesser amounts of metals, such as Ni and Fe, further sulphides and oxides, whereas larger planetary satellites and planets show a variation of salts, silicates, organics and ices, depending strongly on the source body and its surface variations. Dust has been investigated via the analysis of the material [Mothé-Diniz et al., 2005], reflectance spectroscopy and by the investigation of meteorites. Dust particles ejected via cryovolcanism have been directly measured at the site of occurrence (Hillier et al. [2007]; Postberg et al. [2008]; Postberg et al. [2009b]).

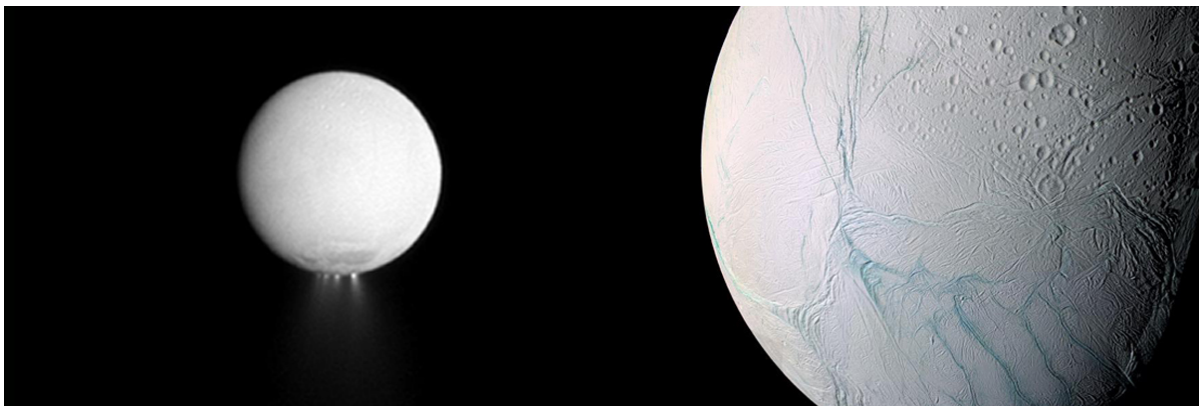

Figure 1.5: The cryovolcanically active moon Enceladus and its jets emanating from the tiger stripes at the south pole, releasing water ice into the Saturnian system (NASA/JPL)

Stream particles originate within planetary systems, such as the Jovian and the Saturnian systems. Here, charged particles are ejected into space with very high velocities. Their composition resembles that of the source region within the particular planetary system. In the Jovian system, the source lies within Io and the Io plasma torus [Graps et al., 2000] and is comprised by mainly NaCl and KCl salts with minor traces of sulphides [Postberg et al., 2006]. In the Saturnian system, the sources are in the A and E rings and show mainly silicates and volatile species [Kempf et al., 2005]. Earth is as well heavily bombarded with cosmic objects, mainly meteorites. Meteorites are rich in silicates, such as olivine and pyroxene, may contain refractory inclusions, such as Fe or Ni, further CAI's (Ca- and Al-rich inclusions). Other types, such as carbonaceous chondrites, contain a lot of hydrous mineral species and organic matter.

1.2 Dust astronomy

What is "*Dust Astronomy*"? Dust astronomy enables us to gain knowledge not only of a very small dust particle's trajectory and composition, but as well of its source environment, via the determination of its trajectory and bulk properties with dust telescopes mounted on space-based "dust observatories" [Grün et al., 2005]. Most of the knowledge of dusty phenomena in space (e.g., ISD) has been established solely through astronomical observations, often ground-based. In the case of IDP'S even real samples could be investigated, either meteoroids found on Earth or particles that have been collected by stratospheric collection cruises with aircrafts at $20\,\mathrm{km}$ altitude [Grün et al., 2005]. Thus, for the investigation of single particles within highly variable environments (e.g., planetary rings, dust streams, or low-dust-flux environments, such as interplanetary space) in situ detection has been

developed as a method during recent decades [Grün et al., 2005]. In this section, I give a brief introduction into aspects of instrument development.

The first dust detectors in space were on the Orbiting Geophysical Observatory (OGO) satellites and on the Lunar Explorer 35, which were launched in 1966 and 1967, respectively. These utilized time-of-flight (TOF) systems to analyze the trajectory of particles with thin film front sensors , an impact sensor in the back and a $5\,\mathrm{cm}^2$ sensitive area [Grün et al., 2005]. However, this mission failed due to wrong presumptions. Only very few impacts could be recorded. Later, dust detectors on the spaceprobes Pioneer 8 and Pioneer 9, moving on heliocentric orbits, were successful. Their detectors consisted of 16 parallel TOF penetration systems, two consecutive sensors with a sensitive area of $100\,\mathrm{cm}^2$, and measured successfully the trajectories of micrometeoroids [Grün et al., 2005]. Thus, the rough orbital elements and trajectrories for 20 particles could be determined (Wolf et al. [1976], McDonnell [1978]).

Following were dust detection systems on Pioneer 10 and 11, exploring meteoroids in the asteroid belt and farther. Onboard were a zodiacal light photometer [Hanner et al., 1976], a penetration detector consisting of 234 pressurized cells ([Humes, 1980]) and the optical Asteroid and Meteoroid detctor (AMD) [Soberman et al., 1974]. This simple dust detector was very successful and measured dust out to 18 AU [Humes, 1980]. A new line of dust collectors combined the impact ionization detector with a mass spectrometer, to analyze the composition of the impactor directly (cf. Auer and Sitte [1968]; [Hansen, 1968], Friichtenicht et al. [1973] and Dietzel et al. [1973]). Such composite instrument (though the mass resolution of these early combined detectors was very low with $\sim$50) was flown on the Helios spacecraft and finally, meteoritic compositions could be classified into chondritic and Fe-rich [Leinert and Grün, 1990].

High-resolution TOF impact ionization mass spectrometer where then flown on VEGA 1 und 2 and Giotto missions to Halley by Kissel [1986] (PUMA and PIA instruments), which marks a breakthrough in the field of instrument development. The detector was a reflectron-type impact ionization TOF mass spectrometer with a mass resolution of up to 200. The instrument CIDA on the Stardust spacecraft, which is a follow-up of the PUMA and PIA instruments, is even more sophisticated. It utilizes a twenty times lager sensitive area and has an improved mass resolution of $\sim$250 (laboratory tests) [Grün et al., 2005]. Further, the dust trajectory detection systems have been improved: the dust detector onboard Cassini, the CDA (2.1), includes a charge sensitive entrance grid system (QP detector, [Srama et al., 2004]), which has reliably detected the charge of individual interplanetary dust grains [Kempf et al., 2004]. Measurements with the CDA onboard Cassini provided new and spectacular new insights, with respect to the Saturnian system and, especially to interstellar dust within our solar system, since successful measurements of ISD with the CDA were reported by (Altobelli et al. [2003]; Altobelli et al. [2013]), which will be described in section 1.4.

1.3 The Cassini-Huygens mission

The Cassini-Huygens mission, named after the French-Italian astronomer Giovanni Domenico Cassini and the Dutch astronomer Christiaan Huygens, is a flagship class mission to the outer planets, i.e. the Saturnian system„ with NASA/ASI providing the orbiter and ESA providing the Huygens probe. Other missions of that class were, e.g. Galileo, Voyager and Viking. The Cassini spacecraft was launched in October 1997 from Cape Canaveral and entered the Saturnian system in 2004 and had its primary mission objectives completed in July, 2008. The mission got extended first until June, 2010 (Cassini-Equinox mission) for more detailed studies of the Saturnian system during Equinox in April, 2009. The second expansion (Cassini-Solstice mission) is currently ongoing until 2017.

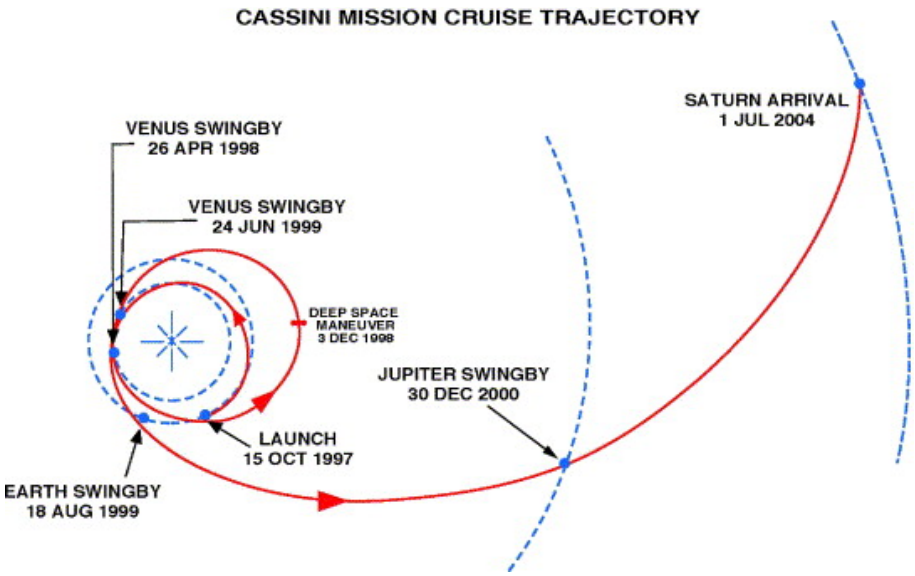

Figure 1.6: The trajectory of the Cassini spacecraft from Earth to the Saturnian system, launched in 1997, and reaching its destination, the Saturnian system in 2004, after paying visits to Venus and Jupiter (NASA)

The Cassini mission had seven primary objectives:

- the investigation of the structure and dynamics of Saturn's' rings
- the investigation of satellite surfaces and their geological history
- investigation of the nature of dark material on Iapetus
- investigation of the structure and dynamics of Saturn's magnetosphere
- investigation of the dynamics of Saturn's atmosphere
- the investigation of Titan's surface
- investigation of of Titan's atmosphere

These investigations were conducted with a number of instruments onboard the spacecraft- a plasma spectrometer (*CAPS*), a direct sensing instrument, measuring electrical charge

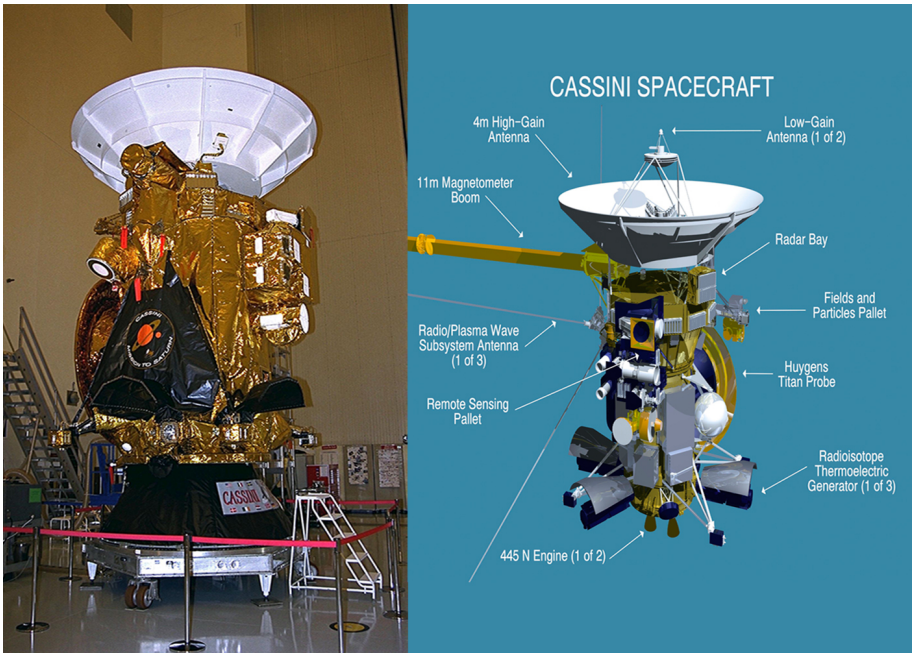

Figure 1.7: The Cassini spacecraft on display (left) and the multitude of instruments on the spacecraft (right) (NASA/JPL)

and energy of particles to investigate Saturn's magnetic field, as well as plasma in these surroundings and the solar wind radiation in the magnetosphere. A composite IR-spectrometer, a remote sensing instrument, measuring IR-waves coming from objects (moons, rings, atmospheres, surfaces) to determine temperatures, thermal properties and composition. Cassini is carrying further an ion and neutral mass spectrometer (*INMS*), directly sensing, to analyze charged and neutral particles in the perimeter of Titan and Saturn, to analyze their atmospheres and the environment around Saturn's icy satellites and rings. The imaging science subsystem (*ISS*) takes images in visible light, as well as IR and UV pictures. The dual technique Magnetometer (*MAG*) is a direct sensing instrument, measuring the magnetic field around Saturn. *MIMI*, the magnetospheric imaging instrument captures data and images of trapped particles in Saturn's magnetosphere, to determine the overall dynamics of the magnetosphere in interaction with the solar wind, including Saturn's atmosphere and its moons. Titans surface is mapped by radar, the radio and plasma wave science instrument (*RPWS*) determines the electric and magnetic wave fields in the interplanetary medium and Saturn's magnetosphere. It is further investigating electron densities and temperatures near Titan and Saturn's magnetosphere, monitors Saturn's ionosphere, plasma and atmosphere. The radio science subsystem (*RSS*) observes how radio waves from the spacecraft change, when sent through certain objects, such as Saturn's rings or Titans' atmosphere. As well, temperatures, pressures and composition of atmospheres and ionospheres are investigated, further the structure of Saturn's rings, grain size distributions and moreover gravitational waves. *UVIS*, the ultraviolet imaging spectrograph investigates the structure and composition of Saturn's clouds and rings via the reflection of UV light off those objects. Furthermore it is capable of supporting investigations of atmospheres. The visible and infrared mapping spectrometer (*VIMS*) takes pictures with visible and infrared light to gain insights of compositions of moon surfaces, atmospheres of Titan and Saturn and rings. Finally, Cassini carries the Cosmic Dust An-

alyzer (*CDA*) to determine the size, speed, trajectory and composition of dust particles within the Saturnian system. The CDA, or better its twin-unit, utilized for this thesis, will be described in detail in 2.1.

Cassini returned spectacular new insights into the Saturnian system and our solar system in general. Some of it shall just be illustrated with the beautiful pictures, returned from the imaging systems onboard Cassini, below.

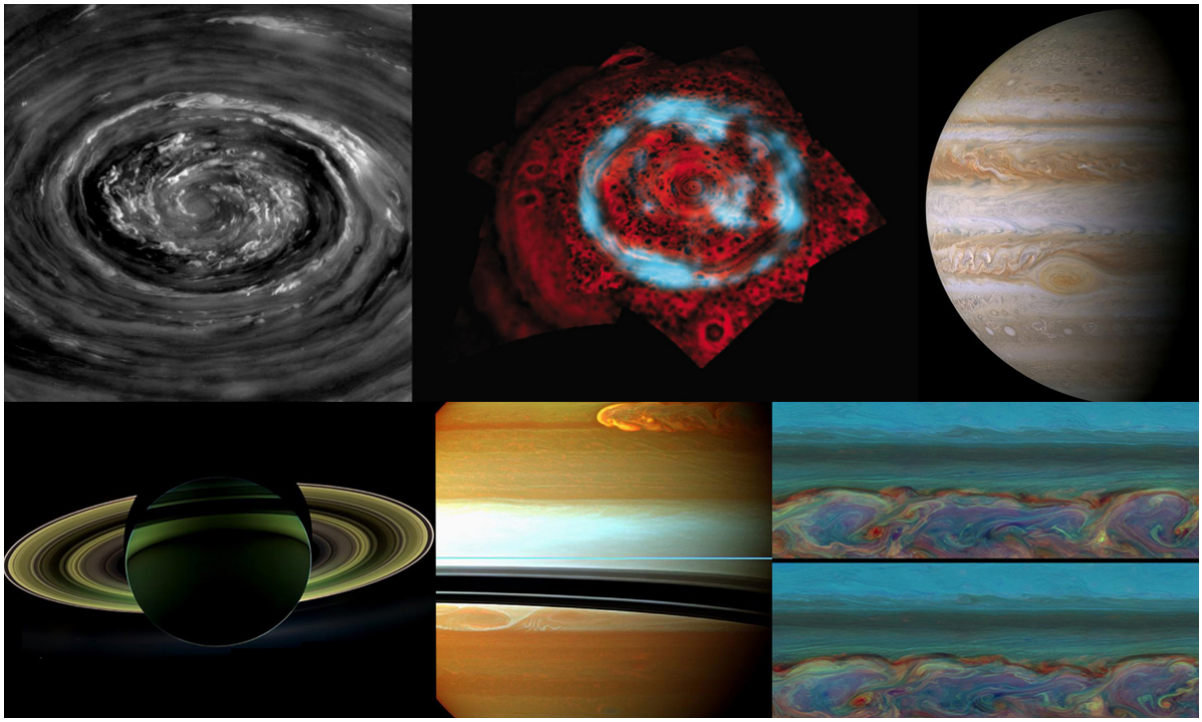

Figure 1.8: The uncalibrated upper left image shows the vortex on Saturn's North pole, as well as the image in the upper middle. In the latter, one can see the hexagonal shape of the vortex and its aurora. The upper right image is one of the highest resolution images from Jupiter taken so far. A backlit impression of Saturn is shown in the lower left image, whereas the middle and right images in the lower panel show heavy storms in the saturnian atmosphere (NASA)

1.4 The detection of interstellar dust in the solar system

As described in 1.1.1, the proportion of ISD within the ISM is ∼1%. ISD is rare. But still, significant amounts of ISD have been detected in the solar system with impact ionization TOF mass spectrometer onboard Ulysses, Galileo and Cassini. ISD enters the solar system from the local interstellar cloud (LIC).

Characteristics of the local interstellar cloud and the heliosphere

The ISM surrounding the solar system contains the Local Bubble and the Loop 1 Superbubble, which are both comprised by low-density ISM gas ([Lallement et al., 2003]). Located in the Local Bubble are two warm interstellar clouds, the G cloud and the Local

interstellar cloud (LIC), in which the Sun, on the edge of both bubbles, moves with a velocity of $\sim 26\,\mathrm{km\,s^{-1}}$ through the LIC, relative to its surroundings and towards the G cloud [Mihalas and Binney, 1981] (Figure 1.9).

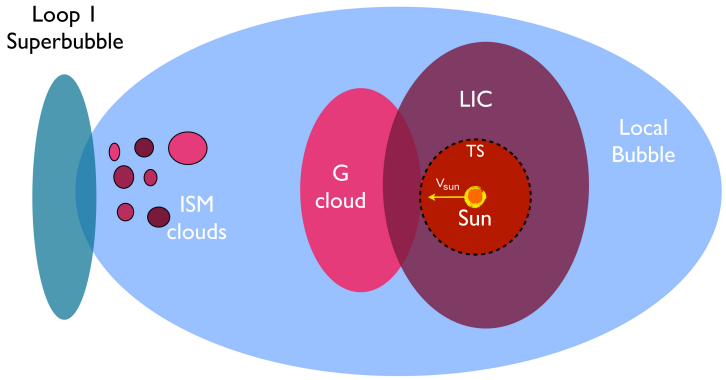

Figure 1.9: Simplified graphic of the close galactic environment of our solar system. The solar system is embedded into the Local Interstellar Cloud (LIC), which itself is located within the Local Bubble, together with the G cloud. (After Mann [2010])

The heliosphere surrounding the Sun, is filled with solar wind plasma and extends up to 100 AU. Its structure shows an elongated "tail", opposite to the direction of the Sun's motion [Mann, 2010]. As a whole (Figure 1.10), the heliosphere is comprised by the termination shock, the heliopause and the bow shock region, establishing somewhat of a hindrance to the interstellar winds entering the heliosphere. The incoming flux and direction of the interstellar wind denotes the upwind direction, with a velocity vector almost parallel to the ecliptic plane. Interstellar dust enters the heliosphere in a similar way, the flow of incoming matter arrives from 259° ecliptic longitude and +8° latitude upstream [Mann, 2010].

The solar wind and the solar magnetic field are highly variable. The solar wind plasma, originating from the solar corona, is comprised by electrons, protons and alpha particles, further highly charged ions of heavier elements, present in cosmic abundances, and pickup ions. It can be distinguished into two distinct, but interacting velocity-dependent components, the fast wind, with speeds between 700-800 $\mathrm{km\,s^{-1}}$, and the slow winds with speeds between 300-500 $\mathrm{km\,s^{-1}}$. The temperatures in the solar wind are very high (10^5 K to 10^6 K) , with a decrease of temperature with increasing distance from the Sun [Mann, 2010]. The termination shock marks the region, in which the radial motion of the solar wind is decelerated to subsonic speed. Beyond the termination shock is the heliopause, probably with increasing plasma temperatures in the space between termination shock and heliopause [Richardson et al., 2008]. Finally, the heliopause marks the boundary of the heliosphere, the boundary between solar wind and the ionized components of the ISM. Even further out lies another shock region for interstellar gas, the bow shock (Holzer [1989]; Mann [2010]) (Fig. 1.10). The average magnetic field is characterized as the Parker spiral (Fig. 1.11). The magnetic field close to the sun is more radial and with more distance from the sun, it becomes about azimuthal. Generally, the magnetic field has a mixed polarity, and can thus be described with a sector-like structure [Mann, 2010]. The field orientation changes two

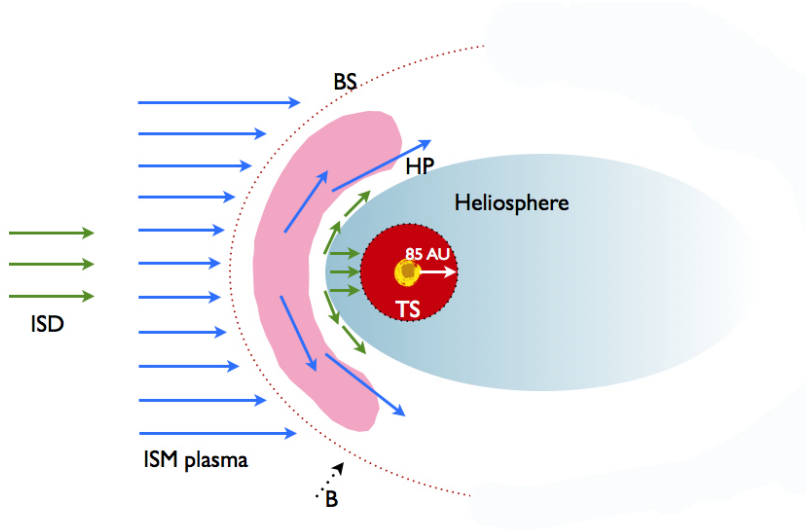

Figure 1.10: A closer look into the heliospheric environment of the solar system. The heliosphere appears to be elongated, opposite to the direction of Sun's motion. Visible as well are the termination shock region (TS), the heliopause (HP) and the bow shock (BS) (After Mann [2010])

to four times within a solar rotation period for a given point in space. These differing polarity regions are distinguished by the thin heliospheric current sheet. Close to the ecliptic plane, the radial extend of a field polarity sector is of the order of a few AU, whereas close to solar maximum, mixed polarity regions increase to all latitudes and field reversal takes place [Mann, 2010].

Figure 1.11: The heliospheric current sheet in its extension. The field is a result from the influence of the Sun's magnetic field onto the plasma within the interplanetary medium

Dynamics of ISD in the inner and outer heliosphere

ISM components entering the heliosphere are galactic cosmic rays, interstellar neutral gas and ISD, with small ratio of surface charge to mass Q/m. [Morfill and Grün, 1979] suggested that incoming ISD particles can pass focussing and defocussing of the solar

magnetic field and maybe as well enter via diffusive processes. If and how ISD enters into the heliosphere, depends, as well as their trajectories, strongly on dust surface charge [Gustafson and Misconi, 1979]. The lack of small ISD grains within the Ulysses data set led to the conclusion that there is a size-dependent filtering processes along the boundary of the heliosphere. Dust particles that do not enter the heliospheric boundary are deflected and stream away from the magnetic field regions around the heliopause [Linde and Gombosi, 2000]. [Landgraf, 2000] modelled ISD dynamics within the heliosphere for several magnetic field configurations and explained how the variability of the ISD flux is influenced by focussing and defocussing of the solar magnetic field, as measured by the Ulysses spacecraft. [Sterken et al., 2012] modelled the ISD flux in the heliosphere for application to the Cassini mission, aiming at the prediction of the flux of ISD in the Saturnian system.

ISD particles larger than $1\,\mu\mathrm{m}$ are scattered due to gravitational heliosperic effects after entering and passing through the heliosphere, which leads to an enhancement of dust densities downstream of the Sun. Smaller grains ($0.1\,\mu\mathrm{m}$ to $0.3\,\mu\mathrm{m}$) on the other hand, are preferentially affected by solar radiation pressure. When β, the ratio of radiation pressure force over gravitational force, exceeds the value 1, particles are deflected from the Sun [Sterken et al., 2012] . The trajectories of interstellar grains are attractive or repulsive hyperbolas, depending on $\beta<1$ or $\beta>1$, with respect to only gravitational force and radiation pressure. If $\beta=1$, the trajectory of a particle entering, resembles a straight line.

Ulysses monitored the flux of interstellar matter for 15 years, starting in 1992. Landgraf et al. [1999] found that the dominating flux was mainly comprised by particles of $\approx 0.3\,\mu\mathrm{m}$ with a maximum $\beta>1$, due to an exclusive area of small particles extending to about 3 AU, which is a remnant of the long term variation within the ISD flow, caused by interaction with the heliosphere.

The detection and identification of ISD in the solar system with the CDA

The dust detector onboard Cassini encountered ISD first in 1999, during its cruise from Earth to the Jovian system [Altobelli et al., 2003]. Cassini entered the Saturnian system in 2004. The data since Saturnian orbit insertion (SOI) in 2004 until 2010 have been revised by [Altobelli et al., 2013]. It is clear, that the Saturnian system is heavily crossed by particles from the interplanetary medium as well as from the ISM, originating within the LIC. Observed were particles with low velocity with respect to Saturn, strongly affected by gravitational focussing, as well as fast particles, not influenced by gravitational focussing. The slow particles may have their origin within the Kuiper Belt or stem from TNO's. Most of the fast population is denoted as interstellar dust, but may as well contain particles released by Oort cloud type comets.

Information about dust in the outer solar system is rare. Three spacecrafts, Pioneer 10 and 11 [Landgraf et al., 2002] and the New Horizons-SDC towards Pluto [Poppe et al., 2010] measured the dust flux at Saturn heliocentric distance for a rather short time. Cassini though, has been orbiting Saturn since 2005 and the CDA collected a vast amount of data from impacts. The CDA's sensitivity to particles ranging from sub-micron to tens of microns in size and a few to tens of $\mathrm{km\,s^{-1}}$ in speed, gives it excellent prepositions for the detection of exogenous particles (particles originating outside the Saturnian system). Unfortunately,

the local dust environment at Saturn, especially the E-ring region, with its high density of icy particles, makes the search for exogenous dust basically the search for "the needle in the haystack" and is thus, extremely complicated.

For the evaluation of the Cassini data set with respect to finding the very rare exogenous particles, all detection subsystems have been analyzed, i.e. the entrance grids (EG), the IID and the chemical analyzer target CAT, with the latter providing TOF mass spectra (further described in 2.1). For this work only the CAT impacts are relevant, since we are able to evaluate the resulting mass spectra, which will be described in detail in 5.3.

So far, most TOF spectra, detected since SOI until 2012, are particles comprised by water ice with sodium salts and minor traces of siliceous and organic contamination. These particles have their origin within the E-ring and are linked primarily to the cryovolcanic activity of the moon Enceladus (Postberg et al. [2008], Postberg et al. [2009b]). However, a very small fraction of selected grains show Mg, Si, Ca and Fe and further C and O, indicating silicate composition, which is unusual for dust composition in this environment. Thus, an exogenous origin can be assumed. After further analysis it was found that the signature of these fast grains is in agreement with the upstream direction of ISD grains of 259° longitude and +8° latitude (e.g. Grün et al. [1993]; Altobelli et al. [2005]; Altobelli et al. [2006]; Landgraf [2000]; Landgraf et al. [2000]; Sterken et al. [2012]) as a highly directional flux. The β and mass values seem to correspond to the astronomical silicate grain model, which would as well agree with the elemental composition derived from the TOF spectra.

2 Experimental set up

It is fairly impossible to find unprocessed and thus chemically unaltered micrometeoroids on Earth. Thus, the only way to obtain an unbiased picture of the elemental composition of particles in our Solar System, and probably beyond, is to perform in situ measurements directly in space. Therefore, dust analyzers, such as the Cosmic Dust Anlayzer (CDA) onboard Cassini and further the Large Area Mass Analyzer (LAMA), yet a prototype, and others, have been developed. It is necessary to determine the dust particle's trajectory, so it can be linked to its source, and of course its accurate elemental composition. Two different dust analyzers have been used for the conducted experiments for this thesis-the flight spare unit of the CDA and the laboratory model of the LAMA, which are described below. Further, I give a short description of the set up of the 2MV Van De Graaff accelerator, located at the Max-Planck-Institut für Kernphysik and operated by the University of Stuttgart, including the operating principle of the dust source used for silicates.

2.1 The Cassini Cosmic Dust Analyzer

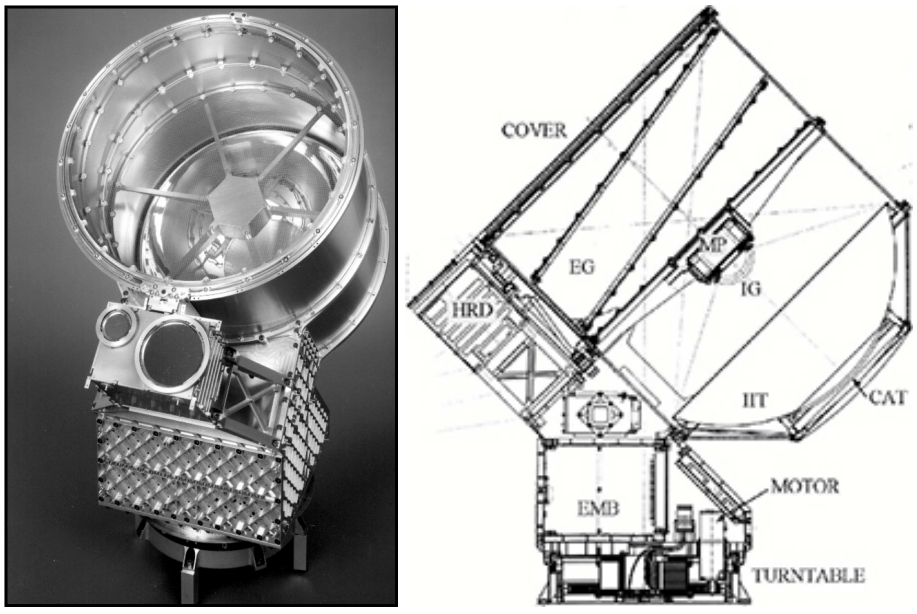

Figure 2.1: The Cosmic Dust Analyzer (CDA) as a photograph (left) and its schematic (right). Visible on the left is the reverse site of the multiplier structure (MP) in the middle, the entrance grids (EG) in front of it and the large gold plated target (Impact Ionization Target, IIT) with the silvery Rh-target (CAT) in the middle, behind the multiplier. Visible as well, below the Dust Analyzer (DA), is the High -Rate-Detector (HRD), with its foil sensors. Further, on the schematic, IG denotes the ion grid, where QI signals are sampled

The Cosmic Dust Analyzer (CDA) (Fig. 2.1) is currently one of the most sophisticated tools for dust measurements on a space mission. It is capable of measuring the flux, charge, velocity and composition of dust particles that enter the CDA. It consists of two subsystems:

- The High Rate Detector (HRD)
- The Dust Analyzer (DA)

The HRD monitors very high impact rates (up to $10000\,\mathrm{s}^{-1}$) in rather dust rich environments, such as Saturn's rings and will not be discussed further here. The DA consists of three subsystems:

- The QP detector - the entrance grid that determine the charge carried by the entering dust particle
- The Impact Ionization Detector (IID)
- The Chemical Analyzer (CA), a linear time-of-flight (*TOF)* mass spectrometer. The CA itself consists of the central rhodium target plate (CAT-Chemical Analyzer Target), with a diameter of 16 cm, which is held at ~1000 V. Approximately 0.003 m above the target is a copper-beryllium grid. This construction leads to an *E* field separating the impact plasma by accelerating the cations into the drift region [Hillier et al., 2006]. Further, the CA consists of a the CAT surrounding gold target (IIT-Impact Ionization Target), with a diameter of 0.40 m.

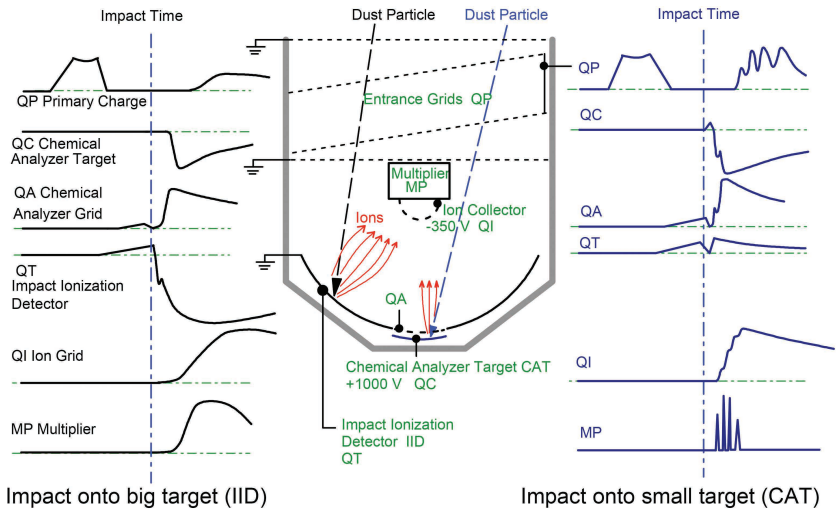

Figure 2.2: Schematic of dust impacting the CDA, showing the appearance of signals resulting from impacts onto the big target (IIT) and the small target (CAT). The process of a dust particle hitting the CAT is described in the text

A particle entering the CDA can, depending on its original trajectory, impacts either the entrance grid, the walls of the instrument, the IIT or, most preferably, the CAT. Since this

work concentrates on high resolution mass spectra, which can only be obtained from impacts on the CAT, other system components will not be described any further. In-depth information are given in e.g. Srama et al. [2004] and Kempf et al. [2004].

A dust particle, impacting onto the CAT with sufficient energy, will be vaporized and ionized. This leads to the formation of an impact plasma, consisting of ions of the impactor and the target material, and further, electrons, atoms and neutral molecules. As described above, the impact plasma will be separated via the electrical field, wherein the cations will be sent into the drift region and any anions and electrons onto the CAT (Fig. 2.2).

2.2 The Large Area Mass Analyzer

The Large Area Mass Analyzer (LAMA) (Fig. 2.3) was developed for dedicated dust astronomy space missions. It is a reflectron-type time-of-flight impact ionization mass spectrometer and its large target area of $0.1\,\mathrm{m}^2$ and wide field-of-view of $> 50°$ are especially suitable for the detection of low dust fluxes, e.g. interstellar dust, in interplanetary space. It achieves a typical mass resolution of up to $\frac{m}{\Delta m} \sim 300$.

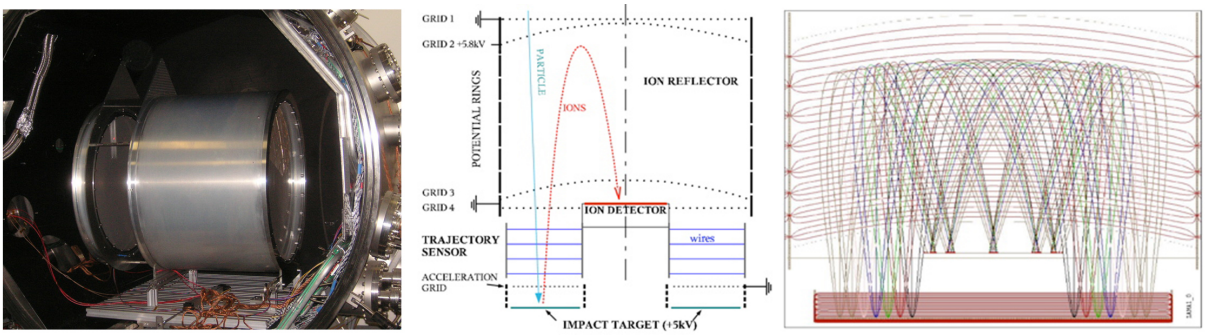

Figure 2.3: A photograph of the LAMA, taken while it was built into the chamber for measurements (right), a schematic of the function principle of the LAMA, further described in the text below (middle) and a SIMION modelling of the ion trajectories within the LAMA, after a particle hit the target.

The LAMA has a cylindrical symmetry and six annular disc electrodes, as well as six ring electrodes generate the electrostatic field of the reflectron. The impact target is held at +5 kV potential with a grounded acceleration grid 50 mm in front of it. Hence, the acceleration distance is much bigger than the CDAs' acceleration distance of 3 mm, which reduces shielding effects within the impact plasma cloud, since the expansion of the plasma cloud can happen within a much larger volume, before the ion acceleration becomes effective. Further, the LAMA has a field-free-drift region in front of the impact detector and two parabolic shaped grids on potentials of 0 V and +6000 V, respectively. The parabolic shape of the grids enhances spatial focussing characteristics (Srama et al. [2005]; Srama et al. [2007]; Sternovsky et al. [2007]).

A dust particle enters the LAMA through the annular disc electrodes, which are made out of very transparent grid materials and after passing the grounded grid, it hits the target. The ions generated from a hyperverlocity impact are accelerated away from the target and

are then focussed onto the detector in groups, according to their charge to mass ratio [Sternovsky, 2005]. The SIMION ion optics package was used to simulate ion trajectories within the instrument (Fig. 2.3, middle).

2.3 The Van-de-Graaff accelerator

For the acceleration of dust analogues, we used a modified Van De Graaff generator, with a potential of 2MV (Fig. 2.4). It utilizes a moving belt to accumulate high amounts of charge onto a hollow metal globe, the terminal. An electrostatically homogenous electrical field can be obtained by decreasing the gained potential over 60 potential rings to ground, with each of them connected via 1.2 GΩ resistors. The stability of the potential is ensured via corona discharge. Further, the generator is situated within a pressurized tank (16 bar) and surrounded by protective gas, here SF_6 and CO_2, to avoid sparking (Mocker et al. [2011]) .

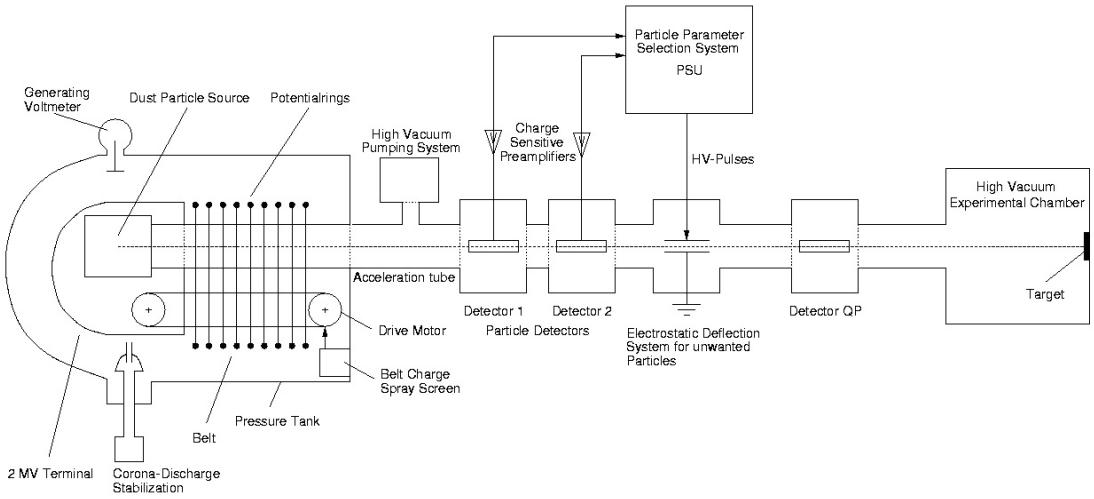

Figure 2.4: Schematic of the 2MV Van de Graaff accelerator, as in use at the Heidelberg Dust Accelerator facility. Visible here is the particle selection unit, a vital and unique part of the accelerator built up.

Within the terminal is the dust source (Fig. 2.5) with its associated circuitry that provides a constant dust stream, due to the charging of conducting particles and their insertion into the accelerators beam line. The positively charged particles are then subsequently accelerated via the electrostatic field of the accelerator. The dust first passes the focusing cathode and then two pairs of charged plates perpendicular to each other. These *steerers* provide a correction of the dust beam, if not perfectly axial, via deflection. The kinetic energies of the accelerated particles arise from the conservation of energy, with v being the particles' velocity, q its charge and m its mass:

$$\frac{1}{2} \cdot mv^2 = q \cdot U_{pot} \quad with \quad U_{pot} = 2MV \tag{2.1}$$

The mass of the particle can be derived from this equation and from the measurement of the particles' charge and velocity.

The dust source (Fig. 2.5) used is a DS2001-type source, redesigned and optimized for coated silicates or latex particles, since the process of applying charge onto the is more complicated. The source consists of a dust reservoir, charged with respect to the reference accelerator potential of 2MV, and with a resulting electrode potential varying between 0 and 20 kV. The particles within the reservoir are electrostatically charged via induction. The potential of the reservoir is pulsed and the charged particles are injected directly into the beamline via a very sharp (few at the tip) tungsten needle (Mocker et al. [2011]). Further, the build up of the accelerator facility contains a particle selection unit, the PSU. Here, particles can be selected with respect to mass, velocity and charge, based on the requirements of the experiment.

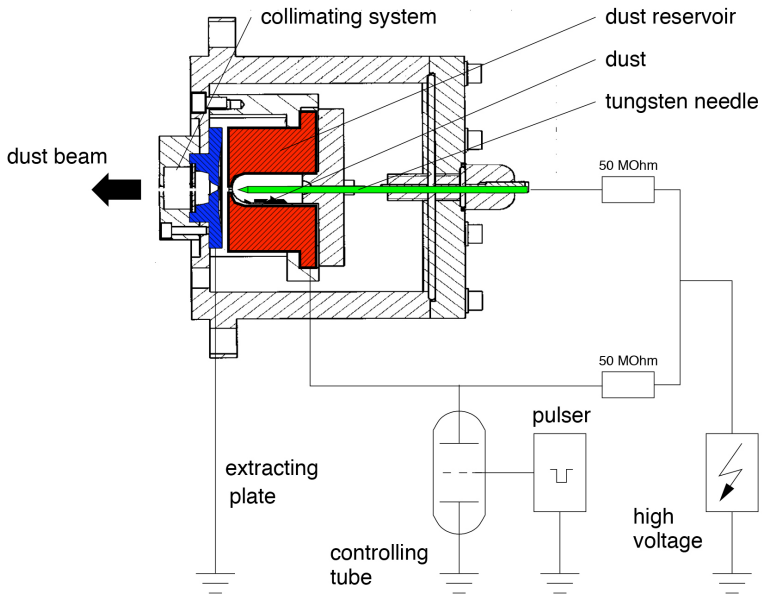

Figure 2.5: Schematic of the DS2001 dust source used with the accelerator, especially developed for the acceleration of silicates.

3 Cosmic dust analogue material

As shown in 5, several ISD candidates have been identified within the vast amount of data of the Cassini CDA dataset. Laboratory tests with cosmic dust analogues, specifically manufactured for a distinct grain population, are mandatory, so in situ spectra can be compared and related to the experimentally obtained spectra and thus, the composition of a specific impactor can be determined.

For our purpose, since a substantial fraction of the ISD are (amorphous) silicates (subsec:elemism), chemically simple ferromagnesian silicates (i.e. olivine and pyroxene) were used. We aimed for samples that

- are variable in Mg- and Fe-content (within the sample series)
- are homogenous in composition and structure
- bear only minimal impurities and inclusions
- can be prepared easily and quickly

The most ideal way of obtaining cosmic dust analogues would be the synthesis of minerals on-demand. This was tried in the first year of the studies and will be described in 3.2. Another way to obtain dust analogues is the preparation from natural rock samples, as described in 3.3.

During the course of the studies we learned that it is necessary to set up an accelerator campaign with a series of olivine and pyroxene dust analogues, containing graded Fe-contents within the series. We aimed to investigate the differences in the appearance of the Mg- and Fe-mass lines within the spectra, with the sample having an otherwise similar chemistry, and thus to answer the question, if we are able to distinguish high and low contents of certain elements within impact ionization mass spectra. The impact ionization process is a non-equlibrium process and thus leads to severe complications in the calibration and interpretation of the mass spectra. This process will be further described in 4.1.2. Further, the sub-micron to micron sized dust particles have to be coated prior to the acceleration, since they need to hold charge for being accelerated through an electrostatic field of 2MV. Coating has become accessible only recently, and thus the acceleration of silicates and other naturally non-conductive materials is now possible. Still, the coating of materials for this very particular purpose is an ongoing research and far from being perfect.

Although the following descriptions are basic mineralogical knowledge, we explain respective principles in detail, as this study also aims at non geoscience colleagues with astrophysical background.

During the course of the studies, we synthesized mineral samples, which, however, could not be used due to their heterogeneity (see 3.2). Further, we prepared a sample series, consisting of a total of five samples (olivine and pyroxene) from natural rocks, plus a specifically synthesized forsterite, which was kindly provided by Dr. Michael Burchard, Geosciences, University of Heidelberg. Only one pyroxene sample from a natural rock could finally be used, which will be described in detail below and may serve as a representative for the analogue preparation from natural rocks. Moreover, this sample proved as a highly valuable representative for the interpretation of impact ionization mass spectra from a natural dust analogue.

Other samples could not be used due to the coating not being effective, or other problems, concerning the dust source in the accelerator. These problems have not yet been resolved. As well, the accelerator campaign was delayed by six months and thus, aside from shortly inserted CDA-calibration campaigns with Fe, SiO_2 and magnetite, only the pyroxene sample could be tested extensively with both CDA and LAMA.

3.1 Introduction to the mineralogy of rock-forming minerals

Minerals of the pyroxene group and olivine belong to the most abundant and important ferromagnesian species in rock-forming minerals on earth. Pyroxene belongs to the group of single-chain silicates and appears either in the monoclinic or in the orthorhombic crystal system. Orthopyroxenes essentially consist of the simple chemical series of $(Mg,Fe)SiO_3$, clinopyroxenes though, show a wider variation of chemical composition, with mainly Ca, Na, and Al accomodated into their structures [Deer et al., 1992]. Further, since we encounter feldspar, spinel, amphiboles and glasses within our natural samples, their basic mineralogy will be described as well.

3.1.1 Olivine

Olivine is one of the most common rock-forming ferromagnesian silicates on Earth. It is a nesosilicate, meaning that its structure consists of independent SiO_4 tetrahedra linked by divalent atoms in six-fold coordination [Deer et al., 1992]. Olivine crystallizes in the orthorhombic system and its structure can be described as a hexagonal close-packing.

The olivine-system describes a solid solution in the series $(Mg,Fe)_2SiO_4$, with Mg_2SiO_4 being forsterite and Fe_2SiO_4 being fayalite, denoting the pure endmembers of this series. Further, much less common than forsterite and fayalite, Mn-olivines (montecellite) and Ca-olivines (kirschsteinite) are possible [Deer et al., 1992].

The general structural formula of olivine can be written as

$$ABSiO_4 \tag{3.1}$$

with *A* being usually occupied by Mg and Fe, where Fe^{2+} is preferred at the *A*-site and Ca^{2+} is preferred on the *B*-site. As well, Cr and Ni are very common minor additions in

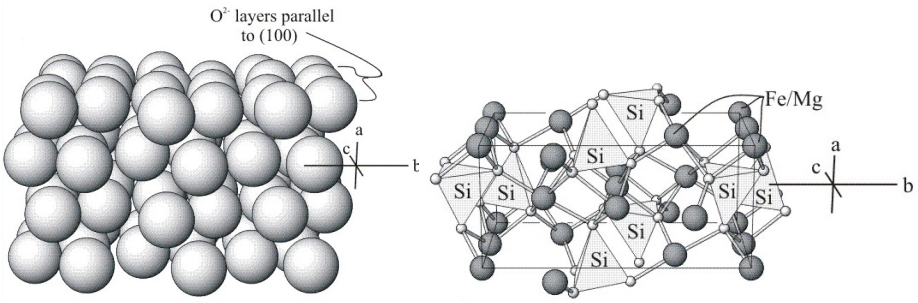

Figure 3.1: The olivine structure. Packing on the left and isolated SiO_4-tetrahedra with their oxygen bonds on the right (Courtesy. Fort Hays State University, USA, 2010)

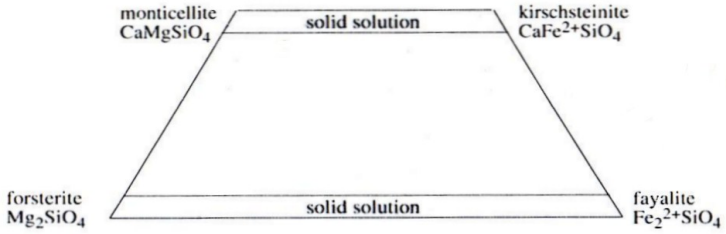

Figure 3.2: The solid solution system of olivine and its endmembers [Putnis, 1992]

Mg-rich olivines.

As stated before, both most common end-members of olivine, forsterite Mg_2SiO_4 and fayalite Fe_2SiO_4, show a solid solution with complete solubility. That means that Fe and Mg can substitute each other throughout the entire range of concentrations, which is possible, because Mg and Fe-ions share similar radii, the crystal structure stays the same (orthorhombic) and the valency is similar [Philpotts and Ague, 1990]. In other words: Between the end-members forsterite and fayalite, olivine can have any composition. Thus, olivine is a substitutional solid solution [Putnis, 1992].

3.1.2 Pyroxene

Pyroxenes belong as well to the most important ferromagnesian silicates, as well with respect to ISD. Pyroxenes are single-chain silicates and occur in two varieties: orthopyroxene, the name owing to the orthorhombic symmetry of their crystal system, and clinopyroxene, with its monoclinic symmetry. Figures below show the structure of orthopyroxene (left) and the nomenclature of ferromagnesian and calcic pyroxenes (right) of the system $MgSi_2O_6$-$FeSi_2O_6$-$CaSi_2O_6$. Orthopyroxene has a rather simple chemistry, whereas clinopyroxenes are more chemically variable and complex. Generally, pyroxenes are divided into several subgroups, namely Mg-Fe-pyroxenes, Ca-pyroxenes, Na-Pyroxenes, and, to a minor extend, Ca-Na-pyroxenes and Li-pyroxenes. For this work, only Mg-Fe-pyroxenes and Ca-pyroxenes are important, and thus, Ca-Na-, Na- and Li-pyroxenes will not be discussed further.

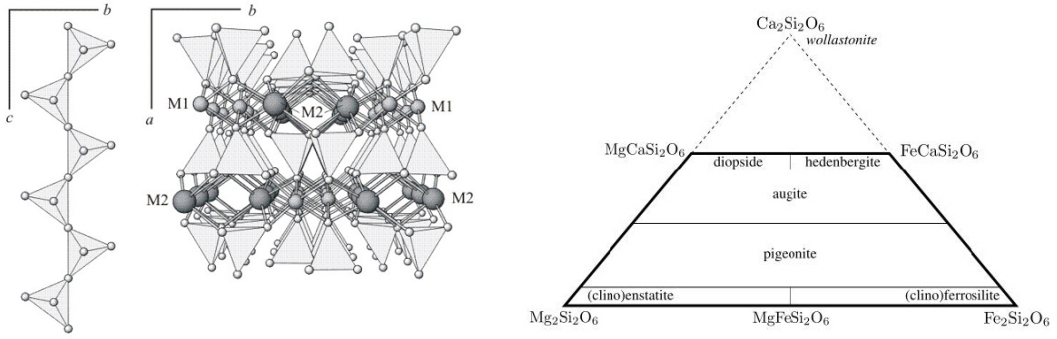

Figure 3.3: The pyroxene structure (orthorhombic) on the left and the geochemical triangle of the chemical system $MgSi_2O_6$-$FeSi_2O_6$-$CaSi_2O_6$, with emphasis on the diopside-hedenbergite-enstatite-ferrosilite-quadrilateral (Fort Hays State University, USA, 2010)

The structural formula for pyroxenes can be commonly written as:

$$ABSi_2O_6 \tag{3.2}$$

but is more accurate in this extensive representation of the common pyroxene formula:

$$(W)_{1-p}(X,Y)_{1+p}Z_2O_6 \tag{3.3}$$

with W = $Ca^{2+}, Mg^{2+}, Fe^{2+}, Na^{2}+$; X = Mg, Fe^{2+}, Mn, Ni, Li; Y = Al, Fe^{3+}, Cr, Ti, and Z = Si, Al. (Deer et al. [1978]; Putnis [1992]).

The most common species within the pyroxenes are orthopyroxenes, forming a solid solution between enstatite ($Mg_2Si_2O_6$) and orthoferrosillite ($Fe_2^{2+}Si_2O_6$). Pyroxenes are rather complex with respect to the formation of solid solutions, since they do not show a complete solubility over the entire range of possible compositions. Here, structure and composition depend strongly on temperature and minor on pressure. The phase relations of ortho- and clinopyroxenes and can be discussed in terms of a ternary system $CaSiO_3$-$MgSiO_3$-$FeSiO_3$, as visible in Fig. 3.4. It is further important to understand the phase relations in the binary system of enstatite and diopside (shown in the left area of the pyroxene quadrilateral in Fig. 3.4). Fig. 3.5 shows the binary phase diagram of enstatite and diopside, with the latter being a calcic clinopyroxene with ∼45 wt% Ca. This diagram shows the complexity of a simple binary phase relation between ferromagnesian and calcic pyroxenes, that naturally coexist within rocks. It helps understanding exsolution processes that occur commonly in such pyroxenes during the cooling process and which we encounter on sub-micron scale in our dust analogue candidates.

At low temperatures, enstatite is orthorhombic, with limited solubility towards diopside. But at high temperatures, enstatite inverts its structure to a monoclinic form and is thus able to solve considerably more Ca-rich diopside. More polymorphs of various pyroxene phases

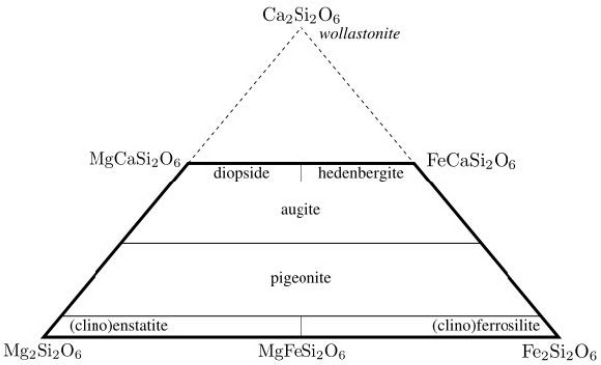

Figure 3.4: The pyroxene quadrilateral

are known, having different solvii at different temperatures that add to the complexity of that system. But most important is that coexisting Ca-poor pyroxene (such as enstatite) and Ca-rich pyroxene (such as diopside) develop exsolution lamellae, when cooling down slowly.

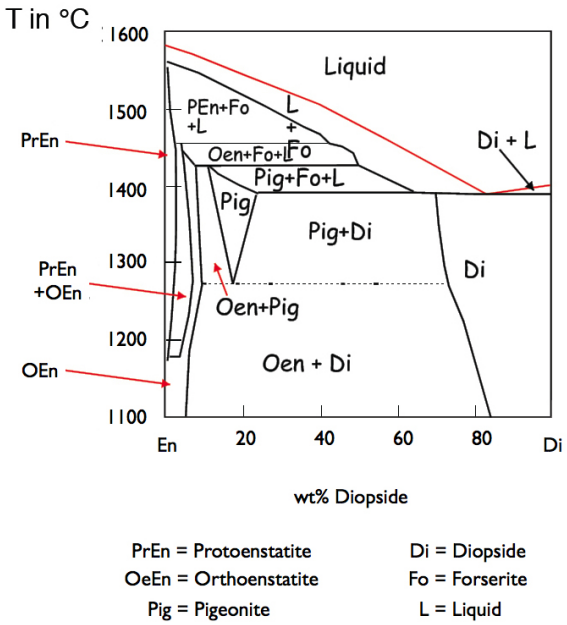

Figure 3.5: Binary phase diagram of enstatite and diopside, depicting the complexity of the phase relations in pyroxenes (Courtesy: University of New Brunswick, 2009)

The monoclinic Ca-rich pyroxene must change its structure to a more stable orthorhombic symmetry during the cooling process. Thus, the solution containing a specific ratio of Ca, Mg and Fe, has to exsolve a significant amount of the Ca-rich phase in order to be able to change towards the stable orthorhombic symmetry. During this required structural inversion process during cooling, exsolution lamellae will be formed by exsolution onto initially, during the cooling, formed surfaces (a detailed overview of this process can befound e.g.

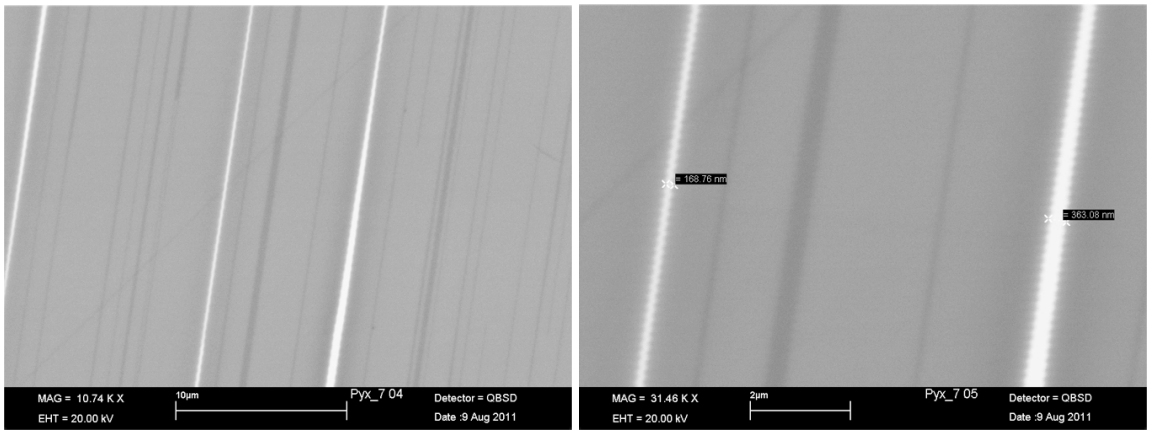

Figure 3.6: Examples of exsolution lamellae on sub-micron scale in two of our pyroxene samples

in [Putnis, 1992] and [Philpotts and Ague, 1990]. Exsolution lamellae on sub micron scale are illustrated in Fig. 3.6.

3.1.3 Feldspar

Feldspar is very abundant on earth, especially in igneous rocks. Feldspars belong to the class of tectosilicates and have a wide range of composition. The majority of feldspars can be displayed within the ternary system Albite (Ab) $NaAlSi_3O_8$, orthoclase (Or) $KAlSi_3O_8$, and anorthite (An) $CaAl_2Si_2O_8$ (Fig. 3.7), with compositions between Or-Ab denoting alkali-feldspars and compositions between Ab-An denoting plagioclase.

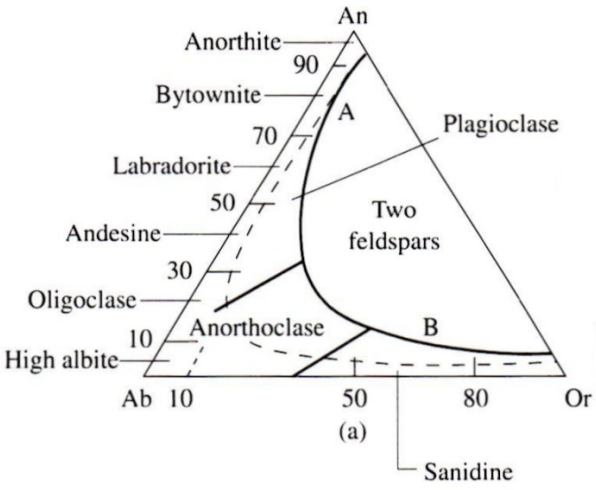

Figure 3.7: Feldspar classification in the ternary system Ab-Or-An [Deer et al., 2001]

The structural formula can generally written as

$$MT_4O_8 \tag{3.4}$$

with M being usually occupied by Na, K, Rb, Ca, Sr or Ba. The T-site is generally occupied by Si and Al, the latter replacing Si by 25-50% [Putnis, 1992]. Feldspar is not only classified due to its composition, but as well by its crystal symmetries, directly tied to formation conditions, i.e., temperature, illustrated in Fig. 3.8

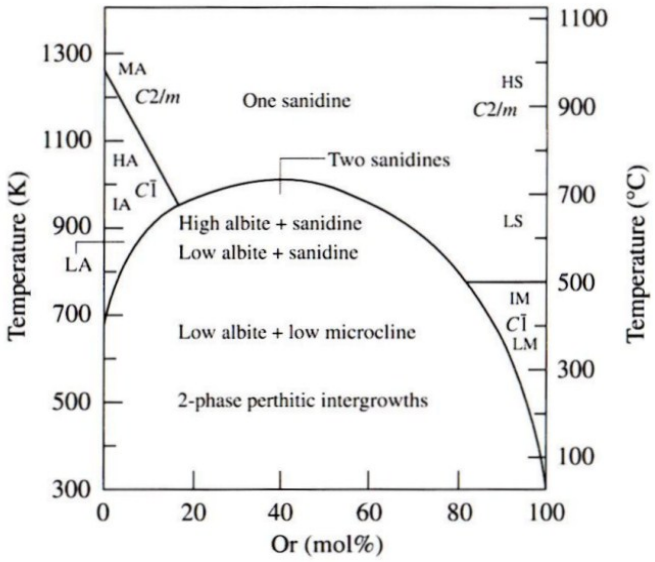

Figure 3.8: Feldspar classification in the ternary system Ab-Or-An [Deer et al., 2001]

3.1.4 Amphibole

Amphiboles show an enormous wide range and complexity in composition, cation distribution and crystal structure. Thus, I will only discuss the main aspects of this mineral, important for this thesis.

Amphiboles belong to the double chain silicates, and due to the chain-structure, they share somewhat similar properties with pyroxenes, but contain two additional cation sites and further a mirror plane in the double-chained $[SiO_4]$-tetrahedral. The additional cation sites can be occupied by a hydroxyl ion (OH^+) or F^+ in the center of the hexagonal rings. The structural formula of Amphibole can be written as

$$A_{0-1}B_2C_5T_8O_22(OH,F)_2 \tag{3.5}$$

with the A-site occupied by large cations, such as Na, K, Ca, or left vacant, the B-sites are commonly occupied by smaller cations, such as Ca, Na, Fe^{2+}, Mg or Mn, the C-sites contain the smallest cations, such as Fe^{2+}, Mg, Fe^{3+}, Al, Ti, Mn, Cr, Li, or Zn. The T-site is generally occupied by Si and Al, here Al as well substitutes Si up to a certain amount. Fig. 3.9.Amphiboles can be divided into four groups: Fe-Mg-Mn-Li-amphiboles, Ca-amphiboles, Na-Ca-amphiboles and Na-amphiboles.

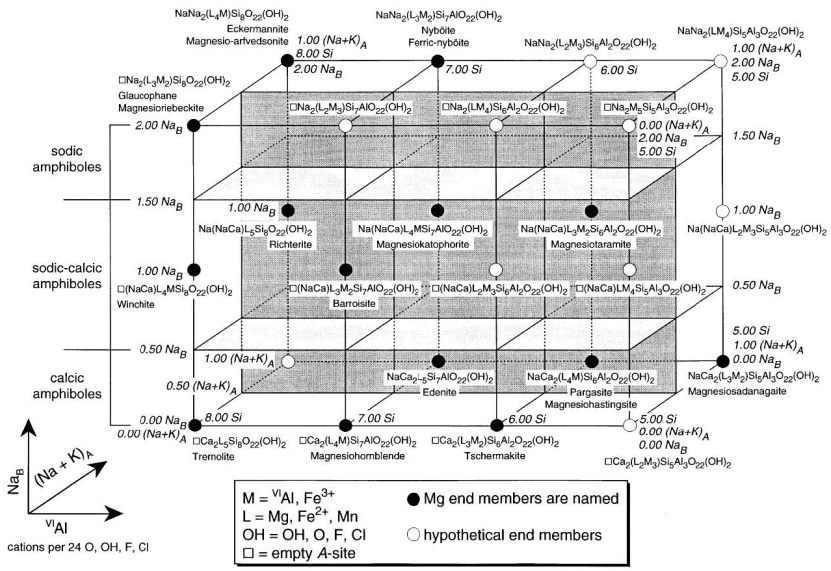

Figure 3.9: Classification of amphiboles, without Fe-Mg-Mn-amphiboles, displayed as a three dimensional box after Hawthorne et al. [1997]

A common and widespread representative of Ca-amphiboles is hornblende, with the formula $Ca_2(Mg,Fe^{2+})_4Al[Si_7AlO_{22}](OH,F)_2$. This mineral can not only be found in igneous and metamorphic rocks, but as well in chondrites (Brearley [1997]; McCanta et al. [2008]) and martian meteorites, e.g., the Chassigny meteorite (McCubbin et al. [2010]).

3.1.5 Spinel

The minerals of the spinel group belong to the class of oxides and can be divided into four groups, depending on which trivalent cation, Mg, Al, Fe, Cr, is incorporated. The group is named after the main representative, spinel, with the formula $MgAl_2O_4$. The common structural formula of the oxides of the spinel group can be written as

$$AB_2O_4 \tag{3.6}$$

with the A- and B-sites being occupied commonly by Mg, Al, Fe, Cr, but rare occupancies of Mn, Zn, Ni, and Ti are possible, too. The cations on the A- and B-sites are in 6-fold coordination with each other. Due to differences of the cation distribution on these sites, two structural types are possible, either normal, or inverse, owing to redistributions of the cations. Oxides, containing a spinel structure are spinel ($Mg^{2+}Al_2^{3+}O_4$), magnetite ($Fe^{3+}(Fe^{2+},Fe^{3+})_2O_4$), and further magnesioferrite ($Mg^{2+}Fe^{3+}O_4$), hercynite ($Fe^{2+}Al_2^{3+}O_4$), chromite ($Fe^{2+}Cr_2^{3+}O_4$) and magnesiochromite ($Mg^{2+}Cr_2^{3+}O_4$). Titanium-chromite can be found in lunar rocks, and chromite can be found as a heavy mineral in meteorites (Deer et al. [1992]; Putnis [1992]). The spinel prism below illustrates the spinel series (Fig. 3.10).

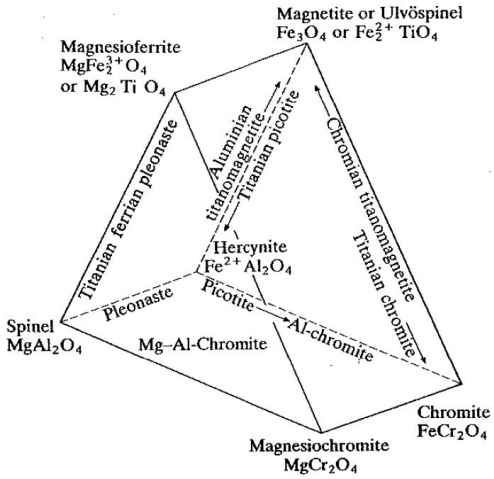

Figure 3.10: Spinel prism illustrating the spinel series, with the bases of the triangles defined by normal spinel and the vertices defined by inverse spinel [Deer et al., 1992]

3.2 The synthesis of dust analogue material via the melt-quench method

Mineral synthesis seems to be the ideal solution in the preparation of cosmic dust analogues. The ability to fully control the synthesis with respect to e.g., contamination or mineral phase purity, the design of a sample as demanded for a particular environment, composition, size or similar is still an ambitious goal within this field of research. Mineral synthesis was not the initial content of this project, but a first idea evolving while investigating the various possibilities of establishing a sample preparation method for the specific needs of the project, I will point out the challenges regarding the quench-melt method used for our dust analogue synthesis in the following.

The analogue materials, olivine and orthopyroxene, were synthesized at the Institute for Astrophysics at the University of Jena, between 1994 and November 2010, originally for the purpose of spectral analysis. The samples were synthesized via the melt-quench-method in order to obtain especially amorphous mineral samples. MgO, FeO and $\mathrm{SiO_2}$ were mixed in suitable stoichiometric ratios for five different samples within a platinum crucible and then molten in an oven at about 1600 ℃. The melting process was graded over multiple steps with several residence times at specific temperatures. The samples should have the following compositions

- Protoenstatite $\mathrm{MgSiO_3}$ - Sample StW25
- Enstatite-Ferrosilite $(\mathrm{Mg_{0.95}Fe_{0.05}})\mathrm{SiO_3}$ - Sample StW12
- Enstatite-Ferrosilite $(\mathrm{Mg_{0.5}Fe_{0.5}})\mathrm{SiO_3}$ - Sample StW04
- Forsterite-Fayalite $(\mathrm{Mg_{0.9}Fe_{0.1}})\mathrm{SiO_3}$ - Sample StW18
- Forsterite-Fayalite $(\mathrm{Mg_{0.8}Fe_{0.2}})_2\mathrm{SiO_4}$ - Sample StW20

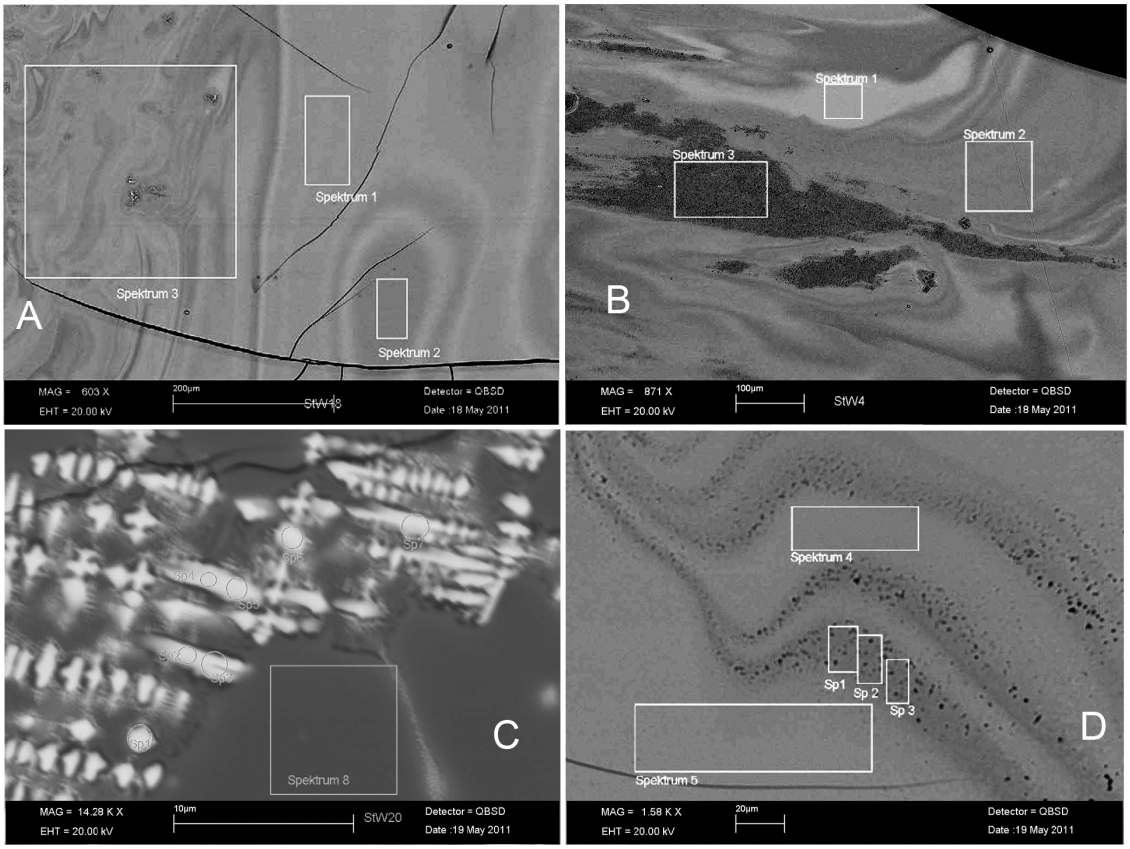

Figure 3.11: Examples of the resulting inhomogenous structures in amorphous olivine and pyroxene samples, synthsized with the melt-quench method under atmospheric conditions

The melts were then taken out of the oven and immediately quenched over two cold copper cylinders, through which the melt was squeezed during the cooling process. The end-product is then a thin and flat mineral-tongue. It is likely that the samples experienced a temperature difference of approximately 400 ℃ between being removed from the oven and quenching through the cold copper cylinders. Thus, the samples might have had an actual temperature of $\approx 1100 - 1300$ ℃ shortly before quenching. The aim was to achieve a homogenous and amorphous distribution of orthopyroxene and olivine within the specific samples. Quenching lead to a certain degree of amorphousness, but unfortunately not to the desired homogeneity. In the end, this procedure resulted in a crystalline partitioning of Fe and Mg, depending strongly on the composition of the single components. Fig. 3.11 illustrates a small choice of the manifold encountered challenges described in this section. Even though, parts of the samples might have shown the desired properties, it was decided not to prepare them out of the samples, but to rather look for a better solution for the production of cosmic dust analogues. An in-depth investigation of the samples and the more detailed discussion summarised below can be found in Auwärter [2010].

3.2.1 Phase stability within the system $MgO\text{-}FeO\text{-}SiO_2$

Why did the melt-quench method not lead to the desired results for our purpose? Fig. 3.12 shows phase stability areas in which, according to designated compositions of the compo-

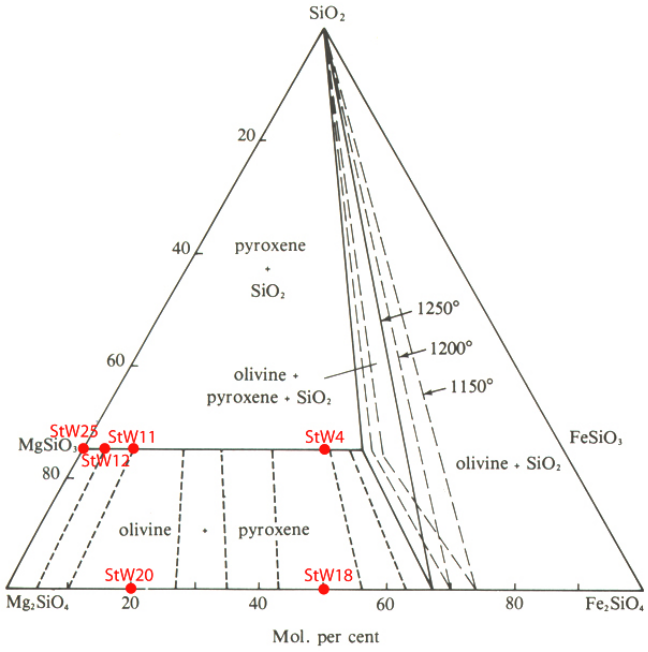

Figure 3.12: Phase stabilities in the system MgO-FeO-SiO_2,1atm pressure at 1150 ℃,1200 ℃ and 1250 ℃, low O_2-partial pressure, (after Nafziger and Muan [1967])

nents Mg, Fe and Si particular mineral phases are stable. The conditions are 1 bar pressure, low oxidation conditions and temperatures between 1150 ℃ to 1250 ℃. At 1150 ℃, in a system with a Mg_2SiO_4 / Fe_2SiO_4- ratio of 70/30 mol% and a Mg_2SiO_4 / SiO_2- ratio of 40/60 mol%, pyroxene and SiO_2 would be stable in coexistence. At higher temperatures the stability areas shift to the left and, with the same composition, olivine and SiO_2 would be now stable in coexistence. The prepared samples lay on the stability *lines* of pyroxene and olivine, and hence, do not experience fractionation into different minerals. A mixture of olivine and pyroxene would crystallize successively during the cooling process, due to the different melting points. But our samples lay on the stability lines of each solid solution, meaning either pyroxene or olivine, and no mixture happens between both systems. At a ratio of Mg_2SiO_4 / Fe_2SiO_4- ratio of 40/60 mol% pyroxene do not remain stable anymore and fractionates into olivine and quartz.

3.2.2 Fractionation processes within the forsterite-faylite system due to quenching

Pure Mg-olivine (forsterite) crystallizes at a temperature of ≈ 1890 ℃ and pure Fe-olivine (fayalite) starts crystallizing at a temperature of ≈ 1205 ℃, as is illustrated in Fig. 3.13. The more Fe is introduced into the system, the lower is the melting point of the system. Further, with a mixture of Fe and Mg a liquidus line and a stability field of olivine + liquid melt is introduced, meaning that a solid phase coexists with a liquid phase as soon as the system falls below the liquidus. The first olivines crystallizing out of the melt are rich in Mg and leave the remaining melt enriched with Fe. Assuming a perfect thermodynamic equilibrium within the system, a solid solution will form, if the cooling is slow. Since the prepared

samples have been quenched rapidly, no solid solution could form. On the contrary, it is highly likely that after cooling Mg-rich olivine coexists with Fe-rich olivine within the sample.

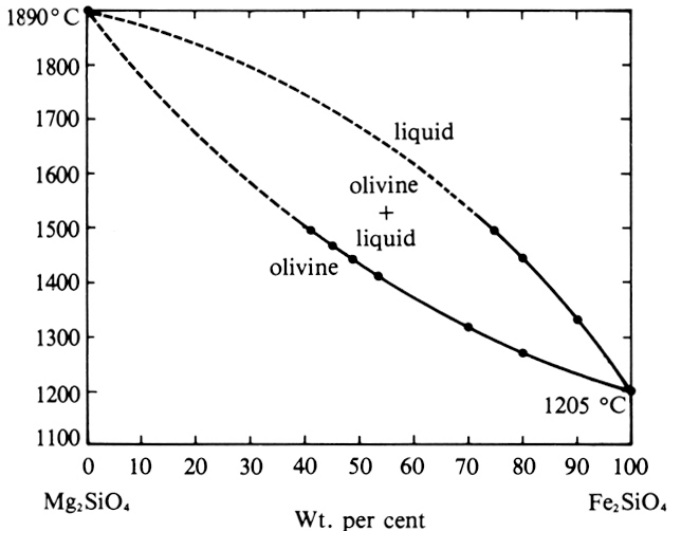

Figure 3.13: Melting diagram of the system forsterite-fayalite (after Bowen and Schairer [1935])

3.2.3 The effect of oxygen fugacity

Another problem is the composition of the resulting samples in dependence from temperature and oxygen fugacity.
The oxygen partial pressure denotes the chemical potential of oxygen as a gas within a system. The unit of oxygen fugacity pressure is atm. Shown in Fig. 3.14 are $P_{O2} \leq 10^{-0.7}$ atm (dashed line), $P_{O2} = 10^{-0.7}$ atm (red line) and $P_{O2} \geq 10^{-0.7}$ atm (continuous line). The samples were prepared under atmospheric pressure, and since the volume proportion of oxygen in the air is 21%, the oxygen fugacity can be described as 0.21 atm or $10^{-0.7}$ atm. The read line in Fig. 3.14 marks the area of oxygen fugacity the samples were exposed to.

The ternary diagram in Fig. 3.14 shows the stability of different phases, depending on the oxygen fugacity and the proportions of the components MgO, FeO, $\mathrm{Fe_2O_3}$ and $\mathrm{SiO_2}$. The lines denote boundaries between two components and the resulting areas denote the liquidus areas. If a melt *m* with an olivine composition cools, more and more olivine will crystallize from the melt, leaving a residual melt, which will be successively poorer in MgO and $\mathrm{SiO_2}$. This reaction moves along the slope of the liquidus area towards the boundary of olivine and magnetite (*n*). Here, a binary eutectic reaction occurs in which magnetite and olivine crystallize out of the melt simultaneously. Now the melt will be continuously enriched in $\mathrm{SiO_2}$, moving along the the slope of the eutectic line toward the ternary point *o*. Here, the the residual melt will crystallize as olivine, pyroxene and magnetite.

The red line, marking the boundary in which our samples are situated, denote a oxygen fugacity that leads to a relatively early formation of magnetite at a point with a relatively low Fe-content within the residual melt. The samples StW25, StW12 and StW4 are located

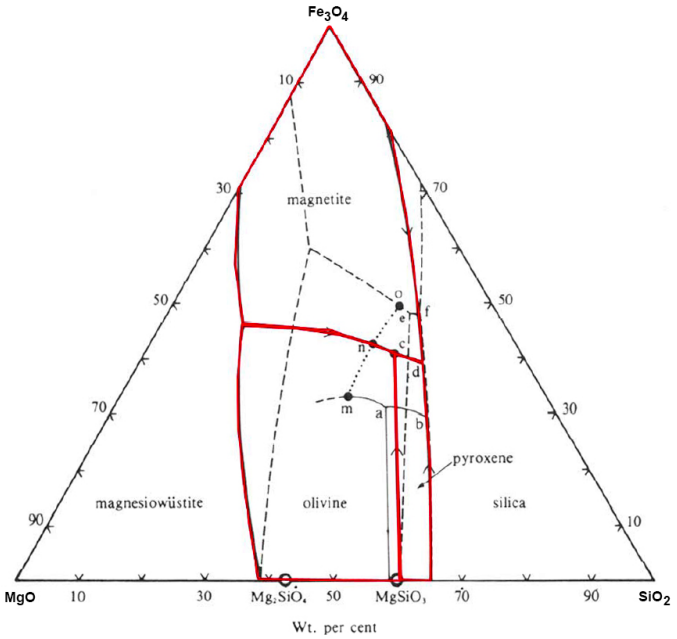

Figure 3.14: Fractionated crystallization in the system MgO-FeO-Fe_2O_3-SiO_2, depending on different oxygen-fugacities (after Osborn and Watson [1977]).

within the pyroxene area and the samples StW18 and StW20 within the olivine area. It can be assumed that more magnetite was formed in the olivine system, since the binary reaction-line is longer than in the pyroxene system. In fact, predicting which products are formed with this method remains impossible, since the quenching of the sample lead to a break of the liquidus areas.

3.2.4 Oxidation reactions in olivines and pyroxenes

Our samples contain a fair amount of magnetite. The formation of magnetite depends strongly on the partial pressure of O_2. Under reducing conditions, Fe^0, or native Fe, remains stable. The higher the oxygen fugacity, the higher are the oxidation effects in Fe, i.e. Fe(II) oxidizes to Fe(III). Under atmospheric conditions, the oxidation of Fe(II) to Fe(III) happens quite rapidly. Due to the quenching, magnetite will be formed predominantly, since it is more stable under the present temperatures than hematite. This leads to an extraction of Fe from the melt and results in a raise of the $\frac{N(Mg)+N(Si)}{N(Mg)+N(Si)+N(Fe)}$-ratio. This, then again, leads to a shift in phase stability and results in the formation of more Mg-rich phases, which finally will result in a partitioning of the melt into Fe-rich phases, such as magnetite, and Mg-rich phases, such as olivine, pyroxene and quartz.

Fayalite, the Fe-rich olivine endmember, remains stable at a low oxygen fugacity of 10^{-18} at 700 °C. At higher oxygen fugacities, faylite will only be stable at much higher temperatures. The stability of magnetite and quartz increases when more oxygen is available within the system.

$$3Fe_2SiO_4 + O_2 \Leftrightarrow 2Fe_3O_4 + 3SiO_2 \tag{3.7}$$

Equation (3.1) shows the oxidation reaction of fayalite to magnetite and quartz. This reaction affected especially the samples StW18 and StW20, the latter being more Fe-rich. At temperatures above 1000 ℃ the fayalite composition of the melt phase reacts directly to magnetite and quartz, which will then coexist in the cooled sample. Further, we can expect a high temperature oxidation reaction of fayalite:

$$(Mg,Fe)_2SiO_4 \xrightarrow{min.1080\,℃} Mg_2SiO_4 + MgSiO_3 + SiO_2 + Fe_2O_3 \tag{3.8}$$

The fast reaction at min. 1080 ℃ results in the formation of cristobalite, a high-temperature modification of quartz, and hematite. The diffusion of magnetite and quartz within the system leads to the formation of unmixing lamellae or patches (Haggerty and Baker [1967]; Champness and Gay [1968]; Champness [1970]). At lower temperatures, the reaction products form cellular structures separated by needle-like structures of amorphous quartz. During the growth of those products, olivine experiences an enrichment in Mg. With higher temperatures the diffusion of iron throughout the system is stronger and faster, and thus the formed forsterite can react with Si to protoenstatite [Koltermann, 1962]. This means for the samples that at temperatures of about 1080 ℃ fayalite can not only fractionate into quartz and magnetite but as well to enstatite and cristobalite, so that we can see cristobalite, magnetite and enstatite within the samples, forming unmixing lamellae or separated needle-like phases.

The above states only the main issues we encounter by synthesizing minerals with the melt-quench method, but other problems occurring, e.g., if there is only minor amounts of calcium within the system, will not be elaborated here further. To summarize, it can be said that the main issue is the high oxidation, the samples were exposed to. Thus, with the set up of the method, the oxidization of Fe-cations, and thus the formation of unexpected phases within the samples, can not be prevented. Here, working under a shielding atmosphere, e.g., CO_2, is mandatory. Further, since a platinum crucible tends to draw Fe out of the system under such unshielded atmosphere, a different crucible material would be advised. Moreover, since the quench process leads to a rapid fractionation of the phases within the system and not to the formation of solid solutions, it would be advised to rather investigate the possibility of working with sol-gels.

3.3 Dust analogue material from natural rocks

Since the synthesis of dust analogues was not a feasible method, and as further investigations were too time consuming and hold a scope of work big enough for another PhD-thesis, dust analogues from natural rocks have been prepared finally. Five samples were subjected to extensive preparation and analysis, but only one sample, pyroxene SA84-132, which was already in use for several campaigns, was finally used for the acceleration campaign onto the CDA and LAMA for this study. The remaining four samples were prepared, analyzed and coated with platinum and later polyprrole (PPY), but could not be accelerated. In the case of the platinum coating, the method could not be applied as professionally as desired, due to the lack of equipment. Further, we detected an enormous pump

Table 3.1: Overview over the samples prepared for the calibration experiments onto CDA and LAMA, with emphasis on the Fe-content

Sample	Mineral	Archive No.	Location	Fe-content
SA 84-132	Orthopyroxene	unknown	Harrat Uwayrid	∼7 wt%
SP2	Olivine	18652	Turkey	∼8 wt%
SP3	Hortonolith	18661	Bushveld, Transvaal	∼35 wt%
SP4	Fayalite	unknown	Bushveld, Transvaal	∼43 wt%
SP5	Fayalite	18669	Juna Hästberg, Sweden	∼69 wt%

oil contamination within the samples, which happened during the freeze drying stage. In the case of PPY-coating, we assume processes within the accelerator source that lead to an electrostatic sticking of the dust analogues, so that they formed aggregates that were too large or heavy for acceleration. The coating issues remain unclear and unsolved so far.

The following description explains the preparation method, which was applied to all samples and focusses on the geochemical analysis of sample SA84-132, which was as well applied to the same extent to all prepared samples. An in-depth description of all samples and their analyses can be found in Guglielmino [2012]. This thesis focusses further on sample SA84-132, which turned out to be the most important and significant sample for the identification of ISD-candidates within the Cassini CDA data base.

Generally, the rock samples chosen after preliminary examination, were cut into slices of about 2 mm thickness and further broken down into to sizes smaller 10 mm. Since avoiding contamination was a main priority, all precautions were taken. Using a manual iron plunger, the samples were broken down to size fractions below 3 mm. Further, the samples were milled down with an agate ball mill, a Frisch Pulverisette P-0150. The ball mill offers ten stages of grinding intensity and the samples were grinded for multiple times 40 minutes at stage 7. After each milling step, the samples were sieved with stainless steel sieves to sizes of 500 μm, 250 μm, 180 μm, 125 μm and <63 μm. The procedure was repeated for several times so that finally the fraction of >500 μm was the smallest fraction. The particle fractions were then washed with distilled water, ethanol and isopropanol, respectively and dried at 55 °C for at least six hours. Usually, samples would be subjected to handpicking now, but the samples were, due to their rather high Fe-content, treated with a high-strength neodymium magnet, to separate the magnetic particles from each size fraction. Not all magnetic particles could be separated from the samples, due to intergrowth or sticking of the particles. Table 3.1 gives an overview of the samples initially prepared for this study, with special emphasis on the Fe-content of each sample.

The grinding of minerals does not remain without certain effects on the treated material. Grinding may change the material due to the magnetic and electrochemical processes during the milling, which becomes especially important for preparation to sub-micron scale [Lin and Somasundaran, 1972]. Xu et al. [2004] reported, that milling under dry, low-energy conditions, such as grinding by hand in a mortar or using a ball mill on low energy, may result in a reduction of magnetic interactions between $\alpha - Fe_2O_3$ nanoparticles. Further, low-energy milling with a ball mill seem to produce more uniformly shaped particles than milling at high energies.

Of all samples, thin sections for scanning electron microscope analysis (SEM) and electron microprobe analysis (EMPA) have been manufactured. In the case of sample SA84-132, we prepared a grain dissection from the large grain fraction of the sample.

3.4 Sample SA84-132: Analysis and results

This sample is already in use since several years for calibration purposes of flight instrumentation, but has not been subjected to an extensive EMPA analysis as conducted for this study. The dust analogue is successfully coated with platinum and is one of our best working silicate sample for the use at the accelerator [Höfer, 2010]. For analysis, sample SA84-132 already came as a separate with grains <1200 μm, which was extensively handpicked before, with the main goal of separating only orthopyroxene out of the sample.

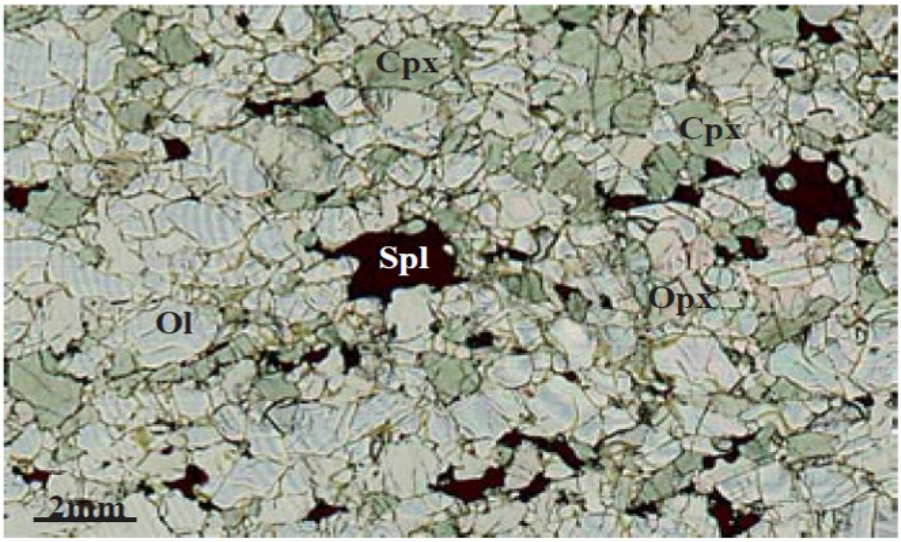

Figure 3.15: Highlight microscope image of the sample SA84-132, showing appearance and distribution of olivine (Ol), orthopyroxene (Opx), clinopyroxene (Cpx) and spinel (Spl) within a representative cutout of the sample

Sample SA84-132 consists of an orthopyroxene separate obtained from a mantle-xenolith, collected in Harrat Uwayrid in Saudi Arabia, and was already examined petrologically and with respect to its light elements and volatile budget by Kaliwoda [2004]. The host rock is a so-called spinel-lherzolite, a peridotite, consisting of predominantly orthopyroxene, olivine, clinopyroxene and spinel, as shown in Fig. 3.15. Both pyroxenes show exsolution lamellae. After extensive analysis with SEM it became apparent that the sample not only consists of the desired orthopyroxene, but as well of seven other mineral species. Analysis of the sample with EMPA lead to the determination of the exact composition of the found species and as well their exact structural formulas could be calculated. The sample bears additionally clinopyroxene (Cpx), spinel (Spl), olivine (Ol), feldspar (Fsp), amphibole (Amph), quartz and glasses. To summarize and give an overview over the mineral content of sample SA84-132, Table 3.2 shows the mean elemental composition of each mineral within the sample, measured via EMPA, in wt% oxide.Fig. 3.16 shows an overview of of the sample

mounted for SEM analysis, the grain sizes of that fraction is <1200 μm, as used for the prior handpicking of the sample. It is visible that the sample seems to be dominated by orthopyroxene, as desired. The image on the left shows the amount of clinopyroxene within that sample fraction.

Table 3.2: Elemental composition of sample SA84-132, measured via EMPA. The chemical content is given in mean wt% oxide

Oxide	Orthopyroxene	Clinopyroxene	Spinel	Feldspar	Olivine	Amphibole
SiO_2	46.41	51.45	2.10	56.73	40.99	42.32
TiO_2	0.07	0.58	0.15	2.25	0.02	2.35
Al_2O_3	4.17	6.13	57.15	22.21	0.03	0.86
Cr_2O_3	0.24	0.61	8.54	0.04	0.03	0.86
Fe_2O_3	0.18	2.08	1.23	2.95	0.00	5.09
FeO	1.48	1.39	9.84	0.00	9.75	0.00
MnO	0.03	0.10	0.08	0.07	0.14	0.07
NiO	0.00	0.00	0.00	0.00	0.00	0.00
MgO	29.72	15.68	21.15	3.13	48.83	17.29
CaO	0.48	19.98	0.05	8.69	0.11	10.20
Na_2O	0.05	1.47	0.01	3.98	0.02	3.81
K_2O	0.00	0.01	0.00	0.09	0.01	0.08
H_2O	0.00	0.00	0.00	0.00	0.00	2.12

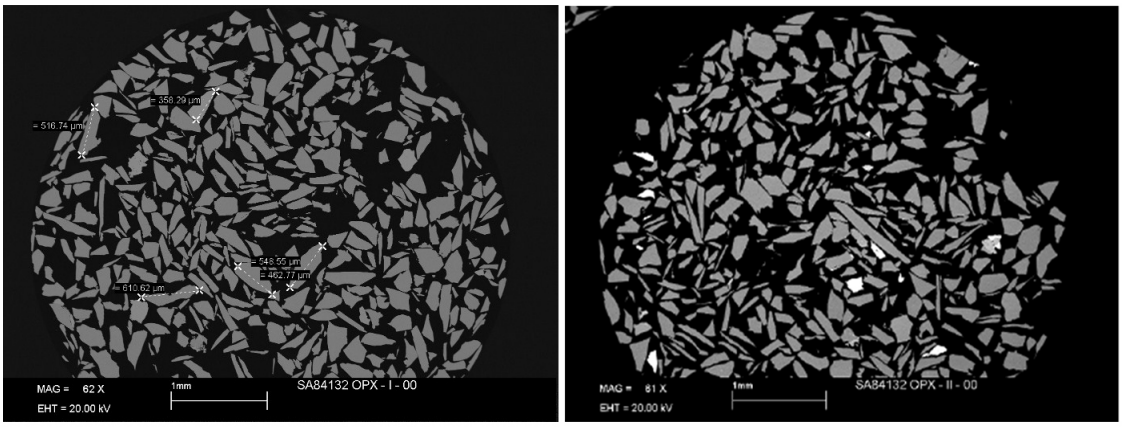

Figure 3.16: Overview of the grain distribution in sample SA84-132. The darker mineral in both SEM-images is the clearly dominating mineral within the sample

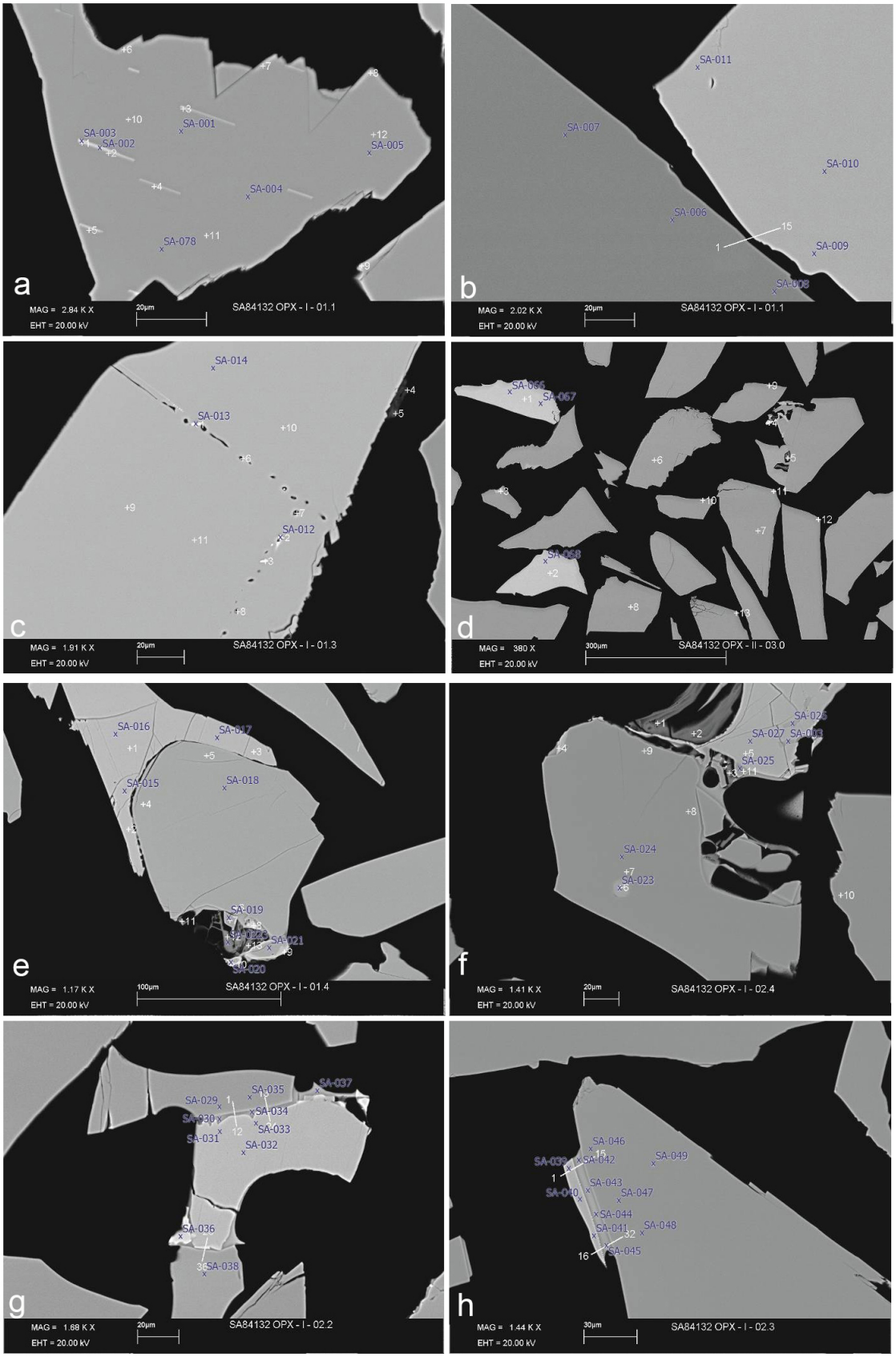

Figure 3.17: SEM-illustration of occurring impurities in sample SA84-132. Picture a shows spinel lamellae in opx, picture b and d show cpx (light) besides opx (right). C illustrates melt droplets within cpx. Pictures e-h illustrate the intergrowth of mineral species and glass with opx. The labels denote the measurements conducted within this sample

SA84-132: Pyroxenes

Orthopyroxene in the sample shows as aluminian ferroan enstatite with accessory subsilicic and chromian proportions. The composition after EMPA analysis is shown in Fig. 3.18.

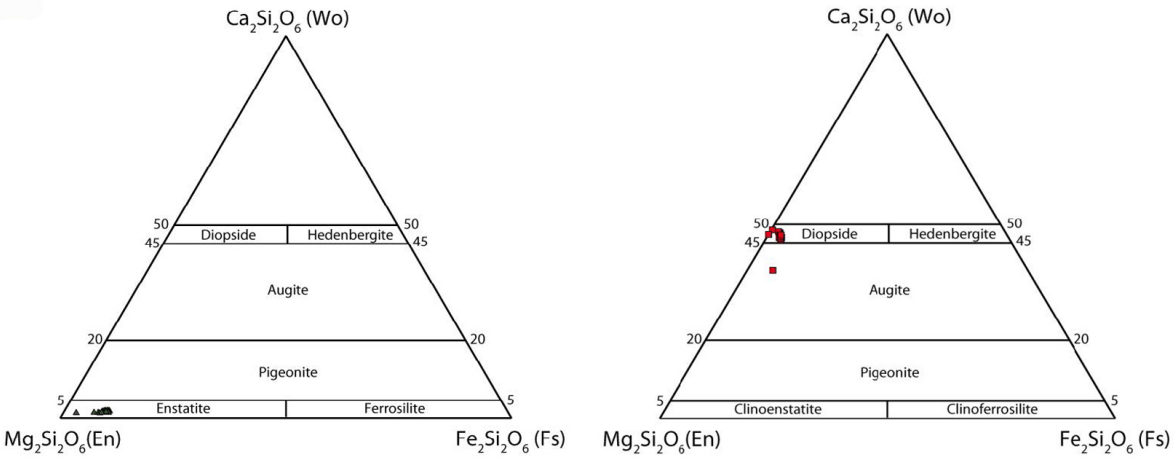

Figure 3.18: Composition of orthopyroxene and clinopyroxene within the sample SA84-132 from EMPA analysis. The Opx (left) measured has an overall enstatite composition, with only minor Ca-content, the Cpx (right) measured has an overall diopsidic composition

The structural formula of the enstatite in the sample can be written as $(Mg_{0.84-1.0})$ $(Al_{0.07-0.15}Fe^{3+}_{0-9.17}Cr_{0.01-0.05}Mg_{0.63-0.88}Fe^{2+}_{0.04-0.19}Mn_{0-0.01})Al_{0.12-0.38}Si_{1.62_1.90}O_6$. Clinopyroxene consists in its majority of aluminian chromian diopsides, with few exceptions showing sodium constituents. As well, fewer Cpx are aluminian magnesian chromian augites, as well showing minor sodium constituents. Here, the structural formula shows as $(Ca_{0.68-0.81}$ $(Na_{0.04-0.15}Mg_{0-0.9})(Al_{0.08-0.15}Fe^{3+}_{0-0.1}Ti_{0.01-0.02}Cr_{0.01-0.03}Mg_{0.83-1.0}Fe^{2+}_{0-0.1}Mn_{0-0.01})$ $Al_{0.03-0.18}Si_{1.87-1.97}O_6$.

SA84-132: Olivine

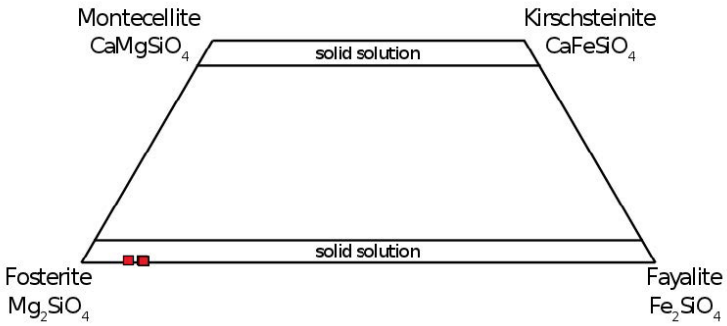

Figure 3.19: Composition of olivine found within sample SA84-132

As visible in Fig. 3.19 The olivine in the sample is Mg -rich an can thus be denoted as forsterite. Its structural formula can be expressed as $(Mg_{1.78}Ca_{0-0.01}Fe^{3+}_{0.15-0.21}\square_{0-0.01})SiO_4$, where the symbol $\square$ connotes cation vacancies, that can be occupied by Ca, Mn and as well to minor extend by Al, Cr, Ti, Na or K.

SA84-132: Feldspar

The feldspar in sample Sa84-132 is plagioclase, namely labradorite, with a chemical composition between albite (Ab_{35-49}) and anorthite (An_{51-64}). The structural formula after EMPA measurement can be written as $(Ca_{0.33-0.48}Na_{0.23-0.41}K_{0-0.01}Mg_{0.14-0.26}Ti_{0.07-0.09})$ $[Fe^{3+}_{0.07-0.14}Al_{1.13-1.20}Si_{2.46-2.68}]O_8$.

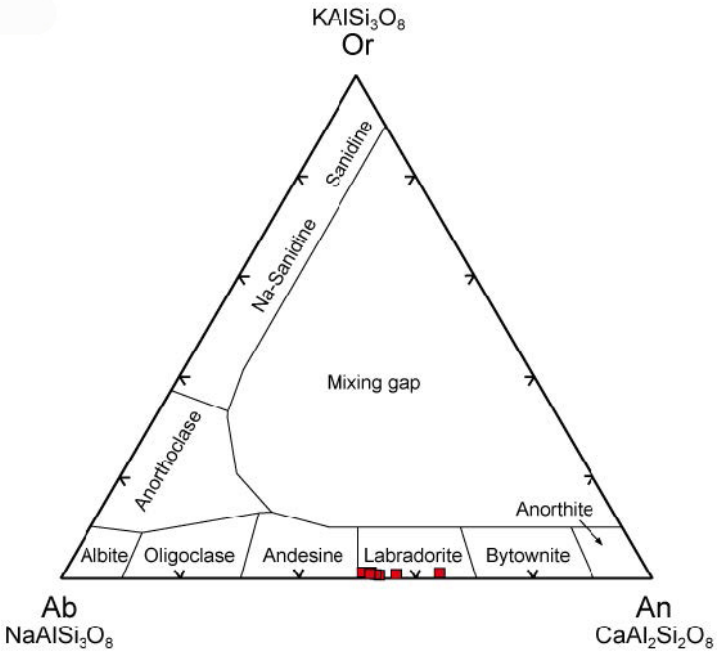

Figure 3.20: Composition of plagioclase found within the sample SA84-132 in the system Ab-An-Or

SA84-132: Amphibole

Amphiboles found in the sample have been classified as Ca-Na-Amphiboles with a general structural formula written as $Na_{0.65-0.69}K_{0.01-0.02}(Ca_{1.51-1.58}Na_{0.3-0.38}Mg_{0.04-0.15}Mn_{0-0.01})$ $(Mg_{3.55-3.58}Al_{0.53-0.58}Fe^{3+}_{0.52-0.57}Fe^{2+}_{0-0.3}Ti_{0.24-0.26}Cr_{0.09-0.11})Si_{5.97-6.01}Al_{1.99-2.03}O_{22}(OH)_2$. Fe on the C-sites is both, Fe2+ andFe3+, but never at the same time. Since it is very difficult to pinpoint amphiboles to a specific mineral within the amphibole series, it is common to classify them by the relationship $Mg/(Mg+Fe^{2+})$. The amphiboles in sample SA84-132 show high Mg-ratios and intermediate Si contribution, as illustrated in Fig. 3.21, and can therefore be considered being either magnesiohastingsite, ferrian pargasite or ferroan pargasite. The occurrence of amphiboles in the form of pargasite is already described in Kaliwoda [2004].

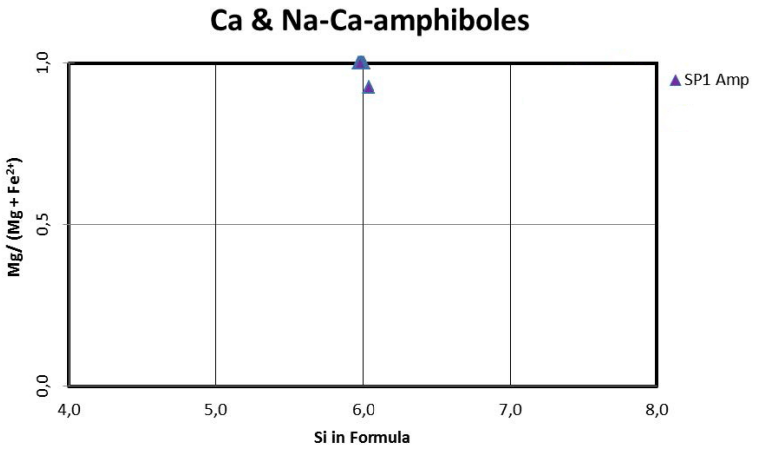

Figure 3.21: $Mg/(Mg+Fe^{2+})$-ratios as a function of Si cations within the structural formula in amphibole

Using the three dimensional diagram after Hawthorne et al. [1997] (Fig. 3.22) for further classification of amphiboles, we can assign an area of composition, with respect to Na+K (A-site), Na (B-site), and Al (T-site).

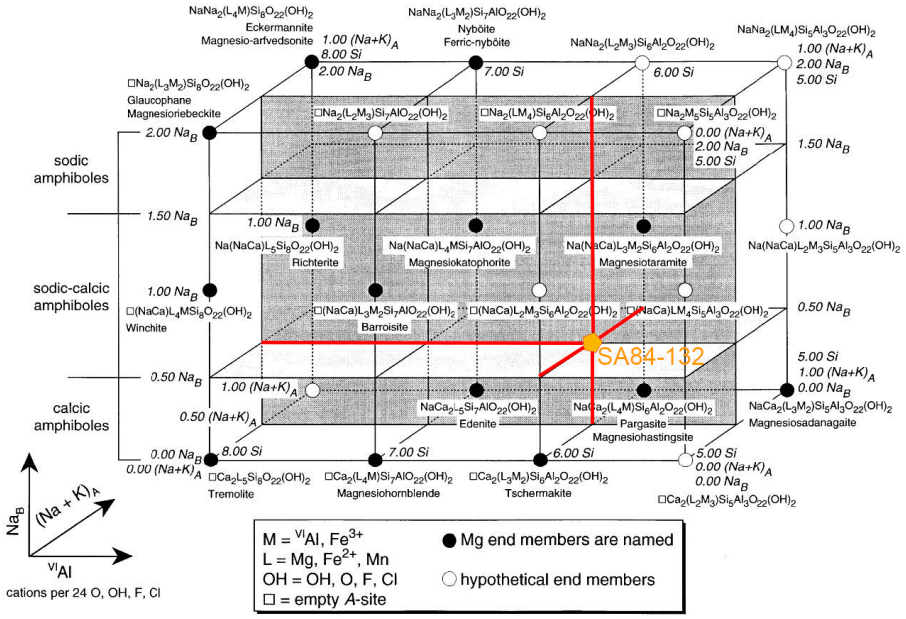

Figure 3.22: Area of composition of amphiboles found in sample SA84-132, here in orange, modified after Hawthorne et al. [1997]

SA84-132: Spinel

Very few minerals of the spinel group have been found within the sample. They show commonly a typical spinel composition, with a structural formula that can be written as $(\mathrm{Mg}_{0.8-0.82}\mathrm{Fe}^{2+}_{0.2-0.23})(\mathrm{Al}_{1.50-1.79}\mathrm{Cr}_{0.17-0.18}\mathrm{Fe}^{3+}_{0-0.03})\mathrm{O}_4$. Minor built in of Si happens at the

cost of Fe2+, due to the very dominant siliceous matrix of the host rock. The mineral can be described as chromian ferrian spinel.

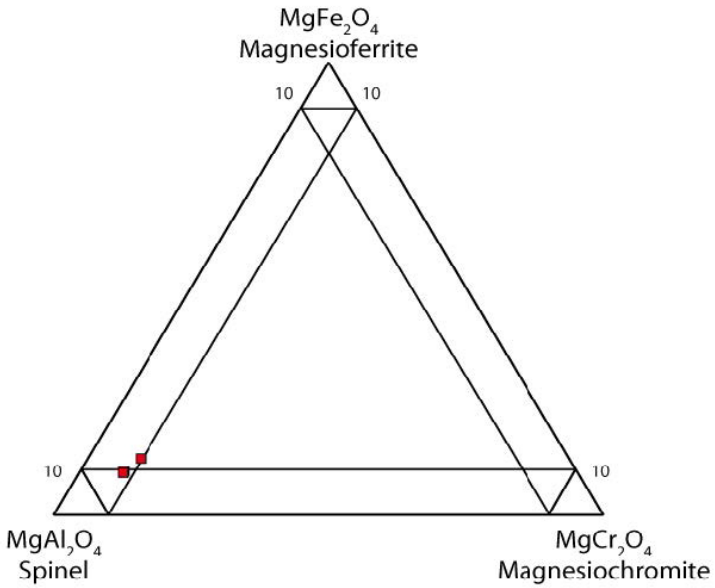

Figure 3.23: Composition of spinel within the sample SA84-132

3.4.1 Analysis of the modal mineralogy of sample SA84-132

After such thorough analysis of sample SA84-132, finding it consisting of at least seven mineral species, it was important to quantify the proportion of each constituent within the sample. Therefore, the SEM is equipped with a tool, the INCA-Microanalyszer Suite from Oxford Instruments. The area measurement feature of this software was used on slow scanned BSE images to investigate the material contrast, due to its density, so that we are able to investigate different grey-scale shades in the sample. Hence, we are able to allocate material abundances through the shaded area distribution in our scanned images. This method bears error sources, such as graphical artefacts, background noise and errors from manual peak selection, but statistics can be used to achieve the most realistic results. Depending on the samples, the x-axis was adjustable by 110-130 pts. per step, possibly affecting the accuracy of peak heights of 50000 pts. by 6.4%, peak heights of 20000 pts. by 2.4%, and on heights of 5000 pts. by 1.0% for each scale. Fig. 3.24 illustrates the accuracy for material contrasts by using grey scale histograms, acquired with the INCA-Microanalyzer Suite. At height pts below 10000 pts it was difficult to select histogram peaks, leaving an averaged error of 2%.

After INCA-analysis we are able to establish a percentage of proportions of the species within this particular sample fraction. We can therefore conclude that orthopyroxene accounts for 90.51% material within the sample, the proportion of clinopyroxene accounts for 4.48% and all others, containing spinel, olivine, feldspar, amphibole and further glasses,

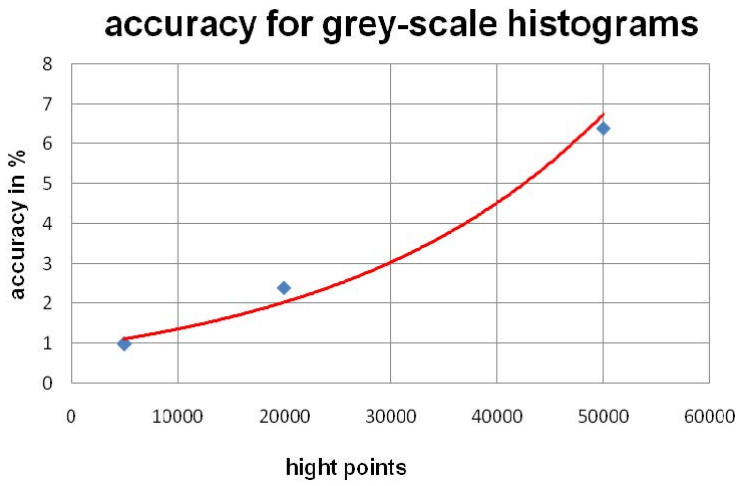

Figure 3.24: Accuracies for materials contrast in grey-scale histograms provided by the INCA-Microanalyzer suite. Hight pts below 10000 pts prove to be most difficult in selecting histogram peaks

make 5% of the sample.

Note that the results of this analysis can only be a rough estimate, since the method bears rather large errors and more important, this sample can not be seen as entirely representative, since we did not look at the entire sample, but only a very small fraction of it to gain basic insights. This grain fraction mount can not be considered as exactly equivalent to the fine grained dust in the accelerator source. It is not ascertained, e.g. if modal mineral abundances were modified by milling, sieving, or coating procedures. These points should be checked in future studies, an overview of remaining open questions and future research to be conducted is given at the end of this thesis.

Sample SA84-132 was coated with a conductive platinum layer prior to acceleration, since particles need to hold charge for moving through a potential of 2MV. The coating of silicates has only recently become possible and is described in Hillier et al. [2009]. Sample SA84-132 was provided as a ready-to-use sample, since it has been utilized for several calibration campaigns before.

4 Principles of impact ionization time-of-flight mass spectrometry

This section gives an overview of the principle of TOF-mass spectrometry and the specific issues regarding the impact ionization process. Further, I will give a short introduction to impact ionization TOF-mass spectra calibration and further address the general contamination issue in space and in the laboratory, visible within the mass spectra.

4.1 Basic principles of time-of-flight mass spectroscopy

TOF mass spectroscopy enables us to analyze the composition of a sample via its transformation, acceleration and separation. The constituents of a sample will be transformed partly into ions. These ions will then be accelerated in an electric field to a constant energy and finally separated, utilizing their different charge-to-mass-ratios, meaning different times of flight over the distance of a field-free drift region [Thomson, 1913].

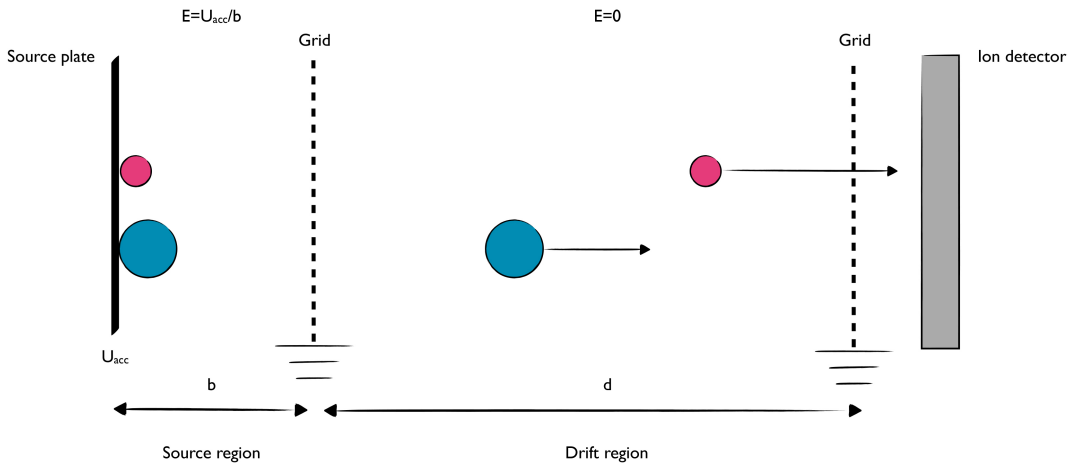

Figure 4.1: A very simple set up of a time of flight mass spectrometer. After Mocker [2011]

The general set-up of a very basic TOF mass analyzer (Fig. 4.1) consists of a source region *b* with a size up to a few centimeters, a drift region *d* and an ion detector. The source region is defined by the source plate and a grid connected ahead of it. A potential difference, existing between the source plate and the grid with he separation distance *b*, defines the electrical field of the source region. The ions are accelerated through this potential difference $E = U_{acc}/b$ and are then drifting through a field free region *d*. The velocities of the

particles are inversely proportional to the square root of their masses, meaning lighter ions will have higher velocities than ions with higher masses. Thus, ions with lower masses will reach the ion detector earlier than heavier ions. The resulting mass spectrum from ions measured at the ion detector, is the conversion of the detected output current as a function of time. Visible within a mass spectrum is the relative intensity of the signal over the mass to charge ratio of the ions. The mass resolution within such a very basic set up will be rather low. To enhance the mass resolution of a TOF mass spectrometer, instruments may have an additional reflectron, devices for energy focussing or may utilize multiple acceleration regions.

4.1.1 The calibration of time-of-flight mass spectra

Ions, emerging from the source plate with zero initial energy, are accelerated through the source region and will finally reach a uniform energy [Cameron and Jr. Eggers, 1948].

$$\frac{1}{2}mv^2 = q \cdot U_{acc} \tag{4.1}$$

with U_{acc} being the accelerating potential, *m* the ion's mass and *v* the final velocity of the ion. Hence, the accelerated ions will traverse the drift region *d* with a uniform velocity *v*. They will then reach the detector at time

$$t = \sqrt{\frac{d^2}{2qU_{acc}}} \cdot \sqrt{m} \tag{4.2}$$

depending on the square root of the ions mass. The mass scale can then be described as

$$t = \mathrm{b} + \mathrm{a} \cdot \sqrt{q/m} \tag{4.3}$$

with *a* being the *stretch factor*, a proportionality constant, determined by the set up of the instrument, and *b* being the *shift parameter*, representing any time offsets between the triggering point and the start of the spectrum. The parameters *a* and *b* have to be determined for the conversion of the detector output current, representing the relative intensity of the signal as a function of time, into a mass spectrum. Several methods can be applied:

- the approximation of both parameters by fitting to two assigned mass lines t_1 and t_2 to the masses m_1 and m_2 . Both parameters can then be derived via equation

$$t_2 - t_1 = a(\sqrt{m_2} - \sqrt{m_1}) \tag{4.4}$$

- the approximation of both parameters by fitting to *n* assigned lines $t = \{t_1, t_2, \cdots, t_n\}$ to the corresponding masses $m = \{m_1, m_2, \cdots, m_n\}$, which then can be approximated with a least square fit.

- cross correlation to a theoretical template spectrum [Lavila, 2002], for the determination of either the stretch parameter, the shift parameter or both.

Finally, the mass resolution for a mass spectrometer is defined as the ratio of ion mass m of a specific species to the deviation of the mass Δm.

$$\frac{m}{\Delta m} = \frac{t}{2\Delta t} \tag{4.5}$$

4.1.2 The impact ionization process

The space instrumentation used for this study utilizes the method of hyper- or high velocity impact (HVI) ionization TOF mass spectroscopy. In space and in the laboratory a particle with a certain, very high, velocity hits the target. Thus, depending on the mass and hence, the velocity of the particle, the impactor will be partially or completely vaporized and/or ionized. The ions will be then, as described above, detected by an ion detection system and converted into a mass spectrum which then can be further analyzed.

The process of HVI-ionization is a non-equilibrium process and thus leads to a variety of challenges with respect to the interpretation of the resulting mass spectra. Fig. 4.2 shows a model of shock wave ionization after Hornung and Drapatz [1981].

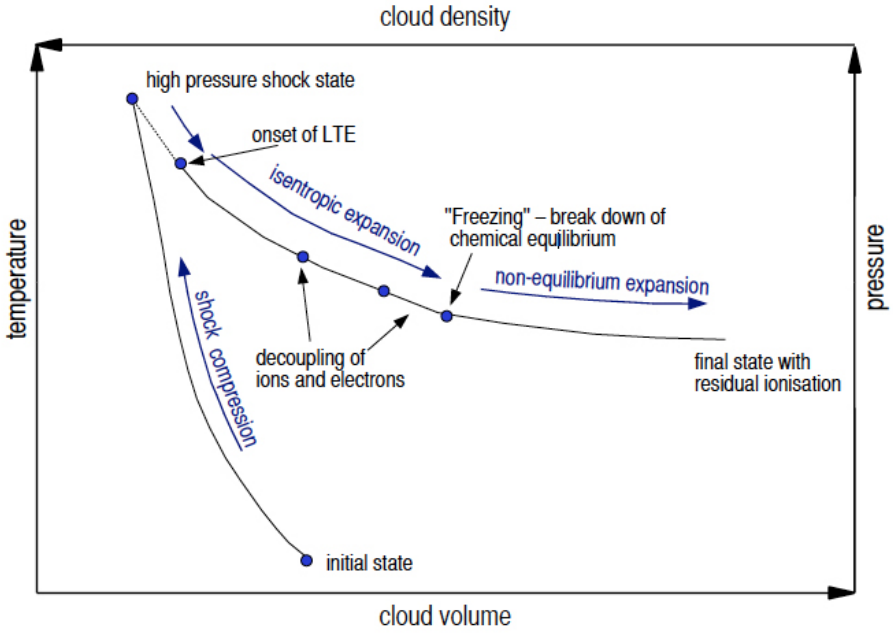

Figure 4.2: The principle of shock wave ionization [Hornung and Drapatz, 1981]

When a particle hits a solid surface with a high velocity, ions from both the particle and the target surface will be produced, which will be visible within the resulting mass spectrum. The main issue we encounter during the attempt of interpreting such mass spectra is that a mineral analysis, obtained via SEM or EMPA, can not be directly compared to an impact

ionization mass spectrum. This results from a variety of processes occurring during and after the impact of a particle onto a target. According to the theoretical shock wave ionization model shown in Fig. 4.2, several phases and processes can be expected for impact ionization. The first phase is characterized by the compression of the impacting particle to high pressures and temperatures, owing to the strong shock experienced upon impact. This results in a gain of the specific internal energy of the system, which will be further partitioned into various processes within the hot dense material, following the impact. The particle then will be either partially or wholly evaporized due to the successive release from the high pressure state, the so-called unloading. It is assumed that molecules with be dissociated and atoms strongly ionized here, if the temperatures are high enough. This expansion should be isentropic and the gas quickly reaches local thermodynamic equilibrium (LTE). In the early stages of subsequent expansion of the plasma or gas, all relaxation processes are assumed to happen rapidly with the gas remaining in equilibrium. Further, due to the expansion, the gas cools rapidly. Processes occurring are ionization and dissociation and later recombination processes. Ionization and dissociation behave exponentially with the temperature, the rates of recombination depend on density and temperature, linked via a power law. Ionization and dissociation eventually stops, with the degrees of both decreasing with time. The same goes for the recombination processes. Thus, the gas expands to infinity in the partially dissociated state with residual ionization, the so-called freezing. The mass spectrum finally shows the recorded residual ions (Mocker et al. [2012], and references therein).

The impact ionization process is not yet clear and remains to be investigated. Since we are not fully aware of how the single processes, evaporation, ionization, dissociation and finally recombination, affect the chemistry and mineralogy of the impactor and thus the resulting mass spectrum, we experience difficulties in the interpretation of the latter, especially, when it comes to spectra of multi-mineralic compounds. For chemical analysis, several questions remain, e.g., concerning the role of electronegativity and electron affinity within the processes (recombination) and further, to which extend ionization energies affect the resulting mass spectra (ionization).

4.2 Contamination problems

When we investigate impact ionization mass spectra, we can expect to see not only ions from the particle and the target, as well as newly formed target-projectile-clusters but further the chemical compounds of the coating material. Additionally, ions from contamination occurring within the accelerator, the experiment chamber, on the target surface and from anthropogenic sources can be seen. In the following, I will give an overview of the contaminating species we encounter in the mass spectra, not only from in situ measurements, but as well in our experimentally obtained spectra. An in-depth analysis of contamination occurring especially on the CDA-target can be found in Postberg et al. [2009a].

- H and C are both very abundant contamination species found within CDA and LAMA mass spectra. They show as dominant peaks especially at speeds exceeding $20\,\mathrm{km\,s^{-1}}$ (in the case of our recorded spectra). H and C might not be appearing at speeds below $10\,\mathrm{km\,s^{-1}}$.

- O is quite abundant as a target contaminant but is as well a constituent of impactors, especially in silicates and oxides. Hence, it is not clear, how to distinguish O into contaminant or impactor-related. O shows up at speeds exeeding $20\,\mathrm{km\,s^{-1}}$ and is less abundant than C and H. If the amplitude of the O-mass line exceeds the C mass line, it indicates very high velocities of a particle. Thus, O can be used for velocity determination, as well as C and H.

- Alkali metals, Na and K, are always present in mass spectra, especially in those obtained experimentally. Na and K can be constituents in silicates, but also occur as target contamination,particular at low impact velocities. Na is usually more abundant than K. Within in situ spectra, Na and K can show up as well, but not as abundant as in experimentally obtained spectra. Here as well, Na is more abundant than K.

- Hydrocarbon molecular clusters are a very abundant contamination in experimentally obtained spectra, due to not only the particle coating, but as well due to residues of pump oil within the vacuum chamber or the entire beam line system of the accelerator. They usually appear at velocities below $10\,\mathrm{km\,s^{-1}}$ and show decreasing abundance at higher speeds. Hydrocarbon clusters play a minor role in in situ CDA spectra.

- Si is a major constituent in silicates, and can occur also as a minor contaminant on the target, or from the coating process when platinum is used.

Contamination within the spectra, here especially hydrocabons, complicates the analysis and thus the interpretation of the spectra, especially at lower velocities, since they may obscure features of the sample material and lead to the confusion of mass lines with other isobaric species.

5 Results and discussion

One of the main tasks for this study was the search for interstellar dust within the Cassini CDA data set. As described in 1.4, ISD is to be expected within our solar system and has been already discovered in data from previous missions, e.g., Ulysses. The search for exogenous dust within the enormous data set is extremely difficult against the enormous background of the local Saturnian dust environment e.g., E-ring particles. However, 13 TOF-mass spectra of ISD candidates have been identified, after analysis of the CDA subsystems data (CAT, IID and EG). These particles have dynamical properties consistent with the ISD upstream direction of $\sim$259° longitude - +8° latitude, a siliceous composition and are in agreement with velocities predicted for interstellar dust streams of $\sim$26 $\mathrm{km\,s^{-1}}$ or higher. Fig. 5.1 shows the two different types of ISD candidates that have been identified in the Cassini data set within day 225 to day 351 of 2010.

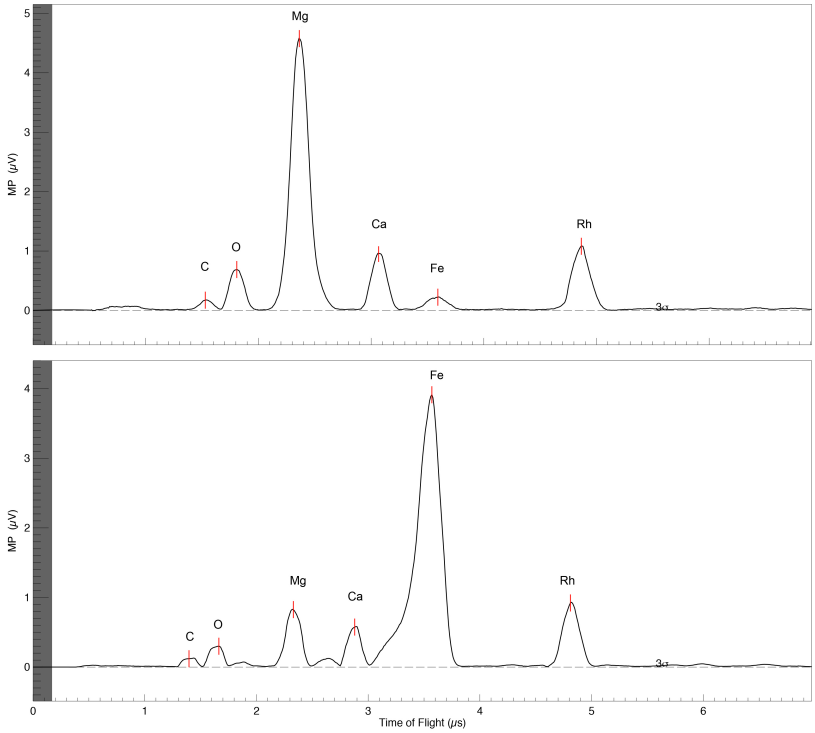

Figure 5.1: Two types of ISD candidates from the Cassini CDA data set. The upper panel shows the co-added spectra of eight Mg-dominated particles, the lower panel shows the co-added spectra of five Fe-dominated particles. The y-axis shows the multiplier signal in μV and the mass lines on the x-axis are given as time of flight units

Calibration of space instrumentation with suitable dust analogues aids the interpretation of in situ mass spectra. It enables correct determination of the initial composition of impacting particles, as well as determination of the impact velocity of a dust grain. Therefore, we

conducted calibration campaigns with the CDA flight spare unit, which is in any respect identical to the instrument onboard Cassini, and further with the LAMA, which has a considerably higher mass resolution than the CDA. Especially the LAMA allowed a thorough chemical analysis of the mass spectra. For the verification of the composition of the Mg-dominated ISD candidates we obtained mass spectra with LAMA and CDA from sample SA84-132, which is described in 3.4. For the Fe-dominated ISD candidates, the plan was to obtain spectra from Fe-rich pyroxenes and olivines. However, these could not be used in the end, as already described in 3. Thus, the following analysis focusses entirely onto sample SA-84-132.

5.1 Impact ionization mass spectra from multi-mineralic analogues measured by LAMA

5.1.1 General evaluation of the recorded mass spectra

Fig. 5.2 shows the size and velocity distribution of the accelerated particles from the orthopyroxene sample onto the LAMA. The data set consists of mass spectra of a total of 1642 particles with sizes ranging from 0.04 μm to 2.0 μm and velocities of 1.4 $\mathrm{km\,s^{-1}}$ to 39.7 $\mathrm{km\,s^{-1}}$, which were recorded in May 2012.

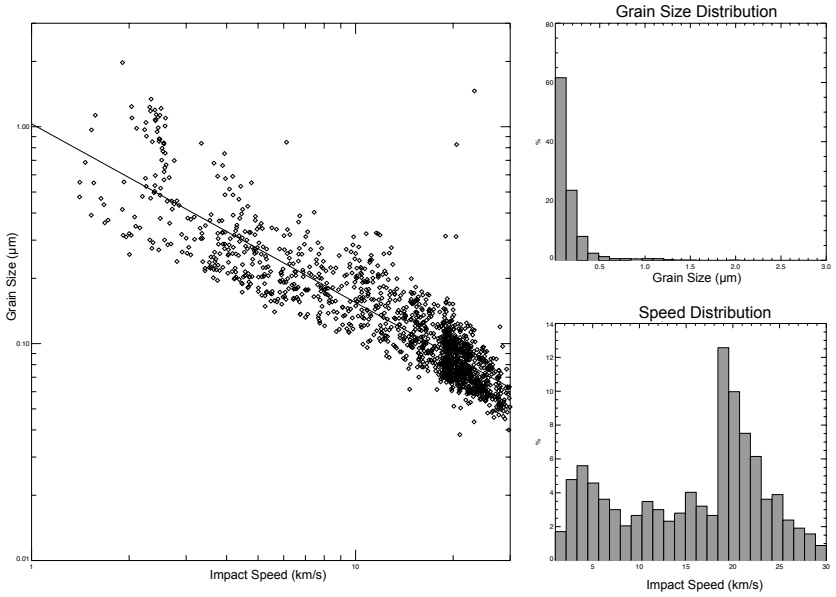

Figure 5.2: Size and velocity distribution of the accelerated mineral grains from sample SA84-132. The particles were accelerated with velocities of 1.4 $\mathrm{km\,s^{-1}}$ to 39.7 $\mathrm{km\,s^{-1}}$ and have sizes ranging from 0.04 μm to 2.0 μm

The recorded mass spectra were further processed and calibrated using the in-house software "SpectrumGUI", to determine the shift and stretch parameters for each individual spectrum. LAMA spectra have, due to the reflectron design of the instrument, rather narrow peaks, which are relatively unaffected by plasma ion energetics. Furthermore, the trigger time of the instrument is quite reliable. Therefore, the calibration to a mass scale

is considerably easier than with linearly designed instruments, such as the CDA (Hillier et al. [2006]; Hillier et al. [2012]). After initial calibration, 1355 spectra with a high calibration quality ($\geq$ mass scale assigned) remained for further analysis. For each spectrum the baseline was adjusted manually. Fig. 5.4 shows a spectrum obtained by summarization of all 1355 mass spectra in the pyroxene data set for all velocities between 1-40 $\mathrm{km\,s^{-1}}$.

The creation of sum spectra can be useful in certain cases, e.g., for better visualization of mass peaks in TOF spectra. If applied to the same type of material, or to a certain velocity range, such a procedure significantly reduces electronic noise and averages variable conditions during the impact ionization process caused by surface roughness, or projectile size, form and orientation. Furthermore, this procedure averages out scatter of peak amplitudes due to variable conditions of the electronic noise, the plasma environment and the stochastic nature of the impact process.

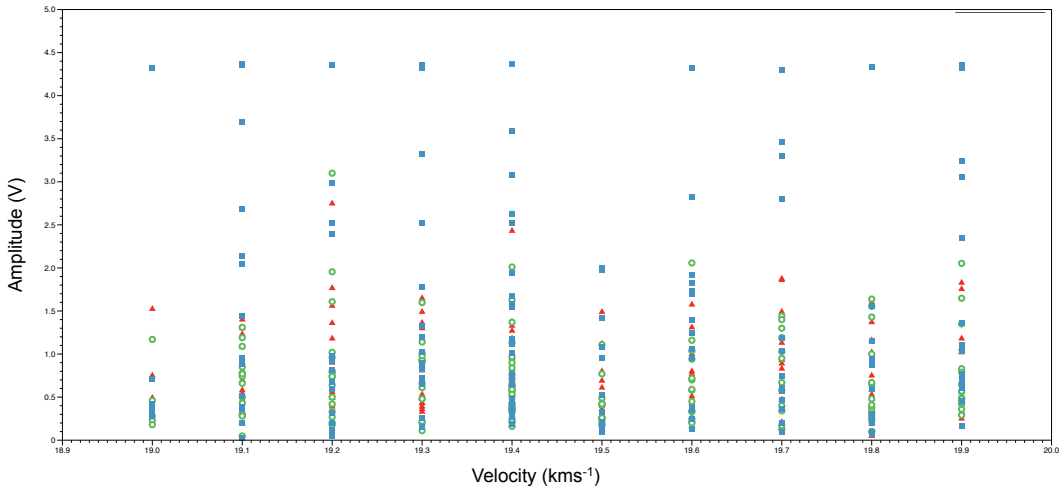

Figure 5.3: Observed scatter of the measured peak amplitudes for the elements Mg (blue), Si (green) and Rh (red) between 19-20 $\mathrm{km\,s^{-1}}$

Fig. 5.3 shows the measured scatter of Mg, Si and Rh peak heights in a very narrow velocity bin of 19-20 $\mathrm{km\,s^{-1}}$. This fluctuation of the peak amplitudes is similar for both target and projectile atomic or molecule masses. The main reason for this is likely size variation, but other factors affecting total energy, energy density and implcitly ion yield and sensitivity are important as well, e.g. heterogeneities of projectile and target surface material.

The total sum spectrum (Fig. 5.4) demonstrates that distinct peaks occur - even above the 3σ line - at nearly every (integer) mass up to mass 103 u, where the Rh peak is located. This indicates the presence of complex organic compounds within the impact plasma. The presence of such complex organic species is expected, due to the coating method that utilizes MPTMS, which contains an aliphatic backbone and further, due to contamination of the particles, the target or both with long-chained hydrocarbons that may stem from vacuum grease or pump oil. However, many major mass lines can be ascribed to projectile material, as outlined below.

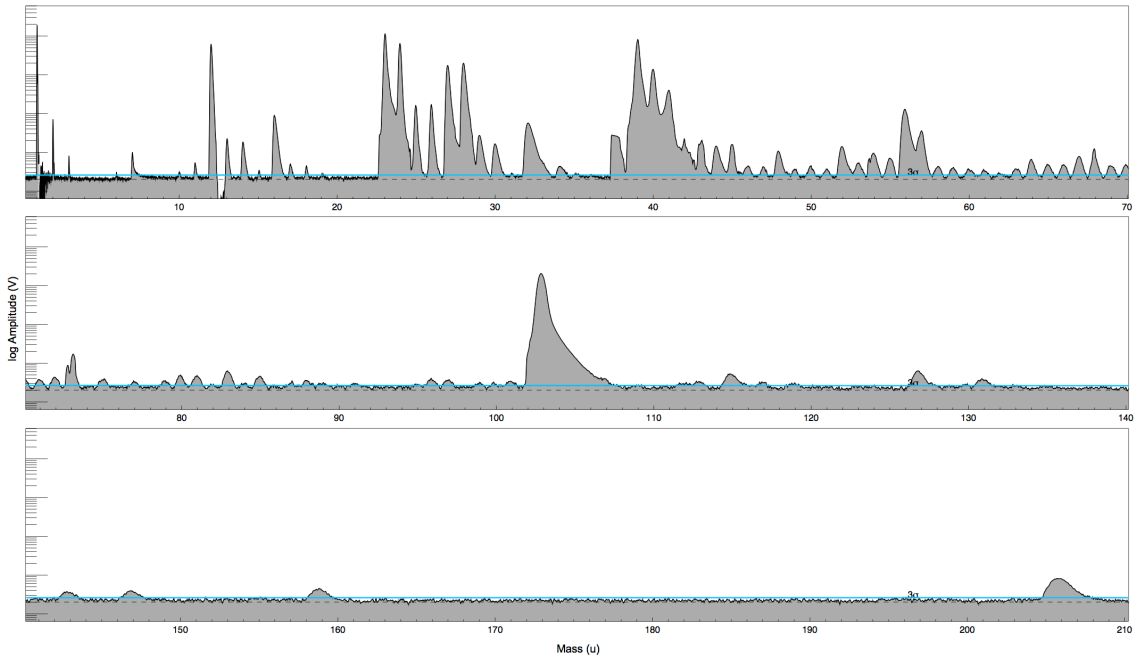

Figure 5.4: Sum impact ionization mass spectra of all 1355 spectra from sample SA84-132. The blue line represents the 3σ line. The mass scale runs from 0 u to 70 u (top), 70 u to 140 u (middle), and 140 u to 210 u (bottom)

5.1.2 The identification of features in impact ionization mass spectra

The spectra were further divided into velocity bins. Table 5.1 below shows the number of the spectra within the individual velocity bins. The width of the velocity bins are $5\,\mathrm{km\,s^{-1}}$ throughout the entire measured velocity range, to show the variation of the mass lines within the spectra with increasing velocity.

For the identification of peaks within the mass spectra, a variety of methods has to be applied. Some peaks can be unambiguously assigned in the low mass range, since they can not be confused with other isobaric species. Unambiguous peak assignment can be applied to e.g., H, H_2, H_3, Li, B and C. Further, the unique isotope pattern can help in identifying the correct species, e.g. H, H_2, H_3, Li and B, further Mg, K, Ca, Ti, Cr and Fe, as well as Pt. Finally, unambiguous mass line assignment is possible for target-projectile clusters. Target projectile clusters are extremely valuable within the spectra, since they can help verify the occurrence of species in the medium mass range, where peaks can be easily confused with other isobaric species.

The identification of peaks is aided by the circumstances that certain species increase, while other species decrease with velocity as shown in Fig. 5.5. Co-added spectra between 1 and $4.9\,\mathrm{km\,s^{-1}}$ show an accumulation of mass lines that are not easily distinguishable from each other. The spectra are dominated by the Na and K peaks that appear to have a very broad basis, which includes all adjunct mass lines. Subsequently, with increasing velocity, other mass lines seem to get "peeled" out and become more and more distinct.

Table 5.1: The number of recorded spectra from the pyroxene sample within the individual velocity bins

Velocity range ($\mathrm{km\,s^{-1}}$)	No of spectra
1-5	202
5-10	129
10-15	139
15-20	352
20-25	379
25-30	118
30-40	46

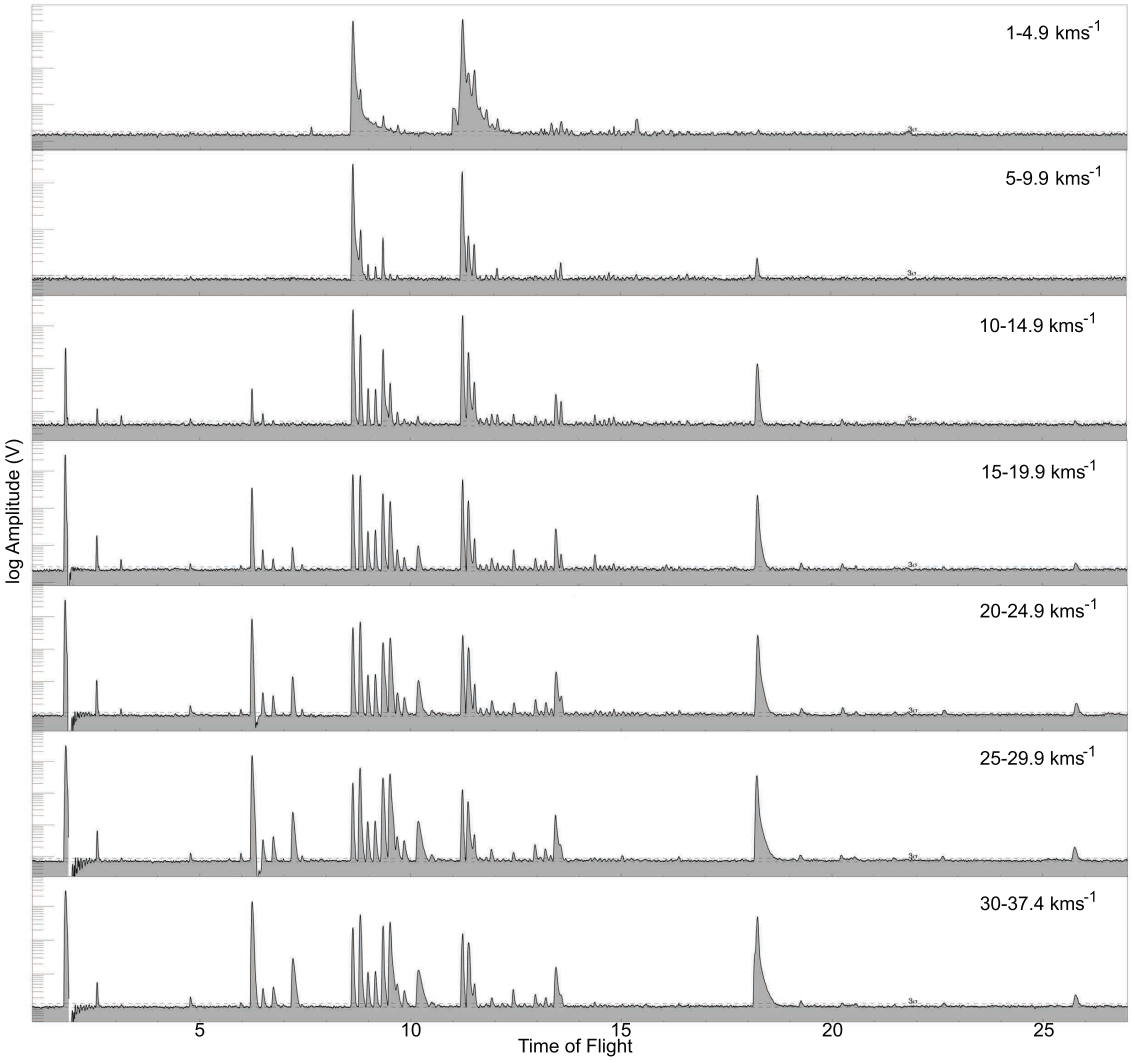

Figure 5.5: Sum impact ionization mass spectra of sample SA84-132 for velocity bins between 1 and 37.4 $\mathrm{km\,s^{-1}}$

Both Na and K have rather low ionization energies and strongly tend to form cations, which is a common feature of species that dominate mass spectra at low velocities, e.g. certain molecular ions of which bonds are not broken up at low impact energy (e.g., Hillier et al. [2012]). Species with high ionization energies do not tend to appear at low impact

velocities, but are present at higher impact velocities. Some of them preferably occur as anions, such as Cl or N. Further, certain species disappear with increasing velocity. At higher velocities, the kinetic energy per particle mass and volume, i.e. the energy density, is higher. This leads to the break up of molecules and disapearance of the corresponding mass lines.

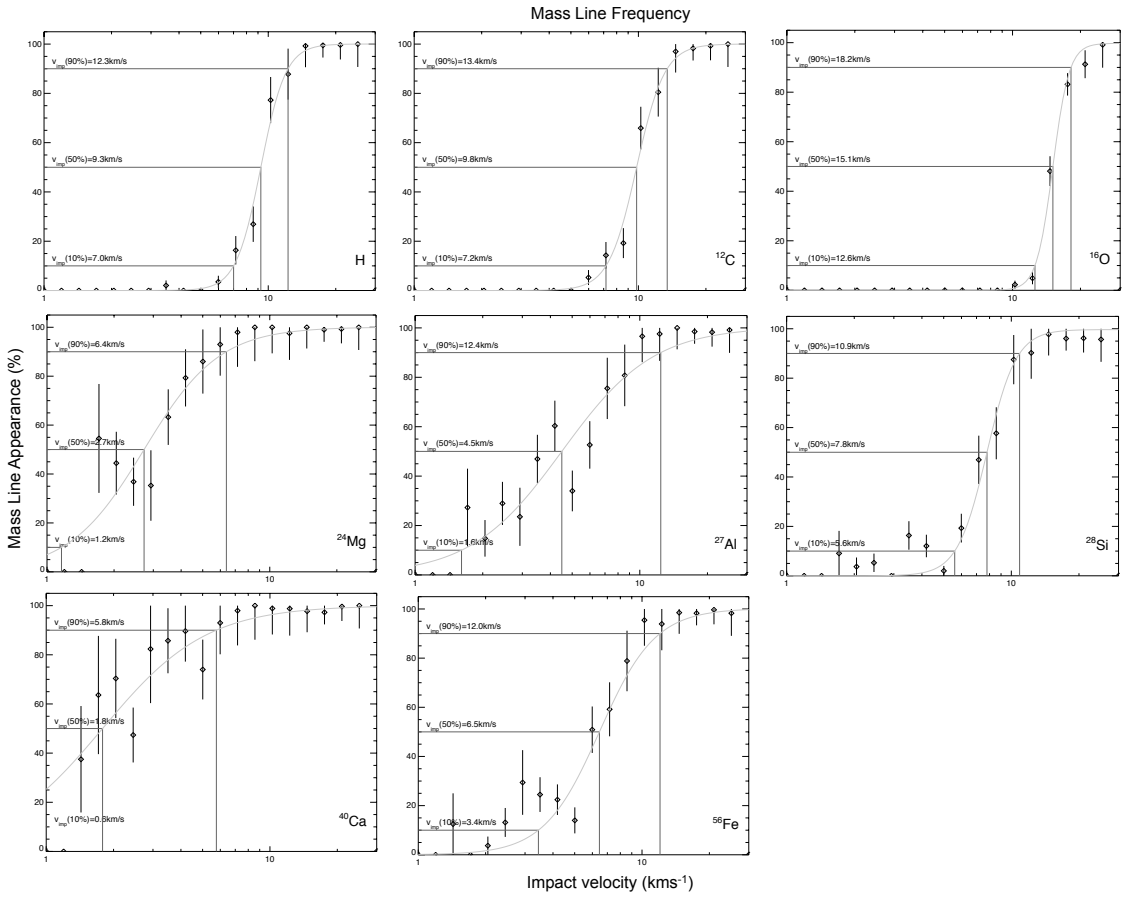

Figure 5.6: Occurence of the mass lines of H, ^{12}C, ^{16}O ^{24}Mg ^{27}Al ^{28}Si, ^{40}Ca and ^{56}Fe versus velocity.

Fig. 5.6 shows the occurrence of important mass lines, here H, ^{12}C, ^{16}O, ^{24}Mg, ^{27}Al, ^{28}Si, ^{40}Ca and ^{56}Fe, depending on the velocity of the impacting particles. The horizontal marks show the velocity at which 10%, 50% and 90% of the spectra show a specific mass line. The velocity thresholds were derived from the pyroxene data set described here, since this data set is one of the largest data sets obtained so far.

We can see here that certain species stemming from the impactor itself, namely ^{27}Al ^{28}Si, and ^{56}Fe can be reliably identified at velocities >10-12 $\mathrm{km\,s^{-1}}$. ^{24}Mg and ^{40}Ca are present throughout the almost entire velocity range and occur already at low velocities above 3 $\mathrm{km\,s^{-1}}$. As at low velocities isobaric interferences with molecular ions may occur, the unambiguous identification may require investigating the Mg and Ca isotopic patterns and the occurrence of target-projectile clusters of Mg, Ca and Rh. In general, the identification of impactor species is most reliable at high impact velocities, where molecular

interferences decrease and all impactor species are above the ionization threshold. H, ^{12}C and ^{16}O are species that can be used to determine the velocity of an impactor. For the estimation of the impact velocities of the ISD candidates, we investigate the ratio of the C/O-amplitudes. The higher the ^{16}O-line, with respect to ^{12}C, the faster is the impactor. As mentioned above, ^{16}O preferably forms anions, so the yield of $^{16}O^+$ monotonically increases with impact velocity. ^{12}C is due to surface contamination of the Rh-target and is used as the normalizing isotope, as the relative contributions of the contaminated target surface layer should decrease with increasing energy and energy density.

Table 5.2: List of features occurring within our LAMA mass spectra above 3σ, including possible isobaric species at all velocities (after Hillier et al. [2012])

Mass	Mineral	Other	Mass	Mineral	Other
1		H	47	Ti	
2		H_2	48	Ti	$SHCH_3$
3		H_3	50	Ti	
6		Li	52	Cr	
7		Li	53	Cr	C_4H_3
10		B	56	Fe	
11		B	57	Fe	C_4H_8
12		C	58	Fe	C_4H_9
13		CH	60		
14		CH_2, N	64	TiO	C_5H_4
16	O	O, CH_4	65		C_5H_5
17			66		C_5H_6
23	Na	Na	67	CaAl	C_5H_7
24	Mg		68		
25	Mg	C_2H	72	CaO_2, AlSiOH, FeOH	
26	Mg	C_2H_2	80		
27	Al	C_2H_3	81		C_6H_9
28	Si	C_2H_4, Si	83	AlCaO	C_6H_{11}
29	Si	C_2H_5, CHO, Si	96	Ca_2O, CaAlSiH, $CaSi_2$	
30	Si	C_2H_6, Si	97		
32	O_2^+	S, O_2^+	103		Rh
34		S	115		RhC
39	K	K	116		RhC
40	Ca	Ca	130		RhAl
41	K, MgOH	K, C_3H_5,	131		RhSi
42	Ca		143		RhCa
44	AlOH		147		RhCa
44	Ca, SiO		158		RhFe
45	SiO, SiOH	CO_2H, CH_2OCH_3	206		Rh_2
46	Ti				

As in high velocity mass spectra the identification and quantification of mass lines are more reliable, and because the velocities of interstellar dust candidates are anyway $26\,\mathrm{km\,s^{-1}}$ or higher, our quantitative evaluation exclusively focusses on spectra with velocities higher than $19\,\mathrm{km\,s^{-1}}$. Moreover, as the number of spectra in the velocity ranges between 25-$40\,\mathrm{km\,s^{-1}}$ was lower than anticipated, the following analysis concentrates on spectra with velocities between 19-$25\,\mathrm{km\,s^{-1}}$. Due to the high energy density, we do not expect a wide range of molecular species within the spectra. ^{23}Na and ^{39}K, which dominate at low velocities and are most likely due to target surface contamination are distinctively present at

abundance levels typical for projectile concentrations. Na can even be used as a reference line for the alignment of the spectra. Table 5.2 shows features occurring within the LAMA mass spectra (signals considered only above 3σ), together with possible other isobaric species, stemming from the impactor itself (2nd column), or from the Pt-coating, from the Rh target and target projectile clusters, and target conatmination (3rd column). We find that certain contaminants, some hydrocarbons and an unknown fraction of ^{23}Na and ^{39}K, remain persistent into the high velocity range. Thus, the isobaric species will be taken into careful consideration for the mass line assignment, nonetheless. Table 5.3 shows the species we expect to occur within the mass spectra, as well as their wt% abundance in the dust projectiles as determined by Electron Microprobe Analysis (EMPA).

Table 5.3: Elemental composition of sample SA84-132 orthopyroxene, measured via EMPA. Elemental concentrations are given in mean wt% oxide. We also detected glasses (amorphous components) within the samples. However, glasses are not listed here, due to their high variability in chemical composition

Oxide	Orthopyroxene	Clinopyroxene	Spinel	Feldspar	Olivine	Amphibole
SiO_2	46.41	51.45	2.10	56.73	40.99	42.32
TiO_2	0.07	0.58	0.15	2.25	0.02	2.35
Al_2O_3	4.17	6.13	57.15	22.21	0.03	0.86
Cr_2O_3	0.24	0.61	8.54	0.04	0.03	0.86
Fe_2O_3	0.18	2.08	1.23	2.95	0.00	5.09
FeO	1.48	1.39	9.84	0.00	9.75	0.00
MnO	0.03	0.10	0.08	0.07	0.14	0.07
NiO	0.00	0.00	0.00	0.00	0.00	0.00
MgO	29.72	15.68	21.15	3.13	48.83	17.29
CaO	0.48	19.98	0.05	8.69	0.11	10.20
Na_2O	0.05	1.47	0.01	3.98	0.02	3.81
K_2O	0.00	0.01	0.00	0.09	0.01	0.08
H_2O	0.00	0.00	0.00	0.00	0.00	2.12

Firstly, I assigned H and H_2 H_3, ^{6,7}Li,^{10,11}B, ^{12}C, CH, since these species are very unlikely to be confused with other isobaric species. Further, at these velocities (19-25 $\mathrm{km\,s^{-1}}$) the species show very distinct peaks. I further identified ^{16}O and ^{23}Na, ^{39}K and ^{103}Rh. Most of the spectra of the chosen bin show features above 103 u, which marks the Rh-peak of the target material. We observe target-projectile or target-contaminant clusters at 115 u and 116 u, which is RhC, further, features at 130 u, 131 u, 143 u, 147 u and 158 u, which denotes RhAl, RhSi, Rh^{40}Ca, Rh^{44}Ca and RhFe, respectively. A peak at 206 u, Rh_2, can be observed in all spectra with velocities above 20 $\mathrm{km\,s^{-1}}$. Target-projectile clusters efficiently help to verify the presence of projectile species, meaning if e.g., RhAl or RhSi occur, we can be fairly certain that features at 27 u and 28 u are due to ^{27}Al and ^{28}Si. Otherwise, with no target-projectile species present, features at 27 u and 28 u may as well be assigned to C_2H_3 and C_2H_4, especially at lower velocities. However, we are able to reliably identify ^{27}Al, ^{28}Si, ^{40}Ca and ^{56}Fe. Only few spectra show RhMg, which would be expected rather frequently, due to the abundance of Mg within the dust analogue. As well, no clusters with Ti, Cr, nor Na, K or O have been observed.

For species that can not be identified via the appearance of target-projectile clusters, or otherwise unbiased, here Mg, Ti and Cr, we can attempt the identification via their very

unique isotope pattern, illustrated in Fig. 5.7. The corresponding table (Table 5.4) shows the ionisation potential of elements of the impactor material, and their isotopic abundances.

Table 5.4: Overview of isotopic abundances of elements expected within the mineral dust spectra. Increasing ionisation potential from left to right.

Ion.Pot.(kJ/mol)	495.8	577.5	589.8	652.9	658.6	717.3	737.7	762.5	786.5	1313.9
Nuclides	^{23}Na	^{27}Al	^{40}Ca	^{52}Cr	^{46}Ti	^{55}Mn	^{24}Mg	^{54}Fe	^{28}Si	^{16}O
			^{42}Ca	^{53}Cr	^{47}Ti		^{25}Mg	^{56}Fe	^{29}Si	^{17} O
			^{44}Ca	^{54}Cr	^{48}Ti		^{26}Mg	^{57}Fe	^{30}Si	^{18}O
					^{49}Ti			^{58}Fe		
					^{50}Ti					
Abundance (%)	100	100	96.94	83.79	8.0	100	78.99	5.8	92.23	99.76
			0.65	9.51	7.30		10.00	91.72	4.67	0.04
			2.09	2.37	73.8		11.01	2.20	3.1	0.2
					5.5			0.3		
					5.4					

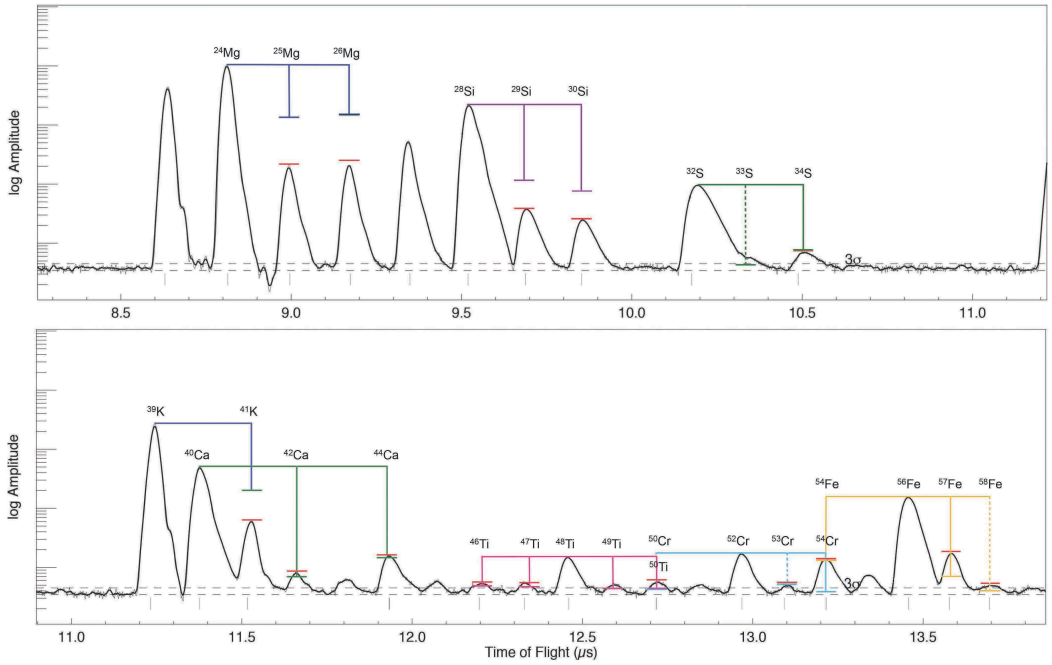

Figure 5.7: Example of a sum spectrum of 414 spectra between 20-25 $\mathrm{km\,s^{-1}}$, showing the heights of the peak amplitudes with respect to their expected isotopic pattern.

In all spectra >10 $\mathrm{km\,s^{-1}}$ we observe distinct mass line patterns in the regions of 24 u-26 u (Mg) and 28 u -30 u (Si), further in the region 39 u-44 u (K and Ca, respectively), 46 u-50 u (Ti) and finally between 52 u-57/58 u (Cr and Fe, respectively). Fig. 5.7 shows 414 co-added spectra at speeds between 20-25 $\mathrm{km\,s^{-1}}$ and the heights of the peak amplitudes with respect to their isotopic pattern, being a fairly representative suite for the appearance of isotopic line patterns within the spectra. The coloured markings denote the actual line heights according to the nominal isotopic abundance, the gap between the latter and the

red bars denote the deviation of the amplitudes from the nominal abundance. With the analysis of the isotopic patterns of the species in every single spectrum, we are able to finally identify Mg, S, Ti and Cr, and to verify the occurrence of Si, K, Ca and Fe.

We can see in Fig. 5.7 that there are rather large deviations between the recorded peak amplitude and nominal isotopic abundance in some features. This value varies strongly from spectrum to spectrum and resembles more the general random fluctuation of the amplitudes, as described before. It seems to be more important, that the lines follow the general isotopic pattern, which is observable in most spectra. The complete isotope pattern is not always visible, especially in Ti and Cr, which might be due to their low abundance within the sample material and their high ionization energy.

5.1.3 A new challenge: multi-mineralic dust analogues

As described in 3.4, sample SA-84-132 is not simply a mono-mineralic dust analogue consisting only of orthopyroxene with a unique chemical composition. Although it contains primarily orthopyroxene mineral grains (ca.90%) there are five additional mineral species present as impurities that could not be completely separated during mineral preparation procedures (Table 5.3). The most urgent question arising is *"Are we able to distinguish the mineral species from each other?"* A first and promising step was to define different types (Mg, Ca, Al, Si) of high-velocity spectra. Fig. 5.8 shows co-added spectra of the four different types assigned, for velocities between 19-25 $\mathrm{km\,s^{-1}}$. Types were assigned according to the dominance of the specific mass line, in terms of line hight, that denotes the signature element of the specific mineral species, with Mg for orthopyroxene, Al for spinel and Ca for clinopyroxene. Si occurred to be the dominating line in a small number of spectra, but always contiguous with another or all other significant mass lines. Table 5.9 shows the number of spectra for each type for velocities between 19-40 $\mathrm{km\,s^{-1}}$.

Table 5.5: The number of recorded spectra from the pyroxene sample within the assigned type bins, named after the most dominant mass line within a spectrum, for velocities between 19-40 $\mathrm{km\,s^{-1}}$

Type	No of spectra	19-24.9 $\mathrm{km\,s^{-1}}$	25-29.9 $\mathrm{km\,s^{-1}}$	30-40 $\mathrm{km\,s^{-1}}$
Type Mg	542	427	88	27
Type Al	51	38	16	7
Type Ca	44	35	5	4
Type Si	36	17	9	10

The sum spectra in Fig. 5.8 illustrate the appearance of the four types that could be assigned to the majority of spectra within the entire data set.

The INCA-analysis (3.4.1), obtained from sample SA84-132, gives us a rough estimate of the proportions of the mineral species within the sample. We expect orthopyroxene to be the major constituent of the dust analogue sample, accounting for about 90.5%. Further, clinopyroxene accounts for roughly 4.5% and others, namely spinel, feldspar, olivine, hornblende and glasses, account for about 5%. Based on the numbers of the typecasted spectra at velocities between 19-40 $\mathrm{km\,s^{-1}}$, type Mg accounts for $\sim$81%, type Ca for $\sim$6.5%, Type Al for $\sim$7.6% and Type Si for $\sim$5.4%. Type Al and type Si account altogether for

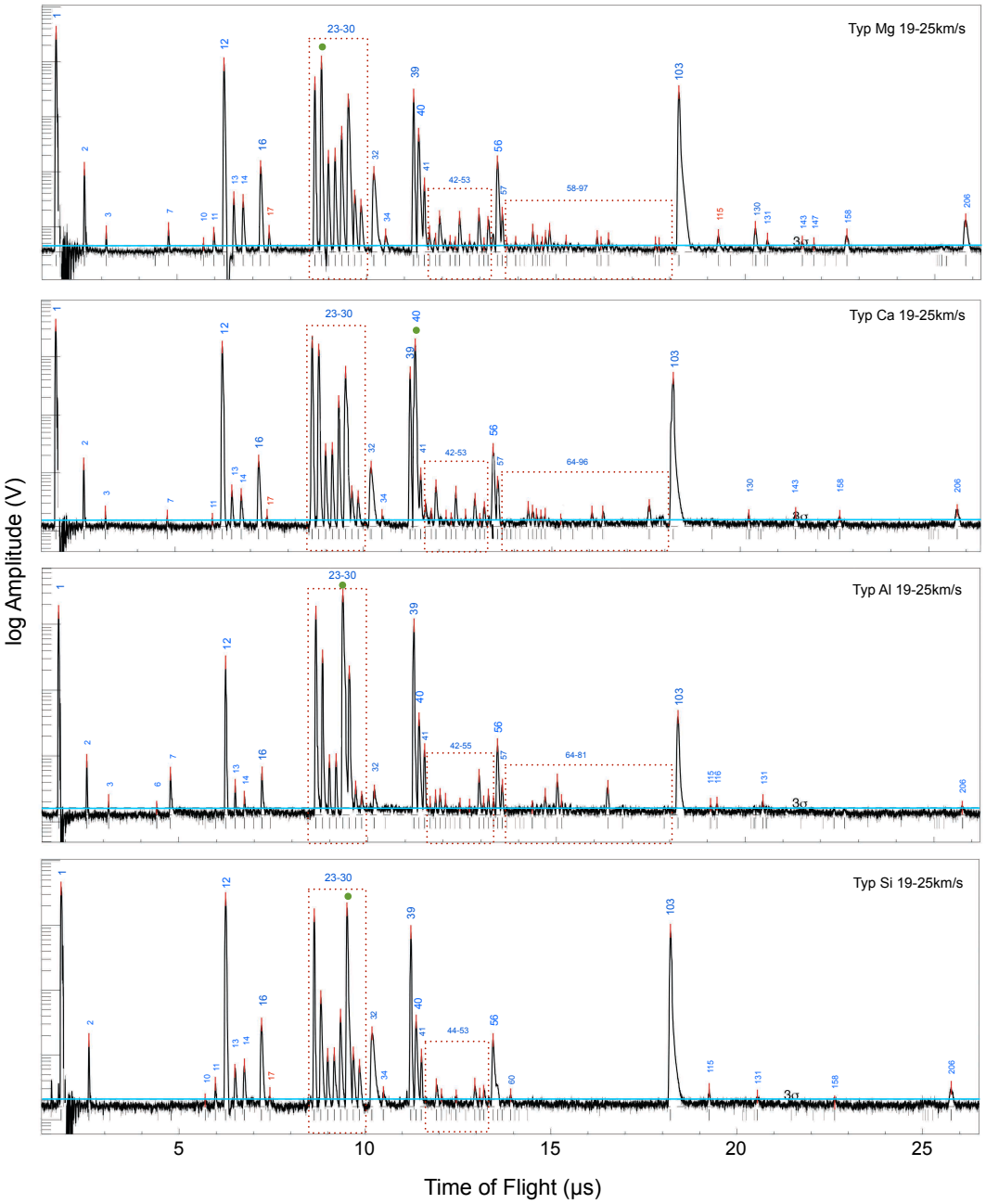

Figure 5.8: Co-added spectra for each type (Mg, Ca, Al, Si) assigned to a data set of 517 spectra with velocities between 19-25 $\mathrm{km\,s^{-1}}$. The blue labels denote the features identified within the spectra and described in Table 5.2. The green dots mark the dominating feature. The light blue horizontal line marks the 3σ-line. The dotted boxes embrace specific mass ranges

$\sim$13%, as "others". These numbers deviate strongly from the INCA-analysis, due to the following possible reasons:

- INCA analysis was not obtained from the entire sample, but only from a very small proportion from the large grain fraction, before milling down to sub-micron size. Thus, this analysis is in no respect representative for a source filling used with the accelerator. Using a sub-micron-sized fraction was not possible, due to analytical restrictions

- It is not clear inhowfar a Ca- (or Al-) type mass spectrum represents a pure clinopyroxene (or spinel) particle, or a mixtures between the main phase orthopyroxene and clinopyroxene and spinel, respectively. Mixtures can be more abundant than spinel or clinopyroxene endmembers.

The question remains, if the classified "types" are genuine and indeed different in chemical composition, or just an artefact due to the random fluctuation of the mass lines, leading to a stochastic accumulation as "types" when co-added? This attempt of type assignment is based on the mere dominance of one of four elements and we may envisage a more sophisticated evaluation.

5.2 A geochemical approach to the evaluation of multi-mineralic dust analogue spectra

For the following evaluation, the absolute line heights of 12 significant mass lines, namely C, O, Na, K, Mg, Al, Si, Ca, Ti, Cr, Fe and Rh and further, the spectra's total integral and the velocity and size of the particles, have been extracted manually out of 673 spectra with velocities between 19-37.4 $\mathrm{km\,s^{-1}}$. The intention of applying a statistical approach is to find hints for the existence of different species, such as clustering or grouping in the data, possible changes with velocity and correlations between signature elements of the different species, as apparent in the mineral analysis.

5.2.1 Data clusters as evidence for the existence of multiple species

Fig. 5.9 shows histograms of the abundances of the mineral signature elements in spectra at velocities between 19-25 $\mathrm{km\,s^{-1}}$. Here, the absolute line heights have been normalized to the main integral of their spectra, to remove mass effects that would otherwise lead to strong bias within the data. The main integral is taken as a proxy for the total ion yield of a spectrum, since the LAMA does not offer this parameter, and thus a mass line can be interpreted as a fraction of the total ion yield of its spectrum. Table 5.6 shows an overview of the elemental content of the signature mineral species with decreasing abundance, supplementing the histograms.

Table 5.6: Content of signature elements (in wt% oxide) in the mineral species with decreasing abundance. The colors show high contents (red), medium contents (orange) and low contents (yellow)

MgO	Mineral	SiO_2	Mineral	CaO	Mineral	Al_2O_3	Mineral
48.83	Ol	56.73	Fsp	19.98	Cpx	57.15	Spl
29.72	Opx	51.45	Cpx	10.20	Amph	22.21	Fsp
21.15	Spl	46.41	Opx	8.69	Fsp	6.13	Cpx
17.29	Amph	42.32	Amph	0.48	Opx	4.17	Opx
15.68	Cpx	40.99	Ol	0.11	Ol	0.86	Amph
3.13	Fsp	2.10	Spl	0.05	Spl	0.03	Ol

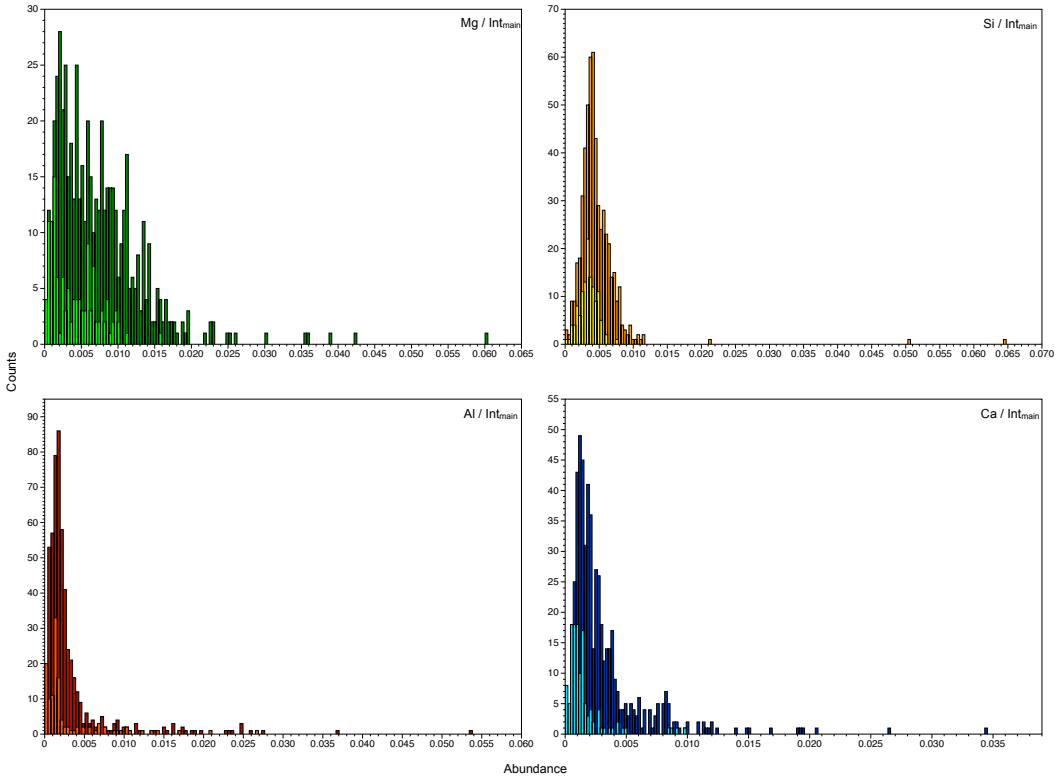

Figure 5.9: Histograms of the abundances of mineral signature elements within spectra at velocities between 19-25 $\mathrm{km\,s^{-1}}$ (dark color) and 25-37.4 $\mathrm{km\,s^{-1}}$ (light color). The histograms show the absolute line heights of the specific element normalized with the main integral of its corresponding spectrum. The x-axis shows the element-to- main integral-abundance and the y-axis shows the number of spectra

As I mentioned above, the majority of particles (549 of 673) have velocities between 19-25 $\mathrm{km\,s^{-1}}$, which is thus the reference velocity bin. Higher velocities are included in this plot, because it is important to know, if they follow the general trend of the majority of the particles or if effects due to velocity have to be considered. It is apparent that particles at higher speeds have a lower average value, which can be explained by decreasing line strengths with increasing velocities (see below 5.2.2).

At first sight, the histograms show a generally smooth one-peaked distribution and thus no clear trends with respect to distinct grouping. At closer inspection, however, the Mg-histogram seems to show a two-peaked distribution which is even better visible in the high velocity spectra. Low abundances might indicate the presence of feldspar, hornblende, clinopyroxene and spinel, while the main peak represents orthopyroxene and few extremely high values olivine. No extreme values are apparent in the Si-histogram, which is in agreement with the general smooth distribution of Si between the mineral species Table 5.6. The Al-histogram illustrates a tail of a low but significant data fraction to high Al-contents. While the majority can be ascribed to orthopyroxene, the high end tail could be due to spinel and feldspar. Finally, the Ca-histogram shows a bulge of intermediate to high abundances. High abundances might indicate the presence of clinopyroxene, whereas the medium ranges hint towards amphibole (hornblende) and feldspar.

5.2.2 Variations of mass line amplitudes with velocity

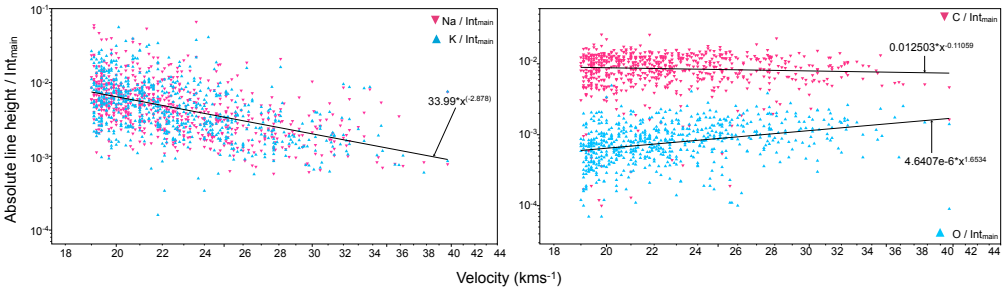

Figure 5.10: The behaviour of elements with velocity with Na and K on the left and C and O on the right. Shown here are the absolute mass line heights normalized to the main integral at velocities between 19-37.4 $\mathrm{km\,s^{-1}}$, with x- and y-axis both on logarithmic scale

Fig. 5.10 illustrates, how elements susceptible to certain degrees of contamination behave with velocity. The plot on the left show the absolute mass line heights normalized to the main integral at velocities between 19-37.4 $\mathrm{km\,s^{-1}}$, with x- and y-axis both on logarithmic scale. Na and K decrease with velocity, following a power law. On the right, C shows a slight tendency to decrease with velocity, whereas O shows an increasing trend with velocity, also following a power-law. C seems to behave fairly steadily, whereas O shows a rather steep slope. Here as well, the general observation for the behaviour of both elements with velocity can be confirmed.

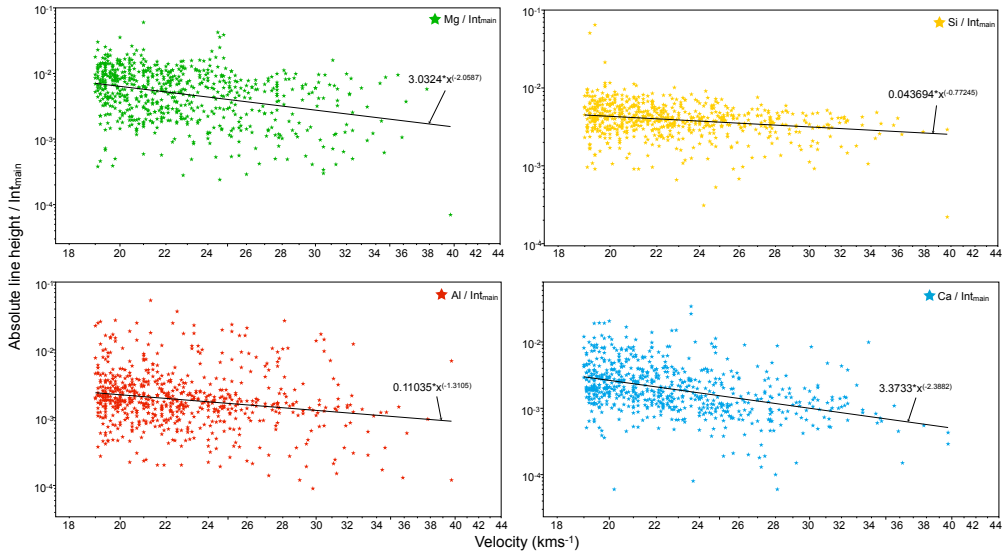

Figure 5.11: The behaviour of mineral elements with velocity with Mg (upper left) and Si (upper right) and Al (lower left) and Ca (lower right). Shown here are the absolute mass line heights normalized to the main integral at velocities between 19-37.4 $\mathrm{km\,s^{-1}}$, with x- and y-axis both on logarithmic scale

How do signature impactor elements behave? The general observation and assumption in impact ionization mass spectra is that impactor species tend to increase, while contamination elements, such as alkalis and hydrocarbons, tend to decrease with velocity.

Fig. 5.11 shows the absolute mass line heights of Mg, Si Al and Ca normalized to the main integral at velocities between 19-37.4 $\mathrm{km\,s^{-1}}$, with x- and y-axis both on logarithmic scale and a power-law fit applied. All species show the tendency to decrease with velocity. A tentative assumption that the trends could be caused by the statistically small number of impacts recorded at velocities above 25 $\mathrm{km\,s^{-1}}$ is not confirmed, as data show the same behaviour at 19-25 $\mathrm{km\,s^{-1}}$. Since we take the main integral of a spectrum as a proxy for total ion yield, an increase of the main integral should mean that a larger number of ions is produced. However, if more ions are produced, why are most impactor ion species decreasing Fig. 5.10 and which species are actually increasing? This question cannot be answered satisfactorily presently.

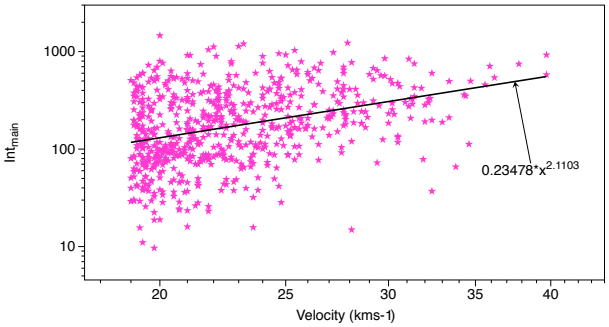

Figure 5.12: Behavior of the main integral of all spectra with increasing velocity. The x-axis shows the velocity and the y-axis shows the main integral, both on logarithmic scale. A power-law fit was applied

5.2.3 Correlations of elements within the data set

We expect to see a positive correlation in the alkalis Na and K, since they share similar properties, e.g., low ionization potential, and behave equally within spectra, i.e., their ubiquitous abundance, appearance at lowest velocities, here as the most abundant species in a spectrum, and their similar decrease with velocity (Fig. 5.13). A similarly positive correlation between Ca and Na is also recognizable. At very low impact speeds, we may discuss the principal possibility that Ca could behave like an alkaline contamination.Actually, within this data set, no spectra > 5 $\mathrm{km\,s^{-1}}$ has been found that does not contain a minimum amount of Ca, generally visible above 3σ. However, Na, K and especially Ca are elemental species within our sample minerals. Ca is the signature element for clinopyroxene, and thus very abundant within that particular mineral. we also find significant amounts of Ca in amphibole, feldspar and orthopyroxene (Table 5.6). It is interesting, that no other similar correlation with Na or K has been found, and thus it is likely that the behaviour is related to similar properties, e.g., that Na, K and Ca are inherent to the particle chemistry.

Fig. 5.14 shows plots to check for correlation between the signature elements of the minerals within our dust analogue. There is no clear distinct positive or negative correlations within our data as such, but what is apparent here is a clear clustering of data points in all plots. The plot "Al vs.Mg " seems to hint to even two groups, the concentration of

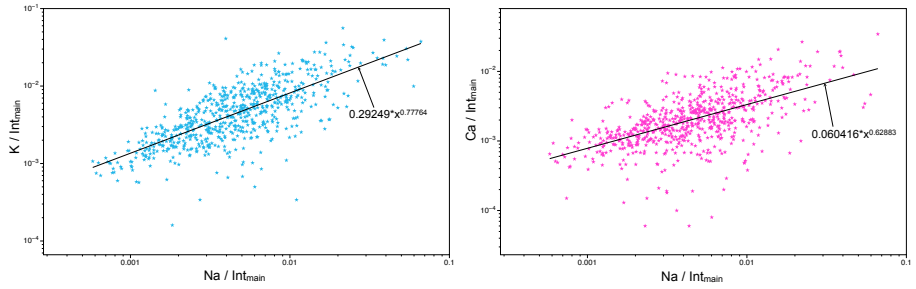

Figure 5.13: Positive correlation between Na and K (left) and between Na and Ca (right). X-and y-axis show the elements normalized with the main integral on logarithmic scale. Shown are all data at velocities between 19-37.4 $\mathrm{km\,s^{-1}}$

most particles with rather high Mg-contents, which appears to indicate a positive correlation with Al, and a separate, though strongly scattering "branch", or single data points at high Al-contents. High Al-contents together with high Mg-contents hint at spinel, whereas low Mg-contents with high Al-contents would indicate feldspar. "Si vs.Mg " shows, what we could already observe in Fig. 5.9 - a fairly smooth distribution, with only few scattered points. The plots "Ca vs.Mg " and "Fe vs.Mg " are both equally scattered, with an accumulation of data towards higher Mg-contents. One could expect to see more significant trends within the "Ca vs.Mg ", since Ca is a signature element in clinopyroxene, but, as described above, Ca appears to be ubiquitous, and thus, smooth transitions towards higher Ca-contents seem to be the logical consequence.

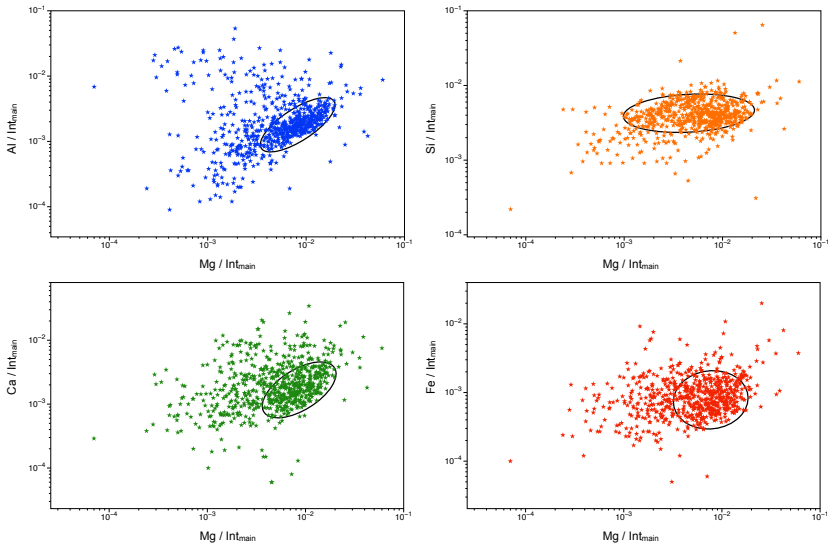

Figure 5.14: Element-to-element plots of Mg with Al (upper left), Si upper right, Ca (lower left) and Fe (lower right), showing distinct concentrations within the data. X-and y-axis show the elements normalized with the main integral on logarithmic scale. Shown are all data at velocities between 19-37.4 $\mathrm{km\,s^{-1}}$

Fig. 5.15 shows ratio to ratio plots of significant element ratios for the dust analogue minerals. Chosen were ratios that distinguish the mineral species in the analogue material from

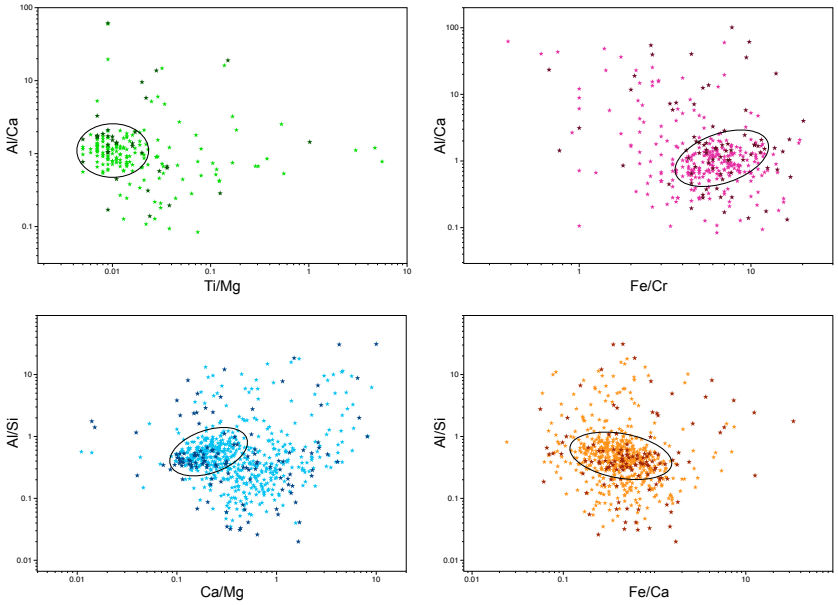

Figure 5.15: Ratio to ratio plots of mineral ratios, showing $\mathrm{Al/\ Ca}$ (upper left) to $\mathrm{Ti/\ Mg}$, $\mathrm{Al/\ Ca}$ to $\mathrm{Fe/\ Cr}$ (upper right), $\mathrm{Al/\ Si}$ to $\mathrm{Ca/\ Mg}$ (lower left) and $\mathrm{Al/\ Si}$ to $\mathrm{Fe/\ Ca}$ (lower right). X-and y-axis show the ratios on logarithmic scale. Shown are all data at velocities at 19-24.9 $\mathrm{km\,s^{-1}}$ (light color). Additionally plotted are particles with velocities at 25-37.4 $\mathrm{km\,s^{-1}}$ (dark color)

each other, e.g., spinel has high Al/Ca, Al/Si and Fe/Cr, hornblende and feldspar have high Ti/Mg and high Ca/Mg-ratios, and clinopyroxene has high Ca/mg and low Al/Ca. The elemental ratios where most data form densely populated clusters can safely be assumed to represent orthopyroxene. However, these elemental ratios reflect both the true composition of orthopyroxene and the sensitivity coefficients of the respective elements related to the measuring method, i.e. impact ionzation TOF mass-spectrometry as performed by the LAMA.

5.2.4 Establishing sensitivities for element detection by LAMA

Standard mineral analysis performed by electron microprobe is a fundamentally different technique when compared to impact ionization TOF mass spectra. An electron microprobe measures the characteristic x-ray radiation of an element, which is emitted, when electrons in the inner atomic orbital of an element, shortly elevated to a higher energy level beforehand by a focussed electron beam, fall back to their initial energy level. The intensity of the radiation is then measured by a wavelength-dispersive spectrometer or an energy-dispersive Si-Li-semi-conductive detector. Impact ionization TOF mass spectrometry on the other hand, measures directly the ionized species originating from a hypervelocity impact, either as atoms, as newly formed clusters or as molecules that are drawn out of the plasma cloud via an electric field.

Routine techniques like electron microprobe analysis use simultaneously measured standards or empirical mathematical relationships to translate line strengths into elemental

abundances and concentrations. Similar standardization procedures are used by time-of-flight secondary ion mass spectrometry (TOF-SIMS), where ionization is achieved by a controlled pulsed primary ion beam of definite intensity and spatial dimension. Such a standardization and calibration procedure lacks for the LAMA and CDA instruments, as the process is highly complex and highly difficult to reproduce. For example, accelerating siliceous particles for impact ionization at high speeds became only possible recently, this work actually describes the first major campaign of silicate particles. In secondary ion mass spectrometry, it is common to translate peak heights into actual compositions by the use of sensitivity coefficients, which are a measure for detection efficiency. Here I use the orthopyroxene composition as measured by electron microprobe to infer impact ionization TOF-SIMS sensitivity coefficients. These coefficients are listed in Table 5.7 and can be compared with TOF-SIMS sensitivities measured by Stephan [2001] on glass standards (Fig. 5.16).

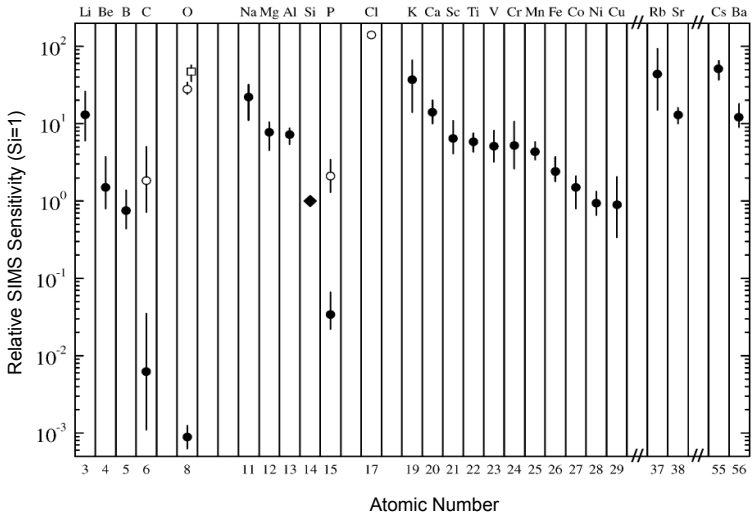

Figure 5.16: Relative TOF-SIMS sensitivities for positive (solid circles) and negative (open circles) secondary ions relative to silicon. The sensitivity for silicon was derived from 8 glass standards with a gallium primary ion source [Stephan, 2001].

According to our calculations, LAMA shows an extraordinary high sensitivity for the alkalies, whereas the sensitivities seem to be somewhat lower the other elements, except for Ca, which, in comparison, behaves similar to TOF-SIMS measurements.

Table 5.7: Sensitivity coefficients for species from impact ionization TOF mass spectra obtained with LAMA in comparison with sensitivity coefficients from TOF-SIMS measurements

	Na	Mg	Al	Si	Ca	Ti	Fe	K
TOF SIMS [Stephan, 2001]	22±10	8±2	7±1	1	14±5	6±1	2.2±0.8	40±30
LAMA (normalized to Si)	210	1.3	2.1	1	16	3.9	0.4	2000 (100)[a]

[a] the K coefficient of 2000 appears exceptionally high - as shown below, the CDA coefficient for K is only about 100, much more similar to conventional TOF-SIMS techniques

The LAMA sensitivity coefficients have relatively large uncertainties, comparable to the scatter of the data cluster in the element ratio plots (Fig. 5.15-Fig. 5.18). This is due to variations e.g. in impact velocity, energy density and its spatial variation, surface roughness, projectile shape. However, there is significant asymmetric scatter for a minority of data points. The next plots (Fig. 5.17-Fig. 5.18) serve to check if this scatter represents compositional variation caused by the other mineral constituents, or if it represents mere stochastic scatter caused by experimental artifacts.

In Fig. 5.17 (upper panel), Al/Ca-ratios are shown versus Ti/Mg-ratios. The data cluster located at Ti/Mg = 0,01 and Al/Ca =1 represents the major phase orthopyroxene. Using the sensitivity coefficients derived from orthopyroxene and the compositions measured by electron microprobe of other mineral phases (clinopyroxene, spinel, hornblende, feldspar), we also plotted the expected ratios for these minerals when measured by the LAMA (large symbols). This procedure actually does not require that the sensitivity coefficients are precisely known, it just assumes that - for a given element - they are the same for orthopyroxene and the other silicates. For example, if electron microprobe measures a 100 fold higher Al/Ca ratio for spinel than for orthopyroxene, this endmember will have a 100 fold higher Al/Ca ratio in Fig. 5.17 as well - however, the absolute values of Al/Ca ratios in Fig. 5.17 differ from electron microprobe results by a constant factor, (i.e. the ratio of the sensitivity coefficients of Al and Ca).

In Fig. 5.17, spinel can be distinguished by high Al/Ca, hornblende (amphibole) and feldspar by high Ti/Mg, and clinopyroxene by low Al/Ca. It can be verified, that there is some asymmetric scatter of data points, partly in direction of these endmembers. Data points between different endmembers can be considered - as in classical geochemical four isotope plots - as mixtures between different endmembers. Based on this plot, we preliminarily classified data points, i.e. data with Al/Ca <0.22 were color-coded as rich in clinopyroxene (pink), data with Al/Ca >10 were color-coded as spinel rich (green), and data with Ti/Mg >0.08 were color-coded as rich in feldspar or hornblende (orange). "Rich" in a certain phase means that these particles are more or less dominated by spinel, clinopyroxene, feldspar or hornblende, but still contain substantial amounts of the main phase orthopyroxene. In this respect, the assignments are just preliminary and could be performed more sophisticated. However, here they simply serve to check, whether the data points - if plotted in other element systems - always consistently plot in direction of the same endmember.

For example, in a plot Al/Ca versus Fe/Cr (Fig. 5.17, lower panel), it can be verified, that data classified as rich in spinel or clinopyroxene still scatter towards their respective endmember composition. Particles rich in feldspar/hornblende plot between these endmembers and orthopyroxene, as expected. In Fig. 5.18 (upper panel) showing Al/Si versus Ca/Mg, particles rich in spinel, clinoproxene, and hornblende/feldspar as well scatter in direction of their corresponding endmembers, confirming the interpretation that these data can be interpreted as compositional mixtures between orthopyroxene and minor minerals present in the dust sample. Few data points (shown in yellow), however, cannot be mixtures involving orthopyroxene, but rather seem mixtures between spinel and hornblende/feldspar.

Figure 5.17: Ratio-to-ratio plot "Al/Ca" vs."Ti/Mg" (upper panel) and "Al/Ca" vs."Fe/Cr" (lower panel), showing LAMA data with velocities at 19-25$\,\mathrm{km\,s^{-1}}$ with light blue, small symbols. Added are the model compositions of the mineral end members for the mineral species in the analogue sample (large symbols), as expected from EMPA analysis for comparison. X-and y- axis are logarithmically scaled.

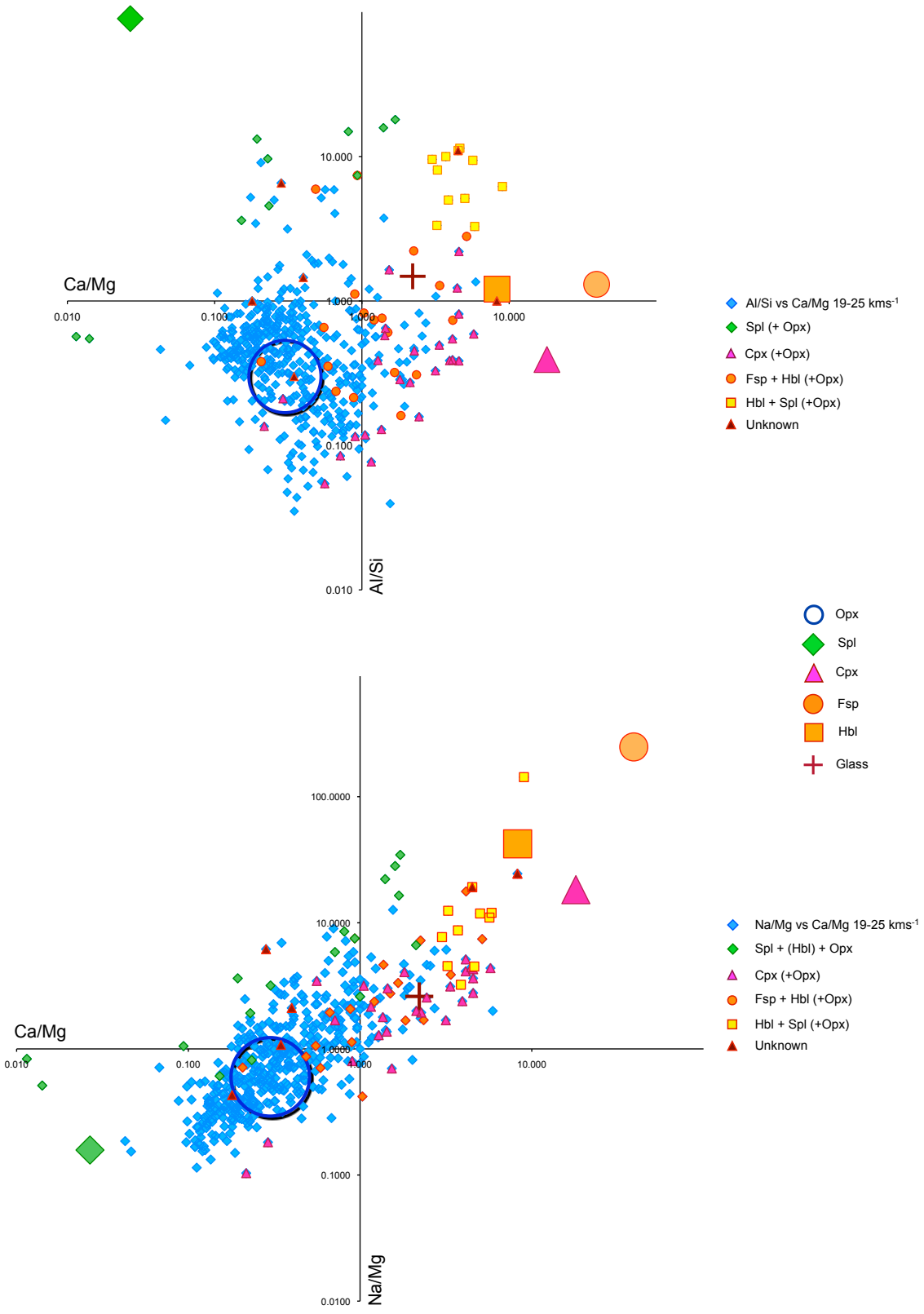

Figure 5.18: Ratio to ratio-plot "Al/Si" vs."Ca/Mg" (upper panel) and "Na/Mg" vs."Ca/Mg" (lower panel) , showing LAMA data with velocities at 19-25 $\mathrm{km\,s^{-1}}$ with light blue, small symbols. Added are the model compositions of the mineral end members for the mineral species in the analogue sample, as expected from EMPA analysis for comparison. X-and y- axis are logarithmically scaled.

Fig. 5.18 (lower panel) displays Na/Mg versus Ca/Mg. Here again, the variation is such that all data fit within the area spanned by the various endmembers, and that data classified as mixtures of orthopyroxene and the minor phases clinopyroxene or hornblende/feldspar scatter asymmetrically in the respective directions. For some spinel data with high Ca/Mg values, the picture is somewhat untidy as these scatter beyond the orthopyroxene field. However, this may be explained by the possibility that these data are similar to the yellow data points resembling mixtures of spinel and hornblende/feldspar. It should be emphasized, that in this plot Na well correlates with Ca in a way prescribed by compositional variation of the various mineral species. This can be interpreted as a clear hint that Na in these data is mainly derived from the impacting particles and not a target contamination.

5.3 Impact ionization mass spectra from multi-mineralic analogues measured by CDA

We performed calibration experiments with the CDA flight spare instrument, which is an exact copy of the Cassini flight instrument [Srama et al., 2004]. The integrated linear time-of-flight (TOF) spectrometer achieves a mass resolution between of $\frac{m}{\Delta m} \sim 20$ for light atomic species such as carbon and oxygen and $\frac{m}{\Delta m} \sim 40$ for heavier atoms such as Rh. The resolution is sufficient for roughly characterizing the elemental composition of the impactor, but does not allow for isotopic analysis above masses of about 40 u. The duration of the recorded TOF signal sampled at 100 MHz is $6.4\,\mu s$, plus another $38.4\,\mu s$ sampled at 10 MHz, corresponding to a maximum detectable atomic mass of ∼7000 u. The low mass resolution of this linear impact spectrometer results from initial energy differences of the plasma ions. The impact experiments with the CDA flight spare unit allow comparisons with in situ spectra of the interstellar dust candidates. However, to enable assignment of the CDA mass lines to atomic or molecular species, we need to compare impact experiments of the low resolution CDA with the high resolution LAMA.

Table 5.8: Distribution of CDA spectra from the pyroxene sample within velocity bins

Velocity range ($\mathrm{km\,s^{-1}}$)	No of spectra
1-5	14
5-10	17
10-15	11
15-20	78
20-25	606
25-30	94
30-40	31
40-50	5

We obtained 1118 CDA spectra from sample SA84-132 in January 2012, with speeds ranging from 1.3-53.1 $\mathrm{km\,s^{-1}}$. 857 spectra were suitable for general evaluation as described below. The spectra at speeds >15 $\mathrm{km\,s^{-1}}$ were divided into velocity bins in steps of 5 $\mathrm{km\,s^{-1}}$. Fig. 5.19 shows typical reference spectra for velocities between 1-15 $\mathrm{km\,s^{-1}}$ in the upper panel. Sum spectra for velocity bins < 15 $\mathrm{km\,s^{-1}}$ could not be produced, due to the rather low quality of most spectra at such low impact velocities. For the velocity bins

Table 5.9: Number of recorded spectra from the pyroxene sample within the assigned type bins, according to the most dominant mass line within a spectrum, for velocities between 19-25 $\mathrm{km\,s^{-1}}$

Type	19-25 $\mathrm{km\,s^{-1}}$
Type Mg	157
Type Ca	88
Type Si/Al	107

15-40 $\mathrm{km\,s^{-1}}$, co-added spectra are shown in the lower panel of Fig. 5.19.

Mass line identification with the CDA is rather complicated, due to the low mass resolution of the instrument and the missing reflectron. In LAMA spectra we are able not only to distinguish between peaks at nearly every integer mass, but are as well able to occasionally recognize isotopic patterns of most elements, if apparent in the spectra. Mass lines in CDA spectra are generally broad, owing to the initial angular- and energy distribution of the ions within the impact plasma. Hence, broad mass lines "swallow" closely adjoining mass lines, which are then not reliably identifiable anymore. However, the experimental CDA spectra shown here, display a similar behaviour like the LAMA spectra in Fig. 5.5. Spectra at velocities between 1-10 $\mathrm{km\,s^{-1}}$ are dominated by the alkali elements Na and K. With higher velocity, here as well, mass lines get peeled out of the alkali-dominated accumulation. At velocities above 15 $\mathrm{km\,s^{-1}}$, it is possible to distinguish at least H, C, O and Rh. Mass lines at masses between 23 u and 32 u, as well as masses at 39 u to 44 u and 52 u to 57 u are hardly distinguishable. We are not able to separate Na (23 u) and Mg (24-26 u), Al (27 u) and Si (28-30 u), K (39 u) and Ca (40 u) and finally Cr (52/53 u), Mn (55 u) and Fe (56/57 u), let alone all the contaminants, such as hydrocarbon clusters, or newly formed clusters from impactor species that may contribute to the peaks as well. Occasionally, spectra show target-projectile clusters, such as RhMg, RhSi or RhFe, which reassures the line assignment. Mass lines in most spectra show "bulges", indicating an adjoining mass line, leading to the conclusion that two species are contributing to one mass line.

After evaluation of all recorded spectra, 357 spectra were chosen for further evaluation at velocities between 19-25 $\mathrm{km\,s^{-1}}$, being the highest quality spectra of the data set. Other spectra were not chosen due to high noise levels, even though the spectrum itself may have been visually suitable. Different compositional types were assigned: Type Mg/Na, type Ca/K, and type Si/Al (Fig. 5.20), owing to the ambiguity in mass line identification. In accord with conclusions drawn from the LAMA spectra (Fig. 5.5 and Fig. 5.18, lower panel), it is assumed that Na and K are from the impacting dust projectiles and only to a minor extend target contamination. Unfortunately, we are not able to conduct the same extensive chemical analysis here as with the LAMA spectra, with respect to mass line behaviour, due to the insufficient mass line assignment.

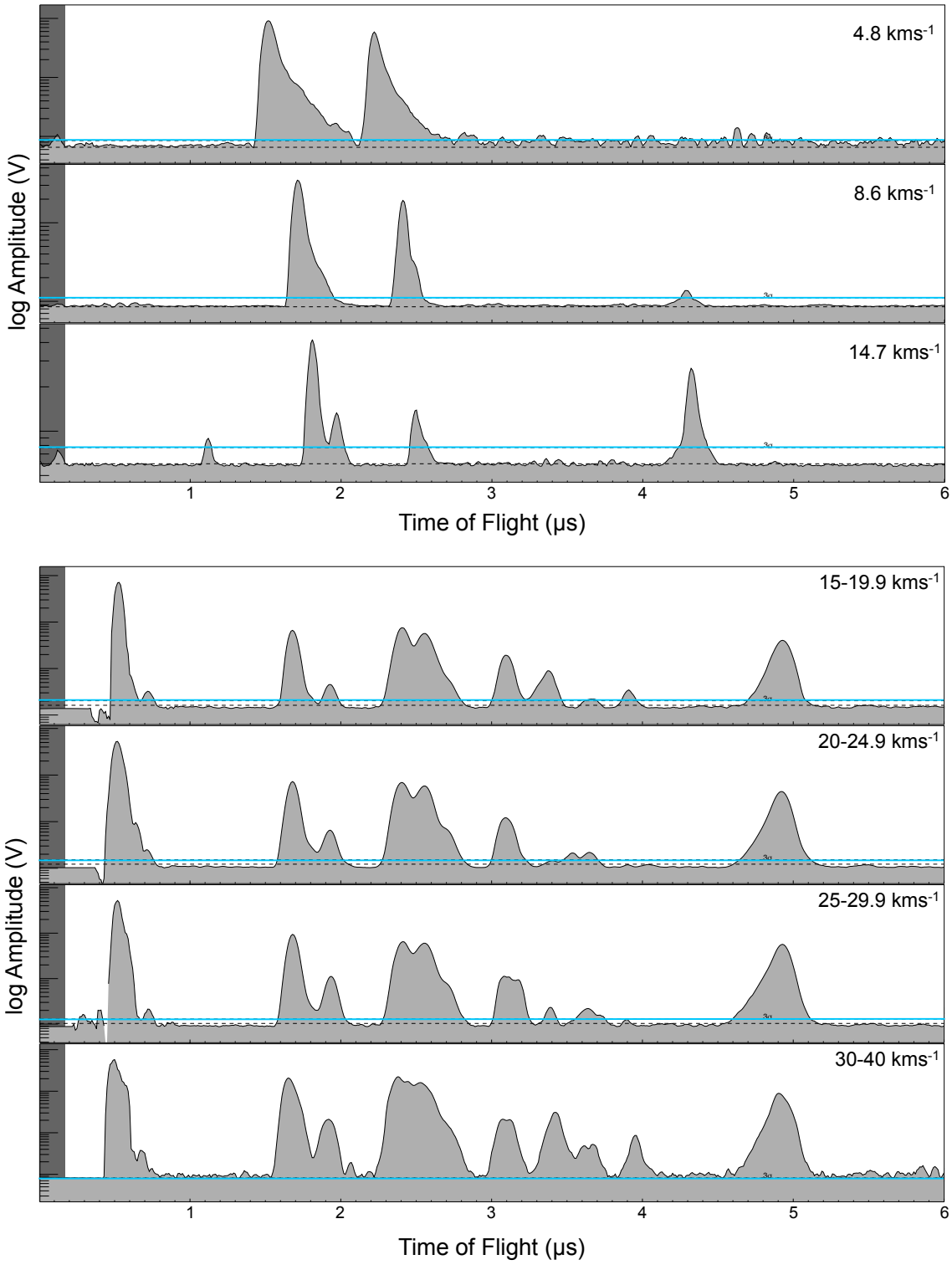

Figure 5.19: Reference spectra for velocities between 1-15 $\mathrm{km\,s^{-1}}$ (top) and co-added spectra for velocities between 15-40 $\mathrm{km\,s^{-1}}$ (bottom)

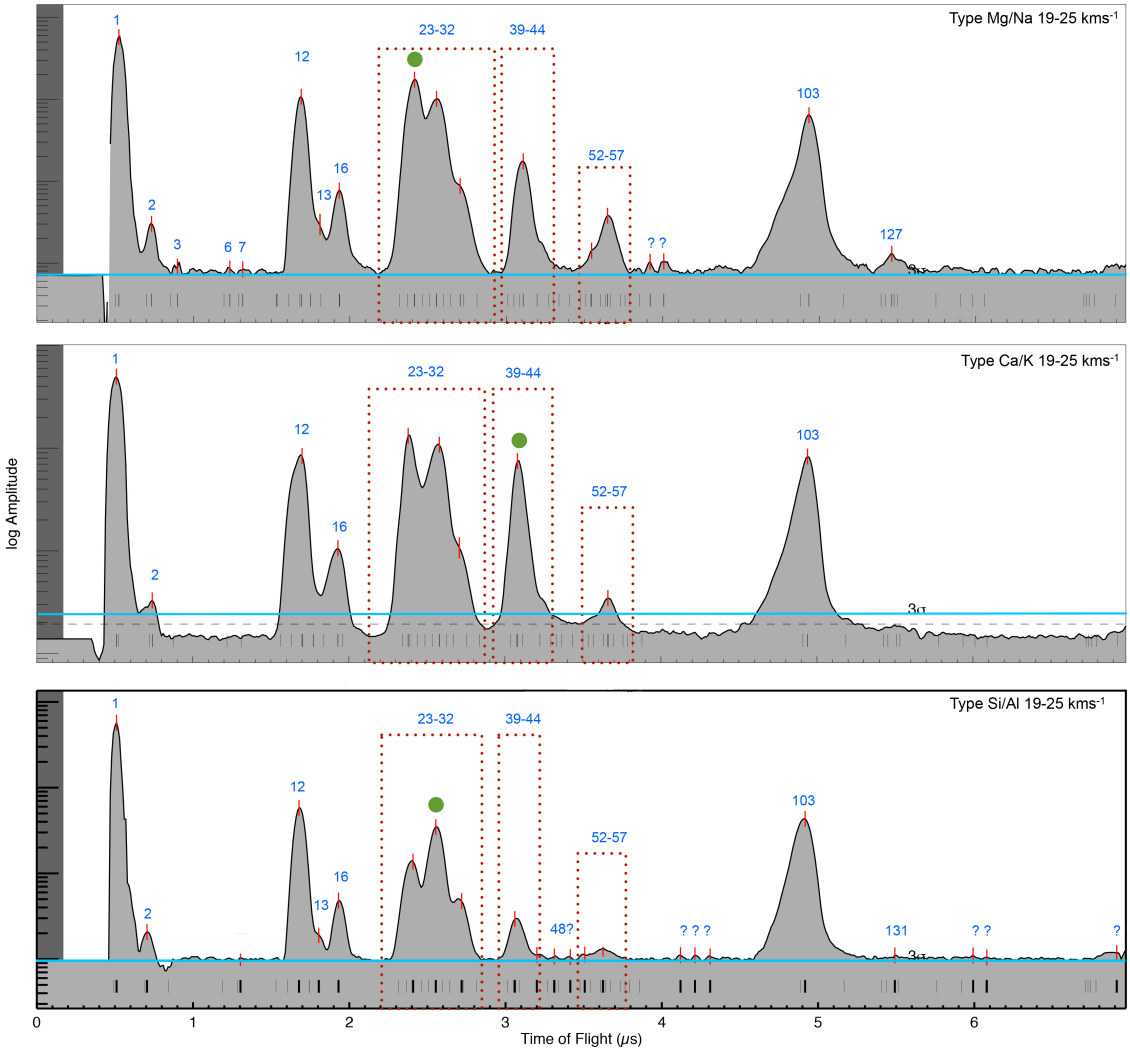

Figure 5.20: Co-added spectra for each type bin assigned to a data set of 357 spectra with velocities between 19-25 $\mathrm{km\,s^{-1}}$. The blue labels denote the features identified within the spectra and described in Table 5.2. The green dots mark the most dominant feature. The light blue horizontal line marks the 3σ-line. The dotted boxes embrace specific mass ranges

5.4 Comparison of mass spectra between CDA and LAMA

Fig. 5.21, Fig. 5.22 and Fig. 5.23 show a comparison between the different types assigned in mass spectra obtained with the LAMA and the CDA..

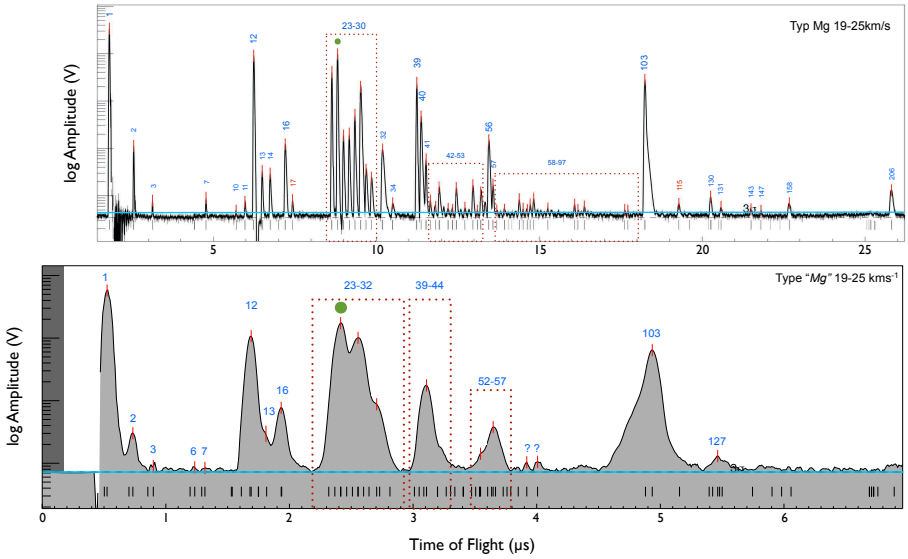

Figure 5.21: Comparison of type Mg LAMA spectra with type Mg CDA spectra with velocities at 19-25 $\mathrm{km\,s^{-1}}$. The blue labels denote the mass at which features occur, the light blue line denotes the 3σ line and the green dots mark the dominating mass line

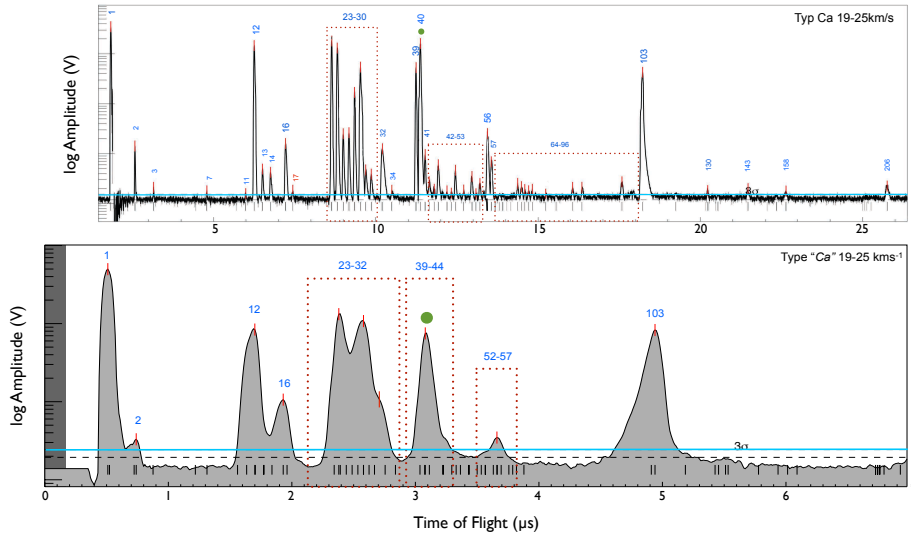

Figure 5.22: Comparison of type Ca LAMA spectra with type Ca CDA spectra with velocities at 19-25 $\mathrm{km\,s^{-1}}$. The blue labels denote the mass at which features occur, the light blue line denotes the 3σ line and the green dots mark the dominating mass line

It is clear that a direct comparison is highly difficult, if not impossible. The reason is that the assignment of spectra to type Mg, Ca,or Al/Si was well viable using the LAMA, but is highly

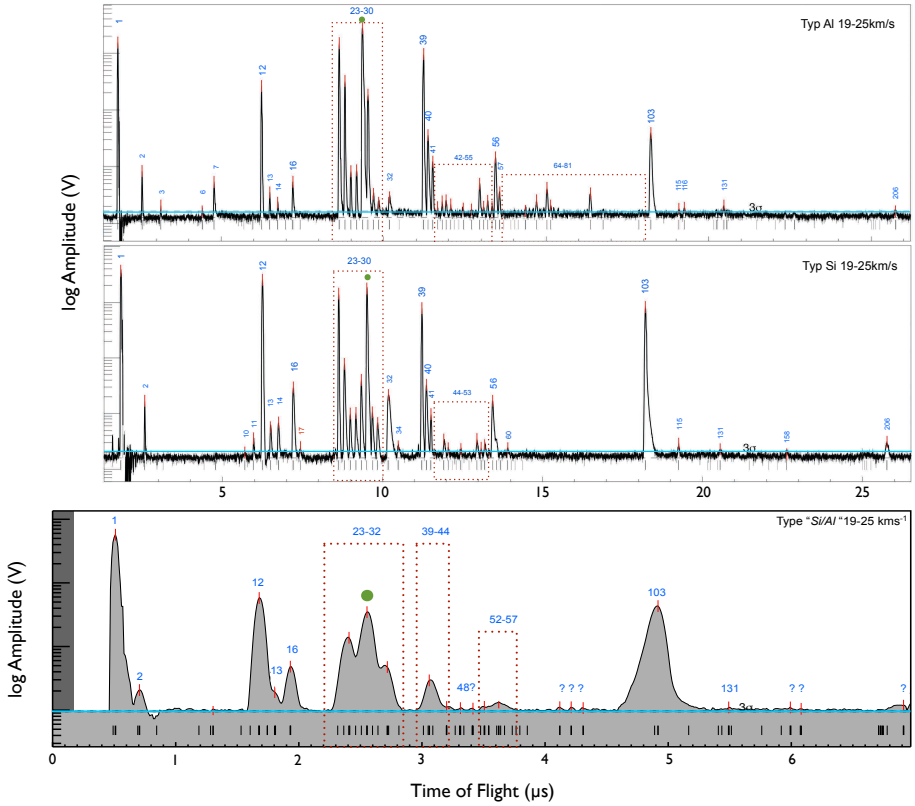

Figure 5.23: Comparison of type Al and type Si LAMA spectra with type Si/Al CDA spectra with velocities at 19-25 $\mathrm{km\,s^{-1}}$. The blue labels denote the mass at which features occur, the light blue line denotes the 3σ line and the green dots mark the dominating mass line

problematic with the CDA spectra, as Mg and Ca-lines are interfered by Na and K to an unknown extent. At this point, it should be kept in mind, that the CDA has been developed as a multi purpose instrument for a variety of space environments, particularly suitable for qualitative distinction of silicate, oxide or water ice particles. However, we will show below that important informations can still be extracted, if we use sum lines of Mg+Na and Ca+K.

5.5 In situ mass spectra of interstellar dust (ISD) candidates

13 ISD candidates were chosen from the CDA data set with respect to their dynamical and compositional properties as described in 5. Table 5.10 shows the ISD candidates with the date (DOY) recorded and the SCET, further their initial assignment to a type. For the assignment of a mass scale, based on the determination of the shift parameter, the cross-correlation method was applied. Here, the relative peak positions of C, O, Rh and Fe, were used as a template for initial calibration. The ratio of C-amplitude to O- amplitude was used to determine the velocities of the particles, since the determination of particle velocities from CAT-impacts cannot be accomplished via signal rise times, as is possible in the case of IIT impacts. In all cases the O-amplitude exceeds the C- amplitude, indicating speeds faster than 26 $\mathrm{km\,s^{-1}}$. Ruling out a great deal of alkaline contamination occurring at these speeds , we assign Mg as a dominant mass line for one part of the spectra suite. As

Table 5.10: List of the ISD candidates with date and time of recording, as day-of-year (DOY), the corresponding SCLK (Spacecraft CLock Kernel), their distance from Saturn (R_S), and the assigned type according to the most dominant mass line, either Fe or Mg.

No	DOY	SCLK	Distance from Saturn (R_S)	Type
1	2010-225	16604099293	7.0	Fe
2	2010-237	1661460235	42.8	Mg
3	2010-245	16622117941	9.8	Fe
4	2010-245	1662124510	9.0	Fe
5	2010-245	1662124809	9.0	Fe
6	2010-245	1662127384	8.6	Fe
7	2010-245	1662129423	8.3	Mg
8	2010-245	1662130347	8.2	Mg
9	2010-267	1664041167	19.6	Mg/Fe
10	2010-284	166504393	37.5	Mg
11	2010-305	1667293160	46.2	Mg
12	2010-330	1669487846	31.0	Mg
13	2010-351	1671246161	31.8	Mg

already described above, the line around mass 23-24 contains both Mg and Na, however, at speeds exceeding $26\,\mathrm{km\,s^{-1}}$, most Na should be derived from the projectile. This conclusion is supported by i) our results of LAMA Na/Mg- and Ca/Mg-data on orthopyroxene and minor mineral phases (Fig. 5.18, lower panel) and ii) spectra from impacts of ultrafast stream particles that indicate the alkaline contamination is low Postberg et al. [2009a]. Alkali contamination is usually more problematic for low impact speeds, because the energy for impact ionisation is more concentrated on the relatively large contact area between the target and the larger and - implicitly slower - projectiles. The surface area of the target, in turn, is where the alkaline contamination is concentrated: According to Postberg et al. [2009a], the alkaline contamination of the CDA target surface reaches maximum values of 45% for Na and 15% for K as measured by TOF-SIMS. It should be considered, however, that the TOF-SIMS technique analyses the uppermost nanometer surface layers, hence, the concentrations of Na and K contamination referred to the volume where impact ionisation occurs is much lower, some orders of magnitude, particular at high impact velocities. Two types were initially assigned as shown in Fig. 5.1: Fe-type spectra, based on dominance of the Fe-mass line, and distinctly different Mg-type spectra. All Mg-dominated particles seem to contain Ca and/or K in variable concentrations. Furthermore, Fe was reliably identified in all Mg-dominated spectra. Si or Al did not appear as a single peak, but in many spectra the presence of both elements could be inferred from a more or less distinct bulge of the mass lines.

5.5.1 Comparison of ISD mass spectra with CDA and LAMA calibration experiments

In order to constrain the composition of the ISD candidates, we compare their spectra with laboratory CDA- and LAMA-spectra of orthopyroxene particles (Fig. 5.24 and Fig. 5.25). Here, a reference mass spectrum is shown for Ca-poor Mg-type and Ca-rich Mg-type ISD candidate particles.

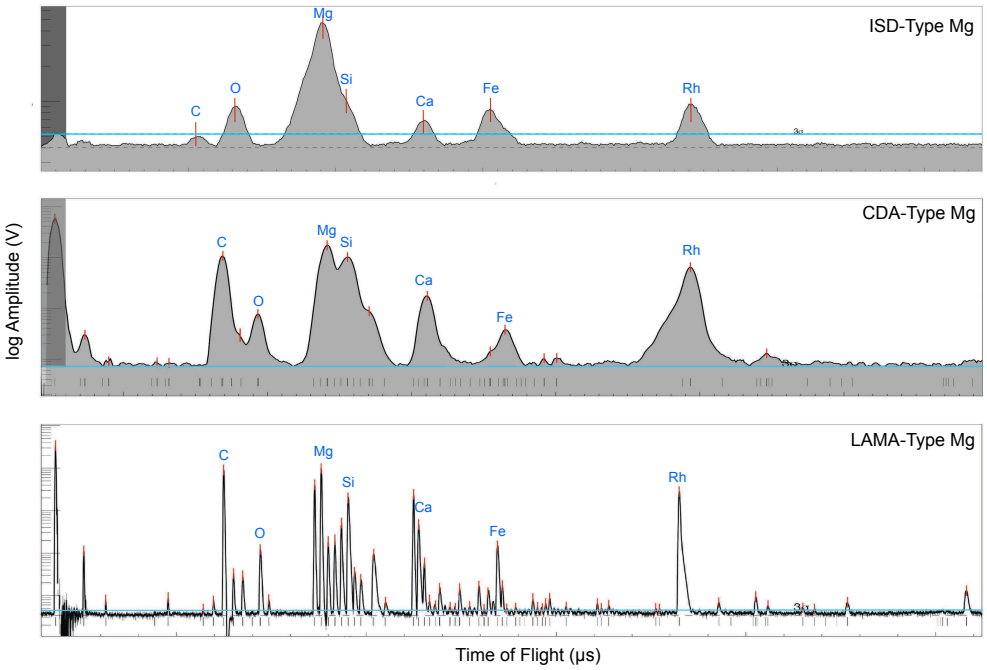

Figure 5.24: Comparison of (Ca-poor) Mg type ISD candidates with Mg-type CDA and LAMA spectra. The blue labels denote the occurring features and the light blue line denotes the 3σ line

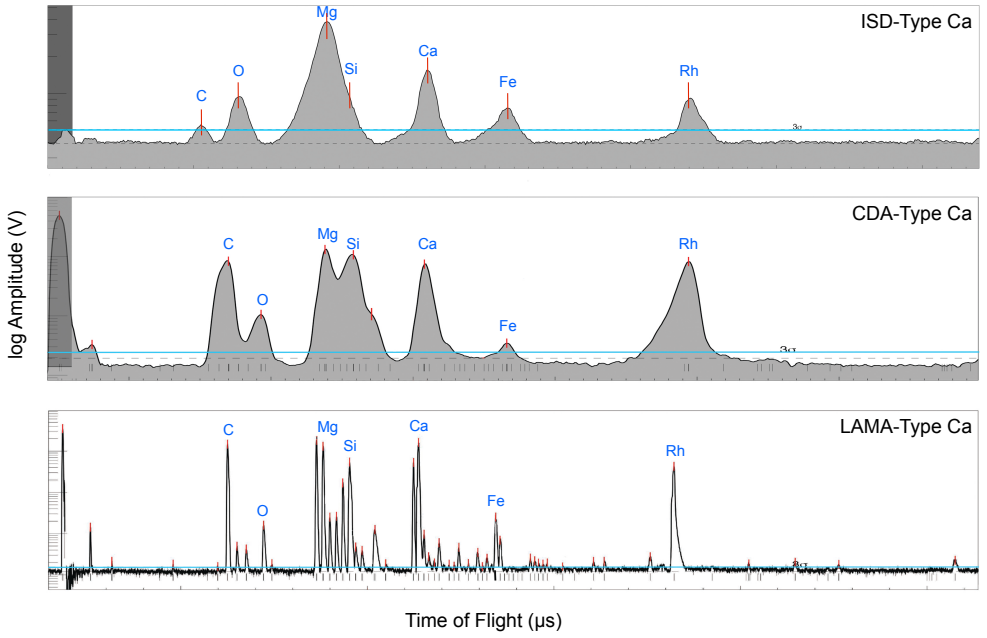

Figure 5.25: Comparison of (Ca-rich) Mg-type ISD candidates with Ca-type CDA and LAMA spectra. The blue labels denote the occurring features and the light blue line denotes the 3σ line

Fig. 5.24 and Fig. 5.25 show, how Ca-poor Mg-type and Ca-rich Mg-type spectra from ISD candidates compare with Mg-type and Ca-type spectra from CDA and LAMA. It is evident that Mg dominated ISD candidates with more or less Ca show some affinitites to experimentally obtained CDA spectra of Mg-rich silicates (pyroxene) with more diopsidic (Ca-

rich) or more enstatitic (Ca-poor) composition. However, refinements of this preliminary conclusion are possible in the following section.

5.6 The composition of ISD candidates: Cosmochemically primitive or evolved?

Fig. 5.26 shows a ratio to ratio plot of (Mg+Na)/(Si+Al) versus (Ca+K)/Fe for both orthopyroxene data of the LAMA and the CDA . Lines , that cannot be differentiated by the CDA are simply added. The comparison of both data sets shows that there is a difference in detection efficiency between LAMA and CDA. When comparing the sensitivity coefficients in Table 5.7, the largest deviation from"normal"TOF-SIMS coefficients occurs for K. If this coefficient is corrected downwards by factor of 20, there is a good agreement between both data sets. It is not clear,why the LAMA is much more sensitive for K. However, no matter what the reason for the difference between the two instruments is, it is certainly reasonable to apply sensitivity coefficients that are valid for the CDA, i.e. the very same instrument with which ISD candidate spectra were measured.

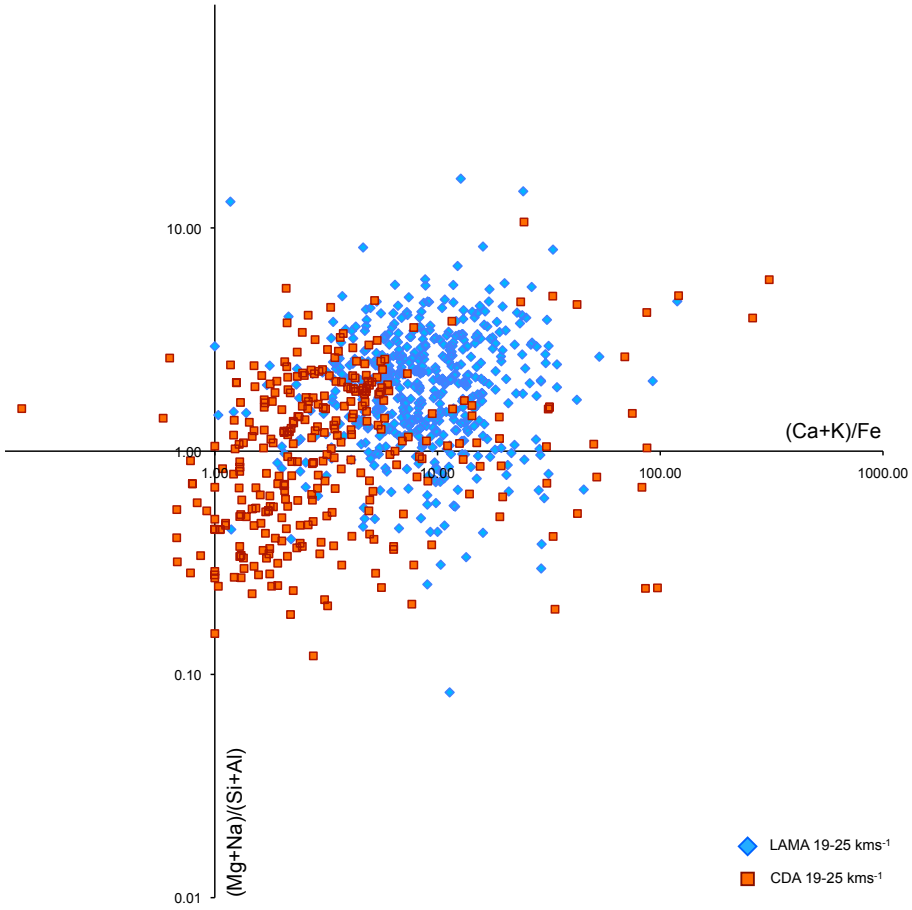

Figure 5.26: Ratio to ratio plot of (Mg+Na)/(Si+Al) versus (Ca+K)/Fe for both orthopyroxene data of the LAMA and the CDA

Fig. 5.27 shows (Mg+Na)/(Si+Al) versus (Ca+K)/Fe plot of ISD candidate spectra in comparison with data points of the orthopyroxene dust separate. Also plotted are mineral compositions expected for orthopyroxene, clinopyroxene, feldspar, hornblende, spinel and Mg-rich olivine (forsterite). These minerals form an array in the plot (from lower left to upper right) that can be interpreted to result from magmatic differentiation of so called "bulk silicate Earth" material, i.e. a kind of primitive mantle material. Furthermore, I plotted compositions of primitive solar system matter, i.e. CI chondritic composition, which is a measure of solar (and implicitly cosmic) elemental abundances, H chondrites, which is another common chondrite class, and CV chondrites that show some affinity to bulk terrestrial composition with respect to their general depletion of moderately volatile elements (particularly the alkalis Na and K) when compared to CI. So the lower (Mg+Na)/(Si+Al) ratio of CV and bulk silicate Earth, when compared to CI and H chondrites, is explained by Na-depletion in CV and terrestrial material. The higher (Ca+K)/Fe-ratio of bulk silicate Earth is due to the circumstance that the terrestrial mantle is significantly depleted in Fe due to terrestrial core formation, while chondritic parent bodies did not form a core and retained roughly cosmic proportions of Fe.

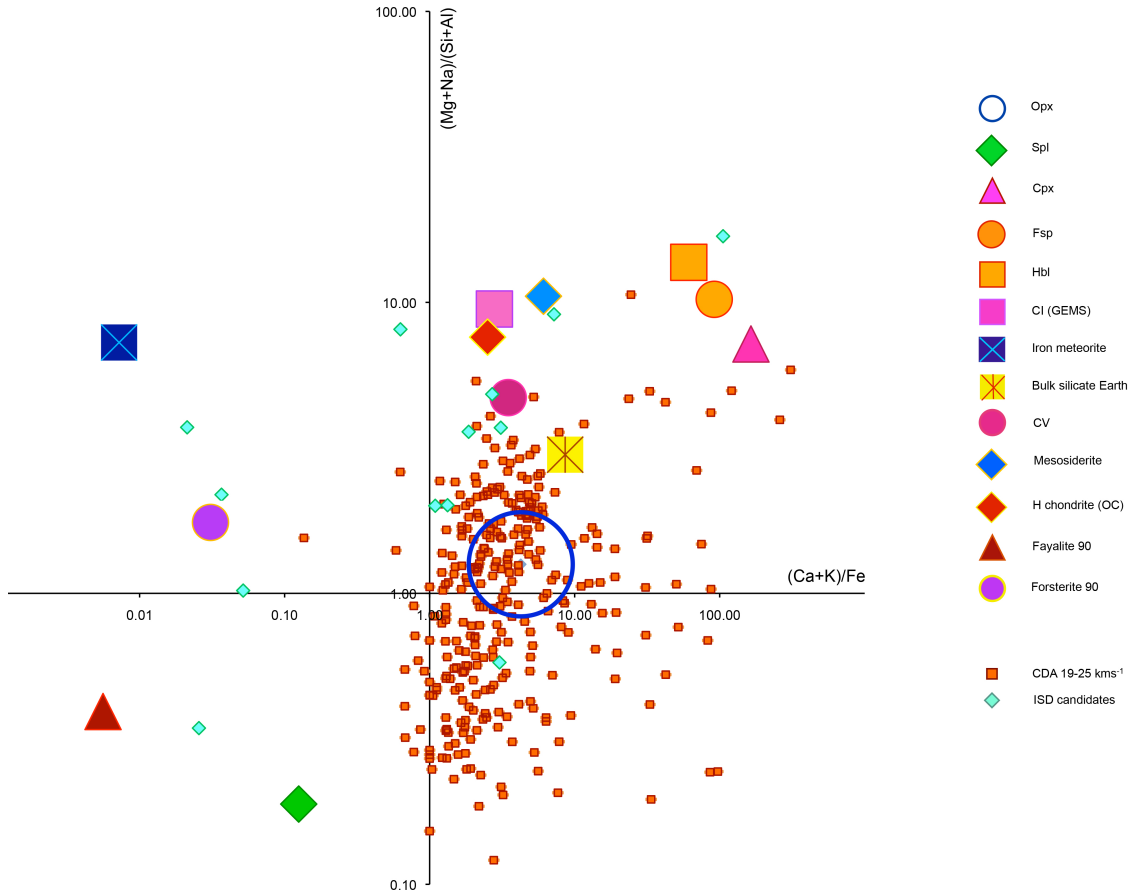

Figure 5.27: (Mg+Na)/(Si+Al) versus (Ca+K)/Fe plot of ISD candidate spectra in comparison with data points of the orthopyroxene dust separate and cosmochemically relevant reservoirs.

Last but not least Fig. 5.27 also displays differentiated meteoritic material: this gives an idea of the effects of core formation, i.e. the formation of iron meteorites with low (ca+K)/Fe and mantle differentiation, i.e. formation of silicate material with higher (Ca+K)/Fe-ratios. Such differentiation processes evidently may occur also with material that was not previously depleted in moderately volatile Na. Detailed analyses of the shown reservoirs can be found in e.g., Lyubetskaya and Korenaga [2007], Scott and Krot [2007], Goldstein et al. [2008], Vinogradov et al. [1965] and Lodders and Fegley [1998].

The following conclusions can be inferred for the interstellar dust candidates:

- The compositional variety is high, particular between Mg and Fe type ISD candidates
- Mg type ISD candidates mostly plot above a line of alkali-depleted and Fe-depleted material, which is typical for the silicate portion of the Earth and of the inner terrestrial planets. This indicates that depletion of moderately volatile elements played a minor role only, but probably as strong as for CV chondrites
- Some Mg-type particles plot close to primitive chondritic composition, indicating that magmatic differentiation did not occur
- Fe-type ISD candidate particles have compositions similar to iron meteorites. This does not mean that they stem from a differentiated body - small metal particles or Fe-rich olivine grains also occur in chondrites. However, at least some process separating or enriching these particles is needed

All in all, there is significant evidence that interstellar particles are heterogeneous on very small spatial scales.

Glossary of terms of cosmochemically relevant reservoirs

In the following, the aforementioned cosmochemically relevant reservoirs and their significance are described in more detail:

Bulk silicate Earth Bulk silicate Earth describes the reference reservoir for primitive mantle composition and denotes the bulk composition of Earth's crust and mantle, without the Fe-rich core. Earth's crust and mantle are especially dominated by silicates. The compositional trend in mantle peridotites is a "melting-trend". Along this trend, a primitive mantle composition should exist [Lyubetskaya and Korenaga, 2007].

Ordinary chondrites Ordinary chondrites belong to the class of stony chondritic meteorites. The H-chondrite included in the plot denotes the most common type of meteorites. The H-chondrite can be probably linked to the S-type asteroid 6 Hebe. H-chondrites are Fe-rich, containing nickel-iron metal and troilite. Most H-chondrites have faced significant degrees of metamorphism.

Carbonaceous chondrites Carbonaceous chondrites include some of the most primordial meteorites. In general, they are mainly comprised by silicates, oxides and sulphides, with olivine and serpentine being characteristic silicates. Some carbonaceous chondrites contain large amounts of water and organic species, which indicates that they have not experienced significant heating, thus some classes of carbonaceous chondrites resemble closely the compositions of the solar nebula, from which the solar system condensed. Other classes contain lesser amounts of volatile compounds and some experienced heating events. Included in this plot are CI and CV carbonaceous chondrites.

CI-chondrites have compositions resembling closely that of the solar photosphere, not taking into account gaseous species and Li. CI chondrites are chemically the most primitive known meteorites. They contain a high amount of water (up to 22%) and organic compounds (amino acids and PAH's). Further, they are comprised by phyllosilicates, magnetite and olivine, due to hydrous alteration processes.

CV chondrites, such as Allende, are comprised by mainly olivine and pyroxene and rich in refractory elements, such as Al, Ca and Ti, but are poor in volatile species. They contain large amounts of CAI's (calcium-aluminum-rich inclusions). Presolar grains have been discovered as well in the Allende meteorite. Ages derived from chondrules and CAI's in the Allende meteorite reveal information about conditions present before and at the onset of the formation of our solar system.

Mesosiderites Mesosiderites belong to the stony-iron meteorites, comprised by equal parts of metallic nickel-iron and silicates. The silicates are mainly olivines, Ca-poor pyroxenes and Ca-rich feldspar. Further they show similarities to eucrites and diogenites, linked e.g., to the asteroid Vesta.

Iron meteorites Iron meteorites consist of iron-nickel alloy, the meteoric iron, which s comprised by kamacite and taenite. Iron meteorites can be linked to M-type asteroids, large differentiated asteroids in the asteroid belt.

6 Summary and outlook

In this work, I evaluated constraints on the composition of interstellar dust candidates, obtained from impact ionization time-of-flight mass spectra by the Cosmic Dust Analyzer (CDA) onboard the Cassini spacecraft at Saturn. The dust candidates were chosen according to their dynamical and compositional properties. Their trajectory is in agreement with the ISD upstream direction of 259° latitude and +8° longitude. Further, the ISD candidates show speeds of $\sim$26 $\mathrm{km\,s^{-1}}$ or higher and their mass and β-values are in agreement with the astronomical silicate model, as is their siliceous composition.

To evaluate compositional constraints on the composition of aforementioned in situ spectra, experiments with specifically manufactured dust analogues have been performed, which have been then accelerated with a 2MV Van de Graaff accelerator onto the laboratory unit of the CDA , which is in any respect identical to the CDA onboard Cassini, and with the Large Area Mass Analyzer (LAMA). The CDA is a linear TOF mass spectrometer with a mass resolution of $\frac{m}{\Delta m} \sim 20 - 50$, whereas the LAMA utilizes a reflectron design and has a mass resolution of $\frac{m}{\Delta m} \sim 300$.

1) Dust analogue material An orthopyroxene separate was selected as analogue material, as it contains several important rock forming elements (Si, Mg, Al, Ca, Fe, Na, Ti, Cr, Mn). Mineral analysis using the electron microprobe showed that besides the main mineral orthopyroxene, the dust analogue consists of six additional mineral species, i.e., spinel, clinopyroxene, feldspar, hornblende, olivine and glass. Possibilities to synthesize other dust analogue materials were explored, particularly Fe-rich silicates, and further natural samples were prepared for future analyses.

2) LAMA analysis LAMA spectra at velocities of 19-40 $\mathrm{km\,s^{-1}}$ were classified according to the dominating mass line (Mg, Al, Ca) reflecting significant compositional variation. Absolute line heights of mineral elements normalized to the main integral of their corresponding spectrum, and diagrams plotting two ratios of four different elements, eliminated bias from particle mass, allowing more detailed insight into geochemical variations.

In such diagrams, most data clustered at specific element ratios representing orthopyroxene compositions. The remaining data points scatter towards compositions expected for the less abundant mineral species, particular spinel, clinopyroxene, feldspar and hornblende.

Remarkably, scattering towards specific endmembers is consistent in diagrams plotting different element ratios. Minor mineral species rarely show the pure endmember composition, but rather appear to be mixtures, mostly with orthopyroxene. It is not yet clear, if this is due to agglomeration of sub-micron sized particles induced by the coating process, or caused by mineral intergrowth inherited from the precursor rock.

3) Establishing sensitivity coefficients for LAMA measurements The identification of most of the data as orthopyroxene allows a calibration of element ratios measured by electron microprobe and LAMA. In this way we inferred impact ionization TOF-MS sensitivity coefficients for various elements, which were compared with classical TOF-SIMS sensitivity coefficients [Stephan, 2001].

Impact ionisation TOF-MS, as measured by LAMA, shows an extraordinary high sensitivity for the alkalis Na and K, whereas the sensitivities for Mg, Al, Ti and Fe appear somewhat lower. The sensitivity for Ca is comparable to classical TOF-SIMS.

4) Constraints on ISD candidate compositions For the ISD candidates (Mg+Na)/(Si+Al) was plotted versus (Ca+K)/Fe. The data were compared with mantle minerals (orthopyroxene, clinpyroxene, Mg-rich olivine, spinel, feldspar and hornblende) that plot along a trend of magmatic differentiation from a primitive mantle composition ("bulk silicate Earth"). This composition is characterized by Fe-loss due to core formation, and volatile (alkali) depletion similar to CV chondrites, but in contrast to CI and H chondrites, which are close to initial solar or cosmic composition in the (Mg+Na)/(Si+Al) versus (Ca+K)/Fe plot. Many ISD candidate data plot close to a cosmic/solar composition, possibly slightly volatile depleted. However, there are Fe-rich ISD candidates, that resemble almost pure metal particles or Fe rich olivine.

6.1 Outlook

Although the extensive analysis performed in this work yielded important constraints on the composition of the ISD candidate particles, significant uncertainties remain. These are in part due to the detection method, as i) the CDA is a strongly attenuated low-weight instrument designed for space missions, and ii) impact ionization time-of-flight mass spectrometry involves highly complex processes, particularly plasma dynamics, which are both theoretically and experimentally poorly understood.

The following suggestions can be made for future studies with focus on the identification of mono- and multi-mineral impactors:

- Generally, dust analogues from natural rocks are a great tool for calibration experiments, especially because they are available in large abundances. However, the production process leads to problems: Often, natural rocks come in mineral assemblages, meaning that the desired species has to be prepared out of the surrounding matrix. Further, due to the petrologic history of most rocks, the minerals are often altered or somehow influenced by pressure and thermal events, influencing strongly the quality of the minerals. The preparation process is long and tedious and the results are often not satisfying, especially when it comes to the preparation of Fe-rich species. It is therefore necessary to evaluate synthesis processes, if possible, e.g. sol-gel-synthesis under a shielded atmosphere.

- A thorough investigation of the grinding process of minerals with respect to possible alteration should be performed.
- Platinum as the coating material is generally excellent to work with, with respect to its high mass, making it easily distinguishable from other species in the mass spectra. However, contamination from the chemical procedures of the coating process is apparent as hydrocarbon clusters, S and Si within the spectra. Moreover, the high atomic mass of Pt leads to problems, when changes of species with impact energy or energy density are investigated. Thus, possible other coating possibilities should be evaluated.
- It is mandatory that acceleration campaigns have to be performed to investigate and understand the impact ionization process with respect to ionization efficiency, the influence of ionization potentials, electronegativity and electron affinity. It is clear that this investigation is extremely difficult
- If working with (possible) multi-mineralic dust analogues, the data sets need to be large at narrow velocity bins, especially at velocities >25 $\mathrm{km\,s^{-1}}$, to improve statistical significance.
- To improve constraints on nature and chemical composition of the Fe-rich ISD candidates, experiments have to be performend with Fe-rich dust analogues.

7 Appendix

7.1 Atomic masses, ionization energies and electron affinities

We define electron affinity as energy released by adding an electron to a neutral atom or molecule to generate a negative ion. Negative numbers here, denote the release of energy. Oxygen, e.g., shows high negative electron affinity and high positive ionization energy, and is likely to form negative ions, whereas Magnesium,needs additional energy to form negative ions, thus the value is set to > 0.00 (after Postberg [2007]).

Table 7.1: Atomic masses, ionization energies and electron affinities of relevant species in experimentally obtained mass spectra (from Handbook of Chemistry and Physics, 89th Edition, 2009)

Species	Main isotope	$E^0 \longrightarrow E^+$	$E^0 \longrightarrow E^+$
H	1 amu	13.60 eV	-0.75 eV
C	12 amu	11.25 eV	-1.26 eV
O	16 amu	13.62 eV	-1.46 eV
Na	23 amu	5.14 eV	-0.55 eV
Mg	24 amu	7.65 eV	> 0.00 eV
Al	27 amu	5.99 eV	-0.43 eV
Si	28 amu	8.16 eV	-1.39 eV
K	39 amu	4.34 eV	-0.50 eV
Ca	40 amu	6.11 eV	-0.02 eV
Ti	48 amu	6.83 eV	-0.08 eV
Cr	53 amu	6.77 eV	-0.67
Fe	56 amu	7.91 eV	-0.15 eV
Rh	103 amu	7.46 eV	-1.4 eV

7.2 Raw data

The following tables show the raw data for LAMA- and CDA-analysis. The data were manually extracted from each spectrum within the data sets. Shown in the LAMA data are the absolute line heights of the mass lines used for the studies, as well as relevant parameters, such as the velocity of the dust grain, the main integral of each mass spectrum, the size of an impacting particle, the energy released upon impact, and the corresponding energy density, as derived from the processing software. Raw data from CDA mass spectra show the absolute line heights of all important mass

lines. Since not all mass lines can be distinguished, the adjunct and most likely contributing mass lines are listed in parentheses.

7.2.1 LAMA-raw data

Nr	v (kms^{-1})	Int$_{main}$	R (µm)	E (nJ)	D (J/m^2)	^{12}C	^{16}O	^{23}Na	^{24}Mg	^{27}Al	^{28}Si	^{39}K	^{40}Ca	^{49}Ti	^{52}Cr	^{56}Fe	^{103}Rh
180	19.0	29.11	0.09	1.17	35.79	0.27	0.02	0.68	0.28	0.13	0.23	0.60	0.35		0.02	0.09	0.24
408	19.0	39.79	0.07		28.40	0.32	0.03	0.47	0.71	0.90	0.18	0.44	0.18			0.07	0.24
335	19.0	50.53	0.09	1.96	37.48	0.52	0.03	0.43	0.35	0.10	0.28	1.34	0.41			0.06	0.49
33	19.0	507.30	0.15	9.38	63.06	1.56	0.06	3.00	4.32	0.97	1.17	2.67	1.47	0.03	0.05	0.37	1.52
17	19.0	80.26	0.09	2.02	37.84	0.99	0.07	0.47	0.42	0.61	0.46	0.68	0.34	0.03	0.05	0.14	0.75
332	19.1	62.87	0.11	3.88	47.12	0.67	0.04	1.05	1.44	0.29	0.50	0.82	0.43			0.08	0.54
362	19.1	195.76	0.09	1.67	35.64	1.56	0.08	0.78	2.05	0.27	0.78	0.55	0.35	0.03	0.03	0.13	0.70
276	19.1	59.04	0.10	2.44	40.41	0.70	0.05	1.34	0.39	0.07	0.30	0.32	0.16			0.09	0.19
261	19.1	376.46	0.11	3.41	45.22	2.13	0.12	2.57	4.36	0.80	1.19	1.31	0.72	0.03		0.22	1.23
368	19.1	198.40	0.10	2.65	41.63	0.99	0.05	2.08	2.68	0.54	0.66	0.76	0.40	0.03		0.14	0.58
107	19.1	82.06	0.08	1.49	34.38	0.90	0.06	0.26	0.36	0.03	0.43	0.65	0.12			0.10	0.79
297	19.1	30.17	0.07		29.39	0.49	0.06	1.80	0.20	0.05	0.29	0.30	0.14			0.05	0.47
410	19.1	85.27	0.10	2.89	42.87	1.09	0.06	0.43	0.51	0.09	0.74	0.79	0.38			0.07	1.08
81	19.1	29.49	0.08	1.48	34.32	0.40	0.04	0.70	0.89	0.16	0.28	0.54	0.19			0.17	0.33
138	19.1	350.04	0.13	5.39	52.81	1.60	0.06	1.85	4.36	0.82	1.09	1.22	0.96	0.04	0.03	0.29	1.30
407	19.1	306.69	0.13	5.33	52.62	1.44	0.05	2.21	3.70	0.66	0.85	1.71	0.64	0.03	0.04	0.18	0.95
5	19.1	478.25	0.14	7.15	57.74	2.23	0.05	3.17	4.35	1.01	1.31	2.21	1.66	0.04	0.04	0.26	1.40
26	19.1	52.10	0.07		27.27	0.05		2.86	0.02	0.31	0.05	1.14	0.18		0.02	0.04	0.03
21	19.1	175.72	0.09	1.88	37.18	0.03		1.01	0.96	4.37		0.38	0.09		0.05	0.07	
10	19.1	253.43	0.10	2.83	42.54	1.64	0.07	2.82	2.14	1.13	0.77	1.00	0.49			0.25	0.90
414	19.2	42.99	0.09	2.11	38.72	0.56	0.06	0.56	0.31	0.07	0.20	0.88	0.20			0.11	0.56
112	19.2	41.50	0.08	1.57	35.13	0.69	0.06	0.39	0.20	0.05	0.27	0.32	0.08			0.09	0.49
65	19.2	169.35	0.08	1.34	33.31	1.40	0.10	1.31	2.40	0.36	0.74	0.35	0.25			0.09	0.41
351	19.2	540.45	0.16	10.98	67.20	1.98	0.10	4.36	4.36	0.97	1.02	2.56	1.63	0.04	0.06	0.40	1.77
16	19.2	61.18	0.08	1.52	34.79	0.45	0.03	0.74	0.82	0.26	3.10	0.54	0.32			0.08	0.22
348	19.2	127.55	0.11	3.35	45.23	1.66	0.07	0.70	0.82	0.13	0.80	1.16	0.48		0.04	0.23	1.36
238	19.2	137.93	0.10	2.73	42.30	0.89	0.05	1.87	0.68	0.46	0.50	2.28	0.23		0.02	0.13	1.18
139	19.2	70.97	0.08	1.20	32.23	0.89	0.09	0.33	0.12	0.20	0.33	0.95	0.18	0.36		0.08	0.61
350	19.2	390.69	0.11	3.60	46.47	1.79	0.12	0.81	2.98	0.62	1.61	1.22	0.53		0.05	0.31	1.56
201	19.2	101.02	0.09	1.76	36.59	1.20	0.07	0.23	0.60	0.06	0.79	0.50	0.19			0.13	0.90
283	19.2	177.08	0.10	2.43	40.76	1.32	0.05	0.79	2.52	0.63	0.96	0.84	0.64	0.03	0.05	0.13	0.53
219	19.2	343.44	0.11	3.14	44.50	1.60	0.16	2.32	4.36	0.57	0.64	1.08	0.51	0.04		0.18	0.39
15	19.2	438.37	0.11	3.63	46.52	1.65	0.08	4.35	0.98	0.91	0.74	0.95	4.35	0.03	0.04	0.30	0.77
31	19.2	178.27	0.11	3.61	46.50	0.64	0.03	1.03	0.68	2.17	0.42	2.77	0.36	0.02	0.04	0.15	0.79
30	19.2	109.08	0.07	1.05	30.83	0.11		1.11	0.05	2.85	0.18	0.81	0.07		0.05	0.03	0.13
4	19.2	405.36	0.10	2.49	41.04	2.73	0.18	0.46	0.92	0.11	1.96	0.76	0.49		0.05		2.75
248	19.3	202.39	0.10	2.68	42.82	2.28	0.17	0.47	0.83	0.20	1.14	1.81	0.39		0.03	0.17	1.30
413	19.3	222.31	0.10	2.34	40.40	2.16	0.17	0.46	0.72	0.10	0.91	0.94	0.20		0.03	0.30	1.65
404	19.3	572.11	0.11	3.77	47.37	2.80	0.21	1.50	4.32	1.03	1.60	1.16	1.13	0.04	0.04	0.32	1.36
312	19.3	112.30	0.11	3.47	46.07	1.39	0.06	0.42	1.20	0.22	1.01	0.83	0.56		0.04	0.19	1.17
101	19.3	232.51	0.10	2.51	41.42	1.33	0.07	1.36	3.33	0.51	0.66	0.77	0.43	0.03		0.56	0.53
241	19.3	29.23	0.07	1.03	30.80	0.41	0.03	0.28	0.26	0.06	0.20	0.42	0.09		0.04	0.05	0.39
202	19.3	303.11	0.10	2.43	41.01	1.74	0.10	1.49	4.36	0.76	0.93	0.89	0.62	0.03	0.05	0.32	0.43
136	19.3	88.64	0.08	1.16	32.09	1.03	0.06	0.52	0.65	0.13	0.48	0.50	0.25		0.02	0.09	0.63
140	19.3	218.87	0.11	3.18	44.88	1.73	0.09	1.76	1.78	0.63	0.93	1.35	0.47	0.04		0.20	1.49
376	19.3	126.70	0.10	2.38	40.72	1.57	0.09	1.31	1.32	0.31	0.98	0.74	0.42		0.03	0.11	0.93
406	19.3	15.60	0.08	1.44	34.48	0.25		0.73	0.15	0.07	0.11	0.38	0.14			0.07	0.33
396	19.3	160.25	0.08	1.20	32.52	0.80	0.05	1.06	0.90	0.13	0.61	2.98	0.22			0.06	0.43
8	19.3	442.88	0.12	4.25	49.42	0.26	0.03	3.66	2.53	4.35	0.48	1.16	0.52		0.07	0.31	0.81

Nr	v (kms^{-1})	Int$_{main}$	R (µm)	E {nJ}	D (J/m^2)	^{12}C	^{16}O	^{23}Na	^{24}Mg	^{27}Al	^{28}Si	^{39}K	^{40}Ca	^{48}Ti	^{52}Cr	^{56}Fe	^{103}Rh
3	19.3	59.12	0.08	1.31	33.40	0.36	0.04	0.98	1.02	0.46	0.22	1.52	0.43			0.07	0.36
399	19.4	296.06	0.08	1.63	36.05	3.87	0.49	0.80	0.41	0.12	1.13	0.89	0.20			0.20	1.33
326	19.4	110.50	0.10	2.46	41.35	1.01	0.07	1.44	1.55	0.27	0.63	1.58	0.42		0.03	0.16	0.97
280	19.4	81.60	0.08	1.40	34.28	1.04	0.05	0.29	0.64	0.27	0.43	0.47	0.17		0.02	0.10	0.59
110	19.4	150.46	0.10	2.30	40.43	0.96	0.05	1.55	1.68	0.27	0.58	1.73	0.49			0.12	0.58
193	19.4	82.44	0.08	1.38	34.12	1.11	0.17	0.41	0.27	0.17	0.35	0.43	0.10			0.11	1.00
164	19.4	102.72	0.10	2.40	41.03	1.33	0.06	1.16	1.01	0.23	0.42	0.91	0.39			0.10	0.83
61	19.4	217.55	0.10	2.38	40.91	2.15	0.13	2.04	0.77	0.12	1.37	1.39	0.43		0.02	0.10	1.27
137	19.4	82.30	0.08	1.18	32.38	1.10	0.09	0.59	0.48	0.11	0.34	0.44	0.18		0.02	0.09	0.76
161	19.4	117.96	0.09	2.28	40.37	1.38	0.09	0.63	1.17	0.42	0.63	0.86	0.43		0.04	0.17	0.90
168	19.4	104.84	0.11	3.55	46.76	0.77	0.05	0.89	0.65	0.19	0.33	1.59	0.93		0.03	0.08	0.95
177	19.4	158.65	0.08	1.52	35.27	1.00	0.05	0.67	1.94	0.25	0.58	0.52	0.26			0.12	0.30
48	19.4	46.93	0.07	1.02	30.93	0.44	0.04	0.26	0.45	0.11	0.37	0.34	0.39		0.02	0.07	0.24
74	19.4	37.91	0.08	1.16	32.33	0.24		0.54	0.73	0.16	0.16	1.04	0.28			0.09	0.23
412	19.4	375.61	0.10	2.32	40.71	1.91	0.12	1.34	3.60	1.02	1.63	0.96	0.86	0.06	0.03	0.22	0.96
409	19.4	597.94	0.12	4.46	50.58	3.22	0.47	1.32	2.63	0.86	2.01	1.87	1.14	0.03	0.02	0.22	2.43
298	19.4	73.95	0.09	1.97	38.55	0.77	0.03	0.25	0.48	0.08	0.51	0.69	0.20			0.09	0.69
292	19.4	173.39	0.09	1.91	38.20	1.34	0.06	0.79	2.52	0.32	0.76	0.51	0.45	0.02	0.04	0.26	0.49
204	19.4	117.68	0.08	1.17	32.44	0.89	0.06	0.82	1.58	0.26	0.54	0.57	0.22	0.02	0.03	0.13	0.25
247	19.4	603.17	0.12	4.87	52.15	2.09	0.19	4.37	4.37	0.73	0.84	1.60	0.85	0.05	0.05	0.38	0.45
342	19.4	101.56	0.07		28.99	0.92	0.07	0.50	1.13	0.20	0.40	1.67	0.16			0.06	0.34
400	19.4	40.47	0.08	1.43	34.71	0.44	0.03	0.49	0.68	0.14	0.21	0.85	0.18	0.05		0.08	0.41
356	19.4	69.15	0.08	1.62	36.22	0.67	0.03	0.24	0.33	0.07	0.37	0.39	0.13			0.07	0.57
192	19.4	236.79	0.08	1.30	33.60	1.65	0.17	1.19	3.07	0.43	0.90	0.23	0.27		0.04	0.15	0.29
334	19.4	151.15	0.11	3.44	46.51	1.21	0.05	2.05	0.35	0.09	0.65	0.82	0.32		0.04	0.15	1.59
18	19.4	324.44	0.10	2.48	41.71	1.56	0.26	3.50	1.12	0.48	0.97	0.73	3.76	0.03	0.03	0.26	1.12
22	19.4	265.06	0.10	2.87	43.75	0.05		3.13	0.19	4.32	0.24	1.25	0.32		0.06	0.16	0.22
29	19.4	429.29	0.10	2.39	41.22	0.20		2.18	0.29	4.36	0.59	2.46	0.27	0.04	0.20	0.58	1.18
1	19.4	11.01	0.08	1.41	34.59	0.49		0.42	0.28	0.08	0.71	0.21	0.21		0.03	0.22	0.38
250	19.5	64.73	0.10	2.65	42.69	0.63	0.05	0.61	0.33	0.14	0.42	0.91	0.20			0.07	0.69
339	19.5	51.82	0.07		28.79	0.44	0.02	0.28	0.21	0.47	0.26	0.27	0.10			0.03	0.10
401	19.5	25.70	0.07		29.49	0.44	0.04	0.32	0.09		0.17	0.21	0.09			0.05	0.28
126	19.5	66.74	0.10	2.57	42.33	0.79	0.05	0.40	0.16	0.03	0.26	0.54	0.10			0.15	0.80
340	19.5	117.86	0.15	9.64	65.75	1.51	0.10	0.61	1.08	0.24	1.11	1.24	0.66		0.03	0.14	1.49
392	19.5	52.73	0.08	1.47	35.11	0.54	0.03	0.77	0.95	0.42	0.23	0.65	0.48			0.08	0.41
353	19.5	38.46	0.07		29.89	0.72	0.07	0.31	0.17	0.07	0.23	0.60	0.07			0.19	0.49
46	19.5	68.60	0.07		30.76	0.92	0.06	0.41	0.12	0.05	0.19	0.45	0.11			0.08	0.61
279	19.5	127.58	0.11	3.56	47.23	1.13	0.04	1.10	1.98	0.35	0.77	0.79	0.38	0.03	0.03	0.22	1.12
176	19.5	72.76	0.12	4.27	50.23	0.74	0.04	1.40	1.42	0.26	0.41	1.12	0.60	0.03		0.12	1.08
213	19.5	43.76	0.07	1.00	31.01	0.49	0.03	0.29	0.19	0.02	0.26	0.61	0.09			0.05	0.40
403	19.5	141.97	0.08	1.52	35.63	1.03	0.06	0.60	2.00	0.26	0.42	0.71	0.26	0.02		0.08	0.36
14	19.5	121.03	0.07	1.07	31.60	0.77	0.05	0.80	0.52	0.81	0.49	2.40	0.14		0.03	0.14	0.46
398	19.6	326.39	0.13	5.51	54.84	1.62	0.07	1.62	2.83	0.81	1.04	1.70	0.73		0.05	0.21	1.57
234	19.6	214.48	0.10	2.42	41.74	2.25	0.24	1.67	1.92	1.96	0.33	1.15	0.93	0.35		0.44	1.31
285	19.6	74.49	0.07		30.35	0.60	0.04	0.72	1.40	0.24	0.45	0.85	0.21	0.02	0.02	0.09	0.16
344	19.6	158.27	0.07	1.01	31.17	1.37	0.06	0.60	1.70	0.28	0.70	1.51	0.22			0.07	0.17
405	19.6	727.01	0.11	3.59	47.62	3.38	0.25	4.30	1.73	1.49	2.06	4.27	0.37		0.03	0.11	1.05
63	19.6	487.95	0.11	4.09	49.76	2.20	0.13	2.33	4.32	0.79	1.16	1.31	0.85	0.06	0.04		
222	19.6	128.42	0.08	1.27	33.68	0.96	0.06	0.52	1.82	0.35	0.58	0.54	0.29	0.02	0.03	0.16	0.51

Nr	v (kms^{-1})	Int$_{main}$	R (µm)	E {nJ}	D (J/m^2)	^{12}C	^{16}O	^{23}Na	^{24}Mg	^{27}Al	^{28}Si	^{39}K	^{40}Ca	^{48}Ti	^{52}Cr	^{56}Fe	^{103}Rh
402	19.6	37.18	0.10	2.97	44.77	0.30		1.43	0.37	0.17	0.25	0.85	0.72			0.12	0.72
71	19.6	78.05	0.08	1.29	33.95	1.03	0.07	0.74	0.25	0.07	0.34	0.22	0.08		0.02	0.17	0.80
273	19.6	81.90	0.09	1.88	38.49	1.10	0.06	0.59	0.35	0.05	0.59	0.75	0.25			0.16	0.77
411	19.6	104.20	0.09	2.08	39.81	1.25	0.08	0.64	1.06	0.19	0.72	0.74	0.21	0.03	0.03	0.17	1.00
210	19.6	89.07	0.07		29.15	1.43	0.18	0.61	0.13	0.30	0.21	0.74	0.11			0.82	0.43
15	19.6	277.28	0.10	2.54	42.50	1.41	0.08	1.01	1.24	4.28	0.94	1.15	0.29	0.04	0.04	0.09	0.59
16	19.6	42.12	0.08	1.34	34.36	0.26		0.77	0.96	0.63	0.20	0.60	0.30	0.02	0.02	0.20	0.25
367	19.7	252.80	0.08	1.41	35.04	2.05	0.41	0.59	1.04	0.20	1.19	0.85	0.22			0.16	1.87
57	19.7	94.86	0.10	2.51	42.52	1.07	0.07	0.42	1.19	0.23	0.58	0.52	0.27			0.34	0.95
175	19.7	194.10	0.08	1.22	33.40	2.52	0.28	0.31	0.61	0.21	1.44	0.33	0.09		0.03	0.09	1.19
87	19.7	534.71	0.13	5.63	55.67	3.07	0.20	2.81	4.30	0.77	1.40	2.59	0.79	0.02	0.04	0.28	1.86
34	19.7	29.49	0.07		29.82	0.31	0.03	0.44	0.20	0.11	0.13	0.40	0.17		0.03	0.09	0.21
336	19.7	149.32	0.08	1.50	35.88	1.45	0.06	1.20	0.74	0.07	1.03	0.91	0.17		0.02	0.07	0.83
102	19.7	255.75	0.10	3.20	46.23	1.10	0.06	2.43	3.30	0.61	0.67	1.81	0.82		0.03	0.17	0.89
246	19.7	256.38	0.10	3.14	45.99	1.69	0.17	1.17	3.46	0.76	0.95	1.23	0.77	0.07		0.23	1.49
215	19.7	46.49	0.10	2.90	44.83	0.64	0.02	0.79	0.36	0.24	0.40	0.68	0.38			0.07	1.13
187	19.7	61.92	0.07	1.13	32.75	0.48	0.03	0.61	0.58	0.26	0.34	0.89	0.17			0.08	0.47
311	19.7	246.12	0.09	2.37	41.92	1.94	0.15	0.88	2.80	0.44	1.30	0.54	0.43		0.04	0.16	0.93
21	19.7	47.87	0.09	2.28	41.39	0.41	0.10	0.58	0.47	0.18	0.17	0.51	0.60			0.05	0.56
4	19.7	256.87	0.08	1.35	34.72	0.03		0.26	0.10	4.33		0.24	0.10		0.04	0.03	
28	19.8	32.62	0.08	1.27	34.12	0.46		1.30	0.30	0.13	0.23	0.61	0.37			0.05	0.25
263	19.8	501.21	0.10	2.70	43.84	2.98	0.48	1.22	4.33	0.96	1.55	0.78	0.78	0.04	0.03	0.26	0.39
361	19.8	67.10	0.10	2.68	43.74	0.62	0.03	0.42	0.25	0.23	1.43	0.42	0.46	0.02	0.07	0.40	0.75
314	19.8	22.40	0.06		27.45	0.29	0.04	0.16	0.20	0.03	0.26	0.42	0.18			0.05	0.19
333	19.8	35.20	0.08	1.44	35.59	0.63	0.02	0.30	0.27	0.06	0.38	0.54	0.19		0.02	0.05	0.59
281	19.8	162.98	0.09	2.34	41.89	1.96	0.17	0.97	1.55	0.32	0.65	0.54	0.26		0.04	0.22	1.16
98	19.8	64.80	0.07		31.09	0.61	0.05	0.33	0.29	0.05	0.33	0.61	0.21			0.08	0.53
379	19.8	9.65	0.06		26.97	0.25	0.02	0.23	0.10	0.03	0.10	0.24	0.08			0.07	1.60
35	19.8	80.69	0.08	1.24	34.00	0.84	0.04	0.42	0.91	0.22	0.41	0.69	0.41	0.03		0.07	0.48
169	19.8	142.79	0.09	1.98	39.72	1.63	0.12	1.20	1.15	0.35	1.00	0.48	0.28		0.03	0.14	0.05
8	19.8	108.48	0.08	1.61	37.10	1.33	0.16	1.17	0.94	0.16	0.48	1.06	0.22	0.03		0.22	1.02
20	19.8	70.04	0.06		29.01	0.71	0.05	0.38	0.60	0.19	0.30	1.01	0.18		0.02	0.07	0.30
28	19.8	641.40	0.13	5.80	56.73	3.15	0.23	4.21	4.33	1.05	1.64	0.89	1.58	0.05	0.05	0.43	1.37
7	19.8	295.22	0.11	3.39	47.34	0.03	0.02	1.98	0.87	3.95	0.67	2.82	0.49		0.05	0.11	0.37
10	19.8	140.17	0.09	2.00	39.79	0.05		0.41	0.07	3.83		0.18	0.05		0.04		
2	19.8	18.74	0.08	1.45	35.80	0.23	0.02	0.52	0.07	0.28	0.10	0.37	0.36	0.39		0.05	0.22
150	19.9	117.58	0.09	1.73	38.02	1.54	0.11	0.99	0.70	0.21	0.49	0.62	0.23	0.02	0.04	0.14	1.07
135	19.9	86.18	0.07		30.04	1.20	0.09	0.53	0.16	0.04	0.36	0.36	0.17			0.08	0.64
262	19.9	82.74	0.08	1.40	35.48	0.79	0.04	0.74	1.36	0.35	0.65	0.62	0.25		0.03	0.17	0.33
27	19.9	91.12	0.07	1.09	32.64	1.03	0.09	0.35	0.45	0.17	0.56	0.67	0.25		0.03	0.09	0.67
79	19.9	73.76	0.01	2.55	43.33	1.05	0.06	0.43	0.61	0.09	0.57	0.79	0.25			0.08	1.03
197	19.9	102.17	0.09	2.31	41.92	1.39	0.07	0.32	0.64	0.07	0.83	1.12	0.21			0.06	1.18
96	19.9	694.65	0.13	6.54	59.34	2.15	0.08	4.36	4.36	1.06	1.35	3.65	1.20	0.06	0.05	0.29	1.06
271	19.9	165.21	0.10	3.03	45.97	0.96	0.06	1.82	2.35	0.42	0.48	1.19	0.46	0.02	0.03	0.14	1.02
173	19.9	403.52	0.11	4.10	50.87	1.79	0.09	3.78	3.05	0.67	0.79	2.50	0.84	0.03	0.05	0.37	1.75
264	19.9	84.29	0.07		31.17	1.09	0.07	0.33	0.77	0.12	0.42	0.65	0.17			0.06	0.38
170	19.9	554.13	0.09	2.41	42.58	3.32	0.38	1.98	4.33	0.77	1.65	1.22	0.64	0.04	0.04	0.24	0.50
393	19.9	523.25	0.10	2.69	44.22	2.51	0.19	2.30	3.24	0.78	2.05	1.07	0.67	0.26	0.03	0.21	1.83
228	19.9	71.08	0.08	1.28	34.57	0.77	0.05	0.44	1.11	0.20	0.44	0.42	0.16			0.11	0.48

Nr	v (kms^{-1})	Int$_{main}$	R (µm)	E {nJ)	D (J/m^2)	^{12}C	^{16}O	^{23}Na	^{24}Mg	^{27}Al	^{28}Si	^{39}K	^{40}Ca	^{48}Ti	^{52}Cr	^{56}Fe	^{103}Rh
155	19.9	90.57	0.08	1.43	35.81	0.39	0.02	0.94	1.04	0.24	0.29	1.77	0.34			0.09	0.25
374	20.0	38.29	0.06		28.31	0.41	0.03	0.19	0.17	0.03	0.24	0.43	0.08			0.04	0.19
64	20.0	82.25	0.09	2.41	42.80	1.04	0.12	0.35	0.17	0.07	0.27	0.68	0.17			0.07	1.34
382	20.0	18.89	0.08	1.24	34.35	0.42	0.03	0.24	0.67	0.10	0.22	0.37	0.10			0.07	0.31
30	20.0	224.50	0.10	2.84	45.52	1.67	0.12	1.13	3.38	0.53	1.00	1.13	0.64	0.03	0.03	0.13	1.28
319	20.0	798.04	0.12	4.96	54.53	3.80	0.46	2.43	4.35	2.07	2.04	1.33	1.19	0.06	0.07	0.54	1.10
93	20.0	50.84	0.08	1.47	36.34	0.57	0.04	0.23	0.25	0.08	0.36	0.48	0.09			0.12	0.38
383	20.0	325.17	0.09	2.43	43.03	2.18	1.10	0.96	4.36	0.59	1.41	1.00	0.51	0.02	0.03	0.18	0.61
131	20.0	117.50	0.10	2.54	43.77	0.98	0.06	0.84	1.65	0.48	0.69	1.26	0.35		0.03	0.16	0.44
198	20.0	347.65	0.12	4.55	53.14	1.62	0.12	2.67	0.50	0.54	0.79	4.36	0.58		0.03	0.33	2.23
188	20.0	97.22	0.07	1.04	32.44	1.01	0.10	0.26	1.55	0.20	0.49	0.45	0.17			0.08	0.43
27	20.0	75.13	0.11	3.41	48.15	0.25		1.18	0.27	0.13	0.22	1.31	1.55	0.02	0.03	0.19	1.26
24	20.0	1463.61	0.14	8.38	64.95	4.36	0.43	4.36	3.89	3.01	2.49	2.10	4.36	0.18	0.06	0.59	0.76
7	20.0	56.98	0.10	2.61	44.08	0.40		1.42	0.47	0.11	0.17	1.78	0.68			0.20	0.73
100	20.1	178.29	0.10	2.51	43.96	1.55	0.07	1.15	2.43	0.49	0.72	1.36	0.86	0.02	0.04	0.19	1.03
40	20.1	69.03	0.07		31.08	0.74	0.06	0.28	0.32	0.09	0.44	0.27	0.07			0.14	0.54
59	20.1	33.88	0.05		23.57	0.45	0.04	0.15	0.29	0.08	0.21	0.24	0.11			0.13	0.25
330	20.1	89.62	0.14	7.19	62.13	1.08	0.06	0.73	0.16	0.16	0.28	0.71	0.41			0.18	0.97
272	20.1	344.85	0.10	2.92	46.09	2.44	0.13	2.50	0.79	0.18	1.52	2.26	0.83			0.09	1.11
120	20.1	99.41	0.10	2.97	46.31	1.37	0.07	0.88	0.87	0.22	0.78	0.58	0.38			0.14	1.06
129	20.1	36.52	0.07	1.06	32.91	0.25		0.33	0.38	0.12	0.23	0.52	0.40			0.07	0.37
208	20.1	59.15	0.07	0.10	32.50	0.38		0.40	0.81	0.31	0.27	0.31	0.23			0.11	0.22
25	20.1	762.80	0.12	4.55	53.42	3.67	0.33	3.90	4.36	1.33	2.34	1.20	1.51	0.05	0.06	0.45	2.78
11	20.1	28.39	0.10	2.72	44.94			0.61	0.07	0.30	0.03	1.59	0.26			0.02	0.13
113	20.2	73.69	0.01	1.96	40.45	0.67	0.03	0.95	0.91	0.22	0.22	1.20	0.60			0.11	0.81
343	20.2	453.55	0.10	3.18	47.50	3.33	0.33	2.73	2.01	0.42	1.59	2.31	0.52		0.06	0.51	1.51
119	20.2	101.16	0.01	2.20	42.05	1.14	0.50	0.97	0.86	0.29	0.83	0.66	0.19			0.10	0.80
12	20.2	80.38	0.07		31.53	1.19	1.00	0.62	0.20	0.11	0.59	0.73	0.39			0.07	0.45
68	20.2	105.29	0.08	1.75	39.02	1.33	0.08	0.53	0.97	0.19	0.94	0.77	0.29		0.03	0.15	1.12
165	20.2	93.86	0.08	1.36	35.89	1.12	0.09	0.40	1.56	0.27	0.61	0.24	0.20			0.16	0.61
167	20.2	99.88	0.07	1.05	32.92	1.27	0.09	0.38	1.06	0.17	0.48	0.65	0.19			0.07	0.55
42	20.2	109.86	0.10	2.56	44.30	1.58	0.11	1.04	0.82	0.30	0.44	0.82	0.42		0.03	0.11	1.15
268	20.2	76.89	0.09	1.97	40.58	0.94	0.07	0.23	0.30	0.09	0.31	0.21	0.30			0.14	0.76
341	20.2	80.74	0.09	1.97	40.64	1.00	0.07	0.56	0.46	0.41	0.43	0.80	0.09			0.09	0.69
3	20.2	473.07	0.08	1.77	39.11	2.04	0.22	1.09	2.13	1.80	3.28	1.23	0.03	0.02	0.02	0.14	0.82
73	20.3	90.93	0.08	1.38	36.20	1.18	0.06	0.61	0.43	0.09	0.75	0.50	0.23			0.06	0.80
158	20.3	504.25	0.12	5.24	56.51	2.47	0.28	2.17	3.50	0.77	1.35	1.69	0.82	0.03	0.03	0.22	2.78
325	20.3	409.23	0.11	3.81	50.93	2.92	0.24	1.42	1.71	0.41	1.36	2.48	0.58	0.04	0.02	0.11	2.18
242	20.3	75.97	0.07	1.16	34.30	1.19	0.06	0.44	0.21	0.31	0.44	0.67	0.57			0.06	0.48
44	20.3	151.23	0.11	3.60	50.14	0.57	0.06	1.27	2.95	0.38	0.38	1.00	0.53	0.04	0.13	0.13	0.82
149	20.3	143.24	0.10	3.32	48.80	1.33	0.09	0.64	0.55	0.16	0.42	0.87	0.30			0.18	1.73
72	20.4	134.78	0.07	1.15	34.30	1.89	0.19	0.45	0.26	0.06	0.61	0.89	0.13			0.09	0.84
160	20.4	107.76	0.07	1.20	34.92	1.30	0.09	0.51	1.34	0.21	0.62	0.47	0.28			0.12	0.52
78	20.4	557.58	0.11	3.50	49.87	3.41	0.29	2.34	4.36	1.04	1.79	0.78	0.86	0.04	0.06	0.45	1.52
205	20.4	276.98	0.10	3.04	47.64	1.28	0.08	1.21	4.36	0.83	0.89	0.68	0.89	0.03	0.04	0.27	1.07
92	20.4	91.41	0.31	89.93		0.43	0.04	2.44	0.91	0.22	0.19	1.06	0.33	0.03	0.07	0.30	0.73
162	20.4	114.40	0.10	2.60	45.22	1.05	0.06	0.90	1.64	0.35	0.51	1.18	0.40		0.04	0.14	1.07
211	20.4	97.02	0.07	1.09	33.86	1.14	0.06	0.39	1.09	0.19	0.51	0.54	0.26		0.01	0.07	0.50
178	20.4	134.44	0.08	1.57	38.28	1.65	0.08	1.01	0.38	0.22	0.72	1.03	0.69		0.03	0.21	0.66

Nr	v (kms^{-1})	Int$_{main}$	R (µm)	E {nJ)	D (J/m^2)	^{12}C	^{16}O	^{23}Na	^{24}Mg	^{27}Al	^{28}Si	^{39}K	^{40}Ca	^{48}Ti	^{52}Cr	^{56}Fe	^{103}Rh
397	20.4	110.06	0.07	1.11	34.12	1.19	0.07	0.43	1.24	0.19	0.64	0.60	0.27	0.02	0.02	0.07	0.49
1	20.4	300.31	0.08	1.53	37.82	1.26	0.07	4.36	2.55	1.25	0.67	1.74	1.61		0.05	0.40	0.76
23	20.4	256.44	0.09	2.37	43.75	0.59	0.04	1.38	4.36	1.18	1.22	0.90	1.54	0.03	0.04	0.20	0.84
9	20.4	45.72	0.09	2.24	42.93	0.14		0.77	0.10	0.86	0.09	1.66	0.30			0.08	0.30
24	20.4	261.79	0.10	2.95	47.20	1.01	0.05	4.35	0.87	1.78	0.44	1.91	0.57		0.06	0.32	0.68
6	20.4	633.64	0.10	2.69	45.69	3.77	0.29	3.73	1.00	0.14	2.69	1.76	0.43		0.03	0.17	1.98
17	20.5	36.29	0.08	1.66	39.05	0.41	0.05	0.16	0.08	0.03	0.11	0.35	0.17			0.04	0.41
2	20.5	48.37	0.07	1.03	33.34	0.46	0.05	0.56	0.78	0.15	0.29	0.81	0.37			0.08	0.64
116	20.5	131.84	0.09	2.30	43.50	1.29	0.07	0.68	1.75	0.36	0.61	0.60	0.35	0.03	0.04	0.28	0.60
142	20.5	528.45	0.10	2.92	47.20	3.99	0.30	1.71	4.36	0.90	1.76	1.30	0.85	0.03	0.04	0.26	1.55
371	20.5	338.76	0.11	3.46	50.01	2.71	0.32	1.23	2.32	0.41	1.16	0.87	0.60		0.05	0.46	1.91
235	20.5	106.38	0.07	1.06	33.76	1.20	0.07	0.80	1.00	0.39	0.86	0.75	0.85	0.03		0.12	0.49
94	20.5	63.31	0.09	1.87	40.79	0.80	0.06	0.25	0.14	0.04	0.31	0.60	0.19			0.06	0.67
199	20.5	361.97	0.09	2.44	44.60	3.86	0.53	1.35	0.60	0.24	1.31	1.75	0.33		0.03	0.25	2.07
84	20.5	93.52	0.09	1.94	41.36	1.20	0.06	1.05	0.52	0.23	0.67	0.71	0.39			0.16	0.73
301	20.5	80.76	0.07		32.36	0.75	0.04	0.52	0.24	0.06	0.43	0.85	0.20			0.19	0.58
221	20.5	109.07	0.09	2.25	43.44	1.18	0.11	0.68	0.91	0.20	0.43	0.63	0.20		0.04	0.17	0.87
389	20.5	32.82	0.07	1.19	35.07	0.38	0.04	0.56	0.86	0.19	0.20	0.29	0.14		0.04	0.09	0.41
4	20.5	297.36	0.83			2.95	0.55	0.76	0.58	0.99	0.95	0.64			0.04	0.25	1.94
130	20.6	187.18	0.08	1.83	40.63	0.79	0.05	1.45	3.69	0.47	0.77	0.68	0.49	0.03	0.04	0.21	0.40
15	20.6	225.28	0.08	1.37	36.89	1.61	0.25	0.69	3.25	0.50	0.97	0.59	0.33			0.14	0.67
360	20.6	334.73	0.10	3.00	48.03	2.50	0.22	0.96	3.95	0.80	1.41	0.55	0.64	0.03	0.03	0.32	1.09
303	20.6	114.65	0.07	1.01	33.48	1.30	0.08	0.60	0.77	0.35	1.10	0.64	0.24			0.11	0.41
144	20.6	87.41	0.08	1.37	37.10	1.36	0.22	0.12	0.17	0.12	0.34	0.22	0.10	0.80		0.11	0.77
256	20.6	85.87	0.07	1.00	33.37	0.92	0.05	0.60	0.78	0.18	0.48	0.67	0.37			0.09	0.46
31	20.6	545.09	0.12	5.72	59.68	3.38	0.28	2.07	4.36	1.05	1.49	1.37	1.47	0.04	0.06	0.51	2.10
287	20.7	23.81	0.07		31.53	0.29	0.03	0.30	0.10	0.03	0.16	0.49	0.12			0.03	0.27
290	20.7	85.44	0.07	1.26	36.12	1.25	0.04	0.21	0.12	0.10	0.24	0.42	0.27			0.06	0.75
316	20.7	99.15	0.07	1.04	33.85	1.12	0.08	0.27	0.76	0.37	0.51	0.60	0.17			0.14	0.67
194	20.7	128.26	0.08	1.34	36.86	1.89	0.15	0.26	0.25	0.09	0.46	0.63	0.22		0.03	0.17	1.05
52	20.7	265.72	0.09	2.28	44.02	2.62	0.45	0.33	0.31	0.08	0.61	0.65	0.12		0.03	0.23	1.91
240	20.7	28.66	0.07	1.25	36.21	0.50	0.03	0.23	0.09	0.03	0.19	0.60	0.22			0.07	0.39
185	20.7	161.42	0.07		32.70	0.87	0.05	3.02	0.65	0.38	0.50	0.93	0.89	0.08		0.08	0.15
30	20.7	55.66	0.09	2.03	42.40	0.11		1.96	0.08	0.07	0.07	1.28	0.66		0.08	0.08	0.37
20	20.7	45.37	0.08	1.42	37.54	0.51	0.03	0.66	0.06	1.13	0.12	0.74	0.34		0.04	0.12	0.64
11	20.7	24.41	0.08	1.34	36.87	0.31		0.95	0.55	0.34	0.19	0.96	0.41			0.07	0.19
151	20.8	53.42	0.08	1.58	39.20	0.75	0.05	0.64	0.33	0.09	0.25	1.14	0.29			0.11	0.64
45	20.8	319.15	0.08	1.31	36.89	2.18	0.22	3.41	1.92	1.15	1.17	1.53	0.44		0.03	0.20	0.59
67	20.8	87.65	0.08	1.37	37.48	0.78	0.05	0.43	0.93	0.19	0.48	0.68	0.29		0.02	0.09	0.50
29	20.8	46.91	0.07		33.44	0.75	0.07	0.32	0.08	0.04	0.19	0.22	0.05			0.08	0.47
377	20.8	90.89	0.06		29.22	1.39	0.10	0.21	0.34	0.08	0.65	0.44	0.16			0.04	0.54
9	20.8	524.12	0.12	4.97	57.54	2.20	0.09	4.37	1.06	0.41	0.75	1.58	4.37	0.04	0.03	0.35	1.47
352	20.9	478.43	0.10	3.46	51.15	2.84	0.12	2.85	2.51	0.93	1.53	3.82	1.32		0.05	0.43	1.92
163	20.9	36.09	0.06		30.37	0.26		0.65	0.16	0.06	0.21	0.76	0.29			0.04	0.17
127	20.9	97.74	0.07	1.08	34.81	1.14	0.08	0.65	0.44	0.05	0.56	0.79	0.15			0.17	0.51
253	20.9	104.18	0.09	2.51	46.14	1.11	0.04	0.97	1.53	0.30	0.40	0.96	0.42		0.03	0.17	0.85
203	20.9	90.50	0.08	1.74	40.91	0.54		0.86	1.71	0.28	0.37	0.10	0.59			0.10	0.29
206	21.0	23.41	0.08	1.41	38.22	0.40		0.36	0.54	0.08	0.18	0.64	0.14			0.10	0.27
153	21.0	79.58	0.07	1.13	35.50	1.11	0.09	0.39	0.51	0.12	0.59	0.44	0.23			0.08	0.56

Nr	v (kms^{-1})	Int$_{main}$	R (µm)	E {nJ)	D (J/m^2)	^{12}C	^{16}O	^{23}Na	^{24}Mg	^{27}Al	^{28}Si	^{39}K	^{40}Ca	^{48}Ti	^{52}Cr	^{56}Fe	^{103}Rh
32	21.0	159.25	0.06		30.03	0.94	0.07	0.79	2.13	0.34	0.52	0.42	0.28	0.08		0.08	0.21
14	21.0	179.83	0.08	1.77	41.20	1.08	0.08	0.93	2.98	0.40	0.77	0.95	0.56	0.03	0.02	0.10	0.57
321	21.0	15.98	0.06		30.76	0.21		0.53	0.96	0.14	0.18	0.43	0.12			0.06	0.11
275	21.0	45.40	0.07	1.19	36.15	0.73	0.06	0.38	0.07		0.13	0.27	0.06			0.08	0.62
196	21.0	113.43	0.09	2.57	46.68	1.43	0.09	0.52	1.52	0.42	0.69	0.87	0.29		0.02	0.11	0.75
91	21.0	918.05	0.12	4.84	57.75	4.36	0.28	4.36	1.68	0.21	3.23	2.82	0.78	0.02	0.05	0.25	2.22
90	21.0	309.19	0.08	1.46	38.71	2.20	0.22	0.49	3.11	0.71	1.30	0.91	0.39	0.02	0.04	0.23	0.62
60	21.0	159.58	0.09	2.63	47.21	1.46	0.21	0.71	0.99	0.25	0.71	1.16	0.41			0.34	1.68
1	21.0	324.53	0.10	2.76	47.96	2.71	0.20	2.28	2.08	0.44	1.38	0.94	0.60	0.03	0.04	0.18	1.54
364	21.0	186.87	0.08	1.34	37.66	2.23	0.25	0.54	0.56	0.17	1.14	0.85	0.20		0.03	0.18	1.31
145	21.0	339.39	0.09	2.58	46.86	2.92	0.19	0.81	3.13	0.54	1.19	0.76	0.69	0.03	0.03	0.18	1.22
388	21.0	36.92	0.07		33.15	0.52	0.03	0.51	0.41	0.11	0.22	0.50	0.31			0.07	0.43
313	21.0	247.35	0.06		31.61	2.93	0.48	0.85	0.41	0.15	0.70	1.12	0.36	0.05		1.07	0.97
19	21.0	595.95	0.11	3.82	53.36	0.18		4.36	0.35	4.36	0.54	4.36	1.14		0.08	0.19	0.10
5	21.0	531.70	0.11	4.59	56.81	0.07		2.96	0.93	4.37		2.24	0.28		0.09	0.26	0.07
13	21.0	156.49	0.07		33.05	1.94	0.34	0.38	0.49	1.10	0.90	0.49	0.16		0.03	0.07	0.99
8	21.0	400.38	0.10	3.45	51.64	2.20	0.23	1.77	4.36	1.16	0.95	1.58	0.86	0.03	0.05	0.29	1.06
114	21.1	75.06	0.07	1.09	35.30	0.79	0.04	0.48	0.45	0.12	0.54	0.62	0.19			0.10	0.55
118	21.1	205.00	0.07	1.12	35.68	1.68	0.08	2.04	0.59	0.05	0.92	1.35	0.33			0.07	0.42
122	21.1	126.95	0.05		25.46	1.28	0.10	0.38	1.41	0.24	0.62	0.41	0.26			0.07	0.34
9	21.1	85.21	0.08	1.57	39.89	1.22	0.18	0.31	0.17	0.07	0.25	0.67	0.12			0.65	0.51
269	21.1	917.33	0.12	5.84	61.88	4.36	0.57	2.02	4.33	1.51	3.08	1.68	1.56	0.05	0.07	0.42	3.41
355	21.1	161.35	0.09	2.39	45.97	1.20	0.05	0.82	1.72	1.17	0.59	0.57	1.03	0.04		0.17	0.59
308	21.1	117.77	0.07		33.54	1.22	0.07	0.66	0.53	0.17	0.70	0.82	0.30			0.11	0.72
41	21.1	102.50	0.07	1.25	37.03	1.48	0.08	0.51	0.36	0.09	0.71	0.79	0.24			0.12	0.74
288	21.1	144.84	0.10	3.27	51.11	1.36	0.07	0.91	2.21	0.49	0.55	1.26	0.87	0.01	0.04	0.20	1.00
26	21.1	153.61	0.07	1.13	35.78	1.05	0.12	1.34	0.94	0.77	1.65	1.09	1.67			0.16	0.60
251	21.2	128.11	0.07	1.27	37.31	1.51	0.13	1.54	0.48	0.65	0.82	0.78	0.20			0.11	0.89
229	21.2	157.88	0.09	2.42	46.37	1.30	0.06	1.13	1.93	0.49	0.65	1.60	0.62		0.03	0.19	1.10
104	21.2	99.90	0.08	1.71	41.33	1.20	0.06	0.66	0.75	0.21	0.57	1.05	0.40			0.06	0.66
7	21.2	152.71	0.09	2.01	43.65	1.92	0.19	0.74	0.42	0.18	0.75	0.75	0.39			0.14	1.27
174	21.2	289.86	0.09	2.20	45.04	2.79	0.37	0.42	2.27	0.45	1.11	0.86	0.32			0.17	1.67
49	21.2	137.09	0.08	1.56	40.18	1.70	0.08	0.96	1.53	0.47	0.71	1.27	0.73	0.03	0.03	0.19	0.49
159	21.2	84.21	0.06		31.89	1.34	0.08	0.20	0.20	0.12	0.35	0.25	0.20			0.04	0.63
258	21.2	155.26	0.12	5.11	59.71	1.64	0.13	0.46	1.06	0.18	1.19	1.13	0.20	0.03	0.04	0.56	1.33
249	21.2	504.32	0.09	2.56	47.41	2.61	0.21	1.45	4.36	0.93	1.64	0.80	0.75	0.02	0.05	0.23	0.63
27	21.2	363.38	0.10	3.05	50.18	0.69	0.04	3.55	0.98	4.36	0.33	1.80	0.19		0.07	0.15	0.66
8	21.2	306.06	0.08	1.54	39.89	2.69	0.20	0.63	1.18	1.40	1.69	0.91	0.27	0.03	0.03	0.12	0.84
317	21.3	70.27	0.07	1.18	36.74	0.71	0.05	0.26	0.17	0.06	0.26	0.46	0.20			0.05	0.56
366	21.3	195.91	0.08	1.71	41.70	1.84	0.13	1.28	2.10	3.50	0.97	0.86	0.32			0.11	0.85
195	21.3	128.28	0.08	1.46	39.52	0.89	0.10	1.10	1.55	0.25	0.42	1.75	0.50		0.03	0.09	0.61
1	21.3	26.28	0.07	1.22	37.08	0.03		1.41	0.05	1.41		0.80	0.08		0.04	0.16	0.07
328	21.4	44.95	0.07	1.23	37.43	0.49	0.04	0.31	0.08	0.23	0.18	0.49	0.27	0.03		0.05	0.61
58	21.4	41.98	0.07		33.69	0.52	0.04	0.36	0.25	0.17	0.27	0.47	0.24			0.06	0.27
106	21.4	120.68	0.07	1.09	35.96	1.49	0.11	0.84	1.18	0.19	0.53	0.39	0.08			0.10	0.63
86	21.4	42.68	0.07	1.11	36.19	0.26	0.02	0.67	0.39	0.26	0.21	0.44	0.16			0.07	0.23
387	21.4	111.58	0.08	1.73	41.96	1.36	0.09	0.56	0.58	0.11	0.72	0.63	0.35			0.10	0.89
121	21.4	49.92	0.08	1.72	41.90	0.41	0.05	1.22	0.17	0.31	0.36	1.61	0.14			0.06	0.79
77	21.4	188.60	0.08	1.47	39.89	2.64	0.30	0.93	0.34	0.17	0.81	0.74	0.33			0.12	1.16

Nr	v (kms^{-1})	Int$_{main}$	R (µm)	E {nJ}	D (J/m^2)	^{12}C	^{16}O	^{23}Na	^{24}Mg	^{27}Al	^{28}Si	^{39}K	^{40}Ca	^{48}Ti	^{52}Cr	^{56}Fe	^{103}Rh
143	21.4	492.36	0.10	3.70	54.26	3.32	0.26	1.47	4.36	0.86	1.46	1.58	0.80	0.05		0.32	0.83
18	21.4	28.12	0.07	1.04	35.55	0.51	0.04	0.23	0.10	0.05	0.23	0.40	0.10			0.07	0.46
146	21.4	69.93	0.07	1.25	37.85	0.88	0.06	0.42	0.28	0.08	0.26	0.70	0.27			0.06	0.76
166	21.5	80.68	0.06		32.91	0.93	0.12	0.47	0.10	0.06	0.16	0.74	0.18			0.13	0.34
55	21.5	74.76	0.08	1.82	42.99	0.94	0.08	0.32	0.37	0.10	0.32	0.64	0.10			0.09	0.74
109	21.5	114.26	0.08	1.41	39.55	0.85	0.07	1.89	1.53	0.39	0.45	0.32	0.34			0.09	0.33
20	21.5	738.88	0.09	2.50	47.70	3.21	0.60	3.73	1.92	0.79	1.75	0.50	4.36	0.06	0.04	0.58	0.82
7	21.5	373.99	0.08	1.40	39.34	3.67	0.61	0.56	0.97	0.41	1.88	0.74	0.42		0.02	0.21	1.59
304	21.6	131.90	0.09	2.47	47.78	1.62	0.12	1.53	0.49	0.78	1.04	1.22	0.45			0.13	0.26
373	21.6	220.68	0.10	3.05	51.28	2.15	0.22	0.80	2.47	0.47	1.11	1.13	0.40	0.03		0.28	1.49
83	21.6	209.85	0.10	2.87	50.38	2.15	0.17	1.73	1.13	0.99	1.41	0.79	0.22		0.06	0.32	1.29
179	21.6	158.41	0.10	2.94	50.84	1.17	0.17	1.11	2.41	0.56	0.61	1.30	0.55			0.21	1.16
62	21.6	245.42	0.09	2.33	47.05	1.53	0.12	1.40	2.34	0.77	1.10	1.43	0.63	0.03		0.19	0.61
274	21.6	87.49	0.08	1.62	41.72	1.11	0.10	0.33	0.13	0.08	0.19	0.52	0.17			0.15	1.19
11	21.6	76.64	0.00	0.00	0.00	1.12	0.06	0.70	0.27	0.13	0.26	0.67	0.27			0.06	0.57
230	21.6	387.57	0.10	3.20	52.35	2.44	0.18	2.12	3.08	0.83	1.45	1.76	0.51	0.04	0.04	0.33	1.22
70	21.6	157.36	0.11	4.32	57.90	1.66	0.13	0.97	2.14	0.34	0.57	1.42	0.48	0.03	0.02	0.10	1.37
12	21.6	170.01	0.07		34.51	0.44		3.71	0.60	1.51	0.23	1.36	0.17		0.05	0.05	0.13
15	21.6	588.92	0.09	2.40	47.61	2.93	0.20	4.00	1.19	0.12	2.75	1.96	0.43		0.04	0.15	1.22
218	21.7	88.10	0.07	1.09	36.59	0.61	0.05	0.26	0.62	0.33	0.40	0.42	0.64	0.07	0.04	0.14	0.45
232	21.7	80.46	0.07	1.28	38.70	0.91	0.07	0.21	0.22	0.06	0.36	0.44	0.11			0.05	0.45
260	21.7	224.76	0.09	2.18	46.35	2.00	0.11	1.21	2.63	0.61	0.86	0.92	1.13	0.02	0.03	0.19	0.71
157	21.8	388.69	0.10	3.37	53.65	3.29	0.26	0.87	2.25	0.51	1.10	1.10	0.72		0.05	0.23	2.32
85	21.8	85.88	0.07		35.17	1.25	0.08	0.66	0.34	0.13	0.56	0.48	0.22		0.05	0.13	0.55
267	21.8	195.68	0.10	3.38	53.72	2.19	0.19	0.97	1.09	0.26	0.85	0.51	0.36		0.02	0.25	1.59
209	21.8	316.53	0.07	1.09	36.89	1.82	0.15	0.58	3.47	0.44	1.07	0.05	0.38	0.02		0.12	0.25
75	21.8	23.12	0.07	1.32	39.30	0.27	0.02	0.42	0.07	0.06	0.13	0.42	0.19			0.07	0.43
33	21.8	140.99	0.08	1.47	40.75	3.63	0.08	0.44	0.26	0.37	1.20	0.35	0.61	0.03	0.07	0.81	0.51
152	21.8	25.83	0.08	1.54	41.47	0.26		0.56	0.16	0.08	0.17	0.88	0.36			0.07	0.47
359	21.8	217.77	0.09	2.54	48.96	1.85	0.17	0.86	2.28	0.53	0.89	1.03	0.90	0.03	0.04	0.16	1.25
154	21.8	161.48	0.08	1.78	43.58	2.05	0.16	0.37	0.47	0.17	1.11	0.44	0.18			0.10	1.34
278	21.8	87.43	0.07	1.08	36.86	1.31	0.15	0.25	0.22	0.05	0.53	0.56	0.21			0.13	0.72
141	21.8	77.42	0.07	1.35	39.71	0.90	0.07	0.36	0.76	0.90	0.51	0.42	0.21			0.06	0.66
22	21.8	167.37	0.07	1.26	38.73	0.40		1.00	0.36	0.13	0.16	3.13	1.64			0.04	0.17
3	21.8	218.87	0.08	1.73	43.08	1.70	0.08	2.10	0.68	0.32	1.21	1.17	1.31	0.03	0.03	0.11	0.92
16	21.8	79.48	0.08	1.80	43.65	1.00	0.07	0.82	0.16	0.09	0.23	1.20	0.66			0.07	1.01
13	21.8	1048.27	0.12	5.43	62.91	1.71	0.22	4.35	0.60	4.36	1.96	4.36	1.35	0.10	0.03	0.28	0.55
124	21.9	69.68	0.06		33.97	0.97	0.05	0.16	0.57	0.12	0.35	0.33	0.26		0.02	0.05	0.62
385	21.9	170.48	0.09	2.21	46.97	2.48	0.30	0.44	0.42	0.11	0.51	0.74	0.23			0.12	1.40
375	21.9	216.66	0.09	2.67	50.06	1.86	0.13	0.72	1.92	0.69	0.79	2.22	0.55		0.02	0.27	1.42
51	21.9	440.49	0.11	4.35	58.94	2.84	0.32	2.65	2.35	0.40	1.09	1.18	0.69	0.03	0.03	0.31	2.34
37	21.9	306.61	0.08	2.01	45.64	2.36	0.20	0.75	2.10	0.71	1.64	1.00	0.54	0.04	0.03	0.24	1.03
9	21.9	448.82	0.10	3.27	53.33	4.36	0.27	2.56	0.95	0.09	2.57	1.13	0.33			0.09	1.35
380	22.0	292.01	0.09	2.12	46.60	2.71	0.35	1.37	2.05	0.43	1.20	0.66	1.13	0.03		0.17	1.34
282	22.0	456.66	0.10	3.17	53.35	2.92	0.30	3.02	2.67	0.43	1.35	0.39	0.53	0.03	0.03	0.22	2.26
184	22.0	192.74	0.08	2.06	46.20	1.44	0.08	2.08	2.15	0.43	0.73	0.74	0.56	0.03	0.03	0.14	0.55
125	22.0	83.26	0.07	1.32	39.83	0.93	0.07	1.17	0.44	0.13	0.40	0.63	0.28			0.05	0.64
132	22.0	104.57	0.07	1.05	37.02	0.97	0.07	1.15	1.34	0.22	0.56	0.93	0.32			0.08	0.37
32	22.0	1119.08	0.12	6.67	68.34	4.36	0.50	4.36	3.40	0.95	2.45	1.65	4.36	0.09	0.07	0.76	2.26

Nr	v (kms^{-1})	Int$_{main}$	R (µm)	E {nJ)	D (J/m^2)	^{12}C	^{16}O	^{23}Na	^{24}Mg	^{27}Al	^{28}Si	^{39}K	^{40}Ca	^{48}Ti	^{52}Cr	^{56}Fe	^{103}Rh
300	22.1	86.89	0.06		34.03	1.06	0.08	1.35	0.67	0.30	0.34	0.31	0.61			0.09	0.47
134	22.1	319.46	0.09	2.68	50.66	1.68	0.29	3.51	3.36	0.62	0.77	0.11	0.60	0.02	0.02	0.19	1.01
189	22.1	273.37	0.09	2.18	47.31	2.18	0.31	0.62	2.58	0.60	1.02	1.03	0.29	0.03	0.04	0.77	1.35
337	22.1	897.04	0.11	4.02	57.99	4.36	0.56	2.13	4.36	1.77	2.40	1.84	1.33	0.04	0.06	0.56	1.96
324	22.1	140.62	0.07	1.34	40.32	1.73	0.13	0.47	0.45	0.13	0.52	0.58	0.18			0.11	1.04
294	22.1	216.20	0.07	1.46	41.49	2.31	0.28	1.26	1.58	0.44	1.20	0.22	0.33		0.03	0.23	1.32
270	22.1	397.11	0.09	2.22	47.80	2.57	0.27	1.89	1.00	0.27	0.71	4.36	1.12		0.04	0.62	0.96
212	22.1	231.00	0.10	3.46	55.37	1.41	0.07	1.91	3.23	0.54	0.68	1.65	0.72	0.04	0.04	0.28	1.08
10	22.1	402.31	0.09	2.21	47.67	3.29	0.47	0.44	1.17	0.17	1.81	0.55	0.20		0.04	0.31	2.02
1	22.1	197.61	0.06		32.35	2.01	0.40	0.43	0.38	0.86	0.77	0.34	0.34	0.20	0.02	0.13	1.19
171	22.2	279.21	0.10	3.47	55.70	1.94	0.10	1.19	2.16	0.35	0.66	1.11	0.57		0.03	0.13	1.84
243	22.2	252.10	0.09	2.46	49.66	1.82	0.09	0.75	2.18	0.37	0.79	1.85	0.47			0.12	1.20
19	22.2	110.04	0.06		33.47	1.07	0.07	0.50	1.14	0.18	0.49	0.30	0.18			0.09	0.22
266	22.2	364.39	0.09	2.40	49.22	3.26	0.26	0.55	2.57	0.71	1.55	0.74	0.45	0.02	0.03	0.26	1.49
386	22.2	434.91	0.10	3.34	55.08	3.43	0.33	1.21	3.34	0.57	1.08	1.38	0.67	0.03	0.03	0.26	1.82
133	22.2	315.37	0.12	6.16	67.52	3.38	0.34	0.54	2.05	0.31	1.53	0.49	0.25		0.03	0.09	1.07
3	22.2	88.72	0.06		33.69	1.29	0.18	0.40	0.17	0.32	0.34	0.18	0.08			0.05	0.65
88	22.2	333.93	0.08	2.09	47.15	3.34	0.39	1.31	1.70	0.41	1.70	0.72	0.40		0.04	0.28	1.49
9	22.2	403.74	0.10	3.01	53.05	2.50	0.24	2.50	4.36	1.36	0.98	0.89	0.86	0.03	0.04	0.24	1.01
31	22.3	100.36	0.06		34.51	1.29	0.15	0.43	0.29	0.12	0.55	0.40	0.10			0.11	0.64
216	22.3	209.94	0.09	2.25	48.37	2.55	0.48	0.44	1.67	0.34	0.67	0.63	0.23		0.03	0.21	1.47
22	22.3	188.66	0.07	1.42	41.55	1.66	0.05	0.64	1.67	0.34	0.79	0.52	0.22			0.16	0.68
50	22.3	37.76	0.05		29.90	0.29	0.02	0.45	0.19	0.17	0.23	0.82	0.23	0.02		0.07	0.27
378	22.3	168.88	0.08	1.75	44.68	1.77	0.11	1.09	0.73	0.08	1.36	0.50	0.23		0.07	0.15	1.16
217	22.3	264.03	0.10	3.05	53.74	1.83	0.17	1.91	2.97	0.55	0.84	0.92	0.47	0.03	0.04	0.36	1.21
233	22.3	201.73	0.08	1.52	42.58	2.54	0.31	1.02	0.87	0.22	1.04	0.59	0.21		0.03	0.17	1.43
394	22.3	217.05	0.07	1.40	41.48	1.65	0.18	1.23	2.45	0.54	1.03	0.46	0.24		0.04	0.20	0.76
23	22.3	88.68	0.09	2.57	50.54	0.13		1.54	0.08	2.20	0.20	1.00	0.36		0.03	0.03	0.31
284	22.4	80.01	0.06		33.39	0.95	0.05	0.41	0.73	0.15	0.33	0.53	0.35			0.09	0.24
310	22.4	139.76	0.09	2.86	52.69	1.15	0.08	2.48	0.14	0.39	0.53	0.52	0.58	0.04	0.04	0.23	0.84
365	22.4	95.88	0.06		36.16	1.06	0.05	0.63	0.36	0.08	0.48	0.44	0.34			0.08	0.36
289	22.4	43.88	0.08	1.61	43.59	0.56		0.41	0.19	0.02	0.26	0.52	0.22			0.05	1.03
223	22.4	87.20	0.06		35.79	1.06	0.15	0.95	0.45	0.48	0.33	0.78	0.18		0.11	0.10	0.52
80	22.5	277.80	0.07	1.49	42.57	1.83	0.10	1.08	3.72	0.72	1.16	0.46	0.42	0.03		0.25	0.49
227	22.5	371.21	0.09	2.47	50.54	3.15	0.32	1.26	2.52	0.53	1.21	0.64	0.42	0.03	0.04	0.26	2.00
293	22.5	331.73	0.08	1.60	43.70	3.22	0.40	0.51	2.74	0.60	1.39	0.58	0.46		0.04	0.19	1.17
338	22.5	48.97	0.07	1.10	38.55	0.76	0.04	0.24	0.14	0.06	0.19	0.42	0.20			0.06	0.63
291	22.5	77.71	0.06		34.87	0.98	0.09	0.42	0.29	0.08	0.26	0.59	0.23		0.03	0.21	0.65
322	22.5	176.51	0.07	1.25	40.35	2.11	0.37	0.70	0.64	0.11	0.55	0.96	0.21			0.09	1.35
108	22.5	163.86	0.07	1.22	40.05	2.26	0.23	0.68	0.43	0.11	0.75	0.50	0.24		0.03	0.15	1.36
147	22.5	314.02	0.08	2.17	48.50	2.93	0.27	0.45	0.55	0.28	0.74	2.75	1.11		0.04	0.18	1.62
12	22.5	370.74	0.09	2.62	51.54	1.78	0.21	4.36	0.94	0.65	0.79	0.94	2.30	0.06	0.04	0.20	0.89
28	22.5	43.39	0.08	1.71	44.63	0.20		0.36	0.08	1.60	0.14	0.44	0.37		0.04	0.09	0.09
43	22.6	353.33	0.07	1.41	42.14	2.52	0.28	0.47	4.11	0.53	1.17	0.33	0.46	0.03		0.14	0.42
117	22.6	572.84	0.09	2.53	51.25	4.02	0.64	0.91	4.36	0.76	2.28	0.96	0.60	0.03	0.05	0.28	1.65
4	22.6	397.74	0.09	2.80	52.95	3.17	0.44	0.64	3.57	0.58	1.40	0.93	0.41		0.03	0.26	1.42
13	22.6	106.28	0.09	2.41	50.37	1.50	0.11	0.43	0.74	0.10	0.86	0.74	0.22			0.07	1.01
8	22.6	509.47	0.09	2.54	51.29	2.59	0.21	2.33	1.38	0.47	1.43	0.77	4.36	0.03	0.06	0.38	0.59
5	22.6	392.37	0.12	6.44	70.05	1.82	0.19	3.33	2.03	1.20	0.99	3.87	0.60		0.04	0.13	1.63

Nr	v (kms^{-1})	Int$_{main}$	R (µm)	E {nJ}	D (J/m^2)	^{12}C	^{16}O	^{23}Na	^{24}Mg	^{27}Al	^{28}Si	^{39}K	^{40}Ca	^{48}Ti	^{52}Cr	^{56}Fe	^{103}Rh
255	22.7	751.46	0.10	3.21	55.67	4.00	0.28	3.36	1.64	0.15	3.17	2.31	0.51		0.04	0.40	2.08
354	22.7	78.06	0.07	1.15	39.56	0.63	0.04	1.09	1.19	0.28	0.27	0.81	0.33		0.03	0.18	0.29
390	22.7	122.92	0.07	1.28	40.96	1.36	0.08	1.94	0.25	0.08	0.42	0.44	0.16			0.12	1.05
231	22.7	241.60	0.07	1.24	40.54	1.80	0.14	0.77	3.10	0.56	1.01	0.60	0.40		0.04	0.24	0.40
357	22.7	791.28	0.10	5.28	65.86	4.36	0.60	1.88	4.36	1.25	1.87	1.80	0.99	0.04	0.06	0.38	2.69
97	22.7	128.88	0.07	1.39	42.17	1.20	0.06	0.29	0.66	0.20	0.94	0.50	0.29			0.08	0.82
69	22.7	237.70	0.07	1.30	41.31	2.47	0.53	0.28	1.87	0.54	0.96	0.67	0.35			0.14	1.13
370	22.7	249.07	0.10	3.42	57.12	1.98	0.18	1.20	2.71	0.42	0.59	1.11	0.62		0.03	0.36	1.59
2	22.7	82.73	0.06		34.82	0.74	0.02	0.98	0.27	0.10	0.26	0.59	1.23			0.09	0.53
14	22.7	292.57	0.07	1.46	42.89	3.20	0.25	1.10	0.70	0.11	1.63	0.88	0.28			0.06	1.06
369	22.8	37.56	0.07	1.08	39.02	0.49	0.04	0.35	0.18	0.09	0.38	0.71	0.12	0.03		0.03	0.62
111	22.8	280.77	0.08	1.64	44.79	3.23	0.44	0.63	1.62	0.32	1.41	0.61	0.39	0.02		0.17	1.43
38	22.8	177.76	0.07	1.18	40.17	1.59	0.26	1.35	2.14	0.26	0.66	0.35	0.33		0.04	0.20	0.85
95	22.8	46.16	0.06		34.99	0.65	0.04	0.37	0.59	0.15	0.29	0.77	0.18			0.07	0.44
10	22.8	447.64	0.07	1.30	41.62	2.57	0.38	1.16	4.36	0.60	1.54	0.70	0.43	0.03	0.03	0.19	0.38
82	22.8	229.54	0.09	2.55	52.09	2.36	0.22	0.51	0.47	0.35	0.81	1.04	0.24			0.13	1.63
309	22.8	138.74	0.08	1.68	45.37	1.12	0.08	0.52	2.15	0.39	0.45	0.68	0.48		0.03	0.12	0.67
14	22.8	251.06	0.09	2.46	51.35	0.11		2.42	0.07	4.36		1.53	0.12		0.08	0.14	0.11
21	22.9	48.68	0.06		36.09	0.37	0.05	0.31	0.58	0.08	0.19	0.59	0.18	0.03		0.07	0.40
306	22.9	200.93	0.07	1.06	39.19	1.86	0.16	0.70	1.13	0.65	1.43	0.53	0.21			0.09	0.44
89	22.9	571.17	0.10	4.02	61.03	4.35	0.68	1.77	1.17	0.26	0.95	1.60	0.38		0.05	0.49	3.60
17	22.9	75.83	0.07	1.36	42.34	0.51	0.03	1.07	0.25	0.11	0.05	0.62	1.14			0.11	0.81
25	23.0	199.08	0.07	1.12	39.95	1.88	0.09	0.43	1.40	0.43	0.95	0.33	0.28	0.04		0.07	0.76
265	23.0	119.35	0.07	1.14	40.20	1.88	0.24	0.23	0.20	0.08	0.39	0.33	0.08			0.10	1.01
214	23.0	215.82	0.11	4.95	65.61	0.89	0.03	4.31	1.60	0.90	0.47	1.13	0.73		0.05	0.39	0.99
259	23.0	110.53	0.06		37.22	1.72	0.18	0.16	0.20	0.08	0.45	0.27	0.10			0.05	0.63
4	23.0	1133.77	0.12	5.92	69.65	4.31	0.55	2.10	4.36	1.68	3.00	1.93	2.50	0.06	0.07	1.00	1.81
3	23.0	424.57	0.09	2.71	53.84	2.56	0.16	3.39	0.94	0.26	1.89	1.69	0.39			0.08	1.29
200	23.1	62.99	0.06		34.43	0.85	0.10	0.20	0.07	0.03	0.10	0.30	0.06			0.08	0.57
323	23.1	104.52	0.06		35.73	1.33	0.15	0.50	0.48	0.24	0.60	0.46	0.28			0.09	0.61
5	23.1	70.45	0.07	1.12	40.39	1.00	0.07	0.27	0.24	0.06	0.43	0.61	0.15			0.08	0.79
299	23.1	195.96	0.06		37.78	2.32	0.28	0.49	1.51	0.43	1.28	0.54	0.37		0.03	0.32	1.03
307	23.2	65.47	0.08	1.96	48.64	0.69	0.04	1.52	1.03	0.22	0.49	0.49	0.26			0.12	0.69
53	23.2	64.83	0.06		36.71	0.77	0.04	0.22	0.13	0.04	0.24	0.63	0.10			0.12	0.41
24	23.2	292.40	0.08	1.68	46.39	1.68	0.64	0.90	3.76	0.54	0.93	0.86	0.43			0.15	0.75
347	23.2	1202.62	0.12	5.92	70.70	4.37	0.27	3.72	4.37	2.54	4.37	1.58	2.94	0.09	0.08	0.67	2.54
181	23.2	190.15	0.06		37.32	2.14	0.19	0.34	1.21	0.22	1.04	0.40	0.24			0.11	0.67
6	23.2	415.06	0.09	3.00	56.07	1.05	0.09	2.34	1.22	4.34	0.45	2.05	0.28		0.09	0.24	0.55
18	23.2	143.30	0.04		26.64	1.75	0.06	0.83	0.07	1.64	0.32	0.53	0.35			0.19	0.98
295	23.3	158.94	0.07	1.17	41.23	1.93	0.19	0.29	0.43	0.08	0.78	0.34	0.16		0.03	0.25	1.12
56	23.3	483.22	1.46			3.85	0.41	0.61	2.18	0.50	1.69	0.75	0.30	0.03	0.03	0.11	1.95
76	23.3	110.42	0.08	0.70	46.87	1.49	0.11	0.26	0.50	0.21	0.77	0.43	0.39			0.09	0.95
363	23.3	39.64	0.07	1.34	43.30	0.47	0.05	0.57	0.24	0.08	0.28	0.65	0.10			0.09	0.36
25	23.3	189.35	0.08	2.26	51.54	0.07		1.13	0.17	4.36		1.10	0.36		0.05	0.05	0.15
17	23.3	246.06	0.06		39.21	0.32		1.79	0.21	4.31	0.29	0.63	0.17		0.03	0.08	0.18
277	23.4	379.12	0.10	4.13	63.17	3.04	0.29	1.71	4.25	0.88	1.42	1.35	0.69	0.03	0.04	0.48	1.05
384	23.4	280.62	0.09	2.67	54.59	2.26	0.20	0.79	3.28	0.69	1.05	0.51	0.59		0.04	0.47	1.27
372	23.5	65.92	0.07	1.10	40.86	0.91	0.08	0.46	0.20	0.08	0.22	0.69	0.18			0.13	0.65
6	23.5	299.14	0.07	1.55	45.80	2.90	0.29	1.63	1.54	0.57	0.87	0.94	0.85	0.47	0.03	0.13	1.54

Nr	v (kms^{-1})	Int$_{main}$	R (µm)	E {nJ)	D (J/m^2)	^{12}C	^{16}O	^{23}Na	^{24}Mg	^{27}Al	^{28}Si	^{39}K	^{40}Ca	^{48}Ti	^{52}Cr	^{56}Fe	^{103}Rh
6	23.5	74.17	0.06		36.76	0.86	0.06	0.59	0.13	0.70	0.21	0.84	0.42		0.02	0.04	0.45
12	23.5	81.68	0.06	1.02	39.95	0.94	0.05	0.32	0.91	0.15	0.38	0.55	0.18			0.09	0.40
7	23.5	117.97	0.06	1.01	39.91	1.52	0.30	0.31	0.22	1.35	0.36	0.62	0.31			0.09	1.07
391	23.6	241.34	0.06		38.67	1.97	0.29	0.60	2.10	0.34	0.98	0.84	0.26			0.20	0.48
156	23.6	88.89	0.06	1.00	39.98	0.85	0.07	0.63	1.42	0.22	0.33	0.41	0.23	0.03		0.10	0.27
345	23.6	87.90	0.07	1.23	42.80	0.12	0.09	0.47	0.83	0.21	0.37	0.43	0.24		0.03	0.24	0.67
395	23.6	71.43	0.07	1.33	43.94	0.93	0.10	0.32	0.14	0.05	0.19	0.51	0.10			0.09	1.14
13	23.6	32.01	0.06		37.45	0.14		0.71	0.22	0.20	0.04	0.70	0.85			0.05	0.27
11	23.6	15.70	0.06		38.02	0.25		1.04	0.17	0.14	0.13	0.59	0.54			0.17	0.57
26	23.7	111.21	0.07	1.16	42.08	1.58	0.20	0.23	0.80	0.15	0.46	0.57	0.19			0.09	0.80
115	23.7	602.41	0.09	3.32	59.93	2.91	0.30	3.63	4.36	0.98	1.73	0.30	0.05	0.04	0.05	0.35	1.33
2	23.7	105.35	0.06		38.27	1.31	0.43	0.36	0.34	1.06	0.18	0.98	0.22		0.02	0.10	0.81
66	23.8	267.17	0.07	1.56	46.75	1.94	0.30	0.46	2.98	0.45	1.34	0.71	0.36		0.03	0.18	0.94
23	23.8	50.99	0.07	1.12	41.83	0.71	0.03	0.58	0.79	0.20	0.36	0.51	0.51			0.08	0.58
191	23.8	37.87	0.06		37.42	0.42	0.03	0.15	0.10	0.03	0.13	0.29	0.06			0.05	0.31
327	23.8	103.99	0.06		40.24	0.95	0.05	0.28	0.85	0.24	0.38	0.51	0.28			0.05	0.36
105	23.9	139.14	0.07	1.26	43.77	1.54	0.19	0.27	1.33	0.28	0.94	0.32	0.21			0.12	1.07
224	23.9	115.99	0.06		40.60	1.53	0.10	0.38	0.73	0.21	0.50	0.51	0.23		0.04	0.09	0.91
190	24.0	359.05	0.06		39.96	3.76	0.70	0.65	0.43	0.17	1.22	0.61	0.31			0.29	1.61
220	24.0	332.28	0.08	2.13	52.44	2.31	0.12	0.89	3.77	0.70	1.55	0.59	0.48	0.03	0.03	0.19	0.99
39	24.0	424.89	0.07	1.24	43.88	2.70	0.68	0.57	4.30	0.63	1.53	0.73	0.58	0.03	0.04	0.43	0.95
239	24.0	100.60	0.06		40.53	1.33	0.11	0.33	0.78	0.13	0.64	0.28	0.14			0.07	0.91
254	24.0	156.24	0.06		37.66	2.07	0.25	0.26	0.16	0.06	0.30	0.91	0.12			0.11	1.01
349	24.0	198.60	0.08	2.52	55.62	1.82	0.08	0.62	1.69	0.33	0.57	0.65	0.50		0.03	0.14	1.55
226	24.0	185.73	0.06	1.09	42.02	1.88	0.22	0.75	1.12	0.28	0.72	0.89	0.27			0.12	0.82
237	24.0	894.48	0.09	2.67	56.67	4.00	0.33	2.44	1.99	0.91	3.63	0.30	0.42		0.06	0.35	2.44
5	24.0	762.30	0.09	2.91	58.33	4.31	0.43	3.90	0.96	0.17	2.79	1.94	0.76		0.04	0.13	2.27
36	24.1	104.91	0.06	1.06	41.78	1.56	0.18	0.30	0.09	0.08	0.25	0.70	0.15	0.05		0.08	1.03
99	24.1	223.28	0.06		40.09	2.66	0.36	0.37	0.28	0.07	0.55	0.61	0.21			0.14	1.09
318	24.1	112.51	0.07	1.43	46.30	0.87	0.08	0.49	1.84	0.35	0.47	0.60	0.42			0.09	0.65
225	24.1	275.15	0.07	1.20	43.67	1.69	0.19	0.63	3.61	0.60	1.09	0.81	0.42			0.18	0.45
320	24.2	68.26	0.06		40.39	0.93	0.08	0.27	0.18	0.04	0.40	2.80	0.07			0.10	0.54
54	24.2	390.22	0.07	1.31	45.13	2.34	0.30	0.79	4.20	0.68	1.20	0.82	0.46	0.08	0.03	0.19	0.43
148	24.2	136.02				1.63	0.16	0.26	0.82	0.12	0.58	0.41	0.11			0.07	0.47
186	24.2	73.21	0.06		36.80	0.55	0.06	0.78	1.60	0.12	0.02	0.61	0.28			0.07	0.30
6	24.3	408.54	0.08	2.58	56.82	3.46	0.39	0.52	1.79	0.71	1.52	1.18	0.35	0.03	0.03	0.18	1.77
182	24.3	267.74	0.08	2.25	54.30	2.49	0.22	0.44	1.56	0.36	0.97	0.68	1.06	0.03	0.03	0.33	1.65
103	24.3	628.53	0.09	2.65	57.32	3.86	0.43	1.25	4.36	1.27	2.06	1.75	0.97	0.05	0.05	0.51	1.73
305	24.3	90.00	0.06		40.45	1.19	0.18	0.70	0.22	0.11	0.82	0.31	0.18			0.10	0.78
11	24.3	415.42	0.06	1.02	41.63	2.59	0.08	0.52	0.62	0.76	2.64	0.93	0.28	0.03	0.04	0.09	1.76
236	24.4	181.78	0.06	1.09	42.83	1.62	0.15	0.34	1.66	0.24	0.75	0.49	0.24			0.09	0.61
252	24.4	170.82	0.06		37.58	2.54	0.21	0.27	0.09	0.06	0.21	0.39	0.17			0.13	0.92
245	24.4	164.57	0.06		41.26	2.30	0.29	0.30	2.90	0.08	0.59	0.34	0.63			0.09	0.99
10	24.4	543.93	0.09	3.27	61.92	4.02	0.48	0.97	2.21	0.47	1.81	1.06	1.92	0.03	0.04	0.30	2.70
13	24.4	286.93	0.08	1.97	52.37	3.04	0.25	0.77	0.85	1.09	2.15	1.45	0.32			0.21	1.22
315	24.5	49.60	0.06		39.58	0.82	0.14	0.39	2.10	0.06	0.13	0.38	0.09		0.04	0.40	0.49
123	24.5	87.35	0.06		40.96	1.56	0.08	0.44	1.10	0.11	0.18	1.32	0.22		0.03	0.09	1.04
128	24.5	475.41	0.09	2.72	58.61	3.47	0.50	0.88	2.48	0.50	1.52	0.57	0.41		0.05	0.29	1.83
296	24.6	257.22	0.06	1.07	43.05	2.62	0.05	0.72	1.93	0.37	0.84	0.50	0.26			0.13	0.77

Nr	v (kms^{-1})	Int$_{main}$	R (µm)	E {nJ}	D (J/m^2)	^{12}C	^{16}O	^{23}Na	^{24}Mg	^{27}Al	^{28}Si	^{39}K	^{40}Ca	^{48}Ti	^{52}Cr	^{56}Fe	^{103}Rh
183	24.6	112.52	0.06		39.68	1.74	0.11	0.43	2.80	0.10	0.67	0.38	0.13			0.07	1.10
331	24.6	64.15	0.06		41.12	0.61	0.08	0.91	2.30	0.42	0.37	1.20	0.24			0.06	0.55
14	24.6	163.24	0.06		41.76	1.78	0.36	0.52	0.26	0.42	0.31	1.13	1.54		0.02	0.31	0.82
12	24.6	294.28	0.07	1.55	48.77	3.04	0.51	1.07	0.87	0.58	1.60	0.81	0.24			0.41	1.62
2	24.6	372.05	0.09	3.56	64.36	2.67	0.09	1.14	0.09	0.07	1.77	2.42	0.14		0.03	0.09	0.62
329	24.7	168.81	0.06	1.09	43.48	1.99	0.23	0.62	1.60	0.23	0.49	0.55	0.38			0.14	0.63
358	24.7	956.19	0.10	3.84	66.23	4.04	0.59	1.04	4.36	1.96	3.19	0.55	1.09	0.07	0.07	0.82	2.47
244	24.7	419.66	0.07	1.50	48.45	2.77	0.24	1.24	3.83	0.62	1.59	0.86	0.55	0.04	0.04	0.23	0.67
16	24.7	484.73	0.08	2.46	57.29	3.11	0.15	1.49	4.37	4.37	1.27	0.84	0.83	0.03	0.05	0.50	0.97
16	24.7	453.04	0.08	2.58	58.15	1.55	0.51	4.37	0.63	1.16	2.49	3.01	0.22			0.21	1.44
15	24.7	41.64	0.06	1.00	42.45	0.25		0.72	0.06	0.82	0.25	0.37	0.35			0.07	0.15
346	24.8	127.53	0.06	1.13	44.36	0.96	0.08	2.24	0.99	0.22	0.48	0.47	0.31			0.09	0.94
381	24.8	307.92	0.07	1.25	45.91	3.18	0.28	0.37	1.86	0.59	1.52	0.53	0.22			0.11	1.15
286	24.8	253.96	0.08	2.03	58.73	3.37	0.34	1.53	4.36	0.94	1.84	0.85	0.71	0.03	0.04	0.46	1.03
302	24.8	537.10	0.08	2.63	58.97	2.49	0.22	1.67	1.52	0.34	0.95	0.87	0.52	0.03	0.04	0.40	1.35
207	24.8	348.74	0.07	1.55	49.41	3.13	0.34	0.58	3.19	0.52	1.29	0.78	0.31			0.22	0.94
172	24.8	28.37	0.06		38.85	0.43	0.05	0.20	1.10	0.04	0.19	0.28	0.32			0.03	0.44
19	24.8	327.92	0.07	1.25	45.75	3.00	0.29	1.67	0.70	0.29	0.75	0.34	2.76		0.05	0.17	0.79
29	24.8	529.30	0.10	3.94	67.38	2.19	0.09	1.66	2.37	0.46	0.28	3.52	3.63	0.03	0.05	0.27	0.83
47	24.9	338.95	0.08	2.04	54.25	3.06	0.37	0.70	2.43	0.65	1.48	0.82	0.35	0.02	0.02	0.38	1.01
257	24.9	108.74	0.06		42.41	1.38	0.23	0.22	1.30	0.28	0.70	0.32	0.16			0.09	0.84
4	25.0	173.07	0.06		43.00	1.83	0.25	0.54	0.50	0.23	0.83	0.59	0.48			0.14	0.81
13	25.0	927.35	0.09	2.99	62.14	4.36	0.80	1.30	4.36	2.06	3.84	1.38	1.09	0.06	0.06	0.64	1.69
68	25.1	269.52	0.06		39.99	3.46	0.44	0.43	0.31	0.07	0.88	0.46	0.21			0.07	1.45
35	25.1	216.38	0.06	1.17	45.61	2.06	0.20	0.85	1.84	0.46	0.71	0.72	0.25		0.03	0.12	0.50
29	25.1	719.69	0.09	3.45	65.49	4.02	0.71	2.33	4.36	1.43	2.29	1.32	0.86	0.04	0.06	0.46	2.19
79	25.1	151.59	0.08	2.46	58.55	2.62	0.16	0.99	1.11	0.24	0.58	1.10	0.34		0.04	0.24	1.37
65	25.1	424.50	0.07	1.77	52.43	3.56	0.58	1.05	2.72	0.50	1.79	1.13	0.44		0.03	0.18	1.58
26	25.1	86.35	0.06	1.19	45.89	1.18	0.14	0.62	0.26	0.06	0.34	0.59	0.21			0.12	1.14
58	25.1	88.30	0.06	1.04	43.94	1.39	0.12	0.36	0.46	0.10	0.63	0.67	0.10			0.12	0.64
67	25.2	138.14	0.05		38.99	1.87	0.18	0.42	0.15		0.58	0.29	0.09			0.09	0.83
60	25.2	157.41	0.06		40.50	1.19	0.09	0.41	1.70	0.54	0.60	0.54	0.32		0.02	0.23	0.41
33	25.2	359.55	0.08	2.62	60.08	2.89	0.29	0.65	1.97	0.49	1.52	0.84	0.33	0.03	0.04	0.25	1.91
50	25.2	304.87	0.06	1.13	45.38	2.39	0.32	0.46	3.30	0.56	1.16	0.54	0.34	0.03	0.03	0.23	0.95
10	25.2	141.41	0.05		39.39	0.86	0.05	0.34	0.19	2.64	0.55	0.43	0.46		0.04	0.06	0.24
7	25.2	184.60	0.06		43.56	0.10	0.05	1.86	0.10	4.36		1.29	0.07		0.13	0.05	0.02
5	25.2	136.04	0.05		39.66	1.64	0.19	0.62	0.49	0.98	0.61	0.42	0.03			0.16	0.86
21	25.3	193.14	0.06		41.79	2.31	0.32	0.29	0.52	0.13	1.14	0.47	0.17			0.08	1.22
9	25.3	649.84	0.08	2.60	60.11	4.25	0.57	0.41	0.94	0.25	2.48	0.66	0.33			0.13	3.86
36	25.4	167.14	0.07	1.41	49.28	2.00	0.27	0.63	1.28	0.21	0.74	0.33	0.18			0.17	1.04
20	25.4	380.82	0.07	1.40	49.17	3.23	0.60	0.56	2.36	0.37	0.90	0.55	0.34			0.16	1.77
48	25.4	106.21	0.07	1.72	52.65	1.55	0.05	0.61	0.99	0.23	0.36	0.85	0.59			0.10	1.37
18	25.4	1030.19	0.09	3.58	67.32	4.31	0.61	2.42	4.37	1.55	2.63	1.30	1.20	0.05	0.06	0.47	1.71
78	25.4	164.31	0.06		41.67	1.94	0.19	0.26	0.39	0.07	0.78	0.47	0.17			0.08	1.14
73	25.4	77.89	0.06		43.72	1.08	0.07	0.86	0.26	0.18	0.43	0.24	0.07		0.04	0.07	0.52
77	25.5	584.59	0.08	2.32	58.42	3.71	0.60	0.71	4.36	1.01	1.95	0.74	0.64	0.03	0.05	0.34	1.45
2	25.5	647.56	0.08	2.05	56.29	3.94	1.16	0.66	3.31	1.02	2.18	0.58	0.50	0.03	0.05	0.36	2.37
54	25.6	206.59	0.06		43.33	2.49	0.28	0.72	0.95	0.39	1.06	0.74	0.75			0.09	0.78
31	25.6	87.55	0.05		35.46	1.31	0.02	0.18	0.08	0.06	0.15	0.35	0.10		0.02	0.15	0.57

Nr	v (kms^{-1})	Int$_{main}$	R (µm)	E {nJ)	D (J/m^2)	^{12}C	^{16}O	^{23}Na	^{24}Mg	^{27}Al	^{28}Si	^{39}K	^{40}Ca	^{48}Ti	^{52}Cr	^{56}Fe	^{103}Rh
55	25.6	160.93	0.06		43.52	1.82	0.24	0.55	0.24	0.06	0.72	0.48	0.12			0.19	1.05
51	25.6	107.29	0.06		42.21	1.58	0.16	0.41	0.06	0.06	0.19	0.58	0.21			0.10	0.91
3	25.6	267.89	0.07	1.41	49.93	0.05	0.03	0.61	0.49	4.36		0.40	0.19		0.07	0.10	
39	25.7	789.99	0.08	2.17	57.72	4.35	0.79	3.62	1.07	2.57	4.35	2.84	1.32	0.02	0.03	0.20	1.14
44	25.7	207.56	0.07	1.58	52.01	2.10	0.18	0.50	1.65	0.27	0.92	0.74	0.41		0.03	0.11	0.95
72	25.7	408.46	0.08	2.06	56.81	3.54	0.37	0.53	2.44	0.71	1.64	0.47	1.23	0.04	0.04	0.21	1.43
6	25.7	350.33	0.07	1.31	48.89	0.47	0.04	4.36	0.56	3.25	0.32	2.31	0.25		0.09	0.58	0.14
7	25.7	185.41	0.06	1.07	45.72	2.48	0.30	0.52	0.39	1.02	0.78	0.68	0.04			0.08	0.94
64	25.9	165.19	0.05		39.46	2.05	0.42	0.69	0.71	0.19	0.67	0.20	0.20		0.03	0.23	1.20
5	25.9	161.19	0.08	2.34	59.86	1.19	0.16	1.25	0.88	2.62	0.32	0.68	0.55	0.03	0.03	0.33	0.91
16	26.0	175.88	0.06	1.05	46.29	2.09	0.24	0.23	0.25	0.04	0.61	0.26	0.12			0.08	1.18
40	26.0	613.88	0.08	2.66	63.05	4.36	1.06	0.73	4.01	0.84	2.10	0.82	0.55	0.04	0.04	0.25	2.51
3	26.0	584.72	0.08	2.08	57.95	3.79	0.50	1.52	1.39	1.03	2.62	0.83	1.62	0.05	0.06	0.40	2.02
9	26.0	207.06	0.06	1.29	49.53	0.45	0.02	1.21	0.06	4.35	0.14	0.72	0.60		0.08	0.27	0.73
12	26.1	503.87	0.09	3.00	65.95	3.71	0.37	0.44	2.55	0.50	1.57	0.46	0.40		0.02	0.20	2.34
1	26.1	238.57	0.06		44.38	1.93	0.45	1.21	1.85	2.11	0.73	1.16	0.36		0.04	0.14	0.46
6	26.2	533.56	0.08	2.18	59.36	4.36	0.72	1.28	0.83	0.48	1.50	1.24	0.72	0.03	0.03	0.23	3.04
3	26.2	133.73	0.08	2.35	60.93	0.25	0.02	2.48	0.56	0.64	0.13	2.10	0.09		0.03	0.14	1.18
66	26.3	286.08	0.06		44.98	2.86	0.57	0.35	1.76	0.34	0.91	0.32	0.27			0.09	1.13
53	26.3	161.65	0.05		37.91	1.68	0.18	0.50	1.00	0.25	0.72	0.43	0.20			0.07	0.54
5	26.3	284.41	0.06		45.53	1.90	0.37	1.02	0.79	0.50	0.97	1.40	2.57	0.03	0.04	0.18	0.75
7	26.3	680.95	0.07	1.85	56.51	4.36	1.09	1.12	0.86	0.14	2.38	2.73	0.27		0.06	0.41	2.47
57	26.5	463.48	0.08	2.28	61.07	2.77	0.27	0.65	3.67	0.88	1.79	0.77	0.56	0.02	0.04	0.25	1.02
63	26.5	77.11	0.06		43.93	1.13	0.17	0.25	0.53	0.13	0.37	0.45	0.13			0.08	0.82
8	26.5	640.85	0.08	2.55	63.53	2.89	0.38	0.48	3.64	0.95	2.98	0.64	0.51	0.03	0.04	0.22	2.35
1	26.5	111.74	0.05		39.02	1.42	0.16	0.80	0.08	0.87	0.20	0.62	0.02		0.03	0.08	0.75
82	26.6	760.03	0.09	3.16	68.59	4.13	0.69	0.86	4.35	1.39	2.58	0.43	0.66	0.04	0.04	0.67	1.90
69	26.7	165.39	0.05		36.98	1.93	0.25	0.34	0.07	0.06	0.21	0.40	0.16			0.09	0.91
2	26.7	390.48	0.07	1.99	59.06	2.77	0.34	0.28	1.05	0.35	2.08	0.41	0.23		0.02	0.24	1.98
1	26.9	208.84	0.06		46.38	2.70	0.23	0.33	0.66	0.19	0.61	0.50	0.33	0.02	0.02	0.34	1.25
75	27.0	205.04	0.07	2.13	61.40	3.86	0.23	0.75	1.40	0.33	0.90	0.79	0.88		0.04	0.22	1.40
83	27.0	218.74	0.06	1.05	48.57	2.63	0.24	0.26	1.16	0.32	0.97	0.43	0.29		0.03	0.13	1.22
49	27.0	138.62	0.06		45.64	1.58	0.14	0.31	0.34	0.80	0.74	0.34	0.19			0.06	0.75
8	27.0	251.73	0.05		40.88	2.00	0.63	1.23	0.62	1.01	1.91	1.17	0.16			0.14	0.59
2	27.1	215.94	0.06	1.43	53.93	2.52	0.42	0.68	0.24	1.36	0.56	0.62	0.04		0.05	0.47	1.18
61	27.2	229.66	0.06	1.26	51.97	1.96	0.21	0.43	1.76	0.63	1.39	0.43	0.32	0.03	0.05	0.24	0.58
71	27.2	353.52	0.06		47.50	3.77	0.58	0.63	0.49	0.10	1.15	0.38	0.10			0.18	2.05
1	27.2	981.08	0.08	3.23	71.18	4.36	0.52	1.97	1.31	0.14	4.36	0.95	0.45	0.03	0.04	0.21	1.91
4	27.2	247.86	0.05		43.04	2.07	0.25	0.42	2.08	1.25	0.89	0.36	0.03		0.04	0.18	0.60
38	27.4	151.18	0.05		41.65	1.80	0.20	0.59	0.38	0.23	0.57	0.34	0.40			0.07	1.00
15	27.4	491.59	0.07	1.82	59.46	3.26	0.30	1.17	4.37	0.64	1.59	1.63	0.83	0.02	0.04	0.24	0.46
24	27.4	306.86	0.06	1.04	49.37	2.58	0.20	0.70	1.68	0.40	1.59	1.27	0.55			0.09	1.13
11	27.4	414.53	0.07	1.81	59.17	0.95	0.15	1.30	0.62	4.36	0.54	0.73	0.08		0.13	0.34	
5	27.5	294.12	0.07	1.82	59.72	3.42	0.21	1.44	1.74	0.47	0.90	1.28	1.05	0.02	0.03	0.10	1.49
32	27.6	104.19	0.05		45.61	1.39	0.40	0.19	0.12	0.07	0.24	0.23	0.13			0.05	0.95
43	27.6	91.98	0.06	1.20	52.35	1.44	0.18	0.58	0.18	0.07	0.44	0.80	0.26			0.10	1.25
4	27.6	380.59	0.06		49.06	2.95	0.31	0.82	0.19	0.47	1.93	0.75	0.26		0.03	0.22	1.32
10	27.7	343.74	0.07	1.58	57.41	3.36	0.43	0.62	1.93	0.29	1.43	0.59	0.22		0.05	0.25	1.55
59	27.7	694.76	0.08	2.34	65.43	2.98	0.66	0.61	4.37	1.15	2.32	0.60	0.65	0.03	0.04	0.42	1.97
28	27.7	599.50	0.07	1.94	61.43	3.84	0.84	0.75	4.36	0.85	2.53	0.77	0.49	0.04	0.04	0.42	1.81

Nr	v (kms^{-1})	Int$_{main}$	R (µm)	E {nJ)	D (J/m^2)	^{12}C	^{16}O	^{23}Na	^{24}Mg	^{27}Al	^{28}Si	^{39}K	^{40}Ca	^{48}Ti	^{52}Cr	^{56}Fe	^{103}Rh
14	27.7	174.19	0.05		47.59	2.23	0.35	0.48	0.48	1.00	0.62	0.40	0.08		0.04	0.21	1.24
3	27.7	236.78	0.05		44.45	2.96	0.28	0.96	1.08	2.20	0.93	0.32	0.16	0.03	0.03	0.17	1.22
27	27.7	650.13	0.08	2.31	65.26	3.47	0.48	0.85	4.36	1.03	1.76	0.78	0.98	0.04	0.04	0.24	1.39
22	27.7	448.96	0.07	1.85	60.60	3.40	0.43	0.26	2.20	0.71	1.72	0.48	0.29		0.05	0.46	1.69
37	27.7	408.11	0.06	1.36	54.83	3.40	0.41	0.97	4.04	0.67	1.31	0.62	0.40	0.03	0.04	0.44	0.83
8	27.7	252.89	0.05		40.71	3.00	0.62	0.59	0.94	1.69	0.61	0.57	0.54		0.03	0.03	0.09
42	27.8	219.18	0.06		48.47	2.65	0.26	0.27	0.23	0.50	0.81	0.32	0.14			0.05	1.42
52	27.8	227.45	0.05		46.32	2.87	0.27	0.46	0.87	1.70	0.69	0.67	0.20			0.19	1.07
23	27.8	180.24	0.05		45.62	1.95	0.35	0.28	0.14	0.21	0.35	0.56	0.26			0.13	1.29
4	27.8	201.78	0.05		46.73	2.51	0.24	0.70	0.24	0.28	0.72	0.74	0.98	0.03	0.03	0.20	1.13
41	27.9	1226.96	0.12	9.48		2.42	1.02	2.13	1.39	3.25	4.36	1.90	0.56	0.03	0.03	0.28	2.86
4	28.0	411.24	0.06	1.44	56.44	2.55	0.37	1.49	0.42	4.25	1.11	1.23	0.04		0.04	0.31	0.97
19	28.1	120.00	0.06	1.15	52.60	1.57	0.22	0.35	1.34	0.27	0.57	0.42	0.33		0.04	0.19	1.14
1	28.1	14.88	0.05		45.10	0.34	0.03	0.31	0.05	0.40	0.06	0.24	0.13			0.02	0.27
8	28.1	773.10	0.07	2.17	65.22	2.26	0.43	3.36	3.52	3.07	1.74	3.13	0.05	0.03	0.17	1.66	1.19
25	28.2	242.44	0.05		44.62	1.80	0.19	0.32	1.98	0.40	1.06	0.38	0.23		0.03	0.16	0.65
70	28.2	186.53	0.06	1.28	54.95	1.74	0.20	0.56	1.86	0.38	0.76	0.98	0.30	0.03		0.15	0.77
2	28.3	411.73	0.05		47.11	1.11	0.17	2.14	0.20	4.36	0.56	0.87	0.23	0.03	0.10	0.21	0.04
74	28.4	295.10	0.05		48.05	3.53	0.26	0.37	0.55	0.08	1.45	0.36	0.57			0.11	0.93
62	28.4	357.32	0.10	5.28	89.02	3.20	0.52	0.68	2.93	0.53	1.21	0.36	0.31	0.03		0.20	1.31
6	28.6	243.15	0.05		42.68	2.67	0.40	0.49	0.33	0.39	0.82	0.46	0.17		0.03	0.14	1.23
9	28.6	183.49	0.05		45.27	1.85	0.19	0.18	0.44	0.28	0.94	0.27	0.27			0.08	1.42
2	28.6	184.03	0.05		47.05	1.61	0.21	0.25	1.05	0.22	1.09	0.34	0.57		0.03	0.19	0.67
46	28.7	298.98	0.05		50.24	1.96	0.63	0.81	2.54	0.77	1.46	0.50	0.27		0.03	0.21	0.94
47	28.8	166.56	0.06		51.62	1.78	0.08	0.50	0.20	0.06	0.49	0.32	0.28			0.05	0.57
17	28.8	240.99	0.05		49.45	1.58	0.19	0.52	2.38	0.41	0.62	0.37	0.48		0.05	0.09	0.60
84	28.9	212.23	0.04		42.62	2.77	0.59	0.42	0.23	0.23	0.42	0.39	0.31		0.04	0.57	1.02
3	29.0	584.12	0.06	1.45	59.45	3.58	0.36	0.56	1.03	0.07	2.71	0.85	0.66			0.16	2.15
11	29.2	312.90	0.06	1.26	57.06	2.85	0.57	1.96	1.86	0.36	1.03	0.69	0.26	0.03	0.03	0.46	1.36
81	29.2	674.22	0.08	2.70	73.91	4.02	0.56	1.29	4.37	0.85	2.15	1.11	0.82	0.04	0.04	0.30	2.34
6	29.2	520.69	0.05		49.79	3.74	1.04	1.23	2.05	1.64	1.42	0.67	0.08		0.03	0.42	2.45
76	29.4	641.14	0.06	1.56	62.06	2.84	0.74	0.85	4.37	0.12	1.74	0.85	0.70	0.04	0.05	0.35	1.58
34	29.4	72.39	0.05		47.31	1.03	0.11	0.14	0.04	0.03	0.13	0.20	0.09			0.06	0.62
7	29.5	279.12	0.06	1.25	57.88	2.46	0.34	0.39	0.38	0.13	0.45	0.38	0.20		0.02	0.09	2.22
80	29.6	568.11	0.06	1.51	61.84	3.56	0.44	0.44	2.79	0.79	2.70	0.43	0.24	0.02	0.04	0.24	1.83
30	29.7	125.20	0.04		40.03	1.60	0.19	0.10	0.19	0.08	0.48	0.17	0.25			0.07	0.74
56	29.8	850.01	0.06	1.60	63.81	4.36	1.05	0.52	4.36	1.10	3.05	0.64	0.79	0.05		0.57	1.86
5	29.8	565.11	0.06	1.11	56.36	3.36	0.26	2.01	0.23	0.05	2.49	0.94	0.38		0.04	0.65	1.39
45	30.0	184.89	0.05		51.98	1.77	0.33	0.39	1.10	0.20	0.63	0.55	0.22			0.12	0.90
6	30.0	231.45	0.06	1.70	65.54	0.85	0.16	2.38	1.40	3.15	0.26	0.70	0.42		0.03	0.11	0.49
1	30.1	518.28	0.05		54.10	1.21	0.48	2.11	1.64	0.61	0.93	0.34	4.38	0.04	0.03	0.29	0.49
26	30.2	254.24	0.05		51.50	1.76	0.31	0.64	2.45	0.46	1.19	1.00	0.27			0.22	0.80
16	30.2	471.93	0.04	45.37		2.67	0.77	0.51	1.98	0.35	0.98	0.56	0.26		0.03	0.34	2.78
20	30.2	296.39	0.05		53.21	2.80	0.33	0.42	2.17	0.46	0.90	0.54	0.40		0.03	0.20	0.97
4	30.3	227.50	0.05		54.64	1.35	0.17	0.54	0.22	3.88	0.21	0.89	0.33		0.10	0.20	0.54
1	30.5	135.74	0.05		52.23	2.07	0.30	0.35	0.57	0.17	0.43	0.50	0.18		0.03	0.17	1.05
24	30.5	474.04	0.04		43.70	3.93	1.05	0.31	0.36	0.36	0.93	0.33	0.23		0.04	0.55	2.35
2	30.5	117.43	0.05		51.82	0.87	0.05	0.36	0.04	1.67	0.19	0.30	0.26				

Nr	v (kms^{-1})	Int$_{main}$	R (µm)	E {nJ)	D (J/m^2)	^{12}C	^{16}O	^{23}Na	^{24}Mg	^{27}Al	^{28}Si	^{39}K	^{40}Ca	^{48}Ti	^{52}Cr	^{56}Fe	^{103}Rh
2	30.5	131.95	0.05		47.87	1.11	0.04	0.34	0.04	1.26	0.63	0.31	0.27			0.03	0.25
6	30.6	438.98	0.06	1.38	62.69	2.47	0.52	0.45	4.17	0.62	1.37	0.36	0.42		0.04	0.22	1.54
5	30.9	302.36	0.05		56.81	1.74	0.49	0.95	2.03	2.10	0.96	0.49	0.22	0.04		0.24	1.03
13	31.1	274.06	0.06	1.44	64.99	1.68	0.24	1.43	4.36	1.03	0.93	1.09	1.31		0.04	0.50	1.25
2	31.1	841.08	0.06	1.85	70.66	4.35	0.86	1.42	0.60	0.18	4.34	0.52	1.02		0.04	0.49	4.07
21	31.2	207.76	0.05		52.07	2.54	0.47	0.35	0.24	0.05	0.63	0.40	0.11			0.15	1.43
5	31.2	331.13	0.05	1.06	59.18	3.06	0.46	0.38	2.16	0.45	1.11	0.51	0.23			0.10	0.95
2	31.3	289.62	0.05		50.56	3.54	0.58	0.59	0.12	0.37	0.69	0.39	0.27			0.11	1.51
7	31.3	324.79	0.05		58.06	3.11	0.27	1.20	0.39	0.05	1.53	0.68	0.17			0.15	0.99
10	31.4	346.87	0.05		56.70	3.11	0.58	0.55	1.34	1.06	1.08	0.67	0.51		0.04	0.46	1.72
23	31.4	751.45	0.07	2.19	75.92	3.68	0.68	0.77	4.36	1.42	2.34	0.79	1.00	0.05	0.06	0.43	1.48
6	31.4	427.63	0.06	1.36	64.60	3.58	0.54	0.54	1.38	0.62	1.72	0.80	0.43	1.41	0.05	0.21	1.55
9	31.8	421.35				3.72	0.27	1.10	0.27	0.15	1.74	0.61	0.42			0.17	1.70
12	31.9	78.43	0.04		47.24	1.11	0.12	0.24	0.10	0.06	0.28	0.26	0.11			0.13	0.79
22	32.0	191.09	0.05		58.69	1.77	0.28	0.34	1.88	0.29	0.79	0.37	0.20		0.03	0.23	1.04
2	32.0	283.43	0.05	1.19	63.30	1.83	0.16	2.42	0.47	0.40	0.50	2.69	1.23			0.12	1.51
18	32.2	325.40	0.06	1.71	72.30	3.40	0.51	0.63	1.56	0.50	1.38	0.53	0.48		0.04	0.36	1.08
9	32.2	299.19	0.05	1.02	61.06	2.95	0.51	0.42	1.47	0.25	1.21	0.35	0.33			0.14	1.56
7	32.3	331.59	0.05		59.38	2.49	0.39	0.33	2.78	0.70	1.20	0.35	0.48			0.13	0.90
3	32.4	198.21	0.04		50.84	2.11	0.52	0.45	0.10	0.06	0.29	0.63	0.13		0.04	0.18	1.48
3	32.4	36.99				0.38	0.05	0.22	0.05	0.45	0.14	0.32	0.14			0.05	0.47
1	32.4	601.21	0.05	1.17	64.21	4.17	0.97	0.97	1.53	0.73	2.31	0.88	0.71	0.03	0.03	0.22	2.63
14	33.0	188.55	0.05	1.19	66.01	2.02	0.28	0.47	1.13	0.25	0.34	0.44	0.42			0.09	1.55
11	33.4	210.45	0.05		57.36	1.99	0.21	0.82	0.65	0.13	0.70	1.76	0.18			0.01	0.09
3	33.4	495.54	0.04		52.49	3.05	0.24	0.92	0.47	0.14	2.10	0.80	0.47			0.18	2.16
3	33.8	65.74	0.05		62.47	0.61		0.53	0.08	0.07	0.07	0.57	0.65			0.07	0.86
19	34.3	360.39	0.05		63.61	2.91	0.42	0.30	2.55	0.43	0.81	0.37	0.30		0.03	0.02	2.03
8	34.4	351.04	0.05		64.94	2.60	0.30	0.34	0.66	0.06	1.70	0.67	0.21		0.04	0.31	1.19
4	34.6	112.24	0.04		49.62	1.48	0.26	0.60	0.07	0.04	0.29	0.29	0.08			0.07	1.26
15	34.7	498.64	0.05		63.73	2.45	0.48	0.35	4.36	0.60	1.74	0.59	0.32		0.04	0.20	0.77
17	35.6	457.14	0.04		63.04	2.46	0.80	0.36	4.34	0.66	1.52	0.35	0.50	0.04	0.04	0.22	1.45
4	35.9	708.84	0.05	1.41	78.22	3.92	0.34	2.47	0.75	0.09	2.89	0.54	0.32		0.04	0.21	1.76
25	36.2	541.15	0.04		66.69	2.78	1.37	0.40	2.02	0.32	1.37	0.55	0.08		0.05	1.01	3.03
8	37.8	747.01	0.05	1.00	74.62	3.84	1.11	0.62	4.31	0.71	2.04	0.45	0.41	0.03	0.05	0.34	2.40
1	39.7	580.08	0.04		72.94	0.95	0.05	4.31	0.04	3.98	0.13	4.36	0.17		0.09	0.06	0.03
5	39.7	925.05	0.05	1.39	88.99	4.32	1.30	0.72	0.77	0.11	2.70	0.80	0.40			0.25	4.36

7.2.2 CDA-raw data

Nr	v (kms^{-1})	(Na)Mg	(Al)Si	(K)Ca	Fe	Rh
1	19.5	8.70	18.30	1.90	1.70	21.00
2	19.6	22.20	28.70	3.50	1.80	26.20
3	19.6	11.40	21.10	5.90	1.20	49.90
4	19.6	6.10	12.00	43.80	2.30	45.30
5	19.7	42.00	46.80	5.40	2.30	67.70
6	19.7	17.50	25.40	2.30	2.30	16.20
7	19.7	45.20	97.10	5.80	2.40	81.10
8	19.7	27.60	16.70	3.00	2.30	14.20
9	19.7	61.20	34.60	5.90	1.90	25.50
10	19.7	5.70	14.00	2.80	0.00	9.40
11	19.7	52.30	57.00	37.80	2.90	61.50
12	19.7	51.10	58.80	19.00	2.90	16.30
13	19.7	462.30	93.00	253.80	2.10	119.90
14	19.7	106.40	55.80	10.90	2.60	37.40
15	19.7	242.10	126.50	22.10	4.60	54.40
16	19.7	323.80	148.00	42.60	8.90	66.70
17	19.7	70.10	65.20	125.70	2.50	20.90
18	19.8	20.60	25.90	2.90	1.70	22.40
19	19.8	7.60	10.10	2.30	0.00	8.20
20	19.8	68.00	81.70	8.50	2.30	102.50
21	19.8	212.80	95.80	11.20	4.00	14.30
22	19.8	44.60	37.80	3.40	2.80	25.10
23	19.8	19.80	97.60	6.10	1.90	83.40
24	19.8	3.10	6.90	3.50	0.00	20.00
25	19.8	85.50	111.50	18.60	2.30	177.10
26	19.9	4.80	5.30	1.40	1.80	13.10
27	19.9	34.70	67.70	7.00	2.20	37.10
28	19.9	150.40	31.80	12.00	2.30	9.70
29	19.9	3.90	4.20	2.10	0.00	10.30
30	19.9	46.80	43.00	3.70	0.00	24.80
31	19.9	150.30	54.10	7.50	3.20	5.20
32	19.9	29.20	12.00	2.00	1.70	17.00
33	19.9	9.10	24.30	4.20	1.70	65.10
34	19.9	6.10	11.20	2.90	0.00	25.40
35	19.9	7.40	27.30	2.10	1.60	55.80
36	19.9	35.40	25.20	13.30	2.30	51.60
37	20	53.60	46.70	7.90	2.90	32.10
38	20	3.30	12.20	1.70	1.70	16.70
39	20	29.20	87.90	3.90	2.90	99.80
40	20	7.50	14.10	3.70	1.10	44.80
41	20	61.40	80.20	155.60	3.00	26.80
42	20.1	151.40	95.20	10.30	2.70	31.00
43	20.1	152.10	91.10	9.80	2.40	35.20
44	20.1	10.20	9.50	2.20	0.00	29.80
45	20.1	208.40	64.50	12.80	3.50	26.80
46	20.1	6.10	13.70	1.90	1.80	17.10
47	20.1	186.40	118.30	73.20	2.30	57.40
48	20.1	17.00	10.70	4.20	1.70	9.00
49	20.1	74.60	36.60	6.30	1.70	41.00
50	20.1	200.40	214.40	18.20	5.30	190.70

Nr	v (kms^{-1})	(Na)Mg	(Al)Si	(K)Ca	Fe	Rh
51	20.1	3.50	14.10	2.80	2.70	30.90
52	20.1	11.70	17.10	1.80	1.40	19.70
53	20.1	6.10	13.70	1.90	1.80	17.10
54	20.1	112.50	48.50	15.30	2.70	110.60
55	20.1	102.80	64.50	12.40	2.70	83.00
56	20.1	186.40	118.30	73.20	2.30	57.40
57	20.1	31.70	17.60	9.80	1.80	22.20
58	20.1	108.00	146.90	12.50	4.00	171.20
59	20.2	145.00	83.40	7.70	3.00	32.10
60	20.2	108.30	55.70	5.30	3.50	28.20
61	20.2	8.00	11.20	2.30	2.90	20.80
62	20.2	30.80	8.20	5.70	2.70	4.90
63	20.2	1.80	8.60	0.00	2.70	23.80
64	20.2	8.00	11.20	2.30	2.90	20.80
65	20.2	5.70	13.30	2.70	1.60	42.70
66	20.2	118.60	70.30	19.50	3.40	63.20
67	20.2	143.50	115.00	13.50	3.30	138.20
68	20.3	151.00	115.50	14.60	2.70	138.80
69	20.3	10.30	9.60	2.70	2.10	14.60
70	20.3	41.20	12.10	4.20	1.70	5.80
71	20.3	6.70	15.40	2.90	0.00	38.70
72	20.3	55.70	87.50	4.80	3.00	165.10
73	20.3	10.10	25.50	2.20	1.10	13.90
74	20.3	5.50	16.30	2.20	1.70	52.00
75	20.3	49.60	88.10	7.70	4.20	56.30
76	20.4	109.10	50.10	10.40	2.50	19.80
77	20.4	57.50	41.80	3.30	2.70	49.10
78	20.4	15.00	6.50	4.60	1.70	30.80
79	20.4	21.00	28.30	2.50	0.00	11.30
80	20.4	21.70	33.90	4.90	1.80	46.90
81	20.4	6.80	8.90	2.30	0.00	36.20
82	20.4	258.30	171.40	26.40	5.50	162.10
83	20.5	52.80	39.20	4.00	2.80	54.20
84	20.5	53.60	43.40	3.60	2.40	51.10
85	20.5	41.60	19.40	5.10	2.40	14.20
86	20.5	66.70	42.40	5.00	3.00	22.10
87	20.5	66.00	85.00	6.20	2.80	108.70
88	20.5	2.00	6.50	1.70	0.00	27.70
89	20.5	94.40	20.80	97.30	2.30	50.60
90	20.5	42.10	65.50	33.40	2.40	52.10
91	20.6	242.10	117.70	14.60	3.00	49.20
92	20.6	67.00	23.90	6.10	1.70	7.30
93	20.6	66.70	69.10	11.00	1.80	36.50
94	20.6	10.80	20.20	2.20	1.30	16.60
95	20.6	23.70	57.00	6.60	1.60	67.90
96	20.6	30.80	45.30	5.90	1.70	42.60
97	20.6	26.20	33.20	3.40	2.80	25.20
98	20.6	48.90	58.60	2.60	2.40	37.20

Nr	v (kms^{-1})	(Na)Mg	(Al)Si	(K)Ca	Fe	Rh
99	20.6	22.30	72.20	5.20	1.40	85.10
100	20.6	63.30	26.50	12.20	5.80	12.00
101	20.6	53.80	50.90	24.40	2.20	45.00
102	20.6	151.60	82.00	17.70	3.70	43.50
103	20.6	350.90	191.00	38.70	7.00	133.40
104	20.6	417.50	133.20	34.30	6.40	37.30
105	20.6	758.30	286.60	402.00	5.80	253.90
106	20.7	110.20	25.00	5.30	1.60	7.30
107	20.7	79.30	64.20	7.90	2.80	21.50
108	20.7	97.10	51.50	4.90	2.30	41.70
109	20.7	0.00	0.00	0.00	0.00	0.00
110	20.7	16.60	16.80	3.60	0.00	16.50
111	20.7	215.00	104.50	9.50	5.00	60.70
112	20.7	73.40	66.90	5.90	1.60	69.10
113	20.7	91.20	114.00	9.50	2.10	113.40
114	20.7	9.70	23.80	4.30	2.30	32.00
115	20.7	38.30	95.10	11.40	2.20	198.80
116	20.7	377.70	176.40	41.20	7.70	140.80
117	20.8	129.50	52.60	9.90	2.10	19.60
118	20.8	22.50	19.00	3.40	1.60	9.30
119	20.8	2.50	11.80	1.80	0.00	27.60
120	20.8	7.40	12.60	1.50	1.80	27.40
121	20.8	6.70	17.90	2.20	1.70	16.60
122	20.8	26.80	47.40	3.90	2.20	27.70
123	20.8	7.90	19.30	2.90	4.30	19.10
124	20.8	6.90	19.90	2.10	1.20	38.90
125	20.9	33.80	49.30	2.60	1.70	31.30
126	20.9	149.10	107.80	9.40	3.70	55.70
127	20.9	5.50	32.40	1.70	0.00	52.30
128	20.9	36.50	93.40	12.90	4.30	156.40
129	20.9	6.60	19.90	2.90	1.70	32.50
130	20.9	8.10	21.50	2.50	0.00	35.60
131	20.9	5.90	11.60	1.80	1.30	24.80
132	20.9	225.70	118.60	21.20	5.20	63.50
133	20.9	140.70	95.30	262.20	3.50	68.20
134	21	4.00	7.90	1.70	0.00	17.40
135	21	57.90	51.10	5.00	2.80	96.20
136	21	13.60	26.00	26.00	3.70	28.30
137	21	37.00	119.70	13.30	1.70	44.80
138	21	12.90	35.20	3.00	1.70	61.30
139	21	5.80	25.90	3.70	0.00	29.70
140	21	39.40	162.20	94.40	1.10	97.10
141	21	29.90	34.80	50.20	2.60	22.80
142	21	116.90	81.20	71.40	5.00	35.60
143	21	96.50	51.80	13.30	2.20	84.00
144	21.1	98.20	71.70	6.30	1.80	25.50
145	21.1	116.00	81.10	5.90	2.50	71.80
146	21.1	92.20	49.80	10.30	2.40	45.00
147	21.1	9.50	29.50	3.60	0.00	23.30

Nr	v (kms^{-1})	(Na)Mg	(Al)Si	(K)Ca	Fe	Rh
148	21.1	159.60	152.30	92.50	3.00	71.10
149	21.2	6.10	22.40	2.20	1.80	62.00
150	21.2	42.40	113.30	10.80	1.70	68.30
151	21.2	142.80	74.20	19.10	3.40	79.40
152	21.2	54.60	76.00	71.20	2.30	68.10
153	21.20	124.60	145.70	46.60	3.00	81.80
154	21.3	79.60	58.50	7.20	3.20	95.20
155	21.3	15.50	75.10	6.90	0.90	43.20
156	21.3	328.60	66.40	154.70	4.70	20.00
157	21.4	138.80	52.90	8.30	2.40	19.70
158	21.4	56.40	72.20	6.70	2.30	26.60
159	21.4	51.60	54.60	3.40	1.60	44.80
160	21.4	111.90	49.10	13.50	4.60	99.80
161	21.4	40.70	37.70	6.30	2.80	30.90
162	21.4	10.70	22.10	4.70	1.70	42.00
163	21.4	18.50	80.50	2.50	1.70	81.10
164	21.4	20.40	29.60	5.20	0.00	25.80
165	21.4	20.40	29.60	5.20	0.00	25.80
166	21.4	5.50	31.80	3.50	0.00	21.40
167	21.4	15.60	25.60	2.70	1.30	42.40
168	21.4	418.60	162.10	37.10	6.40	38.00
169	21.4	97.80	88.10	14.60	2.10	77.40
170	21.4	418.50	106.00	441.80	1.70	57.30
171	21.5	186.30	94.40	17.80	3.60	48.00
172	21.6	126.50	172.30	19.00	2.10	151.90
173	21.6	227.20	166.80	18.80	3.90	92.90
174	21.6	39.50	21.60	4.10	2.20	31.60
175	21.6	64.40	52.70	8.00	3.70	31.20
176	21.6	58.50	56.60	4.80	2.90	38.20
177	21.6	51.80	44.50	5.30	3.60	49.00
178	21.6	1.90	6.70	0.00	0.00	22.60
179	21.6	19.00	54.80	7.70	2.60	29.10
180	21.7	53.70	59.80	5.10	2.30	93.70
181	21.7	138.60	117.70	11.00	3.10	87.70
182	21.7	0.00	0.00	0.00	0.00	0.00
183	21.7	23.10	13.60	3.00	1.80	12.20
184	21.7	9.40	17.40	2.30	2.50	11.20
185	21.7	66.40	27.50	4.20	2.80	4.30
186	21.7	108.80	56.20	7.50	1.90	30.80
187	21.7	47.50	49.20	5.10	1.60	55.00
188	21.7	66.40	237.80	7.70	4.90	114.20
189	21.7	22.80	49.00	1.90	1.70	50.10
190	21.7	11.70	22.50	1.70	1.30	91.00
191	21.8	33.60	37.50	2.20	1.70	33.10
192	21.8	48.30	39.30	4.70	2.30	61.00
193	21.8	10.60	37.60	3.00	1.70	68.50
194	21.8	4.70	16.50	2.10	2.70	37.20
195	21.8	69.40	44.90	25.70	2.20	35.10
196	21.8	187.00	149.20	20.10	3.60	90.50

Nr	v (kms^{-1})	(Na)Mg	(Al)Si	(K)Ca	Fe	Rh
197	21.8	171.00	116.60	15.50	3.70	119.80
198	21.8	125.20	137.00	29.00	7.10	155.00
199	21.9	168.80	189.60	18.60	6.70	107.00
200	21.9	81.90	67.60	4.30	2.10	45.40
201	21.9	59.60	36.70	6.40	2.20	41.20
202	21.9	16.90	10.90	3.40	1.30	14.70
203	21.9	2.30	19.00	3.60	1.30	60.10
204	21.9	3.20	21.00	2.30	2.30	74.30
205	21.9	2.50	10.00	2.30	1.20	25.80
206	21.9	9.40	22.10	11.40	2.30	26.90
207	22	17.30	8.30	3.80	0.00	28.00
208	22	108.70	85.90	6.60	3.00	44.70
209	22	8.20	10.10	2.20	0.00	26.20
210	22	64.90	25.80	6.80	3.30	33.30
211	22	113.70	33.80	8.30	2.20	37.80
212	22	161.90	93.30	10.50	3.80	16.10
213	22	26.10	48.30	4.00	2.30	67.60
214	22	83.40	50.00	7.10	2.70	86.10
215	22	8.20	10.10	2.20	1.70	26.20
216	22	26.10	48.30	4.00	2.30	67.50
217	22	243.10	134.30	18.80	4.00	107.30
218	22	58.00	50.10	17.00	2.30	16.00
219	22.1	131.70	100.70	8.90	2.60	135.00
220	22.1	3.10	15.20	2.00	0.00	114.90
221	22.1	11.30	15.90	3.50	1.70	29.20
222	22.1	30.90	66.10	4.20	1.60	37.90
223	22.1	16.90	69.00	2.80	0.50	54.80
224	22.1	8.90	5.80	4.80	2.40	25.50
225	22.1	73.40	51.60	32.20	1.70	45.80
226	22.1	68.00	19.00	17.20	2.20	19.00
227	22.1	318.00	76.10	182.70	2.10	50.20
228	22.1	106.80	22.90	113.40	4.80	9.60
229	22.2	91.70	134.40	13.30	4.60	108.40
230	22.2	37.80	22.80	5.20	1.10	15.30
231	22.2	8.90	31.20	1.80	0.00	20.20
232	22.2	3.50	12.10	1.60	1.60	22.70
233	22.2	436.00	436.00	201.00	31.20	10.50
234	22.3	40.90	28.70	4.30	1.80	7.90
235	22.3	45.30	3.20	3.30	0.00	8.80
236	22.3	91.70	65.00	8.70	2.10	12.00
237	22.3	14.50	59.00	0.00	2.80	46.90
238	22.3	11.40	33.70	3.60	1.70	87.20
239	22.3	29.70	53.90	2.50	1.70	37.70
240	22.3	413.60	203.10	49.70	9.80	94.80
241	22.3	300.40	100.50	17.70	3.60	23.40
242	22.3	28.90	87.80	35.20	0.00	72.50
243	22.4	11.90	21.40	2.60	1.70	158.10
244	22.4	48.30	53.50	4.90	1.60	39.30
245	22.4	90.10	48.20	9.20	2.00	64.90

Nr	v (kms^{-1})	(Na)Mg	(Al)Si	(K)Ca	Fe	Rh
246	22.4	12.70	53.50	3.60	1.60	79.30
247	22.4	7.80	15.50	3.60	1.80	12.70
248	22.4	1.80	5.90	1.80	1.20	19.30
249	22.4	5.80	13.00	1.90	1.90	19.50
250	22.4	153.10	627.20	194.30	2.00	152.20
251	22.4	92.50	59.90	100.50	3.20	84.30
252	22.5	51.30	42.30	9.00	2.90	28.50
253	22.5	9.10	28.50	1.90	2.80	36.40
254	22.5	2.90	6.10	2.90	1.80	30.40
255	22.5	226.40	21.30	195.60	8.00	5.80
256	22.5	170.40	157.40	77.80	6.20	207.50
257	22.6	119.10	54.60	5.20	3.20	16.60
258	22.6	255.60	80.90	17.20	6.10	36.30
259	22.6	271.70	288.20	223.40	0.00	335.80
260	22.6	17.00	15.30	20.50	2.30	23.90
261	22.6	122.70	209.90	43.10	0.00	106.50
262	22.7	12.70	23.20	2.70	4.00	26.20
263	22.7	9.60	28.20	1.90	2.20	77.30
264	22.7	98.70	61.60	115.50	8.10	11.60
265	22.7	39.40	42.60	19.60	2.30	45.80
266	22.7	52.10	47.80	25.50	1.70	30.60
267	22.8	11.10	7.90	1.70	2.90	20.30
268	22.9	146.80	67.90	6.80	2.90	24.50
269	22.9	18.00	6.20	5.00	1.20	6.20
270	22.9	7.90	15.50	2.20	1.70	32.10
271	22.9	11.70	25.20	2.40	1.60	25.50
272	22.9	18.40	64.80	5.80	1.10	87.90
273	22.9	90.00	79.00	100.60	5.30	22.20
274	22.9	44.90	108.20	79.30	2.40	53.70
275	22.9	500.30	261.20	57.90	12.50	101.70
276	22.9	189.20	112.30	47.50	3.60	60.60
277	22.9	40.50	64.90	60.80	3.10	97.80
278	23	78.90	64.20	5.70	2.70	42.80
279	23	51.80	38.70	5.20	2.30	48.70
280	23	7.70	31.00	1.80	1.00	98.80
281	23	275.60	138.90	22.10	3.70	45.50
282	23	207.60	82.10	16.70	3.00	20.60
283	23.1	130.40	63.50	8.40	2.40	29.40
284	23.1	114.60	49.40	6.70	2.20	4.80
285	23.1	23.80	35.80	3.50	1.70	30.00
286	23.1	7.00	9.80	2.30	1.20	14.30
287	23.1	6.40	29.00	0.00	0.00	30.60
288	23.1	554.80	536.50	261.50	3.00	415.90
289	23.2	63.70	31.40	3.50	2.80	20.50
290	23.2	48.50	44.50	3.90	2.90	4.90
291	23.2	37.40	62.00	9.60	3.50	113.10
292	23.2	12.40	39.40	2.30	1.20	47.90
293	23.2	11.60	23.40	4.20	4.20	82.80
294	23.2	60.60	71.50	3.50	2.70	20.20

Nr	v (kms^{-1})	(Na)Mg	(Al)Si	(K)Ca	Fe	Rh
295	23.2	7.60	55.00	4.30	0.00	85.50
296	23.2	16.80	77.70	5.60	1.80	56.30
297	23.2	261.30	79.30	136.90	0.00	127.10
298	23.2	251.90	115.40	16.90	6.70	28.30
299	23.3	42.90	34.50	3.00	1.80	23.00
300	23.3	20.50	57.80	2.30	0.00	52.70
301	23.3	25.50	42.20	3.70	2.80	35.60
302	23.3	20.70	53.50	2.90	1.20	49.90
303	23.3	9.70	26.30	2.80	1.20	43.80
304	23.3	51.00	33.90	62.40	0.00	69.30
305	23.4	51.40	90.80	5.10	2.40	113.70
306	23.4	34.00	48.50	4.70	2.30	28.70
307	23.4	8.50	19.00	1.70	1.70	27.90
308	23.4	303.50	440.50	223.40	2.70	483.90
309	23.5	44.70	11.00	4.20	1.60	3.20
310	23.5	18.20	10.90	2.90	1.60	17.00
311	23.5	6.50	21.80	2.30	1.70	43.40
312	23.6	7.10	20.80	2.10	1.60	24.40
313	23.6	6.90	19.20	2.80	1.70	26.20
314	23.6	45.90	62.30	9.40	1.90	140.80
315	23.6	120.70	616.30	53.90	1.60	225.10
316	23.7	62.90	28.10	6.20	2.50	15.40
317	23.7	69.20	12.90	4.60	2.20	20.30
318	23.7	99.80	49.90	7.80	4.40	12.30
319	23.8	69.80	42.40	4.70	2.80	41.70
320	23.8	54.40	149.90	10.80	1.70	117.60
321	23.8	588.00	232.50	46.30	10.70	64.70
322	23.9	168.60	79.20	6.40	1.50	9.80
323	23.9	71.70	39.30	4.80	2.20	65.60
324	24	239.70	190.60	16.60	4.80	53.80
325	24	138.00	146.10	28.20	3.40	118.90
326	24	703.60	453.70	3.90	28.70	57.90
327	24	100.30	97.70	8.00	2.40	100.30
328	24.1	50.00	24.70	3.50	2.80	16.10
329	24.1	8.00	7.60	1.80	1.80	20.70
330	24.1	91.60	59.20	6.60	2.10	14.90
331	24.1	114.20	29.90	23.20	2.00	15.00
332	24.2	386.10	246.10	26.70	8.70	103.70
333	24.2	70.60	112.00	5.30	3.00	74.30
334	24.2	5.50	14.60	4.10	1.20	45.20
335	24.2	121.70	184.10	11.80	2.30	223.60
336	24.2	51.80	86.10	3.30	1.40	36.50
337	24.2	77.00	146.50	89.20	2.10	29.70
338	24.2	179.10	121.60	56.80	6.00	127.70
339	24.2	209.60	176.80	21.80	5.30	83.10
340	24.3	56.70	21.70	3.70	5.90	12.40
341	24.3	114.80	130.60	8.50	3.10	133.50
342	24.3	51.20	50.00	3.70	3.00	13.10
343	24.3	4.50	21.60	2.90	0.00	24.90
344	24.3	20.90	46.50	4.40	2.10	24.30
345	24.3	681.20	116.20	493.70	1.60	112.50
346	24.3	57.80	151.90	27.30	2.90	345.90
347	24.4	64.80	59.50	5.30	2.90	55.50
348	24.4	7.20	25.80	2.30	2.30	42.60
349	24.4	2.30	12.40	3.50	1.60	89.00
350	24.4	55.10	25.30	9.80	3.00	19.10
351	24.5	307.20	238.60	15.90	5.50	133.20
352	24.5	49.30	81.60	13.90	2.80	69.70
353	24.5	247.40	86.70	18.60	5.80	11.40
354	24.6	282.50	127.00	18.30	2.50	81.00
355	24.6	20.30	76.30	4.50	0.00	87.11
356	24.7	12.70	38.20	5.30	0.00	31.80

Bibliography

N. Altobelli, S. Kempf, M. Landgraf, R. Srama, V. Dikarev, H. Krüger, G. Moragas-Klostermeyer, and E. Grün. Cassini between venus and earth: Detection of interstellar grains. *J. Geophys. Res.*, 108(A10):7–1, 2003.

N. Altobelli, S.. Kempf, H. Krueger, M. Landgraf, M. Roy, and E. Grün. Interstellar dust flux measurements by the Galileo dust instrument between the orbits of Venus and Mars. *J. Geophys. Res.*, 110:7102–+, July 2005. doi: 10.1029/2004JA010772.

N. Altobelli, E. Grün, and M. Landgraf. A new look into the Helios dust experiment data: Presence of interstellar dust inside the Earth's orbit. *Astron. Astrophys.*, 448: 243–252, 2006.

N. Altobelli, S. Kempf, F. Postberg, V. Steerken, A. Poppe, G. Moragas-Klostermeyer, R. Soja, J. Schmidt, K. Fiege, and R. Srama. Exogenous dust streaming into Saturn's System. Interstellar Dust, Kuiper Belt dust and Cometary dust: The Cassini CDA inventory. in prep., 2013.

A Auer and K Sitte. Detection technique for micrometeoroids using impact ionization. *Earth and Planetary Science Letters*, 4(2):178–183, 1968.

D. Auwärter. Analyse experimentell hergestellter staubproben für die simulation von kosmischen partikeleinschlägen auf das cassini cda-massenspektrometer. Bachelor Thesis, Juni 2010.

O. Berg, H. Wolf, and J.W. Rhee. *Lecture Notes in Physics 48*, volume 233, chapter Interplanetary Dust and Zodiacal Light. Springer, 1975.

N.L. Bowen and J.F. Schairer. The system MgO-FeO-SiO_2. *Amer. J. Sci.*, $5(29)$: $197 - -217, 1935$.

J.P. Bradley, H.J. Humecki, and Germani. M.S. Germani. m.s. *Astrophys. J*, 394 (643pp), 1992.

J.P. Bradley, L.P. Keller, T.P. Snow, M. S. Hanner, G. J. Flynn, J. C. Gezo, S. J. Clemett, D. E. Brownlee, and J. E. Bowey. An infrared spectral match between gems and interstellar grains. *Science*, 285(5434):1716–1718, 1999. doi: 10.1126/science.285.5434.1716.

A. J Brearley. Disordered biopyriboles, amphibole, and talc in the allende meteorite: Products of nebular or parent body aqueous alteration? *Science*, 276(5315): 1103–1105, 1997.

A.E. Cameron and D.F. Jr. Eggers. An ion "velocitron". *Review of Scientific Instruments*, 19(605–607), 1948.

P.E. Champness. Nucleation and growth of iron oxides in olivines,(Mg, Fe)$_2SiO_4$. *Mineralogical Magazine*, $37(291) : 790 - -800, 1970$.

P.E. Champness and P. Gay. Oxidation on olivines. *Nature*, 218:157–158, 1968.

M. Cohen and F.C. Witteborn. Witteborn, f.c. *Astrophys. J*, 294:767–774, 1985.

E. Costantini, MJ Freyberg, and P. Predehl. Absorption and scattering by interstellar dust: an xmm-newton observation of cyg x-2. *Astronomy and Astrophysics*, 444 (1):187–200, 2005.

W. A. Deer, R. A. Howie, and J. Zussman. *Rock-forming minerals: Single-Chain Silicates*, volume 2a. Longman, 2nd edition, 1978.

W. A. Deer, R. A. Howie, and J. Zussman. *An introduction to the rock-forming minerals*. Longman, 2nd edition, 1992.

W. A. Deer, R. A. Howie, and J. Zussman. *Rock-forming minerals: Framework Silicates*, volume 4a. The Geological Society, 2001.

K. Demyk, AP Jones, E. Dartois, P. Cox, and L. d'Hendecourt. The chemical composition of the silicate dust around rafgl7009s and iras 19110+ 1045. *Astronomy and Astrophysics*, 349:267–275, 1999.

K. Demyk, P. Carrez, H. Leroux, P. Cordier, AP Jones, J. Borg, E. Quirico, PI Raynal, and L. d'Hendecourt. Structural and chemical alteration of crystalline olivine under low energy he irradiation. *Astronomy and Astrophysics*, 368(3):38–41, 2001.

H. Dietzel, G. Eichhorn, H. Fechtig, E. Gruen, H.-J. Hoffmann, and J. Kissel. The HEOS 2 and Helios micrometeoroid experiments. *Journal of Physics E: Scientific Instruments*, 6(3):209, 1973.

Y.P. Dikov, E.N. Evlanov, M. Fomenkova, M.A. Muhkin, M.A. Nazarov, O.F. Prilutsky, R.Z. Sagdeev, and B.V. Zubkov. Halley comet dust particle classification according to the data obtained by mass spectrometer puma-2. *Advances in Space Research*, 9(3):253–258, 1989.

J. Dorschner. From dust astrophysics towards dust mineralogy-a historical review. In T. Henning, editor, *Astromineralogy*, volume 815 of *Lecture notes in physics*, pages 1–60. Springer, 2010.

J. Dorschner and T. Henning. Dust Metamorphosis in the Galaxy. *Astron. Astrophys. Rev.*, 6:271–+, 1995. doi: 10.1007/BF00873686.

B. T. Draine. *Physics of the interstellar and intergalactic medium*. Princeton series in astrophysics. Princeton University Press, 1st edition, 2011.

F. J. Molster, L. B. F. M. Waters, A. G. G. M. Tielens, C. Koike, and H. Chihara. Crystalline silicate dust around evolved stars. *Astronomy and Astrophysics*, 382: 241–255, 2002.

G. J. Flynn. Physical, chemical, and mineralogical properties of Comet 81P/Wild 2 particles collected by Stardust. In *Advances in Meteoroid and Meteor Science*, pages 447–459. Springer, 2008.

G. J. Flynn, P. Bleuet, J. Borg, F.E. Bradley, J.P.Pand Brenker, S. Brennan, J. Bridges, D.E. Brownlee, E.S. Bullock, M. Burghammer, et al. Elemental compositions of comet 81P/Wild 2 samples collected by Stardust. *Science*, 314(5806):1731–1735, 2006.

J.F. Friichtenicht, N.L. Roy, and D.G. Becker. The Cosmic Dust Analyzer: experimental evaluation of an impact ionization model. In C N Hemenway, P M Millman, and A. F. Cook, editors, *Evolutionary and Physical properties of Meteoroids*, volume 319, pages 299–310. NASA SP, 1973.

H.P. Gail. Formation and evolution of minerals in accretion discs and stellar outflows. In Thomas Henning, editor, *Astromineralogy*, volume 815 of *Lecture notes in physics*, pages 61–141. Springer, 2nd edition, 2010.

H.P. Gail and P. Hoppe. The origins of protoplanetary dust and the formation of accretion disks. In D. Apai and D. S. Lauretta, editors, *Protoplanetary dust*, Cambridge Planetary Science, chapter 2, pages 27–65. Cambridge University Press, 1st edition, 2010.

J.I. Goldstein, E.R.D. Scott, and N.L. Chabot. Iron meteorites: Crystallization, thermal history parent bodies and origin. *Chemie der Erde*, 69:293–325, 2008.

A.L. Graps, E. Grün, H. Svedhem, H. Krüger, M. Horányi, A. Heck, and S. Lammers. Io as a source of the jovian dust streams. *Nature*, 405:48–50, 2000.

E. Grün, H.A. Zook, M. Baguhl, A. Balogh, S.J. Bame, H. Fechtig, R. Forsyth, M.S. Hanner, M. Horanyi, J. Kissel, B.-A. Lindblad, D. Linkert, G. Linkert, I. Mann, J.A.M. McDonnel, G.E. Morfill, J.L. Phillips, C. Polanskey, G. Schwehm, N. Siddique, P. Staubach, J. Svestka, and A. Taylor. Discovery of Jovian dust streams and interstellar grains by the Ulysses spacecraft. *Nature*, 362:428–430, 1993.

E. Grün, B. A. S. Gustafson, S. Dermott, and H. Fechtig, editors. *Interplanetary dust*. Springer, Berlin, 2001.

E. Grün, R. Srama, H. Krüger, S. Kempf, V. Dikarev, S. Helfert, and G. Moragas-Klostermeyer. 2002 kuiper prize lecture: dust astronomy. *Icarus*, 174(1):1–14, 2005.

M.L. Guglielmino. Preparation and characterization of cosmic dust analogues for calibration of state-of-the-art mass spectrometers onboard space missions. Master's thesis, Universität Heidelberg, Institut für Geowissenschaften, October 2012.

B.A.S. Gustafson and N.Y. Misconi. Streaming of interstellar grains in the solar system. *Nature*, 282:276–78, 1979.

S.E. Haggerty and I. Baker. The alteration of olivine in basaltic and associated lavas. *Contributions to mineralogy and petrology*, 16(3):233–257, 1967.

M.S. Hanner, J.G. Sparrow, J.L. Weinberg, and D.E. Beeson. Pioneer 10 observations of zodiacal light brightness near the ecliptic: Changes with heliocentric distance. In *Interplanetary Dust and Zodiacal Light*, pages 29–35. Springer, 1976.

M.S.S Hanner. Composition and optical properties of cometary dust. In *IAU Colloq. 150: Physics, Chemistry, and Dynamics of Interplanetary Dust*, volume 104 of *ASP Conf. Ser.*, page 367pp, 1996.

M.S.S Hanner, D.K. Lynch, and R.W. Russell. The 8-13 micron spectra of comets and the composition of silicate grains. *The Astrophysical Journal*, 425:274–285, 1994.

D. O. Hansen. Mass analysis of ions produced by hypervelocity impact. *Applied physics letters*, 13(3):89–91, 1968.

F.C. Hawthorne, A. Kato, H. J. Kisch, V. .G Krivovichev, K. Linthout, J. Laird, W.V. Maresch, J.C. Schumacher, N.C.N. Stephenson, E.J.W. Whittaker, et al. Nomenclature of amphiboles: report of the subcommittee on amphiboles of the international mineralogical association, commission on new minerals and mineral names. *The Canadian Mineralogist*, 35:219–246, 1997.

T. Henning. Cosmic Silicates. *Annu. Rev. Astron. Astrophys.*, 48:21–46, September 2010. doi: 10.1146/annurev-astro-081309-130815.

J. K. Hillier, N. McBride, S. F. Green, S. Kempf, and R. Srama. Modelling CDA mass spectra. *Planet. Space Sci.*, 54:1007–1013, August 2006. doi: 10.1016/j.pss.2006.05.013.

J. K. Hillier, S. F. Green, N. McBride, J. P. Schwanethal, F. Postberg, R. Srama, S. Kempf, G. Moragas-Klostermeyer, J. A. M. McDonnell, and E. Grün. The composition of Saturn's E ring. *Mon. Not. Roy. Astron. Soc.*, 377:1588–1596, June 2007. doi: 10.1111/j.1365-2966.2007.11710.x.

J. K. Hillier, S. Sestak, S. F. Green, F. Postberg, R. Srama, and M. Trieloff. The production of platinum-coated silicate nanoparticle aggregates for use in hypervelocity impact experiments. *Planet. Space Sci.*, 2009.

J. K. Hillier, F. Postberg, S. Sestak, R. Srama, S. Kempf, M. Trieloff, Z. Sternovsky, and S. F. Green. Impact ionization mass spectra of anorthite cosmic dust analogue particles. *Journal of Geophysical Research: Planets (1991–2012)*, 117(E9):16 pages, 2012.

C. Höfer. Preparation and analysis of analogue material for extraterrestrial dust. Bachelor Thesis, 2010.

T. E. Holzer. Interaction between the solar wind and the interstellar medium. *Annual review of astronomy and astrophysics*, 27:199–234, 1989.

K. Hornung and S. Drapatz. Residual ionization after impact of large dust particles. In N. Longdon, editor, *The Comet Halley Probe. Plasma Environment*, pages 23–37, Paris, 1981. European space agency.

D. H. Humes. Results of Pioneer 10 and 11 meteoroid experiments - Interplanetary and near-Saturn. *J. Geophys. Res.*, 85:5841–5852, November 1980.

C. Jäger, FJ Molster, J. Dorschner, T. Henning, H. Mutschke, and L. Waters. Steps toward interstellar silicate mineralogy. iv. the crystalline revolution. *Astronomy and Astrophysics*, 339:904–916, 1998.

T.W. Jones and K.M. Merrill. Model dust envelopes around late-type stars. *The Astrophysical Journal*, 209:509–524, 1976.

M. Kaliwoda. *Mantel–Xenolithe des Harrat Uwayrid (Saudi–Arabien): Archive der stofflichen und thermischen Entwicklung des lithosphärischen Erdmantels im Bereich eines passiven Kontinentalrandes*. PhD thesis, Heidelberg University, 2004.

F. Kemper, A. De Koter, L. Waters, J. Bouwman, and A. Tielens. Dust and the spectral energy distribution of the oh/ir star oh 127.8+ 0.0: Evidence for circumstellar metallic iron. *Astronomy and Astrophysics*, 384(2):585–593, 2002.

F. Kemper, WJ Vriend, and A. Tielens. Erratum:"the absence of crystalline silicates in the diffuse interstellar medium"(apj, 609, 826 [2004]). *The Astrophysical Journal*, 633:534–534, 2005.

S. Kempf, R. Srama, N. Altobelli, S. Auer, V. Tschernjawski, J. Bradley, M.E. Burton, S. Helfert, T.V. Johnson, H. Krüger, G. Moragas-Klostermeyer, and E. Grün. Cassini between Earth and asteroid belt: First in-situ charge measurements of interplanetary grains. *Icarus*, 171:317–335, 2004.

S. Kempf, R. Srama, F. Postberg, M. Burton, S. F. Green, S. Helfert, J. K. Hillier, N. McBride, J. A. M. McDonnell, G. Moragas-Klostermeyer, M. Roy, and E. Grün. Composition of saturnian stream particles. *Science*, 307:1274–1276, 2005.

J. Kissel. The Giotto Particulate Impact Analyser. *ESA Special Publication*, 1070: 67–83, 1986.

J. Kissel, F. R. Krueger, J. Silén, and B. C. Clark. The Cometary and Interstellar Dust Analyzer at Comet 81P/Wild 2. *Science*, 304:1774–1776, June 2004. doi: 10.1126/science.1098836.

R.F. Knacke, S.B. Fajardo-Acosta, C.M. Telesco, J.A. Hackwell, D.K. Lynch, and R.W. Russell. The silicates in the disk of beta pictoris. *The Astrophysical Journal*, 418: 440, 1993.

C. Koike, H. Shibai, and A. Tuchiyama. Extinction of olivine and pyroxene in the mid infrared and far infrared. *Monthly Notices of the Royal Astronomical Society*, 264: 654, 1993.

C. Koike, A. Tsuchiyama, H. Shibai, H. Suto, T. Tanabé, H. Chihara, H. Sogawa, H. Mouri, and K. Okada. Absorption spectra of mg-rich mg-fe and ca pyroxenes in the mid-and far-infrared regions. *Astronomy and Astrophysics*, 363:1115–1122, 2000.

M. Koltermann. Der thermische zerfall fayalithaltiger olivine bei hohen temperaturen. *Neues Jahr. Min*, Mh:181–192, 1962.

R. Lallement, B. Y. Welsh, J.L. Vergely, F. Crifo, and D. Sfeir. 3d mapping of the dense interstellar gas around the local bubble. *Astronomy and Astrophysics*, 411 (3):447–464, 2003.

M. Landgraf. Modeling the motion and distribution of interstellar dust inside the heliosphere. *J. Geophys. Res.*, 105:10303–10316, 2000.

M Landgraf, K Augustsson, E Grün, and BÅS Gustafson. Deflection of the local interstellar dust flow by solar radiation pressure. *Science*, 286(5448):2319–2322, 1999.

M. Landgraf, W.J. Baggaley, E. Grün, H. Krüger, and G. Linkert. Aspects of the mass distribution of interstellar dust grains in the solar system from in situ measurements. *J. Geophys. Res.*, 105:10343–10352, 2000.

M. Landgraf, J.-C. Liou, H.A. Zook, and E. Grün. Origins of Solar System Dust beyond Jupiter. *Astron. J.*, 123:2857–2861, 2002.

P. Lavila. Analyzing time-of-flight spectra of cda. Research report, Max Planck Institut für Kernphysik, 2002.

Ch. Leinert and E. Grün. Interplanetary dust. In R. Schwenn and E. Marsch, editors, *Physics of the Inner Heliosphere I*, pages 207–275, Berlin, 1990. Springer Verlag.

I.J. Lin and P. Somasundaran. Alterations in properties of samples during their preparation by grinding. *Powder Technology*, 6(3):171–179, 1972.

T.J. Linde and T.I. Gombosi. Interstellar dust filtration at the heliospheric interface. *J. Geophys. Res.*, 105:10411–10418, 2000. URL http://adsabs.harvard.edu/cgi-bin/nph-bib_query?bibcode=2000JGR...10510411L{&}db_key=AST.

C.M Lisse, K.E. Kraemer, J.A. Nuth, A. Li, and D. Joswiak. Comparison of the composition of the tempel 1 ejecta to the dust in comet c/hale bopp 1995 o1 and yso hd 100546. *Icarus*, 187:69–86, March 2007.

K. Lodders and B. Fegley. The Planetary Scientist's Companion. Oxford University Press, 1998.

T. Lyubetskaya and J. Korenaga. Chemical composition of earth's primitive mantle and its variance: 1. method and results. *Journal of Geophysical Research: Solid Earth*, 112(B3):21 pages, 2007.

I.D.R Mackinnon and F.J.M. Rietmeijer. Mineralogy of chondritic interplanetary dust particles. *Reviews of Geophysics*, 25(7):1527–1553, 1987.

I. Mann. Interstellar Dust in the Solar System. *Annu. Rev. Astron. Astrophys.*, 48: 173–203, September 2010. doi: 10.1146/annurev-astro-081309-130846.

M.C. McCanta, A.H. Treiman, M.D. Dyar, C.M. Alexander, and E.J. Rumble, D .and Essene. The lapaz icefield 04840 meteorite: mineralogy, metamorphism, and origin of an amphibole-and biotite-bearing r chondrite. *Geochimica et Cosmochimica Acta*, 72(23):5757–5780, 2008.

F.M. McCubbin, A. Smirnov, H. Nekvasil, J. Wang, E. Hauri, and D.H. Lindsley. Hydrous magmatism on mars: A source of water for the surface and subsurface during the amazonian. *Earth and Planetary Science Letters*, 292(1):132–138, 2010.

J.A.M. McDonnell. Microparticle studies by space instrumentation. *Cosmic dust*, 1: 337–426, 1978.

D. Mihalas and J. Binney. Galactic astronomy: Structure and kinematics. *San Francisco, CA, WH Freeman and Co.,*, 1(2nd ed.):608 p., 1981.

M. Min, L. B. F. M. Waters, A. de Koter, J. W. Hovenier, L. P. Keller, and F. Markwick-Kemper. The shape and composition of interstellar silicate grains. *Astronomy Astrophysics*, 462(2):667–676, 2007.

A. Mocker. *Comparison of impact ionisation plasma with laser ionisation*. PhD thesis, Heidelberg University, 2011.

A. Mocker, S. Bugiel, S. Auer, G. Baust, K. Drake, K. Fiege, E. Grün, F. Heckmann, S. Helfert, J. K. Hillier, S. Kempf, G. Matt, K. Otto, F. Postberg, H.-P. Röser, Z. Sternovsky, and R. Srama. A 2mv van de graaff accelerator as a tool for planetary and impact physics research. *Rev. Sci. Instr.*, 2011.

A. Mocker, K. Hornung, Z. Sternovsky, T. Kempf, S.and Johnson, E. Grün, and R. Srama. A linear tof mass spectrometer as a tool for the investigation of impact ionisation plasma. In *AIP Conference Proceedings*, volume 1426, page 859pp, 2012.

F. J. Molster, L. B. F. M. Waters, and F. Kemper. The mineralogy of interstellar and circumstellar dust in galaxies. In Thomas Henning, editor, *Astromineralogy*, volume 815 of *Lecture notes in physics*, pages 143–201. Springer, 2nd edition, 2010.

G.E. Morfill and E. Grün. The motion of charged dust particles in interplanetary space—i. the zodiacal dust cloud. *Planetary and Space Science*, 27(10):1269–1282, 1979.

T. Mothé-Diniz, F. Roig, and J.M. Carvano. Reanalysis of asteroid families structure through visible spectroscopy. *Icarus*, 174(1):54–80, 2005.

R.H. Nafziger and A. Muan. Equilibrium phase compositions and thermodynamic properties of olivines and pyroxenes in the system MgO-FeO-SiO_2. *American Mineralogist*, $58 : 457 - -466, 1967$.

E.F. Osborn and E.B. Watson. Studies of phase relations in sub-alkaline volcanic rock series. *Ann. Rept. Dir. Geophys. Lab*, 1976-77:472–478, 1977.

R. Philpotts, A and J.J. Ague. *Principles of igneous and metamorphic petrology*. Prentice Hall New Jersey, 1st edition, 1990.

A. Poppe, D. James, B. Jacobsmeyer, and M. Horányi. First results from the venetia burney student dust counter on the new horizons mission. *Geophysical Research Letters*, 37(11), 2010.

F. Postberg. *A new view on the composition of dust in the solar system: Results from the Cassini Dust Detector*. PhD thesis, Universität Heidelberg, 2007.

F. Postberg, S. Kempf, R. Srama, S. F. Green, J. K. Hillier, N. McBride, and E. Grün. Composition of jovian dust stream particles. *Icarus*, 183:122–134, July 2006. doi: 10.1016/j.icarus.2006.02.001.

F. Postberg, S. Kempf, J. K. Hillier, R. Srama, S. F. Green, N. McBride, and E. Grün. The E-ring in the vicinity of Enceladus II: Signatures of Enceladus in the elemental composition of E-ring particles. *Icarus*, 193:438–454, February 2008. doi: 10.1016/j.icarus.2007.09.001.

F. Postberg, S. Kempf, D. Rost, T. Stephan, R. Srama, M. Trieloff, A. Mocker, and M. Goerlich. Discriminating contamination from particle components in spectra of Cassini's dust detector CDA. *Planet. Space Sci.*, 57:1359–1374, October 2009a. doi: 10.1016/j.pss.2009.06.027.

F. Postberg, S. Kempf, J. Schmidt, N. Brilliantov, A. Beinsen, B. Abel, U. Buck, and R. Srama. Sodium salts in E-ring ice grains from an ocean below the surface of Enceladus. *Nature*, 459:1098–1101, June 2009b. doi: 10.1038/nature08046.

A. Putnis. *An introduction to mineral sciences*. Cambridge University Press, 1st edition, 1992.

J.D. Richardson, J. C. Kasper, C. Wang, J. W. Belcher, and A. J. Lazarus. Cool heliosheath plasma and deceleration of the upstream solar wind at the termination shock. *Nature*, 454(7200):63–66, 2008.

E.R.D. Scott and A. N. Krot. Chondrites and their components. In A. M. Davis, editor, *Meteorites, Comets and Planets*, chapter 1.07. Treatise on Geochemistry Update 1, Elsevier, 2007.

Z. Sekanina. *Cometary Dust*, pages 95–161. Springer-Verlag, 2001.

G. C. Sloan, K. E. Kraemer, P. R. Wood, A. A. Zijlstra, J. Bernard-Salas, D. Devost, and J. R. Houck. The magellanic zoo: Mid-infrared spitzer spectroscopy of evolved stars and circumstellar dust in the magellanic clouds. *The Astrophysical Journal*, 686(2):1056, 2008.

R. K. Soberman, S. L. Neste, and K. Lichtenfeld. Optical measurement of interplanetary particulates from pioneer 10. *Journal of Geophysical Research*, 79(25): 3685–3694, 1974.

R. Srama, T. J. Ahrens, N. Altobelli, S. Auer, J. G. Bradley, M. Burton, V. V. Dikarev, T. Economou, H. Fechtig, M. Görlich, M. Grande, A. Graps, E. Grün, O. Havnes, S. Helfert, M. Horanyi, E. Igenbergs, E. K. Jessberger, T. V. Johnson, S. Kempf, A. V. Krivov, H. Krüger, A. Mocker-Ahlreep, G. Moragas-Klostermeyer, P. Lamy, M. Landgraf, D. Linkert, G. Linkert, F. Lura, J. A. M. McDonnell, D. Möhlmann, G. E. Morfill, M. Müller, M. Roy, G. Schäfer, G. Schlotzhauer, G. H. Schwehm, F. Spahn, M. Stübig, J. Svestka, V. Tschernjawski, A. J. Tuzzolino, R. Wäsch, and H. A. Zook. The Cassini Cosmic Dust Analyzer. *Space Science Reviews*, 114: 465–518, September 2004. doi: 10.1007/s11214-004-1435-z.

R. Srama, M. Rachev, A. Srowig, V. Dikarev, S. Helfert, S. Kempf, D. Linkert, G. Moragas-Klostermeyer, and E. Grün. Performance of an advanced dust telescope. In D. Danesy, editor, *Proceedings of the 4th European conference on space debris*, volume 587 of *ESA Special Publication*, pages 171–176. ESA Special Publication, August 2005.

R. Srama, S. Kempf, G. Moragas-Klostermeyer, M. Landgraf, S. Helfert, Z. Sternovsky, M. Rachev, and E. Gruen. Laboratory Tests of the Large Area Mass Analyser. *Dust in Planetary Systems*, 643:209–212, January 2007.

T. Stephan. Tof-sims in cosmochemistry. *Planetary and Space Science*, 49(9):859–906, 2001.

V. J. Sterken, N. Altobelli, S. Kempf, G. Schwehm, R. Srama, and E. Grün. The flow of interstellar dust into the solar system. *Astronomy & Astrophysics*, 538, 2012.

Z. Sternovsky. The effect of ion–neutral collisions on the weakly collisional plasma-sheath and the reduction of the ion flux to the wall. *Plasma Sources Science and Technology*, 14(1):32, 2005.

Z. Sternovsky, K. Amyx, G. Bano, M. Landgraf, M. Horanyi, S. Knappmiller, S. Robertson, E. Grün, R. Srama, and S. Auer. Large area mass analyzer instrument for the chemical analysis of interstellar dust particles. *Review of Scientific Instruments*, 78(1):014501, January 2007. doi: 10.1063/1.2431089.

J.J. Thomson. On the appearance of helium and neon in vacuum tubes. *Nature*, 90 (2259):645–647, 1913.

A.G.G.M Tielens. *The Physics and Chemistry of the Interstellar Medium*. Cambridge University Press, 1st edition, 2005.

Acknowledgements

My thanks go out to my PhD committee: Prof. Dr. Mario Trieloff, PD Dr.-Ing Ralf Srama, Prof. Dr. Rainer Altherr and Prof. Dr. Wolfgang Stinnesbeck.

Mario and Ralf, thank you very, very much for your excellent supervision, your inspiring ideas and the long fruitful discussions. You have always been there to help and to brainstorm.

Jon and Frank, fellow "spectrolators", I am extremely grateful for your experience, your help, your ideas and the spectrolator-meetings, with our incredible valuable discussions. I might now have knots in my brain, I will never be able to solve..ever.

Sebastian, thank you for your invaluable help with the accelerator-campaigns and all other things! It's just great working with you!

Massimo, thank you so much for your awesome contribution to mineral analysis and preparation. Working with you is "flow". To the future!

Ilona and Oliver, thank you always for preparations, especially quick ones! Thank you for Wallander and for very nice chats in between.

Sascha, thank you for leading me into that field of science.

Ruben, Gerald, Stef, Saskia and Eric, thank you for the music!

Anna, thank you, thank you, thank you!! Thank you for always being there, either transatlantic or local, day and night. Besties!

Above all, I thank my family and my man for their unshakable faith in me, their enduring encouragement, their loyalty and their love. Rob, I know, I wasn't easy in times and I cannot say how grateful I am for your patience and your love.

Eidesstattliche Versicherung gemäß § 8 der Promotionsordnung der Naturwissenschaftlich-Mathematischen Gesamtfakultät der Universität Heidelberg

1. Bei der eingereichten Dissertation zu dem Thema

Composition of interstellar dust as seen by the Cassini Cosmic Dust Analyzer

handelt es sich um meine eigenständig erbrachte Leistung.

2. Ich habe nur die angegebenen Quellen und Hilfsmittel benutzt und mich keiner unzulässigen Hilfe Dritter bedient. Insbesondere habe ich wörtlich oder sinngemäß aus anderen Werken übernommene Inhalte als solche kenntlich gemacht.

3. Die Arbeit oder Teile davon habe ich ~~wie folgt/~~bislang nicht[1)] an einer Hochschule des In- oder Auslands als Bestandteil einer Prüfungs- oder Qualifikationsleistung vorgelegt.

Titel der Arbeit:_____

Hochschule und Jahr:_____

Art der Prüfungs- oder Qualifikationsleistung:_____

4. Die Richtigkeit der vorstehenden Erklärungen bestätige ich.

5. Die Bedeutung der eidesstattlichen Versicherung und die strafrechtlichen Folgen einer unrichtigen oder unvollständigen eidesstattlichen Versicherung sind mir bekannt.

Ich versichere an Eides statt, dass ich nach bestem Wissen die reine Wahrheit erklärt und nichts verschwiegen habe.

_____ _____

Ort und Datum Unterschrift

[1)] Nicht Zutreffendes streichen. Bei Bejahung sind anzugeben: der Titel der andernorts vorgelegten Arbeit, die Hochschule, das Jahr der Vorlage und die Art der Prüfungs- oder Qualifikationsleistung.